10. Measurements of Turbulent Flows

Fluid flows in nature and technology normally depart from laminarity and are turbulent in the majority of cases, including flows around bodies such as airplanes, vehicles, ships, and in internal flows such as in ducts, turbomachines, propulsors, and even in blood circulation in the human body. Laminarity is the anomaly and not the standard. As will be shown in this chapter, the parameter which is fundamental to the transition from laminarity to turbulence is the Reynolds number, i.e., the ratio of inertial to viscous forces. In Sect. 10.1 the statistical Eulerian description of turbulent flows will be developed followed by a section on Reynolds decomposition and Reynolds equations. Section 10.1.3 finally surveys scales in turbulent flows.

In Sect. 10.2 the optical Lagrangian particle-tracking technique, capable of producing robust, single- and multiparticle Lagrangian measurements, is presented. First the image-processing algorithms used to determine the particle trajectories are discussed and then the implementation of the technique in the laboratory is described. A brief presentation of results focusing on the separation of particle pairs in intense turbulence is also given.

In Sect. 10.3 a novel type of random flow in a dilute polymer solution of a flexible high-molecular-weight polymer in two different flow setups that share the same feature of high curvature of the flow lines is discussed. In the first part of this section the hydrodynamic description of dilute polymer solution flows and the nondimensional parameters that follow from these equations to characterize these flows are presented. Variation of one of these control parameter responsible for the elastic properties of a fluid can lead to a new elastic instability in various flows that is distinguished by the presence of curvilinear trajectories. The theoretical criteria for this elastic instability in three different flows together with experimental verification are discussed. To complete the basics, the rheometric properties of the polymer solutions used and their relation to Boger fluids are given.

The first observation of elastic turbulence, in the flow between two plates, is described. Then the experimental measuring techniques used to characterize the flow are given, and a complete description of the results of measurements together with a discussion of the results is presented. Finally, the role of elastic stress, a recent theory of elastic turbulence, and comparative studies of elastic versus hydrodynamic turbulence are discussed. The last part of the section deals with the description of the elastic turbulence in a curvilinear channel or Dean flow, where a particularly detailed experiment on mixing due to elastic turbulence was conducted. A summary of the results is given finally.

Section 10.4 briefly reviews large-eddy simulations (LES) and the specific data requirements for LES (Sect. 10.4.1) and then describes the experimental methods that have been employed to obtain such data starting with arrays of point-measurement techniques (Sect. 10.4.2) and optical planar velocimetry measurement methods (Sect. 10.4.3). Sample results from the latter applied to studies of LES models are presented in (Sect. 10.4.4). The application of optical volumetric techniques for three-dimensional (3-D) velocity measurements are described in Sect. 10.4.5. Scalar fluctuation measurements using optical techniques and their applications to the study of LES variables of interest to scalar mixing and combustion are reviewed in Sect. 10.4.6.

10.1 Statistical Eulerian Description of Turbulent Flows

When dealing with fluid flows in nature and technology, departure from laminarity and the presence of turbulence are normally observed; in fact, flows are turbulent in the majority of cases, such as in external flows around bodies as aeroplanes, vehicles, ships, and in internal flows as in ducts, turbomachines, propulsors, and even in blood circulation in the human body. Laminarity is the anomaly and not the standard.

10.1.1 Basics of Measurements of Turbulent Flows

Differences Between Measurements in Laminar and Turbulent Flows

As will be shown in the following, the parameter which is fundamental to the transition from laminarity to turbulence is the Reynolds number, i. e., the ratio of inertial to viscous forces. Dimensionally,

$$Re = \left|\frac{ma}{F_\mathrm{v}}\right| = \frac{mU^2}{L}\frac{1}{\tau L^2} = \frac{\rho L^3 U^2}{L^3 \mu U/L} = \frac{\rho UL}{\mu} = \frac{UL}{\nu}\,,$$

where m is the mass, a the acceleration, F_v the viscous force, U a characteristic velocity, L a characteristic length, τ the shear stress, μ the dynamic viscosity coefficient, ν the kinematic viscosity coefficient, and ρ the density.

The Reynolds number is a parameter which carries information on the overall behavior of the flow field (regardless of the fact that in many cases, for example in near-wall flows, there could be differences between the characteristic lengths in different regions of the field). When the Reynolds number is below a critical value Re_C (where it would really be more correct to speak about a range of critical values, which also depends on boundary and initial conditions, BC and IC), the viscous forces are high enough to smooth instabilities in the flow (caused by unwanted small changes in BC and IC). On the other hand, above Re_C, the inertia of the flow largely overcomes the dissipative viscous effects and exponential growth of instabilities occurs; the flow rapidly becomes turbulent. The importance of the previous sentence on anomalous laminar flows becomes clearer when we consider that, owing to the small value of the kinematic viscosity of common fluids, the Reynolds number is usually large. Therefore, it is very important to evaluate the value Re_C in each set of experimental conditions. It is not straightforward to derive this value under general assumptions. Empirically, it has been found that, in external flows where the reference length is the size of the body, $(Re_\mathrm{C})_L \approx 3\times10^5$, whereas in internal flows where the reference length is the radius of the duct (orthogonal to the mean flow), $(Re_\mathrm{C})_\delta \approx 3\times10^3$. It is interesting to notice that, when considering the boundary layer over a slender body, the ratio between the length of the body (L) and the boundary-layer thickness (δ) from Prandtl theory [10.1] scales as $(Re)_L^{1/2}$; therefore, the ratio of the Reynolds number based on the size of the body over that based on the transverse characteristic length δ, scales as $L/\delta \approx (Re)_L^{1/2}$. This leads to $(Re)_L/(Re)_\delta \approx 10^2$, which is in remarkable agreement with empirical observations. Whenever $Re > Re_\mathrm{C}$ (external or internal), the flow will start to exhibit all the features of developed turbulence.

These features establish the major differences between laminar and turbulent flows:

- extreme sensitivity to initial and boundary conditions
- unpredictability and randomness
- wide range of structures (scales) in space and time
- fully three-dimensional nature
- higher diffusion compared to the laminar case
- presence of cross-fluctuating terms among fluid-mechanics variables.

The sensitivity to initial conditions is the key point for the understanding of the behavior of turbulent flows; it is not possible, even in principle, to control the BC and IC to an arbitrarily small degree, especially if they pertain to a turbulent flow field (such as the inlet conditions for a channel). In comparison to laminar flow, a turbulent flow will exhibit a substantial (not only apparent due to our ignorance) unpredictable and random nature at any point and any time which originates from this high sensitivity to BC and IC; this also produces correlated fluctuations among the fluid-mechanics variables. These complex behaviors seem to prevent the possibility of an analytical approach when dealing with turbulent flows; in fact, from the mathematical point of view, there is still no theorem proving the existence and uniqueness of solutions to the Navier–Stokes equations in fully three-dimensional conditions (as in turbulent flows), for arbitrary time intervals, whatever the Reynolds number [10.2]. Referring to Sir Horace Lamb [10.3],

> *"I am an old man now, and when I die and go to Heaven there are two matters on which I hope enlightenment. One is quantum electrodynamics and the other is turbulence. About the former, I'm really quite optimistic."*

there is still a lot to do in turbulence investigations (for example consider the $1 000 000 prize being offered by the Clay Mathematics Institute for a proof of the existence and uniqueness of solutions to the Navier–Stokes equations, www.claymath.org/millennium). Nonetheless, some key point is quite clear; it is sure that the fluid-mechanics equations are valid even in the turbulent regime, remembering that they are derived from fundamental conservation principles (the relation between turbulence and equations will be considered in detail in Sect. 10.1.1). Moreover, simplified mathematical descriptions of nonlinear systems reveals that unpredictability and randomness are effectively derived from deterministic equations [10.4].

The observation of a wide range of scales within turbulent flows probably has the most important practical consequences when dealing with experiments in turbulence. This has been recognized since Leonardo da Vinci's (1452–1519) famous pictures of the flowing water of the Arno River and is summarized in poetic style in the well-known verse by *Richardson* [10.5]:

> *"Big whorls have little whorls, which feed on their velocity; And little whorls have lesser whorls, And so on to viscosity (in the molecular sense)."*

(even if for some turbulence quantity the range effectively extends well below the size where viscosity effects act). The previous description clearly points out the presence of several eddies, the interactions between them, and the effect of viscous dissipation.

Flow scales will be considered in detail in Sect. 10.1.2; as an introductory argument, for the velocity field, larger scales in space are related to the previously mentioned reference length L and time $\tau_0 = L/U$, whereas smaller scales are given by the Kolmogorov scales ($\eta = (\nu^3/\varepsilon)^{1/4}$, $\tau_\eta = (\nu/\varepsilon)^{1/2}$, where ε is the mean turbulent kinetic energy dissipation). From a simple dimensional argument, considering the balance between the inertial and dissipative terms in the turbulent kinetic energy equation [10.6], it is possible to derive that $\varepsilon \sim U^3/L$. Therefore, it is quite easy to obtain the ratios

$$\frac{L}{\eta} \sim L\left(\frac{U^3 L}{\nu^3}\right)^{1/4} = Re^{3/4}\,,$$

$$\frac{\tau_0}{\tau_\eta} \sim \tau_0\left(\frac{U^3}{L\nu}\right)^{1/2} = Re^{1/2}\,,$$

i. e., the range between large and small scales $(L-\eta)/\eta$ (and similarly in time) increases as the Reynolds number to the power 0.75 (or 0.5 for time scales). For a moderate Reynolds number (10^4), this means that there are almost three orders of magnitude between the large and small space scales (and about two orders of magnitude in time); refer to Sect. 10.1.2 for further details on this.

Considering the transformed domain in wavenumber ($k = 2\pi/\ell_i$, where ℓ_i is the generic length scale), which allows one to derive the spatial distribution of energy or the energy spectrum, the large and small scales bound a range of interesting wavenumber scales in fluid mechanics from $k_\mathrm{L} = 2\pi/L$ to $k_\eta = 2\pi/\eta$. Similarly, the distribution of energy among the different time scales is investigated by means of the energy spectrum in frequency ($f = 1/\Delta t_\mathrm{i}$, where Δt_i is the generic time scale);

the frequency range is between $f_0 = 1/\tau_0$ and $f_\eta = 1/\tau_\eta$ (note that while f_0 is obtained as U/L, f_η is different from U/η; refer to the sections on Integral Scales and Kolmogorov Scales).

In fact, from both the numerical and experimental points of view, the existence of a wide range of scales determines the maximum and minimum dimensions (and times) to be *resolved* by a particular method (in terms of the previous example, this means that the experimental system should be able to measure over three orders of magnitude in space and two orders in time). In theory, the whole range should be detectable to allow a full description of the flow field; in practice, researchers frequently concentrate separately on intermediate–large or intermediate–small scale ranges. This limitation depends on the fact that, due to the large Reynolds numbers involved in practical investigations, the range of scales is very wide and exceeds the resolution capabilities of existing numerical codes and experimental methods (it should also be considered that the previous range has been evaluated for a one-dimensional space, while in three-dimension investigations or numerical simulations, the range must be increased as the third power).

The full three-dimensional nature of turbulent flows derives from the presence of a large range of scales which correspond to the presence of small and large eddies with shapes and strength depending on the particular flow field. These eddies also ensure more-effective diffusion (of each fluid variable) within the flow field in comparison to the laminar case in which only molecular diffusion acts.

To summarize, it is quite difficult to define turbulence univocally [10.7],

> *"What is turbulence? Turbulence is like pornography. It is hard to define, but if you see it, you recognize it immediately."*

Prerequisites for Measurements in Turbulent Flows

Due to the previous considerations, from the point of view of measurements, even though many techniques can be used both in laminar and turbulent conditions, there are some peculiar characteristics of a measuring system to be considered when dealing with turbulent flows experimentally:

- spatial resolution
- time resolution
- the characteristic size of the system and duration of a measurement
- intrusiveness
- statistical treatment

To resolve the wide range of scales observed in turbulent flows, a measurement system should be able to identify rapid changes in fluid-mechanics variables both in space and time. To do this, the sensor (specifically the probe) of the system, must be small enough compared to the smallest spatial scale in the flow and must respond at least as quickly as the smallest time scale of the flow. The spatial resolution (SR), of a measurement system gives information about the inverse of the minimum detectable length in the flow field,

$$\mathrm{SR} = \frac{1}{d_{\min}} ,$$

where $d_{\min}$ is usually closely related to the characteristic size of the sensor, although for some experimental method, there is not a physical sensor so that this size should be referred to the region which contributes to the measurement, the so-called *measurement volume*. A system with high spatial resolution is able to perform a measurement over a small length (i. e., to capture fluctuations of the considered fluid-mechanics variable over short distances). For example, in hot-wire anemometry (HWA, Sect. 5.2), the sensor is a thin wire (diameter of a few micrometers) and $\mathrm{SR} \approx 10^5\ \mathrm{m}^{-1}$ (the measurement unit is length^{-1}), while in laser Doppler anemometry (LDA), (Sect. 5.3) the sensor consists of the region where the two laser beams cross (with a characteristic size of 10^{-4} m) so that $\mathrm{SR} \approx 10^4\ \mathrm{m}^{-1}$ and a Pitot tube (Sect. 5.1, with a hole diameter of about 3×10^{-3} m) has $\mathrm{SR} \approx 3\times10^2\ \mathrm{m}^{-1}$. In this sense, we can say that HWA is able to detect small moving spatial structures of the velocity field better than LDA and much better than a Pitot tube.

Similarly, the time resolution (TR), gives information on the inverse of the minimum detectable time interval in the flow field,

$$\mathrm{TR} = \frac{1}{\Delta t_{\min}} ,$$

where $\Delta t_{\min}$ is the maximum time among the time interval requested by the whole measurement system to perform a measure (*measurement interval*) and the time interval for the sensor to respond to a variation of the considered fluid-mechanics variable (the *response*

time, which is also connected to the size of the sensor itself). A system with high time resolution is able to take measurements separated by small time intervals (i. e., to capture fast fluctuations of the considered fluid-mechanics variable). For example, in HWA, due to the small sensor size and the fast electronics, the system takes a measurement quite rapidly (it is really an analogue system which is resampled digitally) so that TR $\approx 10^5\,\mathrm{s}^{-1}$ (the measurement unit is s^{-1} or Hz), for LDA the value of $\Delta t_{\min}$ depends on the seeding particle inter-arrival time, which can be reduced to 10^{-4} s, so that TR $\approx 10^4\,\mathrm{s}^{-1}$, while for Pitot tubes the inertia of the manometer fluid limits the time interval to a fraction of a second, so that TR $\approx 10\,\mathrm{s}^{-1}$ (modern pressure transducers are able to respond quite rapidly to pressure changes but are still quite large, so that TR $\approx 10^3$–$10^4\,\mathrm{s}^{-1}$).

Spatial and temporal resolutions give an indication of the achievable lower limit on the scale range. On the other hand, the upper limit is related to the extension (overall size) of the measurement system in space and to the duration of the measurement in time. A single-point measurement system (such as HWA, LDA or a Pitot tube) cannot directly detect the scale spatial structure, even in homogeneous and isotropic turbulence, unless a hypothesis on the relation between behavior in space and time is assumed (see the section on Taylor's hypothesis). The detection of large-scale spatial structures can be accomplished by using multipoint systems such as using light sheets in the particle image velocimetry technique (PIV) (Sect. 5.3.2), which is then able to determine the flow behavior over a length scale $d_{\max}$ (for example, in PIV, $d_{\max}$ is the dimension of the light sheet in the test section). From the temporal point of view, in stationary flow conditions (when the large time scales are closely connected to the large space scales by Taylor's hypothesis), by performing one measurement over a time $\Delta t_{\max}$, it is possible to investigate the evolution of the field up to such a time. On the other hand, in unsteady conditions (when large time scales are not simply attainable from the spatial ones), it is necessary to acquire several time sequences over a time $\Delta t_{\max}$ to derive the large-time-scale behavior; in this case various strategies can be employed (for example, ensemble or phase averaging as illustrated in Sect. 10.1.1).

The smallest ($d_{\min}$, $\Delta t_{\min}$) and largest ($d_{\max}$, $\Delta t_{\max}$) measurable lengths and times must be evaluated preliminarily for the measurement system under consideration and compared to the expected flow scales (for example starting from a simple evaluation in homogeneous and isotropic turbulence) to know the effective range that can be investigated. In small-scale investigations, and in unsteady conditions, it is not possible to derive the information in time from that in space by a simple transformation using the mean velocity (as stated by Taylor's hypothesis) so that both the information in space and time are requested (consider the definitions of the Kolmogorov time scale, or the Kolmogorov frequency, which do not include the mean velocity, as an example of this statement). On the other hand, for large-scale investigations, and in stationary conditions, the time and space behaviors are much more closely related by means of the mean velocity (Taylor's hypothesis).

When considering the distribution of energy among the different wavenumbers, the sampling theorem states that the energy content can be effectively detected only up to $k_{\max} = \pi/d_{\min}$ (and not up to $k_{\max} = 2\pi/d_{\min}$ as expected). Similarly, for the distribution of energy among the different frequencies, the sampling theorem states that the energy content can be effectively detected only up to $f_{\max} = 1/(2\Delta t_{\min})$ (and not up to $f_{\max} = 1/\Delta t_{\min}$ as expected). In this sense, the spatial and temporal resolutions correspond to two times the maximum wavenumber and frequency which can be detected by the measurement system. The situation is summarized in Fig. 10.1, in physical space and wavenumber domains.

The intrusiveness of the sensor within the flow field also seems to be a very important aspect of lami-

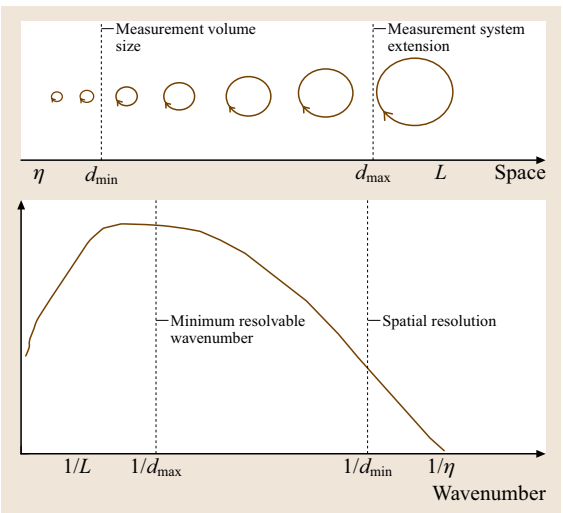

Fig. 10.1 Minimum and maximum size of the measurement system in comparison to flow structures in space and wavenumber domains

nar flow measurement. This is only partially true, due to the fact that in the presence of turbulence the insertion of a probe into the flow itself generates flow structures that modify the previous (unknown) field, whereas in laminar flow this effect is more localized (at least far from the transition regimes); thus, intrusiveness gains importance in turbulence flow measurements. In principle, it is not possible to completely avoid intrusiveness due to the requirement of interaction between the measurement system (the sensor in particular) and the fluid flow when performing experiments. In practice, this interaction should be reduced as much as possible and the effect must at least be evaluated in each case; examples are the evaluation of the interactions between intrusive sensors and boundaries in near-wall flows and the determination of spatial and temporal (wavenumber and frequency) filtering of the tracers used in optical methods (Sect. 5.3.3).

The problem of statistics is closely linked to the random nature of turbulent flows; the reader is referred to Sect. 10.1 for details of how statistics is performed. The effect of statistical accuracy and the required number of samples to attain such an accuracy are considered in the sections on Statistical Accuracy and Chap. 23. However, it is important to remark that instantaneous fields contain information on both the spatial and temporal evolution of the flow and that special care must be taken in averaging procedures (such as in the case of stationary turbulence or in homogeneous and isotropic turbulence).

Errors in experimental techniques will be not considered here because a general treatment of errors is presented elsewhere (Chapter 23) and specific measurement system errors derive from peculiar aspects of each measurement method regardless of whether laminar or turbulent conditions dominate.

Flow Variables Relevant to Turbulence and their Measurement

Once the general characteristics of a system measuring in turbulent flows have been established, it is necessary to establish which fluid-mechanics variables have to be determined for a complete description of the turbulent field. Starting from equations (Chapter 1, Sect. 10.1.1), the following fields are of interest:

- three velocity components
- pressure
- temperature
- density
- species concentration

Many other quantities are important in fluid mechanics, such as the vorticity, strain rate, stresses, dissipation, and enstrophy (which can be derived from the velocity field, although direct measurements are sometimes possible). As mentioned in the introduction, interaction terms among these variables are also of great interest in turbulence (both from the fundamental and applied points of view); these have to be determined by combined simultaneous measurements of two or more of them (examples will be given in Sect. 10.1.2).

It should also be pointed out that the equations themselves establish relations between flow variables so that one can be derived from the others (even if we are dealing with second-order partial differential equations which set severe practical limits when computing derivatives from noisy experimental data).

In these equations, other important quantities such as viscosity and other diffusion coefficients are present. Usually they are derived from constitutive relations and inserted into the equations, and empirical laws are used for their evaluation (Sect. 1.3).

For further information on the techniques and measurements mentioned above, the reader can use the following cross-references to part B of this Handbook:

- Velocity components
  - Pitot and pressure based (Sect. 5.1)
  - Thermal anemometry (Sect. 5.2)
  - Laser Doppler anemometry (Sect. 5.3.1)
  - Particle image velocimetry (Sect. 5.3.2)
  - Sonic anemometers (Sect. 5.7)
- Pressure
  - Manometers and transducers (Chap. 4)
- Temperature
  - Thermocouples (Sect. 6.1)
  - Resistive sensors (Sect. 6.1)
  - Liquid crystals (Sect. 6.3)
  - Other methods (Chap. 6)
- Density
  - Shadowgraph (Sect. 5.6)
  - Schlieren (Sect. 5.6)
  - Interferometry (Sect. 5.6)
- Concentration
  - Laser-induced fluorescence (LIF, Chap. 11)

It should be clear to experimentalists (and similarly to people involved in numerical simulations), that the large number of variables to be determined and the many potentially interesting applications mean that there are still hundreds of years' worth of interesting measurements in turbulent flows to be enjoyed. From the experimental point of view, it is also clear that efforts

must be given in developing almost-nonintrusive, multipoint systems for the simultaneous measurement of various quantities in the flow field. Among others methods, this has almost been achieved for simultaneous multipoint three-component velocity (stereo PIV, 3-D particle tracking velocimetry (PTV) (Sect. 5.3.2), for combined velocity–concentration (PIV LIF , Chap. 11), velocity–temperature (liquid crystals (Sect. 6.3)) and concentration–temperature (LIF–liquid crystals) measurements.

Difficulties in measuring all of these quantities are related to:

- the need to define, determine, and verify a common *measurement volume*
- crosstalk between probes or systems
- simultaneous control and optimization of different setups
- the need for simultaneous triggering of data acquisition
- the need for a common space grid and time step definition between the various measurement systems
- the need for measurement errors of the same order of magnitude
- handling and storing large amounts of data.

To solve such problems great care and expertise must be applied; this could be the reason why advanced multipoint combined measurement systems are still on a prototype level. However, as done in the past, detailed standard procedures will be derived to achieve these requirements to a reasonable degree of accuracy and design relatively simple industrial systems.

Some additional comments should be given on the possibility of measuring pressure and density fields (of course we are still speaking about almost-nonintrusive, multipoint measurement systems). For pressure fields, high-temporal-resolution single-point measurements are already possible on the surface of bodies and on walls in general, but problems are encountered when performing such measurements with high spatial resolution (due to the probe size) within the field, i. e., far from the boundaries (due to intrusiveness of the pressure probes) and in a multipoint approach (due to the intrusiveness and interaction between the probes themselves). At these locations, simultaneous velocity–pressure correlations are also difficult to obtain. The situation is just the opposite for density field measurements, in which quite high spatial resolution in multipoint conditions can be attained far from the boundaries (albeit with low precision, i. e., with large measurement errors due to the analysis of light intensity fields), while it is quite difficult to measure close to solid surfaces (due to light reflection), especially in complex geometrical configurations (due to the almost two-dimensional nature of the measurement methods).

Some other difficulties in the measurement of turbulent flows are related to the evaluation of the derivatives that appear in the equations. Provided that the measuring system has a high spatial resolution, it is necessary to obtain derivatives from finite differences in space and time (such as those obtained as the output from numerical simulations and/or experiments). This is always a difficult task, which can be solved using interpolation algorithms coupled with evaluations of the finite differences over different grid spacings or time steps.

The substantial equivalence of many problems encountered when dealing with turbulent flows (wide range of scales, spatial and time resolution problems, errors and statistics, grid and time step problems) in both numerical simulations and experiments has already been pointed out. Many experiments using well-established measurement systems have been devoted to testing of numerical models, especially in nonstandard conditions and at high Reynolds numbers. On the other hand, well-tested numerical codes can be used to verify the quality of data obtained from advanced or nonstandard application measurement techniques. This allows the establishment of a mutual relationship between numerical simulations and experiments; an example of this is the evaluation of the turbulent kinetic-energy dissipation rate ε, which can be derived from isotropic theories (Sect. 10.1.1 and on *How to measure length and time scales*) or from numerical simulations and be used to derive dimensionless variables from measurements. This quantity, which consists of a squared sum of velocity gradients, is very difficult to evaluate from the experimental point of view with the required high spatial and temporal resolutions; on the other hand, it is quite easy to derive values for ε from numerical simulations in homogeneous and isotropic turbulence (at least at small Reynolds numbers). Thus, the numerical homogeneous and isotropic surrogate for ε can be used as a preliminary indication to evaluate flow scales and the required spatial and time resolutions in real experiments (even in inhomogeneous and anisotropic conditions).

There are large number of fields of common investigations and partnerships between numerical simulations

and experiments based on the advantages of investigating the same problem from different points of view.

Lagrangian and Eulerian Descriptions

The flow field variables mentioned so far are independent of the frame reference due to Galilean invariance (at least for flow velocities much less than that of light, i. e., for all fluid-mechanics applications except for astrophysics). This statement is true for flow variables (except for the velocity itself) and their gradients, but is not true for partial derivatives in time [10.4]. Therefore if we consider all the flow at rest or in motion with a uniform velocity; in fact, the flow is not a rigid body in motion with uniform velocity and each flow element could have a velocity different from the neighbors. The variation of the fluid-mechanics quantities between different flow elements could depend on their relative position and velocity, and thus on the way in which such quantities are evaluated. Therefore, it is not trivial to consider the differences between the flow description obtained at a fixed point and the one in motion with the considered flow element; the former is referred to as Eulerian description, while the latter is known as the Lagrangian description (Sect. 10.2).

Usually, the difference between those two descriptions is clarified by considering a standing rock in a river (Eulerian frame), a leaf carried away by the flow (Lagrangian frame), and a fish moving on its own (i. e., with its own velocity). Clearly, the former undergoes variations of the fluid-mechanics quantities both in time (unsteady conditions) and from point to point (inhomogeneous conditions), while the other two exhibit variations when moving along each trajectory (a sequence of positions in time) or along different trajectories at different times, thus only in time. Such a statement can be clarified by considering the relation between the variations along a trajectory, $\boldsymbol{x}(\boldsymbol{x}_0, t)$, (D/D$t$, substantial or Lagrangian derivative) (where $\boldsymbol{x}_0$ is the fixed initial position) and those at a fixed point in space, $\boldsymbol{x}_0$, ($\partial/\partial t$, the time partial or Eulerian derivative), of a fluid-mechanics variable $A[\boldsymbol{x}(\boldsymbol{x}_0,t), t]$ given by *Batchelor* [10.1]

$$\begin{aligned}\frac{\mathrm{D}A}{\mathrm{D}t} &= \left.\frac{\partial A}{\partial t}\right|_{x(x_0,t)=\text{const}} \\ &= \left.\frac{\partial A}{\partial t}\right|_{x_0=\text{const}} + \left.\left(\frac{\partial x_i}{\partial t}\frac{\partial A}{\partial x_i}\right)\right|_{x_0=\text{const}} \\ &= \left.\left(\frac{\partial A}{\partial t} + u_i\frac{\partial A}{\partial x_i}\right)\right|_{x_0=\text{const}},\end{aligned}$$

where repeated indexes mean sum for $i = 1, 3$ (the sum will be omitted hereafter). The second term on the right-hand side of the last equivalence represents the transport term, which accounts for variations in space due to the motion of the fluid with velocity components u_i.

The former relation also allows one to understand how it is possible to derive one description from the other; when it is possible to know the variation in time of a fluid-mechanics variable at a given point and simultaneously the variation of the same variable between different points then we can derive the substantial derivative. This is just the case of the Lagrangian description in which the knowledge of the variables along flow trajectories allows one to derive their variations in both time and space, and thus to compute the overall variation (i. e., to derive the Eulerian description). On the other hand, given the overall variation of a quantity, it is not possible, in general, to derive the variation in time along a trajectory (i. e., to derive the Lagrangian description); the Eulerian field cannot be integrated to derive trajectories due to sensitivity to the IC (in the laminar case this would be possible). In particular, the possibility of interchange between the two descriptions depends on the specific flow field considered; the hypothesis of *Tennekes* [10.8], generalizing Taylor's hypothesis (Sect. 10.1.1, Taylor's hypothesis), establishes a direct connection between the Lagrangian and Eulerian description in isotropic turbulence, in which at large Reynolds numbers Lagrangian flow scales are larger than Eulerian flow scales (Sect. 10.2 and [10.4]).

Thus, when possible, it would be much better to attain a Lagrangian description rather than a Eulerian. However, from the experimental point of view, it is not simple to obtain fluid-mechanics variables along flow trajectories; only a few techniques allow the Lagrangian description to be obtained. Among the others, the PTV technique (Sect. 5.3.2) is now well established to derive tracer particle velocities (which under certain assumptions are representative of the flow element motions) along trajectories.

The importance of the Lagrangian approach arises in situations in which the determination of the spreading and dispersion of the flow is required (for example in pollutant dispersion or in mixing and combustion investigations) or when the history of the same flow element must be considered (for example when evaluating the deformation and stresses on blood cells in haemodynamics).

The flow variables, the derived quantities (time and space derivatives and so on), and the flow scales defined

in previous paragraphs must be considered separately in the Eulerian or Lagrangian frameworks. More details on this aspect will be given in the following (Sect. 10.1.3, Sect. 10.2), but in general the evaluation of a variable in the Eulerian frame requires an average (in the sense reported in Sect. 10.1.1) at a fixed point in space or among different fixed points; on the other hand, the evaluation in a Lagrangian frame requires an average along trajectories (separating the results on the basis of the starting or arriving positions).

Alternative Approaches to Statistics

The practical consequence of the sensitivity of a turbulent flow to BC and IC is that it exhibits fluctuations in time and space. Within these fluctuations all the essential and interesting flow behaviors are embedded. Thus, the value of a fluid-mechanics variable at a given point and time (q) can be considered as the sum of a *mean* term, $\langle q \rangle$ (the way in which this term is obtained will be specified in the following of this section), plus a term containing all the information on *coherent* structures (at this stage coherent means with a well-defined pattern in the flow field, Chap. 22) in the field (large and intermediate scales) $(q')_c$, plus a random term containing all *incoherent* fluctuations (small scales), $(q')_n$,

$$q = \langle q \rangle + (q')_c + (q')_n \,,$$

where $q = q(\boldsymbol{x}, t)$ is a function of the considered point ($\boldsymbol{x}$) and time (t), as are all terms on the right-hand side of the previous relation. The goal of this description is to try to separate the three contributions from each other, i. e., to determine all possible effects to which the flow variable is subjected under the influence of the flow motion. Therefore, the problem is first to perform an average of the flow variables preserving the *coherent* and *incoherent* parts and secondly to separate these two.

Unfortunately, there is no unique solution to this problem; the result depends on the criterion that is used to quantify the *coherence* or *incoherence* character of the flow variable, i. e., whether we treat them as indistinguishable from each other (no criterion), to determine the energy of the related structures, to evaluate the resemblance with sample structures defined a priori, to minimize some difference in the least-squares sense, and so on. To give an approximate idea of the problem, the most important approaches used are described in the following cross references:

- Direct averaging (Sect. 10.1.1, Sect. 10.1.2)
- Proper orthogonal decomposition (POD) (Sect. 22.4)
- Wavelets (Sect. 23.5)
- Linear stochastic estimation (LSE) (Sect. 22.6)

In this section, only direct averaging will be discussed; in this approach, all flow scales are considered as equivalent (in a Fourier sense) so that it is possible only to separate the average term from the other two in the previous decomposition, but it is not possible to distinguish between the *coherent* and *incoherent* contributions.

Statistical Domain: Ensemble Averaging, Time or Space Averaging

Once the approach to the analysis of a turbulent flow has been defined, it is necessary to specify on what domain the statistics are performed. For direct averaging, the most general way to derive averaged quantities is the ensemble average (indicated with triangular brackets); therefore, the n-th statistical moment of a fluid-mechanics variable q is given by

$$\langle q^n \rangle = \frac{\int_{-\infty}^{+\infty} q^n \, p\,(q)\,\mathrm{d}q}{\int_{-\infty}^{+\infty} p\,(q)\,\mathrm{d}q} \,,$$

where $p(q)$ is the probability density function (PDF) of the variable q (Sect. 23.1 for details) and n is the order of the considered moment (Chap. 23 for details on the evaluation of statistics). Each of the previous quantities (included the PDF) is a function of the considered point and time; for example $p(q) = p(q)(\boldsymbol{x}, t)$.

In principle, the integral of the PDF over all possible values should be equal to 1; the integral is retained in the previous definition to point out that a normalization is required (especially when the integral is evaluated over a discrete set of samples). The PDF could be obtained by acquiring all possible values of the variable q at a given point and time; in practice, this means repeating the same experiment several times from the beginning (with more or less the same IC and BC), evaluating the investigated variable at the same time and position (in the general case of unsteady inhomogeneous phenomena). Such a procedure is summarized in Fig. 10.2; different values of the flow variable at the same point and time are observed for each new experiment; the mean value obtained by averaging over the different experiments is different from the one derived by a time average over a single experiment.

Two problems arise in this practical approach. Firstly, the experiments are discrete and cannot be repeated indefinitely so that the statistical treatment to determine the finite number of independent samples

must be considered (Chap. 23). In this case, the PDF must be derived from a finite number of data (N_T) and the previous integral is replaced by the sum over experiments with the same PDF

$$\frac{\sum_i^N q_i^n\, p\,(q_i)\,\Delta q_i}{\sum_i^N p\,(q_i)\,\Delta q_i} = \frac{\sum_i^N q_i^n\, p\,(q_i)\,\Delta q_i}{\sum_i^N n_i}$$

(where Δq_i and n_i are the width and number of data for each bin of the N-bin histogram); if all events have the same bin width and $p(q)$, then the previous sum reduces to the usual average

$$\frac{1}{N_T}\sum_i^{N_T} q_i^n \,.$$

Secondly, the ensemble over which averaging is performed is a set of several results of the same experiment; thus, it will be necessary to repeat the same experiment systematically several times, which is a difficult problem for experimentalists. Therefore, although it is clear that ensemble averaging would be the most general way of performing averaging (without any a priori assumption about the flow field), in practice, whenever possible, it is necessary to perform the average in a much simpler way. To this end, consider the following special fluid-mechanics conditions (statistically)

- periodic flow field (in time or space)
- stationary flow field
- homogeneous flow field

for each one of which particular average procedures are possible.

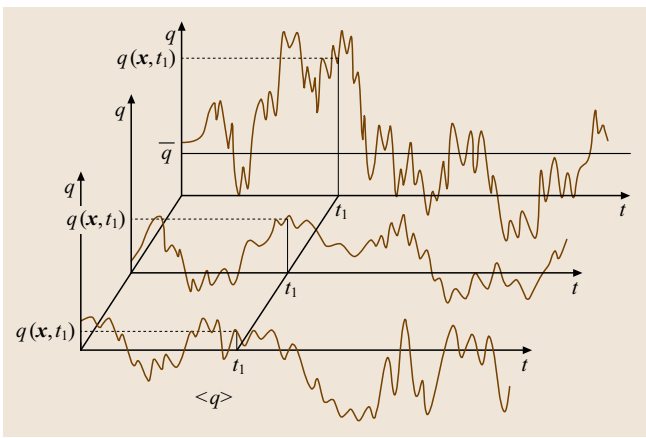

Fig. 10.2 Ensemble average along the axis of *repeated experiments* and time average along the time axis

In a statistically periodic flow field (period equal to T_0), the PDF is the same at time t and time $t+T_0$

$$p(q)\,(x,t) = p(q)\,(x,t+T_0)$$

(or equivalently in space at point $\boldsymbol{x}$ and $\boldsymbol{x}+\boldsymbol{X}_0$), so that the ensemble over which the average is performed reduces to one period of the investigated periodic phenomenon. The mathematical expressions are the same (for continuous or discrete data), but the time (or space) dependence of the results is limited to just one period. In practice, it is completely equivalent to run the experiments over N different periods or to repeat ex novo the experiments N times, providing that the BC and IC are constant (it should be required that the characteristic time, or length, scales of the phenomenon are less than T_0, Sect. 10.1.3). In this case, so-called conditional or phase averaging (i. e., averaging the acquired signal over different phases) allows one to limit the computation of $\langle q\rangle$ to times t_0+mT_0, where m is an integer number and t_0 is the phase in time (and equivalently at positions $\boldsymbol{x}_0+m\boldsymbol{X}_0$). Examples of such averaging are encountered in the analysis of periodic signals in time (such as for daily varying atmospheric data or for data acquired close to propellers and other rotating devices) and of periodic fields in space (such as in the wake of bluff bodies or at the outlet of jets at relatively low Reynolds numbers).

In the case of statistically stationary flow fields, the PDF is completely independent of the considered time

$$p(q)\,(\boldsymbol{x},t) = p(q)\,(\boldsymbol{x})$$

so that, statistically, each instant over a set of the ensemble should be equivalent to the others (mathematically the equivalence would also require that the statistics of the process is independent on the particular selected set of the ensemble; this is a sufficient condition. See [10.9] for further details on this argument). As depicted in Fig. 10.2, in the computation of the n-moment this allows one to replace the ensemble average by the average over a single set (i. e., in time) indicated by $\overline{q^n}$,

$$\langle q^n\rangle = \frac{\int_{-\infty}^{\infty} q^n\, p\,(q)\,\mathrm{d}q}{\int_{-\infty}^{\infty} p\,(q)\mathrm{d}q} = \frac{\int_0^{\infty} q^n\, p\,(q)\,\mathrm{d}t}{\int_0^{\infty} p\,(q)\mathrm{d}t}$$

$$= \lim_{T\to\infty} \frac{\int_0^T q^n\, p\,(q)\mathrm{d}t}{\int_0^T p\,(q)\,\mathrm{d}t} = \lim_{T\to\infty} \frac{1}{T}\int_0^T q^n \mathrm{d}t = \overline{q^n}$$

using the hypothesis that the PDF is not dependent on time. All quantities can be functions of the spatial positions (but not of time after averaging). This is a simplified version of the ergodicity theorem, which states the equivalence between the average over the different sets of the ensemble and over time on a single set; the theorem is valid for a random process that is stationary, providing that all the statistics obtained from a set are equal to that from the others; such a process is referred as ergodic [10.9]. It must be emphasized that the simple verification of stationarity does not imply the ergodicity of a process, i. e., the replacement of the ensemble average with the time average; it is also necessary to verify that independent sets of the ensemble give the same statistics (whereas an ergodic process is automatically stationary). In practice, it is possible to divide the set into subsets and to verify the equivalence of statistics over the subsets. The widespread class of random processes that satisfy ergodicity is known as the class of Gaussian random processes with continuous power spectral density functions, i. e., without infinite-density peaks [10.9].

It is of interest to show examples of ergodic and non-ergodic processes. Consider the following unsteady non-ergodic (to be proved) periodic set

$$q\,(t) = Q\ \sin\,(\omega t + \varphi)$$

in which the amplitude Q and phase φ are constant over the ensemble. Ensemble averaging, at a fixed time, gives the following values for the first two statistical moments and for the correlation function (Chap. 22, Chap. 23)

$$\begin{aligned}
\langle q(t)\rangle &= \int_{-\infty}^{+\infty} Q\sin\,(\omega t+\varphi)\ p(q)\mathrm{d}q \\
&= Q\sin\,(\omega t+\varphi)\ , \\
\langle q^2(t)\rangle &= \int_{-\infty}^{+\infty} Q^2\sin^2\,(\omega t+\varphi)\ p(q)\mathrm{d}q \\
&= Q^2\sin^2\,(\omega t+\varphi)\ , \\
\langle q(t)q(t+\tau)\rangle &= \int_{-\infty}^{+\infty} Q^2\sin\,(\omega t+\varphi) \\
&\quad\times\sin\,[\omega\,(t+\tau)+\varphi]\ p(q)\mathrm{d}q \\
&= Q^2\sin\,(\omega t+\varphi)\sin\,[\omega\,(t+\tau)+\varphi]\ ,
\end{aligned}$$

which depends on time t (i. e., the process is unsteady). On the other hand, the average in time gives (for the same quantities)

$$\begin{aligned}
\overline{q} &= \lim_{T\to\infty}\frac{1}{T}\int_0^T Q\sin\,(\omega t+\varphi)\,\mathrm{d}t = 0\ , \\
\overline{q^2} &= \lim_{T\to\infty}\frac{1}{T}\int_0^T Q^2\sin^2\,(\omega t+\varphi)\,\mathrm{d}t \\
&= \frac{Q^2}{2}\ , \\
\overline{q(t)q(t+\tau)} &= \lim_{T\to\infty}\frac{1}{T}\int_0^T Q^2\sin\,(\omega t+\varphi) \\
&\quad\times\sin\,[\omega\,(t+\tau)+\varphi]\,\mathrm{d}t \\
&= \frac{Q^2}{2}\cos\,(\omega\tau)\ ,
\end{aligned}$$

which are of course independent on the set, but are different from the values obtained from the ensemble averaging; therefore, the process is non-ergodic. Note that, if in the time average the data are collected at the same time and phase ($\omega t+\varphi=$ constant), i. e., conditional or phase averaging is performed, the following results are obtained

$$\begin{aligned}
\overline{q} &= \lim_{T\to\infty}\frac{1}{T}\int_0^T Q\sin\,(\omega t+\varphi)_{\mathrm{const}}\mathrm{d}t \\
&= Q\sin\,(\omega t+\varphi)_{\mathrm{const}}\ , \\
\overline{q^2} &= \lim_{T\to\infty}\frac{1}{T}\int_0^T Q^2\sin^2\,(\omega t+\varphi)_{\mathrm{const}}\mathrm{d}t \\
&= Q^2\sin^2\,(\omega\mathrm{t}+\varphi)_{\mathrm{const}}\ , \\
\overline{q(t)q(t+\tau)} &= \lim_{T\to\infty}\frac{1}{T}\int_0^T Q^2\sin\,(\omega t+\varphi)_{\mathrm{const}} \\
&\quad\times\sin\,[\omega\,(t+\tau)+\varphi]_{\mathrm{const}}\,\mathrm{d}t = Q^2 \\
&\quad\times\sin\,(\omega t+\varphi)_{\mathrm{const}} \\
&\quad\times\sin\,[\omega\,(t+\tau)+\varphi]_{\mathrm{const}}\ ,
\end{aligned}$$

which are identical to the results of the ensemble averaging, so that phase averaging can be used as a surrogate of ensemble averaging.

A similar result is obtained for periodic sets with different amplitudes $Q(k)$ for each set k (all with the same phase)

$$q_k\,(t) = Q(k)\sin\,(\omega t+\varphi)\ .$$

For the same moments as before, ensemble averaging gives

$$\begin{aligned}\langle q(t)\rangle &= \int_{-\infty}^{+\infty} Q(k)\sin(\omega t+\varphi)\; p(q_k)\mathrm{d}q_k \\ &= \langle Q\rangle \sin(\omega t+\varphi)\ , \\ \langle q^2(t)\rangle &= \int_{-\infty}^{+\infty} Q^2(k)\sin^2(\omega t+\varphi)\; p(q_k)\mathrm{d}q_k \\ &= \langle Q^2\rangle \sin^2(\omega t+\varphi)\ , \\ \langle q(t)q(t+\tau)\rangle &= \int_{-\infty}^{+\infty} Q^2(k)\sin(\omega t+\varphi) \\ &\quad \times \sin[\omega(t+\tau)+\varphi]\; p(q_k)\mathrm{d}q_k \\ &= \langle Q^2\rangle \sin(\omega t+\varphi) \\ &\quad \times \sin[\omega(t+\tau)+\varphi]\ ,\end{aligned}$$

which depend on time t (i. e., the process is unsteady). The average in time gives

$$\begin{aligned}\overline{q} &= \lim_{T\to\infty}\frac{1}{T}\int_0^T Q(k)\sin(\omega t+\varphi)\mathrm{d}t = 0\ , \\ \overline{q_k^2} &= \lim_{T\to\infty}\frac{1}{T}\int_0^T Q^2(k)\sin^2(\omega t+\varphi)\mathrm{d}t \\ &= \frac{Q^2(k)}{2}\ , \\ \overline{q(t)q(t+\tau)} &= \lim_{T\to\infty}\frac{1}{T}\int_0^T Q^2(k)\sin(\omega t+\varphi) \\ &\quad \times \sin[\omega(t+\tau)+\varphi]\,\mathrm{d}t \\ &= \frac{Q^2(k)}{2}\cos(\omega\tau)\ ,\end{aligned}$$

which depend on the set (except the mean value), so they are different from the values obtained from the ensemble averaging; therefore, this process is also non-ergodic.

On the other hand, if we consider the following stationary ergodic (to be proved) periodic sets with different phases $\varphi(k)$ for each set (all with the same amplitude)

$$q_k(t) = Q\sin[\omega t+\varphi(k)]\ .$$

The ensemble averaging gives

$$\begin{aligned}\langle q\rangle &= \int_{-\infty}^{+\infty} Q\sin[\omega t+\varphi(k)]\; p(q_k)\mathrm{d}q_k \\ &= 0\ , \\ \left\langle q^2\right\rangle &= \int_{-\infty}^{+\infty} Q^2\sin^2[\omega t+\varphi(k)]\; p(q_k)\mathrm{d}q_k \\ &= \frac{Q^2}{2}\ , \\ \langle q(t)q(t+\tau)\rangle &= \int_{-\infty}^{+\infty} Q^2\sin[\omega t+\varphi(k)] \\ &\quad \times \sin[\omega(t+\tau)+\varphi(k)]\; p(q_k)\mathrm{d}q_k \\ &= \frac{Q^2}{2}\cos(\omega\tau)\ ,\end{aligned}$$

which do not depend on time t (i. e., the process is stationary). The average in time gives

$$\begin{aligned}\overline{q} &= \lim_{T\to\infty}\frac{1}{T}\int_0^T Q\sin[\omega t+\varphi(k)]\mathrm{d}t = 0\ , \\ \overline{q^2} &= \lim_{T\to\infty}\frac{1}{T}\int_0^T Q^2\sin^2[\omega t+\varphi(k)]\mathrm{d}t \\ &= \frac{Q^2}{2}\ , \\ \overline{q(t)q(t+\tau)} &= \lim_{T\to\infty}\frac{1}{T}\int_0^T Q^2\sin[\omega t+\varphi(k)] \\ &\quad \sin[\omega(t+\tau)+\varphi(k)]\,\mathrm{d}t \\ &= \frac{Q^2}{2}\cos(\omega\tau)\ ,\end{aligned}$$

which are independent of the set and equal to the values obtained from the ensemble averaging; therefore, this process is ergodic.

Lastly, consider the stationary non-ergodic (to be proved) periodic sets with different uncorrelated amplitudes and phases [$Q(k)$ and $\varphi(k)$] for each set [10.9]

$$q_k(t) = Q(k)\ \sin[\omega t+\varphi(k)]\ .$$

The ensemble averaging gives

$$\begin{aligned}\langle q\rangle &= \int_{-\infty}^{+\infty} Q(k)\sin\left[\omega t+\varphi(k)\right]\, p(q_k)\mathrm{d}q_k \\ &= 0\,,\\ \left\langle q^2\right\rangle &= \int_{-\infty}^{+\infty} Q^2(k) sin^2\left[\omega t+\varphi(k)\right]\, p(q_k)\mathrm{d}q_k \\ &= \frac{\langle Q^2\rangle}{2}\,,\\ \langle q(t)q(t+\tau)\rangle &= \int_{-\infty}^{+\infty} Q^2(k)\sin\left[\omega t+\varphi(k)\right] \\ &\quad \sin\left[\omega\left(t+\tau\right)+\varphi(k)\right]\, p(q_k)\mathrm{d}q_k \\ &= \frac{\langle Q^2\rangle}{2}\cos\left(\omega\tau\right)\,,\end{aligned}$$

which does not depend on time t (i. e., the process is stationary). The average in time gives

$$\begin{aligned}\overline{q} &= \lim_{T\to\infty}\frac{1}{T}\int_0^T Q(k)\sin\left[\omega t+\varphi(k)\right]\mathrm{d}t \\ &= 0\,,\\ \overline{q^2} &= \lim_{T\to\infty}\frac{1}{T}\int_0^T Q^2(k)\sin^2\left[\omega t+\varphi(k)\right]\mathrm{d}t \\ &= \frac{Q^2(k)}{2}\,,\\ \overline{q(t)q(t+\tau)} &= \lim_{T\to\infty}\frac{1}{T}\int_0^T Q^2(k)\sin\left[\omega t+\varphi(k)\right] \\ &\quad \times\sin\left[\omega\left(t+\tau\right)+\varphi(k)\right]\mathrm{d}t \\ &= \frac{Q^2(k)}{2}\cos\left(\omega\tau\right)\,,\end{aligned}$$

which are dependent on the set and therefore different from the values obtained from the ensemble averaging (note that the values obtained for the correlation coefficients using ensemble ($\langle q(t)q(t+\tau)\rangle/\langle q^2\rangle$) or time ($\overline{q_k(\tau)}/\overline{q^2}$) averaging are both equal to $\cos(\omega t)$): the process is therefore non-ergodic. Thus, mathematical examples of an unsteady non-ergodic process, a steady ergodic process, and a steady non-ergodic process have been given. In practice, the previous examples could correspond to several realizations of an oscillatory behavior as in measurements around propellers (or other rotating devices) and in the atmosphere; amplitudes and phases can change from one sample of the ensemble to the other due to changes in trim at each revolution (propeller) or modifications of weather conditions from day to day (atmosphere).

Returning to the possible ways in which an average can be performed, for homogeneous flow fields, the same arguments used for stationary flows can be converted from time to space. The PDF is independent of the spatial position

$$p(q)\,(x,t) = p(q)\,(t)$$

and the ensemble average can be replaced by the average in space

$$\overline{q^n} = \lim_{V\to\infty}\frac{1}{V}\int_V q^n\mathrm{d}V$$

(all quantities can be function of time after averaging). The same considerations given before are valid in this case. Nevertheless, the assumption of homogeneity in practical fluid flow conditions is much farther from reality than that of stationarity; to this end, it is important to stress that, from the Navier–Stokes equations, it is impossible to have simultaneous homogeneity and stationarity of a flow except for a fluid at rest.

Relevant Statistical Quantities in Turbulence

By performing the average over the ensemble (when possible), in time or space, it is possible to derive all the statistics for the considered fluid-mechanics variable; see Chap. 22, 23 for further information on the evaluation of mean values, higher statistical moments and cross-moments (in turbulence, cross-moments are fundamental quantities appearing in the averaged equations, Sect. 10.1.2).

Particularly interesting are the statistics related to recurrences in space and time domains (correlation functions, Sect. 22.2) or in transformed wavenumber and frequency domains (spectral functions that are related to the former by Fourier-transform operations, Sect. 22.1). In particular, it is important to point out that the general definitions of correlation and spectral functions between two points at $\boldsymbol{x}$ (time t) and $\boldsymbol{x}'=\boldsymbol{x}+\boldsymbol{r}$ (time $t+\tau$) are the following

$$\begin{aligned}R_{q_iq_j}\,(\boldsymbol{x},\boldsymbol{r},t,\tau) &= \langle q_i\,(\boldsymbol{x},t)\,q_j\,(\boldsymbol{x}+\boldsymbol{r},t+\tau)\rangle\,,\\ F^{\boldsymbol{k}}_{q_iq_j}\,(\boldsymbol{x},\boldsymbol{k},t,\tau) &= \Re\mathfrak{e}\{\Im_{\boldsymbol{k}}[R_{q_iq_j}\,(\boldsymbol{x},\boldsymbol{r},t,\tau)]\}\,,\\ F^{f}_{q_iq_j}\,(\boldsymbol{x},\boldsymbol{r},t,f) &= \Re\mathfrak{e}\{\Im_{f}[R_{q_iq_j}\,(\boldsymbol{x},\boldsymbol{r},t,\tau)]\}\,,\end{aligned}\qquad (10.1)$$

where $\Re\{\cdot\}$ means the real part of the argument, and $\Im_f[\cdot]$ and $\Im_k[\cdot]$ mean the Fourier transform in the frequency and three-dimensional wavenumber domain of the quantity in brackets, respectively. The inverse Fourier-transform relations hold when passing from the spectral to the correlation functions (Wiener–Khintchine theorem, Chap. 22 [10.9]). These quantities are vectors if the two variables q_i and q_j are scalars, second-order tensors if one of the two is a vector (i. e., the flow velocity) and third-order tensors if both are vectors (i. e., if all velocity components are considered); this depends on the fact that three projections along the reference axis of the previous quantities can be derived. For example, for the correlation function, the quantity

$$R_{u_i u_j}(x, r_x, t, \tau) = \left\langle u_i(x, t)\, u_j(x + r_x, t + \tau) \right\rangle$$

is the correlation function tensor between the velocity components u_i and u_j at the points x and $x + r_x$ along the x axis of the reference system; varying i and j from 1 to 3, nine of these functions are to be evaluated in a general flow field. Of course, each one of these functions is dependent on the initial spatial position ($\boldsymbol{x}$), the separation distance ($\boldsymbol{r}$), the initial time (t), and the separation in time (τ).

Each one of these correlation functions reduces to the single-point cross-statistical moments (covariance) when the same point ($\boldsymbol{r} = 0$) and time ($\tau = 0$) are considered

$$R_{q_i q_j}(\boldsymbol{x}, 0, t, 0) = \left\langle q_i(\boldsymbol{x}, t)\, q_j(\boldsymbol{x}, t) \right\rangle . \tag{10.2}$$

These quantities (when obtained for the fluctuating fluid-mechanics variables of a turbulent flow field) are of fundamental importance in turbulence investigations (Sect. 10.1.2); in particular, for the velocity field, these represent the Reynolds stress symmetric tensor

$$R_{u_i u_j} = \begin{pmatrix} u_1^2 & u_1 u_2 & u_1 u_3 \\ u_2 u_1 & u_2^2 & u_2 u_3 \\ u_3 u_1 & u_3 u_2 & u_3^2 \end{pmatrix} .$$

As a consequence of the previous single-point limit for correlation functions, the inverse Fourier transform gives for the spectral functions in the wavenumber and frequency domains

$$\int_0^\infty F^{\boldsymbol{k}}_{q_i q_j}(\boldsymbol{x}, \boldsymbol{k}, t, 0)\, \mathrm{d}\boldsymbol{k} = R_{q_i q_j}(\boldsymbol{x}, 0, t, 0) = \langle q_i q_j \rangle ,$$

$$\int_0^\infty F^{f}_{q_i q_j}(\boldsymbol{x}, 0, t, f)\, \mathrm{d}f = R_{q_i q_j}(\boldsymbol{x}, 0, t, 0) = \langle q_i q_j \rangle ,$$

in which, as usual in transformed domains, the single-valued limit in the correlation functions becomes an integral value for the spectral functions. For $i = j$, the integral of the spectral function just gives the mean square value of the variable under consideration.

Returning to Sect. 10.1.1, the situation is simpler when the hypothesis of a stationary flow field can be assumed; in this case, the dependence on the initial time is avoided so that

$$R_{q_i q_j}(\boldsymbol{x}, \boldsymbol{r}, \tau) = \lim_{T \to \infty} \frac{1}{T} \int_0^T q_i(\boldsymbol{x}, t)\, q_j \cdot (\boldsymbol{x} + \boldsymbol{r}, t + \tau)\, \mathrm{d}t ,$$

$$F^{k}_{q_i q_j}(\boldsymbol{x}, \boldsymbol{k}, \tau) = \Re\{\Im_k[R_{q_i q_j}(\boldsymbol{x}, \boldsymbol{r}, \tau)]\} ,$$

$$F^{f}_{q_i q_j}(\boldsymbol{x}, \boldsymbol{r}, f) = \Re\{\Im_f[R_{q_i q_j}(\boldsymbol{x}, \boldsymbol{r}, \tau)]\} .$$

Similarly, for the case of homogeneous flow field the dependence on initial position is avoided

$$R_{q_i q_j}(\boldsymbol{r}, t, \tau) = \lim_{V \to \infty} \frac{1}{V} \int_V q_i(\boldsymbol{x}, t)\, q_j \cdot (\boldsymbol{x} + \boldsymbol{r}, t + \tau)\, \mathrm{d}x ,$$

$$F^{\boldsymbol{k}}_{q_i q_j}(\boldsymbol{k}, t, \tau) = \Re\{\Im_k[R_{q_i q_j}(\boldsymbol{r}, t, \tau)]\} ,$$

$$F^{f}_{q_i q_j}(\boldsymbol{r}, t, f) = \Re\{\Im_f[R_{q_i q_j}(\boldsymbol{r}, t, \tau)]\} .$$

The situation is also simplified when purely spatial variation are considered

$$R_{q_i q_j}(\boldsymbol{x}, \boldsymbol{r}, t) = \langle q_i(\boldsymbol{x}, t)\, q_j(\boldsymbol{x} + \boldsymbol{r}, t) \rangle ,$$

$$F^{\boldsymbol{k}}_{q_i q_j}(\boldsymbol{x}, \boldsymbol{k}, t) = \Re\{\Im_k[R_{q_i q_j}(\boldsymbol{x}, \boldsymbol{r}, t)]\} ,$$

(which can be further simplified if stationary or homogeneous flow fields are assumed, so that the dependence on t or $\boldsymbol{x}$ is avoided and averages in time or space are employed), and for the purely temporally varying case

$$R_{q_i q_j}(\boldsymbol{x}, t, \tau) = \langle q_i(\boldsymbol{x}, t)\, q_j(\boldsymbol{x}, t + \tau) \rangle ,$$

$$F^{f}_{q_i q_j}(\boldsymbol{x}, t, f) = \Re\{\Im_f[R_{q_i q_j}(\boldsymbol{x}, t, \tau)]\} ,$$

(which also can be further simplified if stationary or homogeneous flow fields are assumed so that the dependence on t or $\boldsymbol{x}$ is avoided and averages in time or space are employed).

Is it also possible to define autocorrelation and autospectral functions by performing the previous eval-

uations for $q_i = q_j$ $(i = j)$; for the x axis, this is

$$
\begin{aligned}
R_{q_i^2}(x, r_x, t, \tau) &= \langle q_i(x,t)\, q_i(x+r_x, t+\tau)\rangle \,, \\
F^{k_x}_{q_i^2}(x, k_x, t, \tau) &= \Re\mathrm{e}\left\{\Im_{k_x}\left[R_{q_i^2}(x, r_x, t, \tau)\right]\right\} \,, \\
F^{f}_{q_i^2}(x, r_x, t, f) &= \Re\mathrm{e}\left\{\Im_{f}\left[R_{q_i^2}(x, r_x, t, \tau)\right]\right\} \,,
\end{aligned}
\tag{10.3}
$$

and similarly for the other two axes. In this case, there are always three independent correlation functions to be determined (i. e., the projections along the three axes) for each scalar variable q_i, so that there are nine independent functions for the three components of fluid velocity. The functions in (10.3) are also known as one-dimensional correlation and spectral functions. Normalizing these quantities by the zero-separation ($\boldsymbol{r} = 0$) or zero-time-delay ($\tau = 0$) single-point values ((10.2) with $i = j$), the so-called correlation coefficients are obtained. Relations between one- and three-dimensional correlation and spectral functions can be derived in general flow fields and in the case of isotropy [10.1, 4, 10].

Combined space–time and higher-order correlation and spectral functions can also be defined. In particular, it is interesting for the following (see the Sect. on multipoint equations), to consider the triple-point correlation functions between different velocity components at two points; one of those for the case of purely spatial correlation is written as

$$
\begin{aligned}
R_{u_i u_j, u_k}(\boldsymbol{x}, \boldsymbol{r}, t) &= \langle u_i(\boldsymbol{x}, t)\, u_j(\boldsymbol{x}, t)\, u_k(\boldsymbol{x}+\boldsymbol{r}, t)\rangle \,, \\
F^{\boldsymbol{k}}_{u_i u_j, u_l}(\boldsymbol{x}, \boldsymbol{k}, t) &= \Re\mathrm{e}\{\Im_{\boldsymbol{k}}[R_{u_i u_j, u_l}(\boldsymbol{x}, \boldsymbol{r}, t)]\} \,,
\end{aligned}
\tag{10.4}
$$

where the comma separates the quantity evaluated at the first point from those at evaluated at the second point.

Other important multipoint high-order functions are the spatial structure functions (see also Sect. 22.2 and [10.4, 11])

$$
\begin{aligned}
S^n_{q_i q_j \ldots q_k}(\boldsymbol{x}, \boldsymbol{r}, t) = \langle &[q_i(\boldsymbol{x}+\boldsymbol{r}, t) - q_i(x, t)] \\
&\times \left[q_j(\boldsymbol{x}+\boldsymbol{r}, t) - q_j(\boldsymbol{x}, t)\right] \\
&\times [q_k(x+r, t) - q_k(x, t)]\rangle \,.
\end{aligned}
$$

Equivalently, temporal structure functions can be defined. The purely longitudinal and transversal n-th-order velocity structure functions

$$
\begin{aligned}
S^n_{u_\mathrm{L}}(\boldsymbol{x}, \boldsymbol{r}, t) &= \left\langle [u_\mathrm{L}(\boldsymbol{x}+\boldsymbol{r}, t) - u_\mathrm{L}(x, t)]^n \right\rangle \,, \\
S^n_{u_\mathrm{N}}(\boldsymbol{x}, \boldsymbol{r}, t) &= \left\langle [u_\mathrm{N}(\boldsymbol{x}+\boldsymbol{r}, t) - u_\mathrm{N}(\boldsymbol{x}, t)]^n \right\rangle \,,
\end{aligned}
$$

(where u_L and u_N are the velocity components parallel and orthogonal to $\boldsymbol{r}$, respectively) can be defined. These functions are often indicated by D_L and D_N, see *Monin* and *Yaglom* [10.12]. For $n = 2$, there is a simple relation between the spatial second-order structure function of the same variable and the purely spatial autocorrelation function

$$
\begin{aligned}
S^2_{q_i}(\boldsymbol{x}, \boldsymbol{r}, t) &= \left\langle [q_i(\boldsymbol{x}+\boldsymbol{r}, t) - q_i(x, t)]^2 \right\rangle \\
&= \left\langle q_i^2(\boldsymbol{x}+\boldsymbol{r}, t)\right\rangle + \left\langle q_i^2(x, t)\right\rangle \\
&\quad - 2R_{q_i^2}(\boldsymbol{x}, \boldsymbol{r}, t) \\
&= 2\left[\left\langle q_i^2(x, t)\right\rangle - R_{q_i^2}(\boldsymbol{x}, \boldsymbol{r}, t)\right] \\
&= 2\left[R_{q_i^2}(\boldsymbol{x}, 0, t) - R_{q_i^2}(\boldsymbol{x}, \boldsymbol{r}, t)\right]
\end{aligned}
$$

using (10.2) (and similarly in time). Note that the last two equivalences hold in homogeneous turbulence (steady turbulence for the time functions). Thus, the following relation exists between the second-order structure function and spectral function (using (10.3))

$$
\begin{aligned}
S^2_{q_i}(\boldsymbol{x}, r_x, t) &= 2\Bigg(\int_0^\infty F^{k_x}_{q_i^2}(\boldsymbol{x}, k_x, t)\mathrm{d}k_x \\
&\qquad - \Re\mathrm{e}\{\Im_{k_x}[F^{k_x}_{q_i^2}(x, k_x, t)]\}\Bigg) \\
&= 2\Re\mathrm{e}\Bigg[\int_0^\infty (1 - e^{\mathrm{i}k_x r_x}) \\
&\qquad F^{k_x}_{q_i^2}(\boldsymbol{x}, k_x, t)\,\mathrm{d}k_x\Bigg]
\end{aligned}
\tag{10.5}
$$

using (10.2) (and similarly in time). It is important to notice that from the previous relation if a region in which a power-law wavenumber spectrum exists ($F \sim Ak_x^p$), then the structure function also exhibits a power-law region ($S \sim Br_x^q$), with the following relation among exponents

$$
p = -(q+1) \,,
\tag{10.6}
$$

and vice versa (see *Frisch* [10.11] and *Pope* [10.4] for the details and limitations of this relation).

It is interesting to notice two limiting behaviors for second-order structure functions; firstly, from the fact that the derivatives of a fluid-mechanics variable must be finite when the separation goes to zero (in practice, this means for separations on the order of the Kolmogorov microscale or less), it results that

$$
S^n_{q_i}(\boldsymbol{x}, \boldsymbol{r}, t) = Ar^n \quad \text{for } r \to 0 \,.
$$

Note that this result is derived for the n-th-order moment of the same variable and that for $n = 2$ this can also be derived from properties of the autocorrelation functions for $r \to 0$ (Sect. 10.1.3). With proper normalization, i. e., using Kolmogorov length and velocity scales, this result can be written in an exact form (for example, for the longitudinal component of velocity with $n = 2$ it is $A = 1/15$ [10.12, 13]). For the case of large separation, i. e., $r \to \infty$, which in practice means separations larger than the integral scale beyond which the autocorrelation function is almost null (see the Sections on the behavior of correlation functions and integral scales) one obtains

$$S^2_{q_i}(\boldsymbol{x}, \boldsymbol{r}, t) = 2\langle q'^2_i \rangle \quad \text{for } r \to \infty ;$$

similar relations can be obtained for higher-order structure functions [10.12, 13]).

From the point of view of how statistical quantities are obtained, it is important to point out that in the previous definitions the acquired data are assumed to be continuous while in practice, frequently, discrete data are obtained and the integrals must be replaced by sums. Moreover, it is usually assumed that the data are regularly sampled; in some circumstances this is not the case and irregularly sampled data (in time or space) are encountered (such as in LDA and PTV, see Sect. 5.3.1, 5.3.2). In this case, the problem is how to derive the statistics for such a data set; the simplest solution is the use of interpolation procedures (Sect. 25.1). Other interesting approaches, such as maximum-entropy methods, Kalman filters, and advanced correlation computation are possible; (see Chap. 25, *van Maanen* [10.14], for details).

Relevant Statistical Quantities in Turbulence: Isotropic Flows

In isotropic homogeneous flow conditions the single-point statistical moments of each fluid-mechanics variable are independent of the position and direction of the considered point; therefore fluctuation statistics (and PDFs) are the same in all directions

$$\langle q'^2_1 \rangle = \langle q'^2_2 \rangle = \langle q'^2_3 \rangle .$$

Moreover, all the centered statistical moments of each velocity component are equal and the cross-moments of a fluid variable with the velocity are zero independent of the velocity component involved (except the case when mean square velocity fluctuations are considered)

$$\langle u'_1 q'_i \rangle = \langle u'_2 q'_i \rangle = \langle u'_3 q'_i \rangle = 0 .$$

It is important to point out that equivalence of statistical moments implies isotropy, especially at large scales, but not necessarily at small scales (usually referred to as local isotropy). On the other hand, variable derivatives mainly depend on small scales; thus, the following relations between derivatives are a more-stringent test for local isotropy of the velocity field [10.12]

$$\begin{aligned}
&\left\langle \left(\frac{\partial u'_1}{\partial x_1} \right)^2 \right\rangle = \left\langle \left(\frac{\partial u'_2}{\partial x_2} \right)^2 \right\rangle = \left\langle \left(\frac{\partial u'_3}{\partial x_3} \right)^2 \right\rangle , \\
&2\left\langle \left(\frac{\partial u'_1}{\partial x_1} \right)^2 \right\rangle = \left\langle \left(\frac{\partial u'_1}{\partial x_2} \right)^2 \right\rangle = \left\langle \left(\frac{\partial u'_2}{\partial x_1} \right)^2 \right\rangle \\
&\qquad = \left\langle \left(\frac{\partial u'_1}{\partial x_3} \right)^2 \right\rangle = \left\langle \left(\frac{\partial u'_3}{\partial x_1} \right)^2 \right\rangle \\
&\qquad = \left\langle \left(\frac{\partial u'_3}{\partial x_2} \right)^2 \right\rangle = \left\langle \left(\frac{\partial u'_2}{\partial x_3} \right)^2 \right\rangle , \\
&\left\langle \frac{\partial u'_1}{\partial x_2} \frac{\partial u'_2}{\partial x_1} \right\rangle = \left\langle \frac{\partial u'_1}{\partial x_3} \frac{\partial u'_3}{\partial x_1} \right\rangle = \left\langle \frac{\partial u'_2}{\partial x_3} \frac{\partial u'_3}{\partial x_2} \right\rangle \\
&\qquad = -\frac{1}{2} \left\langle \left(\frac{\partial u'_1}{\partial x_1} \right)^2 \right\rangle ,
\end{aligned}$$

and for the scalar field

$$\left\langle \left(\frac{\partial q'}{\partial x_1} \right)^2 \right\rangle = \left\langle \left(\frac{\partial q'}{\partial x_2} \right)^2 \right\rangle = \left\langle \left(\frac{\partial q'}{\partial x_3} \right)^2 \right\rangle .$$

For multipoint quantities, the definitions presented in the previous section become quite simple in isotropic homogeneous flow conditions where only one correlation function is necessary for a complete description of a scalar field and only two independent correlation functions for a vector field. For the latter, in the case of the velocity field, these two independent functions are referred to as the longitudinal (f) and transverse (g) correlation functions (usually the correlation coefficients are employed); referring to (10.3), for the purely spatial correlation, considering the velocity components parallel (u_1) and orthogonal (u_2) to the direction of separation (it is now possible to take r along the direction x)

$$\begin{aligned}
f(r, t) &= R_{u_1^2}(r, t)/R_{u_1^2}(0, t) \\
&= \langle u_1(\boldsymbol{x}, t) u_1(\boldsymbol{x} + \boldsymbol{r}, t) \rangle / \langle u_1^2(\boldsymbol{x}, t) \rangle , \\
g(r, t) &= R_{u_2^2}(r, t)/R_{u_2^2}(0, t) \\
&= \langle u_2(\boldsymbol{x}, t) u_2(\boldsymbol{x} + \boldsymbol{r}, t) \rangle / \langle u_2^2(\boldsymbol{x}, t) \rangle .
\end{aligned} \tag{10.7}$$

Thus, each correlation among the velocity components in any direction can be expressed as a function of the previous two functions [10.10]

$$R_{u_i u_j}(\boldsymbol{r},t) \equiv \langle u_i(\boldsymbol{x},t)\, u_j(\boldsymbol{x}+\boldsymbol{r},t)\rangle = \langle u_i^2\rangle \left[\frac{f(r,t)-g(r,t)}{r^2} \times x_i x_j + g(r)\delta_{ij}\right], \tag{10.8}$$

where δ_{ij} is the Kronecker delta and x_i and x_j are the coordinates along the reference axis of the first and second point (separated by a distance r).

For an incompressible fluid, it is also possible to derive a relation between the longitudinal and transverse correlations [10.10]

$$g(\boldsymbol{r},t) = f(r,t) + \frac{r}{2}\frac{\partial f(r,t)}{\partial r}\,. \tag{10.9}$$

i. e., the longitudinal correlation can be derived from the transverse, so that only one function is required for the description of velocity correlations. The verification of the previous relation is a stringent test for isotropy in incompressible fluids.

Similarly, it is possible to greatly reduce the number of independent triple-point correlation functions (fourth-order tensors); only three of those 27 (each one along three axis) are different from zero in isotropic homogeneous flow [10.10]. Again, by considering the velocity components aligned with the separation distance (r taken along x), these three functions are

$$k(r,t) = \frac{R_{u_1^2,u_1}(r,t)}{R_{u_1^3}(0,t)} = \frac{\langle u_1^2(x,t)\, u_1(x+r,t)\rangle}{\langle u_1^3(x,t)\rangle}\,,$$

$$h(r,t) = \frac{R_{u_2^2,u_1}(r,t)}{R_{u_1^3}(0,t)} = \frac{\langle u_2^2(x,t)\, u_1(x+r,t)\rangle}{\langle u_1^3(x,t)\rangle}\,,$$

$$q(r,t) = \frac{R_{u_2 u_1,u_2}(r,t)}{R_{u_1^3}(0,t)} = \frac{\langle u_2(x,t)\, u_1(x,t)\, u_2(x+r,t)\rangle}{\langle u_1^3(x,t)\rangle}\,.$$

For an incompressible fluid, a further reduction to only one independent triple correlation is possible [10.10]

$$h(r,t) = -\frac{k(r,t)}{2}\,,$$

$$q(r,t) = \frac{1}{4r}\frac{\partial}{\partial r}[r^2 k(r,t)]\,. \tag{10.10}$$

Regarding the structure functions in homogeneous and isotropic flow conditions it is possible to derive a relation similar to (10.8), relating the second-order structure function among two velocity components separated in a generic direction to the longitudinal and transverse second-order structure functions

$$S^2_{u_i u_j}(r,t) = S^2_{u_2}(r,t)\,\delta_{ij} + \left[S^2_{u_1}(r,t) - S^2_{u_2}(r,t)\right]\frac{x_i x_j}{r^2}\,.$$

As for correlation functions, for incompressible fluid, it is possible to derive a relation similar to (10.9) between longitudinal and transverse second-order structure functions

$$S^2_{u_2}(r,t) = S^2_{u_1}(r,t) + \frac{r}{2}\frac{\partial}{\partial r}S^2_{u_1}(r,t)\,,$$

so that only one scalar structure function is required for a complete description of second-order velocity differences along arbitrary directions.

According to the Kolmogorov similarity hypothesis [10.11], it is possible to derive a functional form for the second-order structure functions in isotropic homogeneous turbulence for separations within the so-called inertial range (i. e., for separations much larger than the Kolmogorov scale and much smaller than the integral scale, $\eta \ll r \ll \Lambda$) (Sect. 10.1.3),

$$S^2_{u_1}(r,t) = C_2(\varepsilon r)^{2/3}\,, \tag{10.11}$$

where C_2 is a constant (in theory not dependent on Reynolds number). Generalizing the previous power-law dependence to n-th order, it is possible to write

$$S^n_{u_1}(r,t) = C_n(\varepsilon r)^{n/3}\,. \tag{10.12}$$

The previous equation has been tested numerically and experimentally in several flow fields. Although the question of effective isotropy to be obtained is raised (i. e., large enough Reynolds numbers), it appeared that departures from Kolmogorov theory due to intermittency of small scales are present; several models have been proposed to account for the nonlinear structure function exponent behavior but none is able to explain the behavior of n-th-order structure functions over the entire range of separations (see *Frisch* [10.11] for details of this argument).

For the spectral functions, using (10.6) and (10.11), it is possible to obtain the following prediction for the behavior in the inertial range

$$F^{k_x}_{u_1^2}(k_x,t) = C_K \varepsilon^{2/3} k_x^{-5/3}\,, \tag{10.13}$$

which is the well known $-5/3$ power law for the inertial range in velocity spectrum of turbulence.

Relation Between Quantities Evaluated in Space and Time: Taylor's Hypothesis

It is important to point out again the differences between statistics obtained at a single point and at different points. Let us take the example of purely spatial or purely time correlation functions of a fluid-mechanics variable (see the previous two sections for details). Of course, from the experimental point of view, the former can only be evaluated by performing multipoint measurements of the variable, while the latter are obtained by measuring the evolution of the same variable in time at a single point. As already pointed out, in general, these are not uniquely linked to one another, especially when considering small vortical structures of the flow field (Sect. 10.1.3). In many circumstances, however, it is much simpler to perform measurements at a single point rather than simultaneously at several points. Therefore, it is important to establish if a relation between the behaviors in space and time holds and the degree of validity of such an approximation.

J. T. Taylor [10.15], devised an hypothesis (since then known as Taylor's hypothesis) in which time and space behaviors (along the mean direction of motion) of a fluid-mechanics variable q are simply related by the convection velocity U_c (along the same mean direction)

$$\frac{\partial q}{\partial t} + U_c \frac{\partial q}{\partial x_1} = 0 \,. \tag{10.14}$$

This hypothesis is equivalent to vanish the mean substantial derivative, i. e., to ignore in the equations of motion the transport of q along directions orthogonal to the mean flow and its diffusion in space (when q is the velocity, the pressure term is also not considered). The hypothesis seems to be a rather coarse approximation with a poor degree of validity in practical conditions; surprisingly, this is not the case and the hypothesis holds quite well in many flow conditions.

Before considering the range of validity of Taylor's hypothesis, it is important to specify in more detail the experimental meaning of the convection velocity and how the hypothesis is applied in practice. The simplest way (as in the original formulation) to apply the hypothesis is to consider the convection velocity as a constant for all flow scales, for example assuming

$$U_c = U_0 \,;$$

this means that the flow pattern is simply *frozen* at a given instant and convected over the observation point in time (this is why Taylor's hypothesis is also known as the frozen-field hypothesis). Thus, the developments in time and space are simply related by a translation from the space to the time axis and vice versa. The purely spatial autocorrelation function is evaluated through the purely time autocorrelation function

$$R_{q_i^2}(x_1, r_x = \tau U_c, t, 0) = R_{q_i^2}(x_1, 0, t, \tau) \quad .$$

This relation is obtained by considering that integration of (10.14) from t to $t - \tau$, assuming U_c to be a constant, gives

$$q_i(x_1, t + \tau) = q_i(x_1 - U_c\tau, t) \,,$$

(when dealing with wavenumber spectral functions, Taylor's hypothesis allows the replacement of the wavenumber along the mean flow direction with the frequency and vice versa, $k_1 = 2\pi f/U_c$, i. e., to replace the wavenumber with the frequency spectra).

Experiments have demonstrated that this simple application of the hypothesis is not effective and that in many circumstances the convection velocity is different from the mean velocity. For example, in near-wall flows, to allow Taylor's hypothesis properly, the convection velocity should be selected between $0.7U_0$ and $0.9U_0$ depending on the distance from the wall [10.16]. Thus, the idea of a frozen field at all flow scales (i. e., regardless of the value of the local convection velocity for each flow scale) is only a first-order approximation. By performing simultaneous time correlation (at a single point) and space correlation (at several points), it is possible to show how valid the hypothesis of constant U_c is.

In Fig. 10.3, a comparison between time and space autocorrelation coefficients is given (see *Romano* [10.16] for details); these results are obtained by performing velocity measurements in a turbulent channel flow at different near-wall locations and different Reynolds numbers by means of two independent LDA systems separated along the streamwise direction (at a separation of r). The spatial correlation is transformed into a time correlation by using the local mean velocity (U_l, i. e., the velocity at the considered location) of each data set (with a constant value of convection velocity). It can be observed that near the centreline ($y^+ = 200$, where the plus indicates nondimensional wall units, refer to Chap. 12) and at the largest Reynolds number (top of Fig. 10.3), the spatial and time correlations agree reasonably well especially in the range between the Taylor and

integral scales (indicated by the vertical dotted lines in the figure; see Sect. 10.1.3 for the definitions of turbulent scales). On the other hand, close to the wall ($y^+ = 20$, $y^+ = 10$) and at low Reynolds numbers (at the bottom of the figure), the space correlation overestimate the time correlation; this means that the convection velocity used to transform space into the time correlation (i. e., the local mean velocity) is too small. A better evaluation of the convection velocity, presented in the following, allows one to obtain space correlations (*dashed curves*) that are quite close to the time correlations. Note that, even with this correction, for scales smaller than the Taylor microscale there is a definite departure between the space and time correlations (as for the cases at the centreline and higher Reynolds numbers). Note also that, the larger the turbulence intensity (indicated at the bottom left corner of each plot), the greater the difference between the space and time correlations.

A possible way to evaluate the correct convection velocity from data is to compute the time delay between the time autocorrelation and the envelope of shifted space cross-correlations between two points separated by r. Such a time delay is given in Fig. 10.4, on the left for a space cross-correlation shifted by r/U_0 (i. e., using the centreline mean velocity) and on the right by r/U_l (i. e., using the local mean velocity).

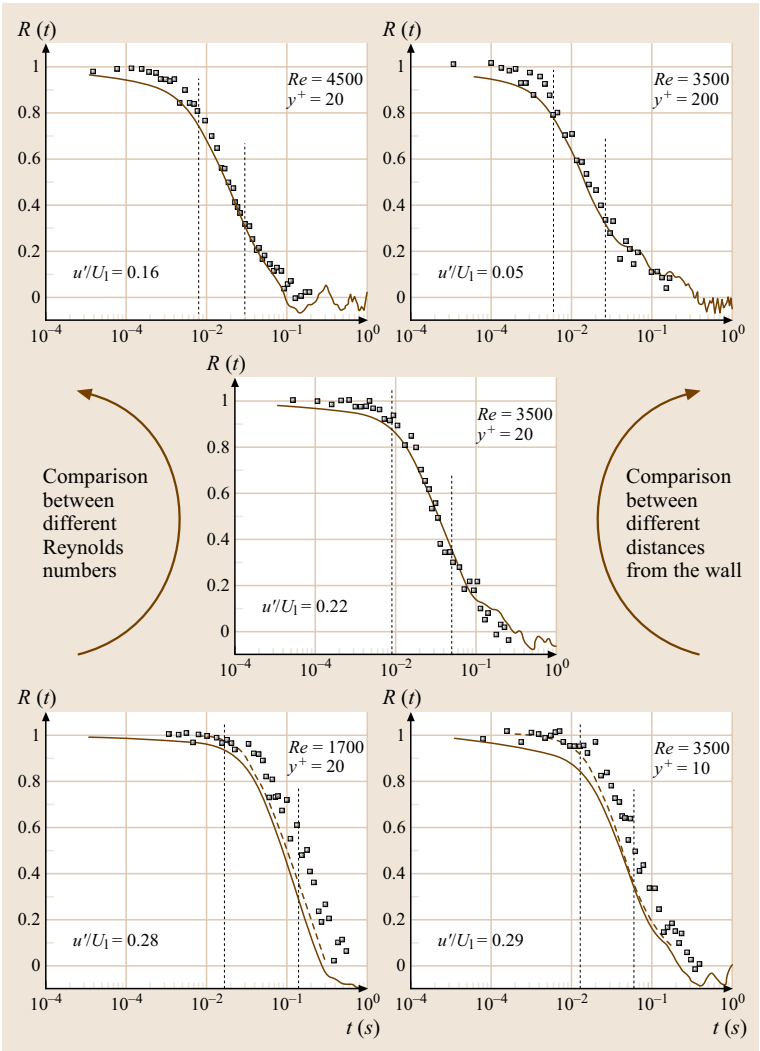

Fig. 10.3 Comparison between time autocorrelation (*continuous lines*) and space autocorrelation (*symbols*) coefficients at different Reynolds numbers and distances from the wall. *Vertical dotted lines* show Taylor and integral time scales. Longitudinal velocity fluctuations normalized by local mean velocity are also indicated. *Dashed curves* show space autocorrelation coefficients with time lag obtained using measured convection velocity rather than local mean velocity (after *Romano* [10.16])

When the centreline mean velocity shift is used, the time delay increases almost linearly; an increase in time delay with separation between points means that the effective convection velocity of turbulent structures is smaller than the centreline mean velocity. A linear increase means that this effective convection velocity is constant (for the separation between points considered); the convection velocity is just the inverse of the slope of the line. Thus, the effective convection velocity is approximately equal to the mean flow velocity at the centreline, while it decreases when moving towards the wall (plot at the bottom left); on the other hand, in comparison to the mean centreline velocity, it is smaller for larger Reynolds numbers (plot at the top left; note that data at the same Reynolds number are acquired at $y^+ = 20$, i. e., close to the wall). When the local mean velocity shift is used (plots on the right), the time delay is almost zero for large Reynolds numbers and far from the wall (indicating that the convection velocity is almost equal to the local mean velocity), whereas

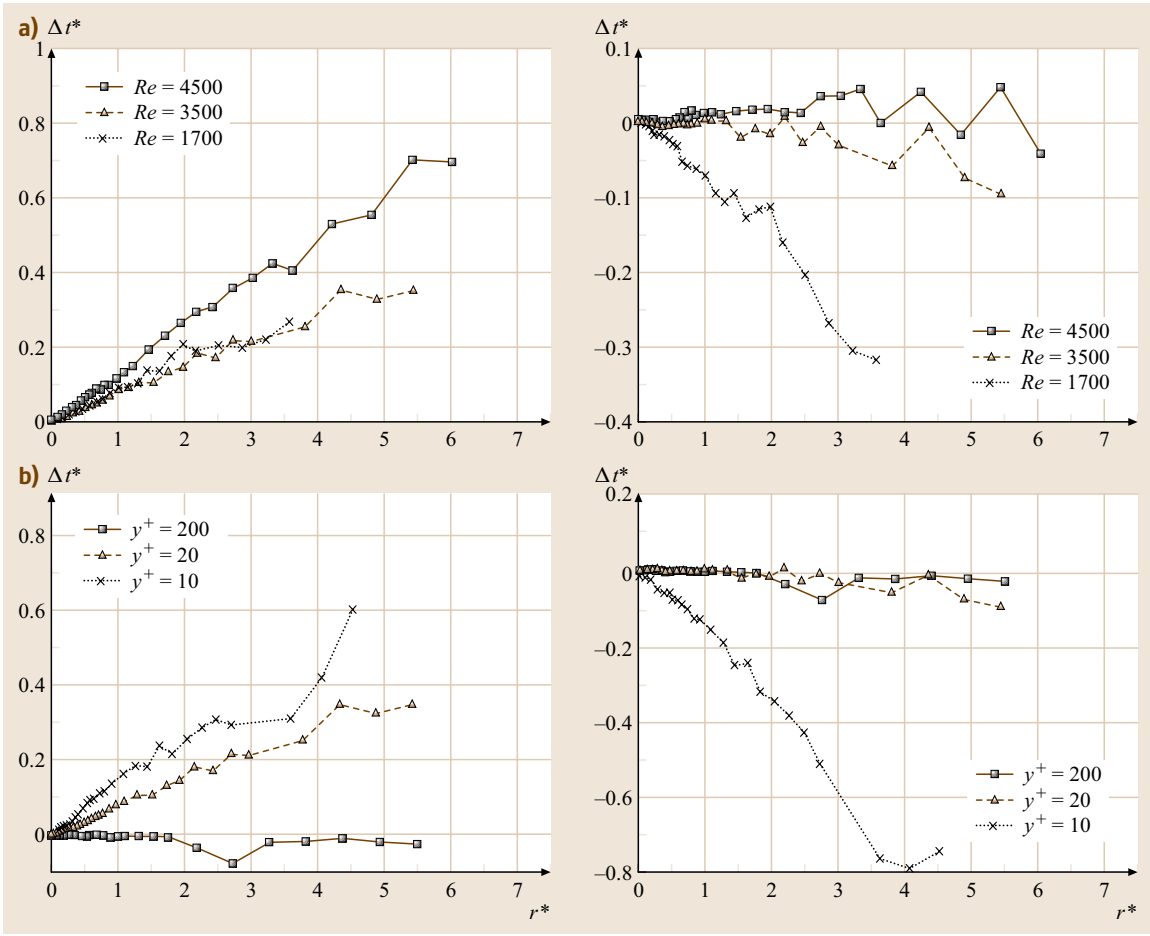

Fig. 10.4 *On the left*: dimensionless time delay (using the integral time scale) between the measured time autocorrelation and the envelope of the space cross-correlation shifted by r/U_0 (where U_0 is the mean flow velocity) versus the dimensionless separation (using the integral length scale). Different Reynolds numbers **(a)** and different distances from the wall **(b)**. *On the right*: dimensionless time delay (using integral time scale) between measured the time autocorrelation and the envelope of the space cross-correlation shifted by r/U_1 (where U_1 is the local mean flow velocity) versus the dimensionless separation (using the integral length scale). Different Reynolds numbers **(a)** and different distances from the wall **(b)** (after Romano [10.16])

it decreases almost linearly for the smallest Reynolds numbers and very close to the wall (indicating that the effective convection velocity is larger that the local mean velocity).

The previous observations lead to a practical criterion for the application of Taylor's hypothesis which connects the variability of the entire flow field (which is usually valuable) to the variation of the convection velocity over the different flow scales (which is not simply valuable):

$$U_c = \begin{cases} \Lambda/\tau_0 \sim U_0 & \text{large scales} \\ \lambda/\tau_\lambda \sim U_0 f(I) & \text{intermediate scales} \\ \eta/\tau_\eta = v_\eta \sim U_0 \mathrm{Re}^{1/4} & \text{small scales} \end{cases}$$
$$\left.\begin{array}{l} (\text{order } \Lambda\,,\, \tau_0) \\ (\text{order } \lambda,\, \tau_\lambda) \\ (\text{order } \eta,\, \tau_\eta) \end{array}\right\}\,,$$

(see Sect. 10.1.3) where $f(I)$ is a function of the turbulence intensity I (the ratio between the root-mean-square fluctuations and mean velocity) and the Reynolds number is based on the large scales. Thus, while large scales are convected by the mean flow velocity and small scales with a much lower velocity (which depends on the Reynolds number), the convection velocity of intermediate scales depends on the turbulent intensity. A practical criterion for Taylor's hypothesis to hold for intermediate scales is to have a turbulent intensity less than 20%. Many investigations have confirmed this limit (even if the hypothesis is used up to turbulent intensities as high as 30%) in a variety of flow conditions [10.16]. Figure 10.4 shows an example of the degree of validity of the hypothesis. The reader is also referred to Sect. 10.1.3 for further details on the application of Taylor's hypothesis at the different flow scales.

10.1.2 Reynolds Decomposition and Equations

Generalities

The statistical Eulerian description of turbulent flows considers the previously defined domains to perform averaging (in particular, in this section we will refer to ensemble averaging) and the decomposition into average and fluctuating terms as introduced in Sect. 10.1.1.

The decomposition in terms of two contributions (average and fluctuations) was introduced by O. Reynolds in 1894; it is substituted into the equation of motion for each fluid-mechanics variable to derive the averaged equations of motion in the presence of turbulence. This may appear a rather strange way to proceed when considering that the equations themselves do not contain any reference to laminar or turbulent conditions. Therefore, the equation of fluid mechanics, as an instantaneous representation of the flow field, must be considered fully valid for a turbulent flow (whatever the Reynolds number). The direct numerical simulation (DNS) approach effectively considers and solves the equations of fluid mechanics without any additional treatment (at least for moderate Reynolds numbers due to resolution problems on the small scales). In DNS, instantaneous fields are computed and their evolution in time and space is evaluated. A similar approach can be adopted for experimental data by measuring the instantaneous flow fields, especially when interest is focused on the generation, interaction, and dissipation of *coherent* vortical structures in turbulent flow fields. Even in this case, some sort of averaging is required to distinguish between casual and repetitive events. On the other hand, the instantaneous representation is not useful when we are interested in the average behavior of the fluid-mechanics variables (not only for mean values but for higher-order moments also) and on the average contribution of each term in the equations of motion, for example in the evaluation of energy balances in flow fields; in these cases, averaging procedure are required.

Hypothesis and Useful Relations

The essential point of Reynolds decomposition is the aforementioned separation between the mean and fluctuating parts for a fluid-mechanics variable q,

$$q = \langle q \rangle + q' \,,$$

where triangular brackets (i. e., ensemble averaging) will be used unless otherwise specified. The fluctuating part q'' averaging the previous relation has a vanishing mean value

$$\langle q' \rangle \equiv 0 \,.$$

The other relations that have to be used before performing averaging of the equations is concerned with the properties of space and time derivatives when averaging (which is a linear operator),

$$\frac{\partial^n q}{\partial x_i^n} = \left\langle \frac{\partial^n q}{\partial x_i^n} \right\rangle + \frac{\partial^n q'}{\partial x_i^n} \,,$$
$$\frac{\partial^n q}{\partial t^n} = \left\langle \frac{\partial^n q}{\partial t^n} \right\rangle + \frac{\partial^n q'}{\partial t^n} \,,$$

where we should note that the exchange between average and space (or time) derivatives is strictly valid only if ensemble averaging is performed, while it is not valid for the case of space (or time) averaging; in these cases, great care must be used when considering the average turbulent equations, i. e., each term should be reconsidered separately. The following also hold:

$$\left\langle \frac{\partial^n q'}{\partial x_i^n} \right\rangle = \frac{\partial^n}{\partial x_i^n} \langle q' \rangle = 0 \,,$$
$$\left\langle \frac{\partial^n q'}{\partial t^n} \right\rangle = \frac{\partial^n}{\partial t^n} \langle q' \rangle = 0 \,.$$

For cross-moments

$$q_1 q_2 = \langle q_1 \rangle \langle q_2 \rangle + \langle q_1 \rangle q_2' + \langle q_2 \rangle q_1' + q_1' q_2' \,,$$

which when averaged gives (due to the vanishing mean value of the fluctuating part)

$$\langle q_1 q_2 \rangle = \langle q_1 \rangle \langle q_2 \rangle + \left\langle q_1' q_2' \right\rangle \,.$$

This result is not true for three or more variables cross-moments, where additional terms are present.

For cross-moment derivatives

$$\left\langle \frac{\partial^n (q_1 q_2)}{\partial x_i^n} \right\rangle = \frac{\partial^n}{\partial x_i^n} \left(\langle q_1 \rangle \langle q_2 \rangle \right) + \frac{\partial^n}{\partial x_i^n} \left(\left\langle q_1' q_2' \right\rangle \right) \,,$$
$$\left\langle \frac{\partial^n (q_1 q_2)}{\partial t^n} \right\rangle = \frac{\partial^n}{\partial t^n} \left(\langle q_1 \rangle \langle q_2 \rangle \right) + \frac{\partial^n}{\partial t^n} \left(\left\langle q_1' q_2' \right\rangle \right) \,.$$

and similarly for cross-moments second-order derivatives.

Derivation of the Equations for Turbulent Flows: Single-Point Results

The equations we are dealing with are those of fluid mechanics (Chap. 1), i. e., the equations of mass conservation, balance of momentum and energy, and the equation of state. In the case of a species in the flow, the equation for species concentration conservation must also be added.

Let us start with the *conservation of fluid mass* for compressible fluid flows

$$\frac{\partial \rho}{\partial t} + \frac{\partial (\rho u_i)}{\partial x_i} = 0 \,,$$

where ρ is the density and u_i the i-th velocity component. It is assumed that the flow variables are continuous functions within the control volume (i. e., discontinuities have to be considered in an integral rather than a differential approach [10.1]). Applying Reynolds decomposition to both the density and velocity components yields

$$\frac{\partial (\langle \rho \rangle + \rho')}{\partial t} + \frac{\partial}{\partial x_i} \left[\left(\langle \rho \rangle + \rho' \right) \left(\langle u_i \rangle + u_i' \right) \right] = 0$$

and evaluating the average equation (i. e., the average of all terms in the equation due to the linearity of the averaging operations)

$$\frac{\partial \langle \rho \rangle}{\partial t} + \frac{\partial}{\partial x_i} \left(\langle \rho \rangle \langle u_i \rangle \right) + \frac{\partial}{\partial x_i} \left\langle \rho' u_i' \right\rangle = 0 \,,$$

which is different from the starting equation (even if average values are considered rather than instantaneous one) due to the presence of the cross-terms $\langle \rho' u_i' \rangle$; these terms must be considered as new variables in turbulent flows; in principle they cannot be derived from the other unknowns. This equation is valid for all flows with density changes (also temperature changes as in convective flows or in the presence of flows with different densities). For flows in which density fluctuations can be neglected, this reduces to

$$\frac{\partial \langle \rho \rangle}{\partial t} + \frac{\partial}{\partial x_i} \left(\langle \rho \rangle \langle u_i \rangle \right) = 0 \,,$$

which is formally equivalent to the original equation for the conservation of mass, if we replace the velocity components and density with their mean values. If the density is also constant over space and time, as in incompressible fluid flows,

$$\frac{\partial \langle u_i \rangle}{\partial x_i} = 0 \,.$$

As the divergence of the instantaneous and average velocity fields is equal to zero, the Reynolds decomposition means that the divergence of the fluctuating velocity field must also vanish

$$\frac{\partial u_i'}{\partial x_i} = 0 \,.$$

Thus, for the case of small density fluctuations, the equation of mass conservation for the turbulent field does not add another unknown to the list of fluid-mechanics variables.

The equation for the *balance of momentum* for a Newtonian fluid (i. e., the Navier–Stokes equations) is given by (under the hypothesis of constant dynamic viscosity coefficient for a perfect gas, while for liquids

the last term on the right-hand side vanishes)

$$\rho\left(\frac{\partial u_i}{\partial t}+u_j\frac{\partial u_i}{\partial x_j}\right)=-\frac{\partial p}{\partial x_i}+\rho f_i+\mu\frac{\partial^2 u_i}{\partial x_j^2}+\frac{\mu}{3}\frac{\partial}{\partial x_i}\left(\frac{\partial u_j}{\partial x_j}\right) .$$

where p is the pressure, μ is the viscosity coefficient, and f_i are the components of the external mass forces (as the gravity force). The terms on the left-hand side of the equation can be grouped to form the substantial derivative. Let us assume that the viscosity coefficient and the mass forces are constant with respect to turbulent fluctuations, and apply the Reynolds decomposition to the velocity components, pressure, and density. After averaging, the previous equation becomes

$$\begin{aligned}&\langle\rho\rangle\frac{\partial\langle u_i\rangle}{\partial t}+\left\langle\rho'\frac{\partial u_i'}{\partial t}\right\rangle+\langle\rho\rangle\langle u_j\rangle\frac{\partial\langle u_i\rangle}{\partial x_j}\\&+\langle\rho\rangle\left\langle u_j'\frac{\partial u_i'}{\partial x_j}\right\rangle+\langle u_j\rangle\left\langle\rho'\frac{\partial u_i'}{\partial x_j}\right\rangle\\&+\left\langle\rho' u_j'\right\rangle\frac{\partial\langle u_i\rangle}{\partial x_j}+\left\langle\rho' u_j'\frac{\partial u_i'}{\partial x_j}\right\rangle\\&=-\frac{\partial\langle p\rangle}{\partial x_i}+\langle\rho\rangle f_i+\mu\frac{\partial^2\langle u_i\rangle}{\partial x_j^2}+\frac{\mu}{3}\frac{\partial}{\partial x_i}\left(\frac{\partial\langle u_j\rangle}{\partial x_j}\right) ,\end{aligned}$$

where the right-hand side of the equation, which contains linear terms, is the same as in the original case (if we replace the variables with their mean values), while the left-hand side contains many cross-terms. Again, if we assume that the density is constant over the ensemble (i. e., no turbulent fluctuations in the density), we obtain

$$\begin{aligned}&\langle\rho\rangle\frac{\partial\langle u_i\rangle}{\partial t}+\langle\rho\rangle\langle u_j\rangle\frac{\partial\langle u_i\rangle}{\partial x_j}+\langle\rho\rangle\left\langle u_j'\frac{\partial u_i'}{\partial x_j}\right\rangle\\&=-\frac{\partial\langle p\rangle}{\partial x_i}+\langle\rho\rangle f_i+\mu\frac{\partial^2\langle u_i\rangle}{\partial x_j^2}+\frac{\mu}{3}\frac{\partial}{\partial x_i}\left(\frac{\partial\langle u_j\rangle}{\partial x_j}\right) ,\end{aligned}$$

where only the cross-term between the velocity fluctuations is different from the original case. For the constant-density case (over space and time), using the conservation of mass for the fluctuating part, we can write the above cross-term as

$$\langle\rho\rangle\left\langle u_j'\frac{\partial u_i'}{\partial x_j}\right\rangle=\langle\rho\rangle\frac{\partial}{\partial x_j}\langle u_i' u_j'\rangle$$

which better highlights that, when compared to the starting equations, the new variable $\rho\langle u_i' u_j'\rangle$ is added (the Reynolds stress). As before, in principle, this variable cannot be obtained from other variables unless a new equation is written for it.

Applying the *conservation of energy* (total energy, including thermal and kinetic contributions, from the first law of thermodynamics), the following equation is obtained

$$\rho\frac{\mathrm{D}U}{\mathrm{D}t}+\rho u_i\frac{\mathrm{D}u_i}{\mathrm{D}t}=-\frac{\partial(pu_i)}{\partial x_i}+\rho f_i u_i+\frac{\partial}{\partial x_j}\left(\sigma_{ji}u_i\right)+\rho Q-\frac{\partial q_i}{\partial x_i} ,$$

where U is the internal energy ($=c_V T$ for a perfect gas, where c_V is the specific heat at constant volume and T the temperature), $\sigma_{ji}=\mu\left[\left(\frac{\partial u_j}{\partial x_i}+\frac{\partial u_i}{\partial x_j}\right)-\frac{2}{3}\frac{\partial u_k}{\partial x_k}\delta_{ji}\right]$ is the viscous part of the stress tensor, Q and q are the heat fluxes exchanged by radiation and conduction, respectively, (q is usually given in terms of the Fourier constitutive relation $q_i=-k\frac{\partial T}{\partial x_i}$, where k is the fluid thermal conductivity). This equation contains an independent (from the other equations) part that is purely a balance of thermal energy

$$\rho\frac{\mathrm{D}U}{\mathrm{D}t}=-p\frac{\partial u_i}{\partial x_i}+\sigma_{ji}\frac{\partial u_i}{\partial x_j}+\rho Q-\frac{\partial q_i}{\partial x_i} ,$$

which can also be given in terms of entropy, and a part that contains the balance of kinetic energy

$$\rho u_i\frac{\mathrm{D}u_i}{\mathrm{D}t}=-u_i\frac{\partial p}{\partial x_i}+\rho f_i u_i+u_i\frac{\partial\sigma_{ji}}{\partial x_j} ,$$

which is not independent of the other equations of fluid mechanics, being derivable from the balance of momentum by scalar multiplication with the velocity.

When applying the Reynolds decomposition to the thermal energy balance, the following equation is obtained

$$\begin{aligned}&\rho c_V\left(\frac{\partial\langle T\rangle}{\partial t}+\langle u_i\rangle\frac{\partial\langle T\rangle}{\partial x_i}+\left\langle u_i'\frac{\partial T'}{\partial x_i}\right\rangle\right)\\&=-\langle p\rangle\frac{\partial\langle u_i\rangle}{\partial x_i}-\left\langle p'\frac{\partial u_i'}{\partial x_i}\right\rangle+\mu\left[\frac{\partial\langle u_j\rangle}{\partial x_i}\frac{\partial\langle u_i\rangle}{\partial x_j}\right.\\&+\left\langle\frac{\partial u_j'}{\partial x_i}\frac{\partial u_i'}{\partial x_j}\right\rangle+\left(\frac{\partial\langle u_i\rangle}{\partial x_j}\right)^2+\left\langle\left(\frac{\partial u_i'}{\partial x_j}\right)^2\right\rangle\\&\left.-\frac{2}{3}\left(\frac{\partial\langle u_k\rangle}{\partial x_k}\right)^2-\frac{2}{3}\left\langle\left(\frac{\partial u_k'}{\partial x_k}\right)^2\right\rangle\right]\\&+\rho\langle Q\rangle+k\frac{\partial^2\langle T\rangle}{\partial x_i^2} ,\end{aligned}$$

assuming that c_V, μ, k, and Q are constant, and that the density has no fluctuations over the ensemble. Under the assumption of a zero-divergence flow field, this reduces to

$$\rho c_V \left(\frac{\partial \langle T \rangle}{\partial t} + \langle u_i \rangle \frac{\partial \langle T \rangle}{\partial x_i} + \frac{\partial \langle u_i' T' \rangle}{\partial x_i} \right) = \mu \left[\frac{\partial \langle u_j \rangle}{\partial x_i} \frac{\partial \langle u_i \rangle}{\partial x_j} + \left\langle \frac{\partial u_j'}{\partial x_i} \frac{\partial u_i'}{\partial x_j} \right\rangle + \left(\frac{\partial \langle u_i \rangle}{\partial x_j} \right)^2 + \left\langle \left(\frac{\partial u_i'}{\partial x_j} \right)^2 \right\rangle \right] + \rho \langle Q \rangle + k \frac{\partial^2 \langle T \rangle}{\partial x_i^2} ,$$

which (apart from the average terms, which are similar to the original equation) contains the cross-term $\langle u_i' T' \rangle$ similarly to the previous equations, plus the cross-derivative terms

$$\left\langle \frac{\partial u_j'}{\partial x_i} \frac{\partial u_i'}{\partial x_j} \right\rangle ,$$
$$\left\langle \left(\frac{\partial u_i'}{\partial x_j} \right)^2 \right\rangle .$$

The same procedure applied to the pure kinetic-energy equation leads to

$$\begin{aligned} &\rho \langle u_i \rangle \left(\frac{\partial \langle u_i \rangle}{\partial t} + \langle u_j \rangle \frac{\partial \langle u_i \rangle}{\partial x_j} + \left\langle u_j' \frac{\partial u_i'}{\partial x_j} \right\rangle \right) \\ &+ \rho \left(\left\langle u_i' \frac{\partial u_i'}{\partial t} \right\rangle + \langle u_j \rangle \left\langle u_i' \frac{\partial u_i'}{\partial x_j} \right\rangle + \langle u_i' u_j' \rangle \frac{\partial \langle u_i \rangle}{\partial x_j} + \left\langle u_i' u_j' \frac{\partial u_i'}{\partial x_j} \right\rangle \right) \\ &= \rho f_i \langle u_i \rangle - \langle u_i \rangle \frac{\partial \langle p \rangle}{\partial x_i} - \left\langle u_i' \frac{\partial p'}{\partial x_i} \right\rangle + \\ &\mu \left[\frac{1}{3} \langle u_i \rangle \frac{\partial^2 \langle u_j \rangle}{\partial x_i \partial x_j} + \frac{1}{3} \left\langle u_i' \frac{\partial^2 u_j'}{\partial x_i \partial x_j} \right\rangle \right. \\ &\left. + \langle u_i \rangle \frac{\partial^2 \langle u_i \rangle}{\partial x_j^2} + \left\langle u_i' \frac{\partial^2 u_i'}{\partial x_j^2} \right\rangle \right] \end{aligned}$$

under the assumptions of constant μ, f_i, and ρ (with respect to the ensemble). For constant density, this equation reduces to

$$\begin{aligned} &\rho \langle u_i \rangle \left(\frac{\partial \langle u_i \rangle}{\partial t} + \langle u_j \rangle \frac{\partial \langle u_i \rangle}{\partial x_j} + \frac{\partial \langle u_i' u_j' \rangle}{\partial x_j} \right) \\ &+ \rho \left(\left\langle u_i' \frac{\partial u_i'}{\partial t} \right\rangle + \langle u_j \rangle \left\langle u_i' \frac{\partial u_i'}{\partial x_j} \right\rangle + \langle u_i' u_j' \rangle \frac{\partial \langle u_i \rangle}{\partial x_j} \right. \\ &\left. + \frac{1}{2} \frac{\partial \langle u_i'^2 u_j' \rangle}{\partial x_j} \right) \\ &= \rho f_i \langle u_i \rangle - \frac{\partial \langle u_i \rangle \langle p \rangle}{\partial x_i} - \frac{\partial \langle p' u_i' \rangle}{\partial x_i} \\ &+ \mu \left[\langle u_i \rangle \frac{\partial^2 \langle u_i \rangle}{\partial x_j^2} + \left\langle u_i' \frac{\partial^2 u_i'}{\partial x_j^2} \right\rangle \right] \end{aligned}$$

Under the previous hypothesis, sometimes the third and sixth terms on the left-hand side are grouped into the term [10.17]

$$\frac{\partial \langle u_i \rangle \langle u_i' u_j' \rangle}{\partial x_j} ,$$

which can be further separated into a part for the average kinetic energy, i. e., the kinetic energy of the mean flow ($\langle K \rangle = \langle u_i \rangle \langle u_i \rangle / 2$), which can also be obtained directly from the Navier–Stokes equations by scalar multiplication by $\langle u_i \rangle$,

$$\begin{aligned} &\rho \left(\frac{\partial \langle K \rangle}{\partial t} + \langle u_j \rangle \frac{\partial \langle K \rangle}{\partial x_j} + \langle u_i \rangle \frac{\partial \langle u_i' u_j' \rangle}{\partial x_j} \right) \\ &= \rho f_i \langle u_i \rangle - \frac{\partial \langle u_i \rangle \langle p \rangle}{\partial x_i} + \mu \langle u_i \rangle \frac{\partial^2 \langle u_i \rangle}{\partial x_j^2} , \end{aligned}$$

plus a part for the fluctuating kinetic energy, i. e., the turbulent kinetic energy (TKE), $K' = \langle u_i' u_i' \rangle / 2$, which is obtained by subtracting the equation for the mean from the total kinetic-energy equation and averaging [10.10, 17]

$$\begin{aligned} &\rho \left(\frac{\partial K'}{\partial t} + \langle u_j \rangle \frac{\partial K'}{\partial x_j} + \langle u_i' u_j' \rangle \frac{\partial \langle u_i \rangle}{\partial x_j} + \frac{\partial \langle K' u_j' \rangle}{\partial x_j} \right) \\ &= - \frac{\partial \langle p' u_i' \rangle}{\partial x_i} + \mu \left\langle u_i' \frac{\partial^2 u_i'}{\partial x_j^2} \right\rangle . \end{aligned}$$

The equation for kinetic energy of the mean motion contains cross-terms already recognized from the other equations for turbulent motions ($\langle u_i' u_j' \rangle$). On the other hand, the second term on the right-hand side of the TKE

equation can be rewritten as

$$\mu\left\langle u_i'\frac{\partial^2 u_i'}{\partial x_j^2}\right\rangle = \mu\left(\frac{\partial}{\partial x_j}\left\langle u_i'\frac{\partial u_i'}{\partial x_j}\right\rangle - \left\langle\frac{\partial u_i'}{\partial x_j}\frac{\partial u_i'}{\partial x_j}\right\rangle\right)$$
$$= \mu\left(\frac{1}{2}\frac{\partial^2\langle u_i'^2\rangle}{\partial x_j^2} - \left\langle\left(\frac{\partial u_i'}{\partial x_j}\right)^2\right\rangle\right),$$

where the quantity $\varepsilon = \nu\langle\left(\frac{\partial u_i'}{\partial x_j}\right)^2\rangle$ is usually referred to as the homogeneous TKE dissipation rate. Therefore, using the previous relations, the TKE equation can be written as (dividing by the density)

$$\frac{\partial K'}{\partial t} + \langle u_j\rangle\frac{\partial K'}{\partial x_j}$$
$$+\langle u_i'u_j'\rangle\frac{\partial\langle u_i\rangle}{\partial x_j} + \frac{\partial\langle K'u_j'\rangle}{\partial x_j}$$
$$= -\frac{1}{\rho}\frac{\partial\langle p'u_i'\rangle}{\partial x_i} + \nu\frac{\partial^2 K'}{\partial x_j^2} - \varepsilon$$

which contains cross-terms ($\langle u_i'u_j'\rangle$, $\langle K'u_j'\rangle$, $\langle u_i'p'\rangle$) and cross-derivatives terms in ε. Note that in homogeneous turbulence the previous equation reduces to $\mathrm{d}K'/\mathrm{d}t = -\varepsilon$.

The quantity ε in the previous equation is only a part of the whole dissipation rate, so that the total dissipation rate is given by

$$\varepsilon_T = \frac{1}{2}\nu\left\langle\left(\frac{\partial u_i'}{\partial x_j} + \frac{\partial u_j'}{\partial x_i}\right)^2\right\rangle$$
$$= \nu\left[\left\langle\frac{\partial u_j'}{\partial x_i}\frac{\partial u_i'}{\partial x_j}\right\rangle + \left\langle\left(\frac{\partial u_i'}{\partial x_j}\right)^2\right\rangle\right]$$
$$= \nu\left[\frac{\partial}{\partial x_j}\left\langle u_i'\frac{\partial u_j'}{\partial x_i}\right\rangle + \left\langle\left(\frac{\partial u_i'}{\partial x_j}\right)^2\right\rangle\right],$$

although strictly speaking the first term on the right-hand side is not a dissipation, but rather a diffusion term. In this relation, the first part in the second square brackets (which contains three diagonal square terms plus three cross-terms) is different from zero only in imhomogeneous turbulence, where [10.12, 18]

$$\left\langle\frac{\partial u_1'}{\partial x_2}\frac{\partial u_2'}{\partial x_1}\right\rangle + \left\langle\frac{\partial u_1'}{\partial x_3}\frac{\partial u_3'}{\partial x_1}\right\rangle = -\left\langle\left(\frac{\partial u_1'}{\partial x_1}\right)^2\right\rangle,$$
$$\left\langle\frac{\partial u_2'}{\partial x_1}\frac{\partial u_1'}{\partial x_2}\right\rangle + \left\langle\frac{\partial u_2'}{\partial x_3}\frac{\partial u_3'}{\partial x_2}\right\rangle = -\left\langle\left(\frac{\partial u_2'}{\partial x_2}\right)^2\right\rangle,$$
$$\left\langle\frac{\partial u_3'}{\partial x_1}\frac{\partial u_1'}{\partial x_3}\right\rangle + \left\langle\frac{\partial u_3'}{\partial x_2}\frac{\partial u_2'}{\partial x_3}\right\rangle = -\left\langle\left(\frac{\partial u_3'}{\partial x_3}\right)^2\right\rangle,$$

while the second part (which contains nine square terms) is different from zero in homogeneous turbulence and is just the quantity referred to as ε in the previous equations. In isotropic turbulence, the second part reduces to (refer to Sect. 10.1.1 on isotropy)

$$\varepsilon = 15\nu\left\langle\left(\frac{\partial u_1'}{\partial x_1}\right)^2\right\rangle,$$

where the derivative of the axial velocity component is performed along the same direction of the velocity. Refer to Sect. 10.1.3 for how to measure the scales for further expressions of the TKE dissipation rate (Sect. 10.1.3).

The TKE dissipation rate is one of the most difficult quantities to derive in turbulence velocity measurements due to the requirement for three simultaneous velocity derivative measurements.

The final equation required to close the set of fluid-mechanics equations is the *equation of state*, i. e., an equation relating the thermodynamic variables p, ρ, and T. For an ideal gas, this law is

$$p = \rho RT$$

where $R = 287\,\mathrm{JK/kg}$ for air is the ideal gas constant. Applying Reynolds decomposition and averaging this equation, one obtains

$$\frac{\langle p\rangle}{R} = \langle\rho\rangle\langle T\rangle + \langle\rho'T'\rangle \qquad (10.15)$$

for constant density (or temperature) over the ensemble, the last term can be neglected. Subtracting the previous equation from the instantaneous equation one obtains

$$\frac{p'}{\langle p\rangle} = \frac{\rho'T'}{\langle\rho\rangle\langle T\rangle + \langle\rho'T'\rangle}$$
$$+\frac{T'}{\langle T\rangle + \frac{\langle\rho'T'\rangle}{\langle\rho\rangle}} + \frac{\rho'}{\langle\rho\rangle + \frac{\langle\rho'T'\rangle}{\langle T\rangle}} - \frac{1}{1 + \frac{\langle\rho\rangle\langle T\rangle}{\langle\rho'T'\rangle}}$$
$$\approx \frac{\rho'T'}{\langle\rho\rangle\langle T\rangle} + \frac{T'}{\langle T\rangle} + \frac{\rho'}{\langle\rho\rangle},$$

where the last relation holds if $\langle\rho'T'\rangle \ll \langle\rho\rangle\langle T\rangle$. In such a condition, the first term in the previous relation can also be neglected and the linear perturbation ideal gas law is obtained [10.14]. In this case no additional cross-terms are present in the equations of turbulence, while density–temperature cross-terms were present in (10.15).

In the case of a species present in the flow (say a pollutant, smoke or dye), a *conservation for the mass of the species* (concentration equation) must be added to

the previous set of equations in the form of

$$\frac{\partial c}{\partial t}+\frac{\partial}{\partial x_j}(cu_j)=D\frac{\partial^2 c}{\partial x_j^2}\,,$$

where D is the species diffusivity into the fluid (which is assumed constant), and c is the species concentration.

Applying Reynolds decomposition and averaging

$$\frac{\partial\langle c\rangle}{\partial t}+\frac{\partial\langle c\rangle\langle u_j\rangle}{\partial x_j}+\frac{\partial\langle c'u'_j\rangle}{\partial x_j}=D\frac{\partial^2\langle c\rangle}{\partial x_j^2}$$

which, in the case of constant density (zero velocity divergence), reduces to

$$\frac{\partial\langle c\rangle}{\partial t}+\langle u_j\rangle\frac{\partial\langle c\rangle}{\partial x_j}+\frac{\partial\langle c'u'_j\rangle}{\partial x_j}=D\frac{\partial^2\langle c\rangle}{\partial x_j^2}\,,$$

where the cross-term $\langle c'u_j'\rangle$ is including in addition to the original equation, together with the substitution of instantaneous with average variables.

The derived equations are all those required to describe a turbulent flow; they contain terms similar to those encountered in laminar flows (providing that average rather than instantaneous variables are used) plus cross-terms between fluctuating variables that retain the effect of turbulence. Such cross-terms represent turbulent kinematic fluxes (of mass, momentum, energy or concentration) that are added to the fluxes due to the mean motions. While mean kinematic fluxes are driven by the advection velocity, for turbulent fluxes positive and negative instantaneous values are usually in balance unless a correlation between velocity and the variable fluctuation under consideration holds. Thus, a turbulent flux different from zero at a point indicates a net relation between velocity and the variable fluctuation fields. Mathematically, the cross-terms are additional unknowns to the averaged values of the fluid-mechanics variables. They cannot be derived from other fundamental principles; however, there are several possibilities to derive additional equations for these cross-terms, as will be shown in the following sections.

Derivation of the Equations for Turbulent Flows: Multi-Point Results

The preceding equations were obtained at a single-point (i. e., for statistics computed at a point). From the equations of motions it is possible to derive equations for *multipoint statistics* (refer to Sect. 10.1.1 for details on these statistical quantities). Following *Hinze* [10.10], assuming a zero-divergence velocity field, it is possible to obtain for double-point correlation (10.1)

$$\frac{\partial}{\partial t}R_{u'_iu'_j}-\frac{\partial}{\partial x_k}R_{u'_iu'_k,u'_j}+\frac{\partial}{\partial x_k}R_{u'_i,u'_ku'_j}$$
$$=-\frac{1}{\rho}\left(\frac{\partial}{\partial x_j}R_{u'_ip'}-\frac{\partial}{\partial x_i}R_{p'u'_j}\right)+2\nu\frac{\partial^2}{\partial x_k^2}R_{u'_iu'_j}\,,\qquad(10.16)$$

where the correlations are computed between velocity component fluctuations or between velocity and pressure fluctuations. In the previous equation, as in the single-point equations, higher-order terms (triple correlations) are introduced and the solution should involve some additional constraints. In isotropic incompressible turbulence, the pressure–velocity correlations vanish [10.10], the double correlation functions can be expressed as in (10.8), using (10.7) (and similarly for triple correlations), and the previous equation reduces to (considering two points separated by a distance r)

$$\frac{\partial}{\partial t}\left(\langle u'^2\rangle f\right)-\langle u'^2\rangle^{3/2}\frac{1}{r^4}\frac{\partial}{\partial r}(r^4k)$$
$$=2\nu\langle u'^2\rangle\frac{1}{r^4}\frac{\partial}{\partial r}\left(r^4\frac{\partial f}{\partial r}\right)\,,\qquad(10.17)$$

which is known as the Karman–Howarth equation (where fluctuating variables are used). Double and triple correlation (f and k, respectively) functions depend on time t and separation r. This is the fundamental equation for two-point statistics in isotropic incompressible turbulence; the presence of derivatives makes it very difficult to compute terms of the equation from experimental data.

An equation equivalent to the Karman–Howarth equation can be derived between second- and third-order structure functions,

$$\frac{\partial}{\partial t}S^2_{u_1}+\frac{1}{3r^4}\frac{\partial}{\partial r}\left(r^4S^3_{u_1}\right)=\frac{2\nu}{r^4}\frac{\partial}{\partial r}\left(r^4\frac{\partial S^2_{u_1}}{\partial r}\right)-\frac{4}{3}\varepsilon\,,\qquad(10.18)$$

where the second- and third-order structure functions depend on time t and separation r. The integral of the previous equation (over r) is known as the Kolmogorov equation [10.11]; for the stationary case,

$$S^3_{u_1}=6\nu\frac{\partial S^2_{u_1}}{\partial r}-\frac{4}{5}\varepsilon r\,.$$

Kolmogorov himself realized that in isotropic homogeneous stationary turbulence, the term containing

second-order structure function is almost zero and thus the 4/5 law holds

$$S^3_{u_1} = -\frac{4}{5}\varepsilon r \,,$$

a result which justifies (10.12)

Similarly, an equation for cross scalar-velocity structure functions (for the stationary case) has been derived [10.12]

$$S^3_{u_1\mathrm{T}^2} = 2\alpha\frac{\partial S^2_{\mathrm{T}}}{\partial r} - \frac{4}{3}\varepsilon_{\mathrm{T}} r \,,$$

where ε_{T} and α are the energy dissipation rate and the diffusivity of the scalar field, respectively. For isotropic homogeneous stationary turbulence, the previous equation reduces to

$$S^3_{u_1\mathrm{T}^2} = -\frac{4}{3}\varepsilon_{\mathrm{T}} r \,.$$

Recently, some researchers have tried to derive equations for longitudinal and transverse correlation and structure functions in more-general flow conditions to generalize the Karman–Howarth results (10.17) and (10.18); see *Zhou* et al. [10.19], *Anselmet* et al. [10.20] and *Danaila* et al. [10.21] for details.

Similar equations can be derived in the wavenumber domain using Fourier transforms of the double and triple correlation functions (10.1) and (10.4); for isotropic incompressible turbulence one can derive [10.10]

$$\frac{\partial}{\partial t}F^k_{u'_i u'_j} = T^k - 2\nu k^2 F^k_{u'_i u'_j} \,,$$

where the nonlinear spectral transfer function T^k is related to the third-order spectral function $F^k_{u'_i u'_j, u'_l}$; the previous equation is known as the Lin equation. Integration over wavenumber in the first term in the previous equation gives

$$\frac{\partial}{\partial t}\int_0^\infty F^k_{u'_i u'_i}\mathrm{d}k = \frac{\partial}{\partial t}\left\langle u'^2_i\right\rangle .$$

On the other hand, integration of the last term in the previous equation gives [10.4, 10]

$$\varepsilon = 2\nu\int_0^\infty F^k_{u'_i u'_i} k^2 \mathrm{d}k \,, \tag{10.19}$$

which can be also proved starting from the spectral transform of the velocity related to that of the velocity derivative. Considering the $-5/3$ law (10.13), from these relations it is also possible to obtain the wavenumber behaviors of the TKE and TKE dissipation in the inertial range

$$K' \approx C_K \varepsilon^{2/3} k^{-2/3} \,, \quad \varepsilon \approx \nu C_K \varepsilon^{2/3} k^{4/3} \,,$$

i. e., in the inertial range, the TKE content decreases as the wavenumber increases (and the slope is negative), whereas the TKE dissipation continues to increase with wavenumber (and the slope is positive). As a consequence, the peak for TKE is at much lower wavenumbers in comparison to that of TKE dissipation.

The Problem of Closure of Equations; Hierarchy of Turbulence Equations

As shown in previous sections, the equations of fluid mechanics for a turbulent flow field retain terms similar to the original equations (using averaged variables) plus cross-terms containing the turbulent flux effects. These cross-terms are unknowns and the so-called problem of closure of turbulence equations arises; to solve the turbulent field, it is necessary to balance the number of equations with the number of unknowns. In so-called Reynolds-averaged Navier–Stokes (RANS) modeling, additional constraints on the turbulent fluxes are included into the system of equations. The zeroth-order closures simply equate the cross-terms to a constant; this is practically unsuitable for all flow field conditions. Thus, referring to first-order closures, usually known as eddy viscosity or Boussinesque closures, the turbulent kinematic fluxes of the generic fluid-mechanics variable q is given in terms of the gradient of the variable itself

$$-\left\langle u'_i q'\right\rangle = K^q_{\mathrm{T}}\frac{\partial\left\langle q\right\rangle}{\partial x_i} \,,$$

where K^q_{T} is the turbulent diffusion coefficient of the considered variable, which in general is unknown and could depend on the point considered. Algebraic or differential models aim to give useful expressions for the quantity K^q_{T}.

Before considering in some detail these models, let us consider the previous relation in detail for each cross-term in the equations of motion. In the equation for mass conservation the previous relation gives

$$-\frac{\partial}{\partial x_i}\left\langle u'_i \rho'\right\rangle = \frac{\partial}{\partial x_i}\left(K^\rho_{\mathrm{T}}\frac{\partial\left\langle\rho\right\rangle}{\partial x_i}\right) \,,$$

where K^ρ_{T} is the turbulent diffusion coefficient for the density. Thus, the turbulent diffusion (which is usually

unknown) is related to the molecular (laminar) diffusion (which is measurable). For the equation of momentum

$$-\frac{\partial}{\partial x_i}\left\langle u'_i u'_j\right\rangle = \frac{\partial}{\partial x_i}\left[\nu_\mathrm{T}\left(\frac{\partial\langle u_j\rangle}{\partial x_i}+\frac{\partial\langle u_i\rangle}{\partial x_j}\right)\right],$$

where ν_T is the turbulent kinematic viscosity (eddy viscosity). In the equation of thermal energy

$$-\frac{\partial}{\partial x_i}\left\langle u'_i T'\right\rangle = \frac{\partial}{\partial x_i}\left(\alpha_\mathrm{T}\frac{\partial\langle T\rangle}{\partial x_i}\right),$$

where α_T is the turbulent thermal diffusivity. In the equation of species concentration

$$-\frac{\partial}{\partial x_i}\left\langle u'_i c'\right\rangle = \frac{\partial}{\partial x_i}\left(D_\mathrm{T}\frac{\partial\langle c\rangle}{\partial x_i}\right),$$

where D_T is the turbulent species diffusivity. A similar result holds for the cross-terms appearing in the TKE equation.

Returning to the estimation of the eddy viscosity coefficient, it is necessary to point out that characteristic scales for turbulence are usually considered; for example for the momentum [10.4, 22],

$$\nu_\mathrm{T} \sim u_\mathrm{c} L_\mathrm{c},$$

where u_c and L_c are characteristic velocity and length scales for turbulence to be specified by modeling.

In pure *algebraic models* (zero-equation or eddy-viscosity models), the velocity and length scales are given algebraically; for example in Prandtl mixing length (l_m) theory [10.1]

$$L_\mathrm{c} = l_\mathrm{m}, \quad u_\mathrm{c} = l_\mathrm{m}\left|\frac{\partial\langle u\rangle}{\partial x_2}\right|,$$

where x_2 is taken orthogonal to the direction of the average velocity, so that

$$\nu_\mathrm{T} = l_\mathrm{m}^2\left|\frac{\partial\langle u\rangle}{\partial x_2}\right|.$$

Another possibility, due to Smagorinsky [10.4], relates eddy viscosity to the mean rate-of-strain tensor $\langle s_{ij}\rangle = \frac{1}{2}\left(\frac{\partial\langle u_i\rangle}{\partial x_j}+\frac{\partial\langle u_j\rangle}{\partial x_i}\right)$,

$$\nu_\mathrm{T} = l_\mathrm{m}^2\left(2\langle s_{ij}\rangle\langle s_{ij}\rangle\right)^{1/2},$$

which reduces to the Prandtl mixing length theory for unidirectional flows. The problem of these models is related to the evaluation of a proper mixing length; for example, in near-wall turbulence $l_\mathrm{m} = \kappa y$, where y is the distance from the wall and κ is the von Karman constant, can be assumed, so that a logarithmic law for the wall is obtained, while in other flow conditions there are few arguments for guiding this choice.

In mixed *algebraic–differential models* (one-equation models), both the velocity and length scales are given in terms of the TKE, K'

$$L_\mathrm{c} = \frac{K'^{3/2}}{\varepsilon}, \quad u_\mathrm{c} = \sqrt{K'},$$

so that

$$\nu_\mathrm{T} = \frac{K'^2}{\varepsilon},$$

where coefficients have been omitted. The TKE is obtained by solving the corresponding equation, while ε is obtained from L_c under mixing-length arguments (with similar limitations).

In pure *differential models* (two-equation models), the expression for eddy viscosity is the same as before, with both TKE and TKE dissipation equations to be solved by proper equations; the latter is obtained from the momentum equation by differentiation and multiplication by fluctuating derivatives so that the inertial term on the left-hand side of the equation represents the variation of homogeneous TKE dissipation, ε [10.17]

$$\begin{aligned}\frac{\partial\varepsilon}{\partial t}+\langle u_j\rangle\frac{\partial\varepsilon}{\partial x_j} = &-2\nu\left\langle\frac{\partial u'_j}{\partial x_i}\frac{\partial u'_j}{\partial x_k}\right\rangle\frac{\partial\langle u_i\rangle}{\partial x_k}\\ &-2\nu\left\langle\frac{\partial u'_i}{\partial x_k}\frac{\partial u'_j}{\partial x_k}\right\rangle\frac{\partial\langle u_i\rangle}{\partial x_j}\\ &-2\nu\left\langle u'_k\frac{\partial u'_i}{\partial x_j}\right\rangle\frac{\partial^2\langle u_i\rangle}{\partial x_k\partial x_j}\\ &-2\nu\left\langle\frac{\partial u'_i}{\partial x_k}\frac{\partial u'_i}{\partial x_j}\frac{\partial u'_k}{\partial x_j}\right\rangle\\ &-2\nu\frac{\partial}{\partial x_i}\left\langle\frac{\partial p'}{\partial x_j}\frac{\partial u'_i}{\partial x_j}\right\rangle\\ &-\nu\frac{\partial}{\partial x_k}\left\langle u'_k\frac{\partial u'_i}{\partial x_j}\frac{\partial u'_i}{\partial x_j}\right\rangle\\ &+\nu\frac{\partial^2\varepsilon}{\partial x_j^2}-2\nu^2\left\langle\left(\frac{\partial^2 u'_i}{\partial x_j\partial x_k}\right)^2\right\rangle.\end{aligned}$$

These models are also known as *k–ε models* (or closures). Note, that, as for the equation for fluctuating TKE, the previous equation adds other unknowns in the form of triple cross-derivatives terms so that the problem is still not closed (even if applied to higher order).

This is an example of the first step of a hierarchy of equations; further equations can be derived for the triple cross-terms which would contain quadruple cross-terms and so on (similar hierarchies exist in many nonlinear systems described statistically). Numerically, this hierarchy can be truncated at some order by an approximation similar to that of Boussinesque (i. e., by relating higher-order cross-terms to lower-order terms) or with algebraic models. Another possibility is to assign initial values to the unknowns and try to find a solution iteratively, although it is not proven that this solution exists and is unique (see*Pope* [10.4], for further details).

The last equation is simplified in the case of homogeneous isotropic turbulence [10.17] to

$$\frac{\partial \varepsilon}{\partial t} + \langle u_j \rangle \frac{\partial \varepsilon}{\partial x_j} = -\frac{\varepsilon^{3/2}}{\nu^{1/2}} \frac{7}{3\sqrt{15}} S_{\partial u_1/\partial x_1} - \frac{\varepsilon^2}{K} \frac{7}{15} G \,,$$

where the skewness of the derivative field,

$$S_{\frac{\partial u_1}{\partial u_1}} = \frac{\left\langle \left(\frac{\partial u_1}{\partial x_1} \right)^3 \right\rangle}{\left[\left\langle \left(\frac{\partial u_1}{\partial x_1} \right)^2 \right\rangle \right]^{3/2}} \,,$$

and the quantity (known also as the palenstrophy coefficient),

$$G = \frac{\left\langle \left(\frac{\partial^2 u_1}{\partial x_1^2} \right)^2 \right\rangle}{\left[\left\langle \left(\frac{\partial u_1}{\partial x_1} \right)^2 \right\rangle \right]^2} \,,$$

have been introduced. Even in this case, there are higher-order terms (contained in S and G) so that the importance of experimental verification is raised again.

The other possible approach to the closure problem is to derive an exact equation for the Reynolds stress cross-term $R_{u'_i u'_j} = \langle u'_i u'_j \rangle$; by manipulating the momentum equation, according to which we obtain [10.17]

$$\begin{aligned}
&\frac{\partial R_{u'_i u'_j}}{\partial t} + \langle u_k \rangle \frac{\partial R_{u'_i u'_j}}{\partial x_k} \\
&= -R_{u'_i u'_k} \frac{\partial \langle u_j \rangle}{\partial x_k} - R_{u'_j u'_k} \frac{\partial \langle u_i \rangle}{\partial x_k} - 2\nu \left\langle \frac{\partial u'_i}{\partial x_k} \frac{\partial u'_j}{\partial x_k} \right\rangle \\
&\quad - \frac{\partial}{\partial x_k} \langle u'_i u'_j u'_k \rangle \\
&\quad - \frac{1}{\rho} \left(\frac{\partial}{\partial x_j} \langle p' u'_i \rangle + \frac{\partial}{\partial x_i} \langle p' u'_j \rangle \right) \\
&\quad + \frac{1}{\rho} \left\langle p' \left(\frac{\partial u'_i}{\partial x_j} + \frac{\partial u'_j}{\partial x_i} \right) \right\rangle + \nu \frac{\partial^2 R_{u'_i u'_j}}{\partial x_k^2} \,, \qquad (10.20)
\end{aligned}$$

which, as expected, contains higher-order terms causing a hierarchy to exist even in this case; it can be closed with iterative solutions or with further constraints similar to those already considered (but at a higher order).

Similar equations can be derived for the other turbulent fluxes, for example in the presence of species [10.17].

Let us now consider the validity of the Boussinesque hypothesis; it is important to point out that the relation itself cannot be retained as valid for at least three reasons. Firstly, if we consider the term $\langle u'_i u'_i \rangle$ and we sum from $i = 1$ to $i = 3$ (which is basically the TKE), for incompressible fluid we obtain:

$$-\langle u'_i u'_i \rangle = 2\nu_T \frac{\partial \langle u_i \rangle}{\partial x_i} = 0 \,,$$

i. e., the turbulence should have null TKE, which makes no sense. This point can be overcome by the following modified expression of the Boussinesque hypothesis using the TKE,

$$-\langle u'_i u'_j \rangle = \nu_T \left(\frac{\partial \langle u_j \rangle}{\partial x_i} + \frac{\partial \langle u_i \rangle}{\partial x_j} \right) - \frac{2}{3} K' \delta_{ij} \,.$$

Secondly, the turbulent diffusion coefficients are not of the fluid itself but pertain to each particular flow field and also depend on the point and instant considered. Thirdly, the Reynolds and velocity deformation tensors are not aligned, i. e., their principal directions are not the same. In practice, the hypothesis is valid only if the velocity–velocity correlations are small, i. e., if we look at the phenomenon on scales that are much larger than the largest turbulent scale (Sect. 10.1.3). Nonetheless, there are several numerical codes that use the Boussinesque hypothesis; this explains why it is important to verify the hypothesis experimentally in different flow conditions.

Closure schemes have also been developed for the multipoint equations, such as the Karman–Howarth equation (10.17). It is interesting to note that the double correlation equation for the multipoint description (10.16) reduces to (10.20) when the two points coincide. The reader is referred to *Mc Comb* [10.23] for details of this argument.

It is also important to consider that, in numerical codes based on large-eddy simulation (LES), the stress tensor must also be modeled on subgrid scales while direct solution of the equations is performed at grid levels; models such as that of Smagorinsky are frequently used. Even in this case, experiments can help in evaluating the effectiveness of the models considered (*Pope* [10.4]).

Further Equations for Derived Quantities: Vorticity and Enstrophy

In many circumstances, it is useful from the conceptual and numerical points of view to consider equations for derived quantities rather than the conventional equations of fluid mechanics. In particular, it is of interest for special numerical approaches (such as vorticity–stream function methods) and for vortex dynamics to consider an equation for the *vorticity*. This can be derived by taking the vector product of the Navier–Stokes equations; for the case of incompressible flows

$$\frac{\partial \omega_i}{\partial t} + u_j \frac{\partial \omega_i}{\partial x_j} = \omega_j \frac{\partial u_i}{\partial x_j} + \nu \frac{\partial^2 \omega_i}{\partial x_j^2} \,,$$

which allows one to eliminate the pressure term (as not in Navier–Stokes equations; this is a big advantage of vorticity-based methods). Note that a Poisson equation for the pressure can be derived by considering the scalar product of the Navier–Stokes equations [10.1]. Performing Reynolds averaging on the previous equation yields

$$\frac{\partial \langle \omega_i \rangle}{\partial t} + \langle u_j \rangle \frac{\partial \langle \omega_i \rangle}{\partial x_j} = \langle \omega_j \rangle \frac{\partial \langle u_i \rangle}{\partial x_j} + \left\langle \omega'_j \frac{\partial u'_i}{\partial x_j} \right\rangle + \nu \frac{\partial^2 \langle \omega_i \rangle}{\partial x_j^2} - \frac{\partial}{\partial x_j} \left\langle u'_j \omega'_i \right\rangle \,,$$

which also contains higher-order terms such as the turbulent vorticity flux (the last term on the right-hand side), and vortex stretching by the fluctuating field (the second term on the right-hand side); these must be modeled by zero- or higher-order closures as for other turbulent fluxes. Consider also that, due to the solenoidal vorticity field, the second of these terms reduces to a form similar to the first.

Another derived quantity is the *enstrophy* (i. e., the square of the vorticity $\zeta = \langle \omega'_i \omega'_i \rangle$), which is related to the vorticity as TKE is to the the velocity. Enstrophy is also closely related to the TKE dissipation rate

$$\begin{aligned} \nu\zeta &= \nu \left\langle \left(\frac{\partial u'_i}{\partial x_j} \right)^2 \right\rangle - \nu \left\langle \frac{\partial u'_i}{\partial x_j} \frac{\partial u'_j}{\partial x_i} \right\rangle \\ &= \varepsilon - \nu \left\langle \frac{\partial u'_i}{\partial x_j} \frac{\partial u'_j}{\partial x_i} \right\rangle \,, \end{aligned}$$

which in homogeneous turbulence reduces to $\nu\zeta = \varepsilon$. An equation for the enstrophy can be derived as for TKE dissipation rate [10.17]

$$\begin{aligned} \frac{\partial \zeta}{\partial t} + \langle u_j \rangle \frac{\partial \zeta}{\partial x_j} &= 2 \left\langle \omega'_i \omega'_k \right\rangle \frac{\partial \langle u_i \rangle}{\partial x_k} + 2 \left\langle \omega'_i \frac{\partial u'_i}{\partial x_k} \right\rangle \langle \omega_k \rangle \\ &\quad - 2 \left\langle u'_k \omega'_i \right\rangle \frac{\partial \langle \omega_i \rangle}{\partial x_k} + 2 \left\langle \omega'_i \omega'_k \frac{\partial u'_i}{\partial x_k} \right\rangle \\ &\quad - \frac{\partial}{\partial x_k} \left\langle u'_k \omega'_i \omega'_i \right\rangle + \nu \frac{\partial^2 \zeta}{\partial x_j^2} \\ &\quad - 2\nu \left\langle \frac{\partial \omega'_i}{\partial x_k} \frac{\partial \omega'_i}{\partial x_k} \right\rangle \,, \end{aligned}$$

which does not contain pressure terms, while still containing higher-order terms. The modeling of the enstrophy equation is similar (although not exactly the same) as that of the TKE dissipation rate equation [10.17].

The Experimental Evaluation of Turbulent Fluxes and High-Order Closures

It should be clear from the previous sections that accurate numerical modeling of turbulent flows requires the determination of the cross-terms representing turbulent fluxes and cross-derivative terms. The relations and equations derived for these cross-terms shift the problem to higher order; at some point of the hierarchy a closure approximation is required. A given closure can be valid for a specific region of the flow field, but not everywhere, and also requires changes when moving to a different flow field. Numerically, a possible solution to this problem is to give initial values to the unknowns and try to converge to a solution of the system of equations for a given flow field [10.4]. Otherwise, advanced numerical methods as direct numerical simulation (DNS) and large-eddy simulation (LES) are able to find solutions on a wide range of scales; however, the former (DNS) is still limited to low-Reynolds-number flows with quite poor resolution in time, whereas the latter (LES) also requires a sort of closure for the small scales [10.4].

Therefore, experiments must answers the question of to what extent and approximation the closure hypothesis is valid in each flow field. To do this, direct measurements of the cross and cross-derivatives terms must be performed. Let us recall those terms for the single-point equations

$$\begin{aligned} &\left\langle \rho' u'_i \right\rangle \,, \quad \left\langle u'_i u'_j \right\rangle \,, \quad \left\langle p' u'_i \right\rangle \,, \\ &\left\langle T' u'_i \right\rangle \,, \quad \left\langle K' u'_i \right\rangle \,, \quad \left\langle T' \rho' \right\rangle \,, \quad \left\langle c' u'_i \right\rangle \\ &\left\langle \frac{\partial u'_i}{\partial x_j} \frac{\partial u'_j}{\partial x_i} \right\rangle \,, \quad \left\langle \left(\frac{\partial u'_i}{\partial x_j} \right)^2 \right\rangle \end{aligned}$$

and for the multipoint case

$$\left\langle u'_i u'_j, u'_k \right\rangle ,$$

and similarly for the correlation and spectral functions. It is clear that the evaluation of the former single-point terms requires the simultaneous determination of the two fluctuating variables or velocity derivatives. This is one of the challenges for modern experimental fluid mechanics. While it is reasonable to measure multiple velocity components simultaneously (refer Sect. 5.3 on HWA, Sect. 5.3.1 on LDA, and Sect. 5.3.2 on PIV), it is not straightforward to measure multiple velocity derivatives with sufficient resolution in space (or time if Taylor's hypothesis is used). Refer to the papers by *Browne* et al. [10.24], *Antonia* and *Mi* [10.25], *Benedict* [10.26], *Romano* and *Bagnoli* [10.27] for details. It is also difficult to measure simultaneous fluctuations of velocity and temperature (or species concentration) in a global sense, unless special tracers are used (as in LIF, or liquid crystals techniques, Sect. 6.3). On the other hand, to date it is practically impossible to perform simultaneous measurements of velocity and density (or velocity and pressure) fluctuations at any point of the flow field (Sect. 5.6). In any case, advanced measurement techniques with high spatial and temporal resolutions are required for such measurements. To this point, it is important to emphasize that the determination of the velocity derivatives at one point requires measurements of the velocity at two points that are close but finitely spearated. In practice, this means two measurement systems separated by one or a few Kolmogorov lengths ($\Delta r = 2-3\eta$), which can easily interfere with one another unless special precautions are taken (see *Antonia* and *Mi* [10.25], or *Romano* and *Bagnoli* [10.27] for details of the effect of spatial resolution and for experimental measurements of velocity derivatives).

The use of Taylor's hypothesis (Sect. 10.1.1) allows the replacement of velocity derivatives along the direction of motion with velocity derivatives in time

$$\left\langle \left(\frac{\partial u'_i}{\partial x_1} \right)^2 \right\rangle = \frac{1}{U_c} \left\langle \left(\frac{\partial u'_i}{\partial t} \right)^2 \right\rangle ,$$

which does not require measurements at two close points but only in time. However, even in this case the required resolution in time is high (of the order of a few Kolmogorov time scales) and noise problems arise.

Regarding derived quantities such as vorticity and enstrophy, the cross-terms to be measured are velocity–vorticity fluctuations and velocity–vorticity derivative fluctuations. The direct measurement of vorticity itself is not straightforward due to the requirements of high resolution, which are similar to highlighted previously for velocity derivatives in general. For simultaneous measurements of velocity and vorticity (and derivatives) very complex systems with multiple probes are required (see *Browne* et al. [10.24], *Antonia* and *Mi* [10.25] for details).

In summary, Table 10.1 holds [10.22] for the different quantities.

The experimental evaluation of turbulent fluxes and higher-order closures is the subject of a lot of papers in the recent literature on turbulence. There is a huge amount of work on this argument, and the reader is referred to *Pope* [10.4], and *Bernard* and *Wallace* [10.17], for details (as well as Sect. 10.4 of this book).

Table 10.1

Mean values $\langle u_i \rangle , \langle K \rangle , \langle p \rangle , \langle T \rangle , \langle \rho \rangle , \langle c \rangle$	Primary numerical codes validation
Turbulent fluxes (cross-terms) $\langle \rho' u'_i \rangle , \langle u'_i u'_j \rangle , \langle p' u'_i \rangle , \langle T' u'_i \rangle , \langle K' u'_i \rangle , \langle c' u'_i \rangle , \langle u'_i \omega'_j \rangle$	Turbulence models testing
Dissipation, cross-derivative terms, higher-order correlation, and spectra $\varepsilon , \left\langle \frac{\partial p'}{\partial x_k} \frac{\partial u'_i}{\partial x_k} \right\rangle , \left\langle \frac{\partial u'_i}{\partial x_k} \frac{\partial u'_i}{\partial x_j} \frac{\partial u'_k}{\partial x_j} \right\rangle , \left\langle \frac{\partial u'_i}{\partial x_k} \frac{\partial u'_i}{\partial x_k} \right\rangle , \left\langle u'_j \frac{\partial u'_i}{\partial x_k} \frac{\partial u'_i}{\partial x_k} \right\rangle ,$ $\langle u'_i u'_j, u'_k \rangle , \langle \omega'_i \omega'_k \rangle , \left\langle \frac{\partial \omega'_i}{\partial x_k} \frac{\partial \omega'_i}{\partial x_k} \right\rangle$	Model refinement and novel developments

Statistical Accuracy and Number of Samples

A few words must be dedicated to the accuracy required for the determination of higher-order statistics; roughly speaking, to evaluate the variance of the n-th-order statistical moment of the variable q, $\sigma^2(\langle q^n\rangle)$, it is necessary to know the value of the $2n$-th-order moment, $\langle q^{2n}\rangle$, (see Chap. 23, and *Benedict* and *Gould* [10.28], for details). Experimentally, these higher-order moments are particularly difficult to obtain, especially when cross-moments and cross-derivative moments are involved. Therefore, approximations of the variance estimation (for example, assuming a Gaussian distribution of the data) that use lower statistical moments are employed (see Chap. 23). A useful relation for the relative error on the n-th-order moment is

$$\frac{\sigma\left(\langle q^n\rangle\right)}{\langle q^n\rangle} = \frac{\left[A\sigma^n(\langle q^2\rangle)\right]^{1/2}}{N^{1/2}\,\langle q^n\rangle} ,$$

where $\sigma(\langle q^2\rangle)$ is the standard deviation of the variable q. The factor A depends nonlinearly on the considered moments (approximately, it is $A = 1$ for $n = 1$, $A = 2$ for $n = 2$, $A = 6$ for $n = 3$, $A = 100$ for $n = 4$, and so on). Therefore, for a given moment (fixed n) the relative error estimation goes as the inverse square root of the number of samples. On the other hand, the error for a given number of samples (N) increases as the moment order increases (there is a factor equal to about 8 passing from $n = 1$ to $n = 2$ and a factor of 2.5 passing from $n = 2$ to $n = 4$).

Another important point, related to the way in which the statistics is obtained, is concerned with the statistical independence of the acquired data. For the previous relations concerning the accuracy of statistical moments to hold, it is necessary to ensure effective independence of the acquired data. In ensemble averaging, this is ensured by the fact that a new experiment is repeated starting from more or less the same boundary and initial conditions (Sect. 10.1.1). For time (or space) averaging, it is necessary to verify that the data are separated by at least one characteristic time (or space) scale of the phenomenon under investigation; therefore, a preliminary evaluation of such a scale is required (see Sect. 10.1.3 for details on flow scale evaluation). Nevertheless, when recurrence in time, space or transformed domains are considered (i. e., when correlation or spectral functions are evaluated), what is really under investigation is the relation (i. e., the dependence) between one piece of data and the others; in this case, the acquired data must be dependent [i. e., acquired on time (or space) intervals much lower than the characteristic time (or space) scale of the phenomenon].

10.1.3 Scales in Turbulent Flows

Generalities

The term *scale* indicates the characteristic size along one direction (if the behavior in space is considered) or duration in time (for the behavior in time) of a fluid-mechanics event that partially preserves itself in space and time. In this sense, these events could be related to the vortical structures embedded in a turbulent flow field (refer to the beginning of Chap. 10). The determination of the scales (in length and time) is an objective both for fundamental research in fluid mechanics and for many practical applications; indeed, the values of such scales allow one to derive the size, shape, and traveling times of turbulent vortical structures. From the experimental point of view, in addition to the previous goals, there is also the requirement for a practical way to determine the optimal resolutions in space or time and extension or the duration of data acquisition (see Sect. 10.1.2). Regarding the resolution of the measurement systems, the link is to the smallest space and time scales of the phenomenon. For the extension and duration of data acquisition, in theory, time or space averaging should be performed over an infinite duration or extension; in practice, the acquisition time or the volume extension will be limited by two factors:

- they should be sufficiently larger that the largest time (or space) scale of the phenomenon (by at least a factor 100);
- they should be sufficiently smaller than the characteristic scale for possible unsteady (or inhomogeneous) phenomena (by at least a factor 10).

In the second case all the considerations mentioned for phase averaging in Sect. 10.1.1 should also be taken into account. Thus, a preliminary knowledge of the time and space scales of the phenomenon is required.

Overall Behavior of Correlation Functions

As will be shown later, turbulent flow scales are derived by analysis of correlation functions (in particular of autocorrelation coefficients). Referring to purely spatial or temporal autocorrelation coefficients, the following definitions hold where, in respect to Sect. 10.1.1, we now specify that only the fluctuating part of the variable (q'_i) is used,

$$\rho_{q'^2_i}(\boldsymbol{x}, \boldsymbol{r}, t) = \frac{\left\langle q'_i(\boldsymbol{x}, t)\, q'_i(\boldsymbol{x}+\boldsymbol{r}, t)\right\rangle}{\left\langle q'^2_i(\boldsymbol{x}, t)\right\rangle^{1/2}\left\langle q'^2_i(\boldsymbol{x}+\boldsymbol{r}, t)\right\rangle^{1/2}} ,$$

$$\rho_{q'^2_i}(\boldsymbol{x}, t, \tau) = \frac{\left\langle q'_i(\boldsymbol{x}, t)\, q'_i(\boldsymbol{x}, t+\tau)\right\rangle}{\left\langle q'^2_i(\boldsymbol{x}, t)\right\rangle^{1/2}\left\langle q'^2_i(\boldsymbol{x}, t+\tau)\right\rangle^{1/2}} .$$

Therefore, it follows that

$$\rho_{q'^2_i}(\boldsymbol{x}, 0, t) = 1 \,,$$

$$\rho_{q'^2_i}(\boldsymbol{x}, t, 0) = 1 \,,$$

i. e., the value of the correlation function at the origin is just the mean-square value of the fluctuating part, so that the correlation coefficient is just equal to one. Note that this is not the case for the cross-correlation coefficient between two variables, which at the origin attains the value

$$\rho_{q'_i q'_j}(\boldsymbol{x}, 0, t) = \frac{\left\langle q'_i(\boldsymbol{x}, t)\, q'_j(\boldsymbol{x}, t)\right\rangle}{\left\langle q'^2_i(\boldsymbol{x}, t)\right\rangle^{1/2}\left\langle q'^2_j(\boldsymbol{x}, t)\right\rangle^{1/2}} \,.$$

It is also important to point out that the maximum degree of correlation of the variable q'_i with itself is obtained when

$$q'_i(\boldsymbol{x}+\boldsymbol{r}, t) = q'_i(\boldsymbol{x}, t)$$

for all data used in the average. On the other hand, the maximum anticorrelation is obtained when

$$q'_i(\boldsymbol{x}+\boldsymbol{r}, t) = -q'_i(\boldsymbol{x}, t)$$

and similarly for time separation. Thus, considering that

$$\left\langle q'^2_i(\boldsymbol{x}, t)\right\rangle \geq 0$$

we obtain the Schwartz inequality

$$-1 \leq \rho_{q'^2_i}(\boldsymbol{x}, \boldsymbol{r}, t) \leq 1 \,,$$

$$-1 \leq \rho_{q'^2_i}(\boldsymbol{x}, t, \tau) \leq 1 \,.$$

For the case of homogeneous flow field, the spatial autocorrelation coefficients (as the autocorrelation functions) are also even functions of the space separation $\boldsymbol{r}$,

$$\begin{aligned}\rho_{q'^2_i}(x, -r, t) &= \frac{\left\langle q'_i(\boldsymbol{x}, t)\, q'_i(x-r, t)\right\rangle}{\left\langle q'^2_i(\boldsymbol{x}, t)\right\rangle} \\ &= \frac{\left\langle q'_i(x'+r, t) q'_i(x', t)\right\rangle}{\left\langle q'^2_i(x', t)\right\rangle} \\ &= \rho_{q'^2_i}(\boldsymbol{x}, \boldsymbol{r}, t) \,,\end{aligned}$$

where the hypothesis of homogeneity is used in the last equivalence, where the replacement $\boldsymbol{x}' = \boldsymbol{x} - \boldsymbol{r} \to \boldsymbol{x}$ was made.

Similarly, for the case of stationary flow field, the time autocorrelation coefficients (and the autocorrelation functions) are even functions of the time interval τ,

$$\rho_{q'^2_i}(x, t, -\tau) = \rho_{q'^2_i}(x, t, \tau) \,.$$

The limiting behavior of the autocorrelation coefficients for space separation (or time interval) going to infinity can be retrieved from the following considerations. Unless the phenomenon is laminar (which in the stationary case is equivalent to a constant value, for which the autocorrelation coefficient is always one) or periodic in space or time (which gives an oscillatory autocorrelation coefficient), it is expected that for $\boldsymbol{r} \to \infty$ the samples are statistically independent and fluctuations at a point are independent of the other point (and similarly in time separation for $\tau \to \infty$). Thus, when one of the two is positive the other could be positive or negative; statistically, the average value of these negative and positive contributions vanishes (as for the case of pure noise). Therefore the limiting values of the autocorrelation coefficients are

$$\rho_{q'^2_i}(x, r \to \infty, t) = 0 \,,$$

$$\rho_{q'^2_i}(x, t, \tau \to \infty) = 0 \,.$$

In practice, this limit to infinity is understood to apply for separations much larger than the largest scale in the flow field. The overall shape of an autocorrelation coefficient is given in Fig. 10.5 for the case of a purely space function in homogeneous flow conditions (note that the fact that the tangent is zero at the origin has not been strictly demonstrated).

Integral Scales

At this point, it is possible to specify in greater detail the scales introduced at the beginning of Sect. 10.1, starting from the largest towards the smallest. Consider

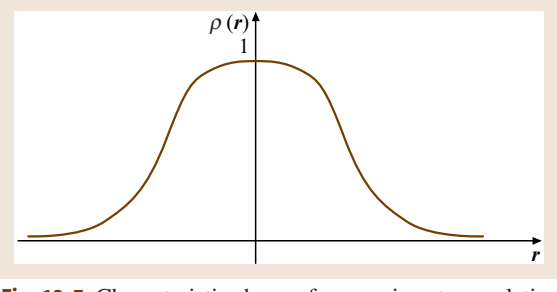

Fig. 10.5 Characteristic shape of a generic autocorrelation coefficient

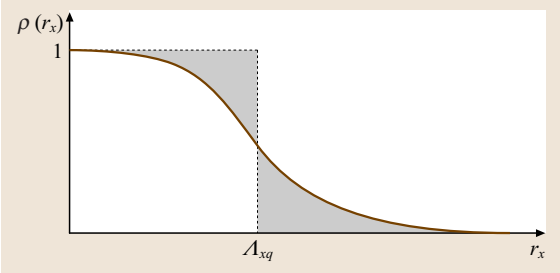

Fig. 10.6 A simple meaning for the integral scale

the purely spatial autocorrelation coefficient evaluated along the longitudinal (r_x) direction; flow scales referred to two different flow variables can be similarly introduced starting from cross-correlation coefficients. The longitudinal integral length scale of the variable q_i is defined as

$$\Lambda_{xq_i}(x,t) = \int_0^\infty \rho_{q'^2_i}(x, r_x, t)\,\mathrm{d}r_x ,$$

which is independent of position along the axis x only in the case of a homogeneous flow field and is independent of time t only in the stationary case (note that this integral scale has dimensions of a length and can be defined even in inhomogeneous or unsteady conditions when the correlation coefficient is not symmetric).

Similarly, it is possible to define transverse integral length scales of the same variable along the directions r_y and r_z . Therefore, as for the number of independent autocorrelation functions (Sect. 10.1.1), if q is a scalar there are three independent integral length scales, while if q is a vector (with scalar components q_i, as for the flow velocity) there are nine integral length scales.

These scales are a measure of the largest structures in a flow field, i. e., of those structures that maintain a high degree of relation with themselves. For points separated by distances larger than the integral length scale there is no longer any dependence of the velocity at one point on the velocity at another. In Fig. 10.6, this is explained by considering that the previous definition of integral length scale required equivalence between the shaded areas; therefore, points separated by a distance much larger than Λ_x are practically uncorrelated ($\rho \approx 0$).

The evaluation of the integral length scales along different directions (and of different velocity components) gives information on the form of the largest structures in the flow field; for example, if the vertical and transverse integral length scales are approximately equal and smaller than the longitudinal one, the turbulent structures will appear on average in axisymmetrical elongated forms. On the other hand, if the longitudinal and transverse scales are almost equal and much higher than the vertical one, the turbulent structures have the form of disks, and so on.

In the case of a homogeneous and isotropic field, the independent autocorrelation functions reduce to just one for a scalar field and two for the velocity field [$f(r)$ and $g(r)$, described before] along arbitrary directions. Therefore, the integral length scales also reduces to one for the scalar and two for the velocity field

$$\Lambda_q(t) = \int_0^\infty \rho_q(r,t)\,\mathrm{d}r ,$$

$$\Lambda_f(t) = \int_0^\infty f(r,t)\,\mathrm{d}r , \quad \Lambda_g(t) = \int_0^\infty g(r,t)\,\mathrm{d}r ,$$

where the dependence on the position along the axis is avoided and the dependence on time is avoided in the stationary case (note that in this case the autocorrelation function is symmetric). Using (10.9), it is easy to show that for incompressible homogeneous and isotropic fluid flows the following holds

$$\begin{aligned}\int_0^\infty g(r,t)\,\mathrm{d}r &= \int_0^\infty f(r,t)\,\mathrm{d}r + \int_0^\infty \frac{r}{2}\frac{\partial f(r,t)}{\partial r}\mathrm{d}r \\ &= \int_0^\infty f(r,t)\,\mathrm{d}r + \frac{fr}{2}\Big|_0^\infty \\ &\quad - \frac{1}{2}\int_0^\infty f(r,t)\,\mathrm{d}r \\ &= \frac{1}{2}\int_0^\infty f(r,t)\,\mathrm{d}r ,\end{aligned}$$

that is

$$\Lambda_f = 2\Lambda_g ,$$

i. e., the transverse integral length scale is one half of the longitudinal one.

For a general flow field, from the purely temporal autocorrelation coefficient, it is also possible to define an integral time scale as

$$\tau_{0q_i}(x,t) = \int_0^\infty \rho_{q'^2_i}(x,t,\tau)\,\mathrm{d}\tau ,$$

which is independent of position along the axis (x_1) only for the homogeneous case and is independent of time t in the stationary case. There is only one integral time scale for each scalar variable: three integral time scales for the velocity, one for each component.

Using Taylor's hypothesis for the large integral scales it is possible to write

$$\tau_{0q_i}(x,t) = \frac{\Lambda_{xq_i}(x,t)}{U_\mathrm{c}} ,$$

where U_c is the convection velocity along the axis of mean motion. This relation is a reasonable connection between the spatial and time scales, which allows the derivation of one from the other.

Taylor Microscales

An evaluation of the intermediate scales is given by considering a Taylor series expansion of the autocorrelation coefficient near the origin; for the pure spatial case with separation along the longitudinal axis this yields

$$\rho_{q'^2_i}(x, r_x, t) = \rho_{q'^2_i}(x, 0, t) + \left(\frac{\partial \rho}{\partial r_x}\right)_{r_x=0} r_x + \left(\frac{\partial^2 \rho}{\partial r_x^2}\right)_{r_x=0} \frac{r_x^2}{2} + O\left(r_x^3\right), \quad (10.21)$$

where $\rho_{q'^2_i}(x, 0, t) \equiv 1$, and similarly for the other axes r_y and r_z.

Neglecting the terms of order higher than r_x^2, a parabolic approximation to the autocorrelation coefficient is obtained. The separation at which the autocorrelation coefficient vanishes (i. e., the intersection of the parabola with the horizontal r_x axis) defines the so-called Taylor's microscale $\lambda_{xq_i}(x, t)$,

$$1 + \left(\frac{\partial \rho}{\partial r_x}\right)_{r_x=0} \lambda_{xq_i}(x, t) + \left(\frac{\partial^2 \rho}{\partial r_x^2}\right)_{r_x=0} \frac{\lambda^2_{xq_i}(x, t)}{2} = 0, \quad (10.22)$$

which is a quadratic relation with unknown λ_{xq}, given the first and second derivative of the autocorrelation coefficient in the origin. This is explained graphically in Fig. 10.7; the Taylor's microscale gives indications of the size of intermediate (i. e., lower than the integral length scales) flow structures.

Even for the Taylor's microscale in space, there are three scales (one along each axis) for a scalar variable and three scales for each component of a vector.

The evaluation of Taylor's microscale is simpler when the hypothesis of a homogeneous flow field is assumed; in this case, the first-order term in the previous expansion vanishes. This can be shown by considering relation (10.21) for negative r_x values as well and subtracting and adding the two terms

$$\rho_{q'^2_i}(r_x, t) - \rho_{q'^2_i}(-r_x, t) \equiv 0 = 2\left(\frac{\partial \rho}{\partial r_x}\right)_{r_x=0} r_x + O\left(r_x^3\right),$$

$$\rho_{q'^2_i}(r_x, t) + \rho_{q'^2_i}(-r_x, t) = 2 + \left(\frac{\partial^2 \rho}{\partial r_x^2}\right)_{r_x=0} r_x^2 + O\left(r_x^4\right).$$

In the last relation, as the two left-hand terms are equal, it is then possible to obtain

$$\left(\frac{\partial \rho}{\partial r_x}\right)_{r_x=0} = O\left(r_x^2\right)$$

$$\left(\frac{\partial^2 \rho}{\partial r_x^2}\right)_{r_x=0} = \frac{2}{r_x^2}\left[\rho_{q'^2_i}(r_x, t) - 1\right] + o\left(r_x^2\right),$$

i. e., the first-order derivative vanishes and the second-order derivative is always nonpositive. In this case, from (10.22), the Taylor's microscale results as

$$\lambda^2_{xq_i}(t) = \frac{-2}{\left(\partial^2 \rho / \partial r_x^2\right)_{r_x=0}}$$

or equivalently

$$\rho_{q'^2_i}(r_x \to 0, t) \approx 1 - \left(\frac{r_x}{\lambda_{xq_i}}\right)^2$$

and similarly for the other axes r_y and r_z; for the stationary case the scales are not dependent on time. Regarding third-order correlations, it is possible to show that they are odd functions of the separation distance and that in isotropic turbulence the values of the function and its derivative for zero separation vanish [10.10]. Thus, for the function k, it is possible to write (10.10)

$$k(r \to 0, t) = \frac{r^3}{6}\left(\frac{\partial^3 k}{\partial r^3}\right)_{r=0} + \frac{r^5}{120}\left(\frac{\partial^5 k}{\partial r^5}\right)_{r=0} + O(r^7).$$

Another useful expression is obtained by considering that for a homogeneous flow

$$\left(\frac{\partial^2 \rho}{\partial r_x^2}\right)_{r_x=0} = \left[\frac{\partial^2}{\partial r_x^2}\left(\frac{\left\langle q'_i(x, t)\, q'_i(x + r_x, t)\right\rangle}{\left\langle q'^2_i(t)\right\rangle}\right)\right]_{r_x=0} = -\frac{\left\langle\left(\frac{\partial q'_i(t)}{\partial r_x}\right)^2\right\rangle}{\left\langle q'^2_i(t)\right\rangle} \quad (10.23)$$

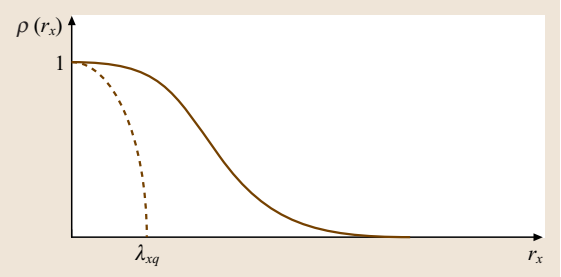

Fig. 10.7 Meaning of the Taylor microscale

so that

$$\lambda^2_{xq_i}(t) = \frac{2\langle q'^2_i(t)\rangle}{\left\langle \left(\frac{\partial q'_i(t)}{\partial r_x}\right)^2 \right\rangle} \tag{10.24}$$

and similarly for the other axes r_y and r_z (for the stationary case the scales are not dependent on time).

For homogeneous isotropic flows, the previous Taylor's microscales reduce to only one in the case of a scalar and two for the velocity field (longitudinal and transverse Taylor's microscales)

$$\lambda^2_q(t) = \frac{-2}{(\partial^2\rho/\partial r^2)_{r=0}},$$

$$\lambda^2_f(t) = \frac{-2}{(\partial^2 f/\partial r^2)_{r=0}},$$

$$\lambda^2_g(t) = \frac{-2}{(\partial^2 g/\partial r^2)_{r=0}}$$

or equivalently

$$\lambda^2_q(t) = \frac{2\langle q'^2(t)\rangle}{\left\langle \left(\frac{\partial q'(t)}{\partial x_1}\right)^2 \right\rangle},$$

$$\lambda^2_f(t) = \frac{2\langle u'^2_1\rangle}{\left\langle \left(\frac{\partial u'_1}{\partial x_1}\right)^2 \right\rangle},$$

$$\lambda^2_g(t) = \frac{2\langle u'^2_2\rangle}{\left\langle \left(\frac{\partial u'_2}{\partial x_1}\right)^2 \right\rangle}, \tag{10.25}$$

where x_1 is taken as reference axis. Note that in these relations the two numerators are the same due to isotropy, $\langle u'^2_1\rangle = \langle u'^2_2\rangle$.

Regarding the velocity field, note that, even without the assumption of isotropy, for the case of incompressible fluid flows, it is possible to show (10.9) that

$$\frac{\partial g}{\partial r} = \frac{3}{2}\frac{\partial f}{\partial r} + \frac{r}{2}\frac{\partial^2 f}{\partial r^2}, \quad \frac{\partial^2 g}{\partial r^2} = 2\frac{\partial^2 f}{\partial r^2} + \frac{r}{2}\frac{\partial^3 f}{\partial r^3}.$$

The second equation, for $r = 0$, gives

$$\lambda^2_f(t) = 2\lambda^2_g(t). \tag{10.26}$$

while in the same limit the first equation gives equivalence of first-order derivatives at the origin.

Recalling the expressions for the TKE dissipation ε for the case of homogeneous isotropic incompressible turbulence (refer to Sect. 10.1.2), the longitudinal and transverse Taylor microscales (10.25) in terms of ε are

$$\lambda^2_f(t) = \frac{30\nu\langle u'^2_1\rangle}{\varepsilon},$$

$$\lambda^2_g(t) = \frac{15\nu\langle u'^2_2\rangle}{\varepsilon}. \tag{10.27}$$

where again relation (10.26) is retrieved. The reverse relations allow one to derive the TKE dissipation rate from Taylor's microscales

$$\varepsilon = \frac{30\nu\langle u'^2_1\rangle}{\lambda^2_f(t)} = \frac{15\nu\langle u'^2_2\rangle}{\lambda^2_g(t)}. \tag{10.28}$$

This result also implies that ε is related to the correlation coefficient by

$$\varepsilon = -15\nu\langle u'^2_1\rangle\left(\frac{\partial^2 f}{\partial r^2}\right)_{r=0} = -\frac{15}{2}\nu\langle u'^2_2\rangle\left(\frac{\partial^2 g}{\partial r^2}\right)_{r=0};$$

thus, using relations (10.3) between the autocorrelation and spectral functions and (10.7), it is also possible to write

$$\varepsilon = 2\nu\int_0^\infty F^k_{u'_i u'_i} k^2 \mathrm{d}k,$$

which has already been obtained (10.19). Lastly, using the Karman–Howarth equation (10.17) for zero separation ($r = 0$), the properties of third-order correlations, and (10.28), the simplified equation for TKE is obtained [10.4]

$$\frac{\mathrm{d}}{\mathrm{d}t}u'^2_1 = -10\nu\frac{u'^2}{\lambda^2_g} = -\frac{2}{3}\varepsilon, \tag{10.29}$$

which is equivalently obtained from the TKE equation.

Returning to (10.24) and (10.25) for the case of a *variable different from the velocity* that possesses a dissipation term (for example the temperature and its mean square value, or the species concentration), it is possible to consider the limit for the isotropic case. In particular, the temperature or species dissipation rates can be written as (see Sect. 10.1.2)

$$\varepsilon_T = \alpha\left\langle\left(\frac{\partial T'}{\partial x_j}\right)^2\right\rangle = 3\alpha\left\langle\left(\frac{\partial T'}{\partial x_1}\right)^2\right\rangle,$$

$$\varepsilon_c = D\left\langle\left(\frac{\partial c'}{\partial x_j}\right)^2\right\rangle = 3D\left\langle\left(\frac{\partial c'}{\partial x_1}\right)^2\right\rangle,$$

where, as usual, sums over repeated indexes are used and α and D are the thermal and species diffusivities). Thus, similarly to (10.27), it is possible to write the Taylor's microscales for the temperature or concentration fields for the isotropic case as

$$\lambda^2_T(t) = \frac{6\alpha\langle T'^2\rangle}{\varepsilon_T},$$

$$\lambda^2_c(t) = \frac{6D\langle c'^2\rangle}{\varepsilon_c},$$

which can also be inverted to derive the dissipation rates from Taylor's microscales.

For the time autocorrelation coefficient, the previous arguments can be repeated exactly, so that

$$1+\left(\frac{\partial\rho}{\partial\tau}\right)_{\tau=0}\tau_{\lambda q_i}(x,t)+\left(\frac{\partial^2\rho}{\partial\tau^2}\right)_{\tau=0}\frac{\tau^2_{\lambda q_i}(x,t)}{2}=0$$

defines the Taylor's microscale in time $\tau_{\lambda qi}$ (only one for each scalar variable), where the dependence on position and time vanishes for homogeneous and stationary turbulence. For stationary flow field, the previous definition reduces to

$$\tau^2_{\lambda q_i}(x)=\frac{-2}{(\partial^2\rho/\partial\tau^2)_{\tau=0}}=2\frac{\langle q'^2_i\rangle}{\left\langle\left(\frac{\partial q'_i}{\partial t}\right)^2\right\rangle},$$

i. e., the autocorrelation time coefficient close to the origin is given by

$$\rho_{q'^2_i}(x,\tau\to 0)\approx 1-\left(\frac{\tau}{\tau_{\lambda q_i}}\right)^2.$$

For the velocity field, recalling the relations for the TKE dissipation rate in the isotropic case, we obtain (in agreement to what was previously done for the spatial separation)

$$\tau^2_\lambda(x)=\frac{30\nu\langle u'^2_1\rangle}{\varepsilon U_c^2},$$

where U_c is the convection velocity, and the reverse, which allows ε to be derived from Taylor's microscale in time. Thus, from the relation between the space and temporal derivatives derived from Taylor's hypothesis (Sect. 10.1.1), we obtain for the velocity component along the mean flow direction

$$\tau_\lambda\approx\frac{\lambda_f}{U_c},$$

which is a reasonable, although not exact, relation between time and space microscales.

Kolmogorov Scales

As already described in Sect. 10.1, the smallest scales are defined in terms of the TKE dissipation rate ε. For such small scales, it is necessary to distinguish clearly between the flow variables, as the definition for large and intermediate scales was based on correlation functions, while smallest scales are based on dissipation rates, which depend on the flow variable under consideration. Consider first the flow velocity, for which the smallest scales are known as the Kolmogorov length and time scales, defined as

$$\eta=\left(\frac{\nu^3}{\varepsilon}\right)^{1/4},\quad \tau_\eta=\left(\frac{\nu}{\varepsilon}\right)^{1/2}.$$

Note that the previous definition of the space scale does not contain any information on the velocity component or the reference axis. Therefore, the assumption of isotropy is implicit in its definition; at these scales, flow structures have the same size, η, along all the axes, although the anisotropies are contained in the way in which the TKE dissipation rate is computed. It is simple to show using the above definition that a Kolmogorov velocity scale can be defined as

$$\mathrm{v}_\eta=\frac{\eta}{\tau_\eta}=(\varepsilon\nu)^{1/4}. \tag{10.30}$$

The Reynolds number obtained using the Kolmogorov length and velocity is identically equal to 1

$$Re_\eta=\frac{\mathrm{v}_\eta\eta}{\nu}\equiv 1,$$

thus confirming that for flow structures with characteristic size η and velocity v_η, inertial forces are balanced by viscous forces; smaller structures will be rapidly dissipated by viscosity (with a characteristic Reynolds number less than 1).

These scales can also be retrieved in another way [10.29]. Let us consider a vortical structure (eddy) with characteristic rotational velocity v_r and size r; the *eddy turnover time* is defined as

$$t_e=\frac{r}{\mathrm{v}_r}; \tag{10.31}$$

(for large scales the relation leads to $\Lambda/\langle u'^2\rangle^{1/2}$ [10.6]). If it is assumed that this eddy loses almost all of its energy during a turnover time, then the TKE dissipation rate will be given by

$$\varepsilon\sim\frac{\text{energy density}}{\text{turnover time}}\approx\frac{\mathrm{v}_r^2}{(r/\mathrm{v}_r)}=\frac{\mathrm{v}_r^3}{r}.$$

(The eddy turnover time can also be defined in terms of the TKE and TKE dissipation $t_e=K'/\varepsilon$, so that the Reynolds number based on the velocity scale $\sqrt{K'}$ and on the length scale $t_e\sqrt{K'}=K'^{3/2}/\varepsilon$ will be $Re_T=K'^2/\nu\varepsilon$.) From the previous relation, we obtain

$$\mathrm{v}_r\approx(\varepsilon r)^{1/3}.$$

By assuming as the characteristic velocity $\mathrm{v}_r=\mathrm{v}_\eta$ and as the characteristic size $r=\eta$, it is possible to obtain

a first relation between these two quantities related to the TKE dissipation rate

$$v_\eta \approx (\varepsilon\eta)^{1/3} \ . \tag{10.32}$$

This relation, when applied to large scales, leads to $\varepsilon \approx (E[u])^3/\Lambda$, as described in the next section.

A second relation between those two quantities is obtained from

$$\varepsilon = 15\nu\left\langle\left(\frac{\partial u'_1}{\partial x_1}\right)^2\right\rangle \approx \nu\left(\frac{v_\eta}{\eta}\right)^2 \ ,$$

that is,

$$v_\eta \approx \left(\frac{\varepsilon}{\nu}\right)^{1/2}\eta \ . \tag{10.33}$$

From (10.32) and (10.33), we obtain

$$v_\eta\eta \approx \nu \ , \quad \eta \approx \left(\frac{\nu^3}{\varepsilon}\right)^{1/4} \ , \quad v_\eta \approx (\varepsilon\nu)^{1/4} \ ,$$

so that the eddy turnover time for these structures is [from (10.31)]

$$\tau_\eta \approx \frac{\eta}{v_\eta} \approx \left(\frac{\nu}{\varepsilon}\right)^{1/2}$$

as defined before.

In the case of isotropic flow field, the useful expression for TKE dissipation rate can be used in the definitions of the scales to obtain

$$\eta = \left[\frac{\nu^2}{15\left\langle\left(\partial u'_1/\partial x_1\right)^2\right\rangle}\right]^{1/4} \ ,$$

$$\tau_\eta = \left[\frac{1}{15\left\langle\left(\partial u'_1/\partial x_1\right)^2\right\rangle}\right]^{1/2} \ ,$$

$$v_\eta = \left[15\nu^2\left\langle\left(\partial u'_1/\partial x_1\right)^2\right\rangle\right]^{1/4} \ ,$$

which can be used as approximate evaluations of the microscales (see Sect. 10.1.3 for different possible evaluations of ε to be used in the measurement of microscales).

As a consequence of the definition of the space and time microscales, the relation between the two is not derivable using mean flow (or convection) velocities

$$\tau_\eta \neq \frac{\eta}{U_c}$$

so that they have to be evaluated separately.

The different flow scales are summarized in Fig. 10.8 [10.30].

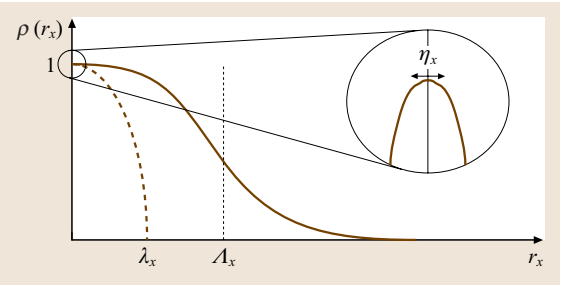

Fig. 10.8 The different flow scales

Consider now flow variables different from the velocity; in particular, for temperature or concentration fields, equations for the temperature or concentration gradients similar to those for TKE dissipation and enstrophy can be derived (see Sect. 10.1.2, Vorticity and Enstrophy). In comparison to the velocity, due to the fact that both temperature (or species concentration) and velocity fields are involved, there are four (rather than two, kinematic viscosity ν, and TKE dissipation rate ε) quantities that can be used to derive the smallest temperature or species scales; the kinematic viscosity, the TKE dissipation rate, the thermal diffusivity α (or the species diffusivity, D), and the temperature dissipation rate ε_T (or the species dissipation rate ε_c) [10.6].

In analogy with the velocity (following the arguments from (10.31)), it is possible to derive an expression for the latter variable from the definition of a temperature (or species) diffusion eddy with characteristic size (η_T), velocity ($v_{\eta T}$), time ($\eta_T/v_{\eta T}$), and temperature square fluctuation $\langle T'^2\rangle$

$$\varepsilon_T \approx \frac{v_{\eta T}\langle T'^2\rangle}{\eta_T} \tag{10.34}$$

and similarly for the species concentration.

Moreover, from the definition of ε_T (refer to Taylor's microscales for the temperature and concentration fields), it is possible to write in the isotropic case

$$\varepsilon_T = 6\alpha\left\langle\left(\frac{\partial T'}{\partial x_1}\right)^2\right\rangle \approx \frac{\alpha\langle T'^2\rangle}{\eta_T^2} \ , \tag{10.35}$$

and similarly for the concentration field.

Combining (10.34) and (10.35), we obtain

$$v_{\eta T}\eta_T \approx \alpha \ , \quad (v_{\eta c}\eta_c \approx D \ , \text{for the species,})$$

which is analogous to the result for the velocity field. So far, independently of the definition of the smallest scales for the temperature or species concentration, we always

Table 10.2 Summary of scales for velocity and scalar fields in homogeneous and isotropic turbulence in which the dissipation terms can be expressed as $\varepsilon = 15\nu\left\langle\left(\frac{\partial u'_1}{\partial x_1}\right)^2\right\rangle$ and $\varepsilon_T = 3\alpha\left\langle\left(\frac{\partial T'}{\partial x_1}\right)^2\right\rangle$

		Integral	Taylor	Kolmogorov
Length	Velocity field	$\Lambda_f = \int_0^\infty f(r)\,\mathrm{d}r$	$\lambda_f^2 = \frac{30\nu\langle u'^2_1\rangle}{\varepsilon}$	
		$\Lambda_g = \int_0^\infty g(r)\,\mathrm{d}r$	$\lambda_g^2 = \frac{15\nu\langle u'^2_2\rangle}{\varepsilon}$	$\eta \approx \left(\frac{\nu^3}{\varepsilon}\right)^{1/4}$
		$\Lambda_f = 2\Lambda_g$	$\lambda_f^2 = 2\lambda_g^2$	
	Scalar field	$\Lambda_q = \int_0^\infty \rho_q(r)\,\mathrm{d}r$	$\lambda_T^2 = \frac{6\alpha\langle T'^2\rangle}{\varepsilon_T}$	$\mathrm{Pr} > 1\,\eta_T = \left(\frac{\alpha^2\nu}{\varepsilon}\right)^{1/4}$
				$\mathrm{Pr} < 1\,\eta_T = \left(\frac{\alpha^3}{\varepsilon}\right)^{1/4}$
Time	Velocity field	$\tau_{0q_i} = \int_0^\infty \rho_{q_i}(\tau)\,\mathrm{d}\tau$	$\tau_{\lambda u}^2 = 2\frac{\langle u'^2_1\rangle}{\left\langle\left(\frac{\partial u'_1}{\partial t}\right)^2\right\rangle}$	$\tau_\eta = \left(\frac{\nu}{\varepsilon}\right)^{1/2}$
	Scalar field	$\tau_{0q} = \int_0^\infty \rho_q(\tau)\,\mathrm{d}\tau$	$\tau_{\lambda u}^2 = 2\frac{\langle T'^2_1\rangle}{\left\langle\left(\frac{\partial T'_1}{\partial t}\right)^2\right\rangle}$	$\mathrm{Pr} > 1\,\tau_{\eta T} = \left(\frac{\nu}{\varepsilon}\right)^{1/2}$
				$\mathrm{Pr} < 1\,\tau_{\eta T} = \left(\frac{\alpha}{\varepsilon}\right)^{1/2}$

have

$$Re_{\eta_T}\,\mathrm{Pr} = 1\,, \quad (Re_{\eta_c}\,Sc = 1, \text{for the species})\,,$$

where the Prandtl (Pr) and Schmidt (Sc) numbers have been used [i. e., the ratio of momentum to thermal (or species) diffusivities]. These relations confirm the definition of the smallest scales in the context of temperature or species diffusion. The product $Re\,Pr$ (or $Re\,Sc$) is often reported as the Peclet number.

In contrast to the velocity field, due to the presence of temperature (or species concentration), it is not possible to obtain unique relationships for the length, velocity, and time scales. It is necessary to consider another equation for the temperature (or species) fluctuation gradients; in analogy with the vorticity gradient equation, it is possible to obtain [10.6]

$$\left\langle\left(\frac{\partial T'}{\partial x_j}\frac{\partial T'}{\partial x_i}\right)\left(\frac{\partial u'_i}{\partial x_j} + \frac{\partial u'_j}{\partial x_i}\right)\right\rangle \approx \alpha\left\langle\left(\frac{\partial^2 T'}{\partial x_j \partial x_i}\right)^2\right\rangle$$

where, for the species concentration, α is replaced by D and T' by c'. This equation can be roughly evaluated as

$$\frac{\langle T'^2\rangle}{\eta_T^2} s'_{ij} \approx \alpha\frac{\langle T'^2\rangle}{\eta_T^4}\,,$$

where

$$s'_{ij} = \frac{1}{2}\left\langle\left(\frac{\partial u'_i}{\partial x_j} + \frac{\partial u'_j}{\partial x_i}\right)^2\right\rangle^{1/2}\,;$$

thus

$$\eta_T \approx \left(\frac{\alpha}{s'_{ij}}\right)^{1/2}\,,$$

and similarly for the concentration. Once s'_{ij} has been specified for the particular range involved, the smallest length scale for the temperature (concentration) field are derived from the previous relation, and in the same way for velocity and time scales.

Two main situations hold [10.6]. When $\alpha < \nu$ (or $D < \nu$), i. e., when $Pr > 1$ (or $Sc > 1$), the fluctuating temperature dissipation is expected to occur at scales η_T smaller than η (temperature fluctuations are sensible to all possible fluctuations of velocity down to the smallest velocity scale). In this case, the quantity s'_{ij} entirely depends on the kinematic viscosity and TKE dissipation, i. e.,

$$s'_{ij} \approx \left\langle\left(\frac{\partial u'_i}{\partial x_j}\right)^2\right\rangle^{1/2} \approx \left(\frac{\varepsilon}{\nu}\right)^{1/2}\,,$$

so that [10.6, 31]

$$\eta_T = \left(\frac{\alpha^2\nu}{\varepsilon}\right)^{1/4}\,, \quad \tau_{\eta T} = \left(\frac{\nu}{\varepsilon}\right)^{1/2}\,,$$
$$v_{\eta T} = \left(\frac{\alpha^2\varepsilon}{\nu}\right)^{1/4}\,, \qquad (10.36)$$

with α replaced by D for species concentration. Note that the smallest time scale for temperature is the same as that for velocity.

On the other hand, when $\alpha > \nu$ (or $D > \nu$), i. e., when $Pr < 1$ (or $Sc < 1$), the smallest eddies for temperature fluctuations (size of order η_T) are larger than the smallest eddies for velocity (size of order η) as not all possible fluctuations of velocity are involved in the temperature fluctuations. In this case, an evaluation of the strain rate at scales of order η_T differs from above and is smaller than $(\varepsilon/\nu)^{1/2}$. In particular, for scales $\eta_T > \eta$, s'_{ij} must be independent of the kinematic viscosity, but will depend on the specific value of η_T; this gives

$$s'_{ij} \approx \frac{\langle u'^2 \rangle^{1/2}}{\eta_T} \approx \frac{\varepsilon^{1/3}}{\eta_T^{2/3}} ,$$

using (10.32), so that [10.6]

$$\eta_T = \left(\frac{\alpha^3}{\varepsilon}\right)^{1/4} , \quad \tau_{\eta T} = \left(\frac{\alpha}{\varepsilon}\right)^{1/2} ,$$
$$v_{\eta T} = (\alpha\varepsilon)^{1/4} , \tag{10.37}$$

with α replaced by D for concentration. In this case, in comparison to the velocity, at the smallest scales the thermal (or concentration) diffusivity replaces the kinematic viscosity. The reader is referred to Chap. 17, 18 for details of cases in which temperature does not act as a passive flow variable (convective flows). In Table 10.2, some of the previous evaluations of turbulent scales for the velocity and scalar fields are summarized.

Relations Between Flow Scales and Reynolds or Prandtl Numbers

As shown in the previous section, there are at least three classes of characteristic lengths (and times); for the velocity field, these are the integral, Taylor, and Kolmogorov scales. The first argument of this section concerns the relations among these scales; this topic was preliminary considered at the beginning of Sect. 10.1.1 with the aim of quantifying the range of flow scales. We first consider the velocity field and the possible relation between the integral and Taylor scales. From the Navier–Stokes equations, balancing inertial and viscous terms for incompressible stationary flow without external forces (i. e., neglecting the effect of pressure gradient and external forces), we obtain (see Sect. 10.1.2)

$$\langle u_i \rangle \frac{\partial \langle u_j \rangle}{\partial x_i} \approx \nu \frac{\partial^2 \langle u_j \rangle}{\partial x_i^2} ; \tag{10.38}$$

cross-terms between velocity fluctuations can be considered in terms of fluctuating velocities, but are usually much smaller than the term containing the average velocity gradient even for high fluctuations levels. Considering orders of magnitude, the previous equation can be rewritten as

$$\frac{\langle u \rangle^2}{\Lambda} \sim \frac{\nu \langle u \rangle}{\lambda^2} ,$$

where $\langle u \rangle$ is the characteristic velocity of the problem, Λ is the characteristic large-scale length (i. e., the integral scale that drives the inertial term), and λ is the characteristic length scale for small-scale derivatives (i. e., Taylor's microscale). Thus,

$$\frac{\Lambda}{\lambda} \sim \left(\frac{\Lambda \langle u \rangle}{\nu}\right)^{1/2} = Re^{1/2} , \tag{10.39}$$

where Re is the Reynolds number based on the integral scale, which shows that the Taylor microscale is much smaller than the integral scale, the larger the Reynolds number.

Defining the Reynolds number based on the Taylor microscale

$$Re_\lambda = \frac{\lambda \langle u'^2 \rangle^{1/2}}{\nu} ,$$

it is possible to rewrite this relation between the integral and Taylor scales (10.39) as a connection between Reynolds numbers

$$Re_\lambda \sim I Re^{1/2} , \tag{10.40}$$

where $I = \langle u'^2 \rangle^{1/2} / \langle u \rangle$ is the turbulence intensity. Thus, the Reynolds number based on the Taylor microscale is proportional to the square root of the large-scale Reynolds number. Using the definition of Re_λ, we find

$$\frac{\Lambda}{\lambda} \sim \frac{Re_\lambda}{I} .$$

Considering that, to a reasonable approximation, both the integral and Taylor microscales in time can be simply derived by the corresponding lengths using Taylor's hypothesis (see the previous section), it is possible to state that this relation between length scales also holds for time scales, i. e.,

$$\frac{\tau_0}{\tau_\lambda} \sim Re^{1/2} . \tag{10.41}$$

Another relation between the integral and Kolmogorov scales can be derived by equating the total kinetic-energy production and dissipation rates (i. e., for the stationary, without external forces, case neglecting contributions from pressure and from fluctuating cross-terms, see Sect. 10.1.2)

$$\langle u_i \rangle \frac{\partial \left(\langle u_j \rangle \langle u_j \rangle \right)}{\partial x_i} \approx \varepsilon ,$$

which can be evaluated, as an order of magnitudes, in the form

$$\frac{\langle u\rangle^3}{\Lambda} \sim \varepsilon \,. \tag{10.42}$$

As already stated, this relation is useful in evaluating the TKE dissipation rate from the large-scale variable $\langle u\rangle$ and Λ.

Introducing the latter approximation into the definition of the Kolmogorov scales for length, time, and velocity (see previous section), it is possible to write

$$\frac{\Lambda}{\eta} \sim Re^{3/4} \,, \quad \frac{\tau_0}{\tau_\eta} \sim Re^{1/2} \,, \quad \frac{\langle u\rangle}{v_\eta} \sim Re^{1/4} \,, \tag{10.43}$$

which give approximate evaluations of almost the entire observable range of scales in a turbulent flow from the large-scale Reynolds number.

By comparing the previous relations with those obtained between integral and Taylor scales, the ratios of the Taylor to Kolmogorov scales are also obtained

$$\frac{\lambda}{\eta} \sim Re^{1/4} \,, \quad \frac{\tau_\lambda}{\tau_\eta} \sim 1 \,. \tag{10.44}$$

The behavior of the flow length scales as a function of Reynolds number is summarized in Fig. 10.9. While the large scale is almost constant (depending on the boundaries of the flow field), the microscales decreases with the Reynolds number so that turbulence, corresponding to the fact that turbulence has been reported having the same appearance when observed for long with different enlarging factors.

More-precise relations among the flow scales can be derived under the assumption of isotropy; considering (10.28) for ε inserted into (10.42), we obtain for the ratios of the integral to the Taylor length and time scales

$$\frac{\Lambda}{\lambda_f} \sim \frac{Re^{1/2}}{30^{1/2} I} \,, \quad \frac{\tau_0}{\tau_\lambda} \sim \frac{Re^{1/2}}{30^{1/2} I} \,, \tag{10.45}$$

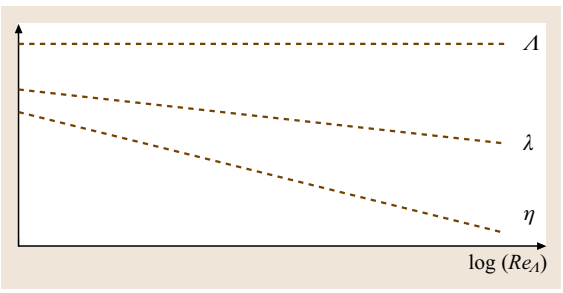

Fig. 10.9 Turbulence scales as a function of Reynolds number

where in the second relation Taylor's hypothesis has been used. These relations replace (10.39) and (10.41) in the case of isotropic flow. On the other hand, inserting the isotropic expression for ε (10.8) into the definitions of the Kolmogorov length, time, and velocity scales (see previous section), we obtain

$$\eta = \frac{\lambda_f}{30^{1/4} Re_\lambda^{1/2}} \,, \quad \tau_\eta = \frac{\lambda_f}{30^{1/2} \langle u'^2_1\rangle^{1/2}} \,,$$
$$v_\eta = \frac{30^{1/2} I \,\langle u\rangle}{Re_\lambda^{1/2}} \,. \tag{10.46}$$

Using these relations, the connection between Reynolds numbers based on large and microscale (10.40) and Taylor's hypothesis (to convert the Taylor length microscale to time) we obtain for the ratios of the Taylor and Kolmogorov scales

$$\frac{\lambda_f}{\eta} = 30^{1/4} Re_\lambda^{1/2} \sim 30^{1/4} I^{1/2} Re^{1/4} \,,$$
$$\frac{\tau_\lambda}{\tau_\eta} \sim 30^{1/2} I \,, \tag{10.47}$$

which replace (10.44) in the case of isotropy. Considering together (10.45) and (10.47) (and using (10.46) for the velocity), it is possible to write the ratio of the integral to Kolmogorov scales for the isotropic case as

$$\frac{\Lambda}{\eta} \sim \frac{Re^{3/4}}{30^{1/4} I^{1/2}} \,, \quad \frac{\tau_0}{\tau_\eta} \sim Re^{1/2} \,,$$
$$\frac{\langle u\rangle}{v_\eta} \sim \frac{Re^{1/4}}{30^{1/4} I^{1/2}} \,, \tag{10.48}$$

which replace (10.43).

Consider now a flow variable different from the velocity (see also the previous section). For the temperature and species concentration, it is possible to repeat arguments similar to those involved in deriving (10.37) (considering energy and concentration equations in this case) to obtain the ratio between the integral and Taylor scales for the temperature

$$\frac{\Lambda_\mathrm{T}}{\lambda_\mathrm{T}} \sim (Re_\mathrm{T} Pr)^{1/2} \,, \tag{10.49}$$

where the Reynolds number based on the integral length scale for the temperature, Re_T, has been used (for the concentration field, the Schmidt number instead of the Prandtl number will appear). The result is similar to that for the velocity scales with a multiplication factor given by the Prandtl (or Schmidt) number.

For time scales, as for the velocity, assuming that Taylor's hypothesis holds, we find

$$\frac{\tau_{0\mathrm{T}}}{\tau_{\lambda\mathrm{T}}} \sim (Re_\mathrm{T} Pr)^{1/2} \,. \tag{10.50}$$

Table 10.3 Summary of scale ratios as functions of the Reynolds and Prandtl (or Schmidt) numbers

		Integral Kolmogorov	Integral Taylor	Taylor Kolmogorov
Length	Velocity field	$Re^{3/4}$	$Re^{1/2}$	$Re^{1/4}$
	Scalar field	$Pr > 1$, $Re^{3/4} Pr^{1/2}$	$(RePr)^{1/2}$	$Pr > 1$, $Re^{1/4}$
		$Pr < 1$, $(RePr)^{3/4}$		$Pr < 1$, $(RePr)^{1/4}$
Time	Velocity field	$Re^{1/2}$	$Re^{1/2}$	1
	Scalar field	$Pr > 1$, $Re^{1/2}$	$(RePr)^{1/2}$	$Pr > 1$, $Pr^{-1/2}$
		$Pr < 1$, $(RePr)^{1/2}$		$Pr < 1$, 1

By considering (10.42) in the definition of smallest length and time scales for temperature (or concentration) (10.36) and (10.37)), the ratios of large to small scales for the $Pr > 1$ ($Sc > 1$) case (assuming integral length and time scales for temperature, or concentration, equal to that for velocity) are evaluated as

$$\frac{\Lambda_T}{\eta_T} \sim Re_T^{3/4} Pr^{1/2} , \quad \frac{\tau_{0_T}}{\tau_{\eta_T}} \sim Re_T^{1/2} \tag{10.51}$$

and for the $Pr < 1$ ($Sc < 1$) case

$$\frac{\Lambda_T}{\eta_T} \sim (Re_T Pr)^{3/4} , \quad \frac{\tau_{0_T}}{\tau_{\eta_T}} \sim (Re_T Pr)^{1/2} \tag{10.52}$$

with the Schmidt number replacing the Prandtl number for concentration. These relations show how the range of scale for temperature (or concentration) is enhanced or restricted depending on the value of the Prandtl (or Schmidt) number. The case $Pr > 1$ ($Sc \gg 1$) is typical of water (in which $Pr \approx 7$, and $Sc > 10^3$ when a dye is used), thus exhibiting a larger (for temperature) or much larger (for concentration) range of scales in comparison to those of velocity. For a gas, $Pr \approx 1$ and $Sc \leq 1$, so that the range of scales for temperature (or concentration) is more or less the same as for the velocity. These considerations have a correspondence in the spectral behaviors of temperature (or concentration) fluctuations in comparison to those of the velocity [10.6].

By combining (10.48) and (10.49) with (10.51) or (10.52), the ratios of the Taylor to the smallest temperature (or concentration) scales can be derived; for $Pr > 1$ (or $Sc > 1$), we find

$$\frac{\lambda_T}{\eta_T} \sim Re_T^{1/4} , \quad \frac{\tau_{\lambda_T}}{\tau_{\eta_T}} \sim \frac{1}{Pr^{1/2}} ,$$

while for $Pr < 1$ (or $Sc < 1$), this reads

$$\frac{\lambda_T}{\eta_T} \sim (Re_T Pr)^{1/4} , \quad \frac{\tau_{\lambda_T}}{\tau_{\eta_T}} \sim 1 ,$$

with the Schmidt number replacing the Prandtl number for concentration.

Let us also consider the ratios of temperature (or concentration) to velocity scales. For Taylor's microscales, considering (10.39) and (10.48) for lengths, and (10.41) and (10.49) for times, we obtain

$$\frac{\lambda_f}{\lambda_T} \sim Pr^{1/2} , \quad \frac{\tau_\lambda}{\tau_{\lambda_T}} \sim Pr^{1/2} ,$$

where the Schmidt number would replace the Prandtl number for the concentration result, assuming that the integral scales for temperature (or concentration) and velocity are almost equal, which is a reasonable approximation as both are convected by the mean velocity field. Thus, for gases, Taylor's microscales of temperature (or concentration) and velocity are almost equal, while for water Taylor's microscale for temperature is about three times smaller than that for velocity, and for dye concentration, Taylor's microscale is about a factor 30 smaller than that of the velocity.

For the smallest time scale, from the definitions (10.36), i. e., for the $Pr > 1$ ($Sc > 1$) case, we obtain

$$\frac{\eta}{\eta_T} \sim Pr^{1/2} , \quad \frac{\tau_\eta}{\tau_{\eta_T}} \sim 1 , \quad \frac{v_\eta}{v_{\eta_T}} \sim Pr^{1/2} ,$$

and from (10.37), for the $Pr < 1$ ($Sc < 1$) case,

$$\frac{\eta}{\eta_T} \sim Pr^{3/4} , \quad \frac{\tau_\eta}{\tau_{\eta_T}} \sim Pr^{1/2} , \frac{v_\eta}{v_{\eta_T}} \sim Pr^{1/4} ,$$

where the Schmidt number would replace the Prandtl number for the species concentration result. These relations confirm the findings already noted in Sect. 10.1.3 about the Kolmogorov scales for $Pr > 1$: the smallest scales for temperature are smaller than those for velocity (and those for concentration are much smaller when $Sc \gg 1$), whereas for $Pr \leq 1$ the smallest scales are similar. In Table 10.3, the different scale ratios for the velocity and scalars as functions of the Reynolds and Prandtl numbers are summarized.

How to Measure Length and Time Scales in a Turbulent Flow

The practical measurement of turbulent scales in flow fields leads to some potential difficulties, which are considered in this section. At the outset, it is necessary to evaluate the correlation coefficient of the flow variable under consideration in space, which requires the measurement of data at different spatial positions, and/or in time, which requires long sequences of data in time. As mentioned in Sect. 10.1.1, to derive such coefficients it is necessary to perform data sampling in space and/or time with small spatial or time separations (i. e., at high resolution); thus, the data must be correlated and not independent as required for single-point statistics (see Chap. 23).

For the evaluation of the integral scale, the integral to be performed is theoretically defined up to infinity; in practice, it is limited. One possibility is to stop at the first zero crossing, i. e., at the first space or time separation, r_{max} or τ_{max}, for which the correlation coefficient vanishes. However, in many cases the correlation coefficients start to exhibit oscillations before this zero is attained, as shown in Fig. 10.10; this is due to poor statistics (due to the fact that the number of cross-products is reduced for increasing separations) and to the random nature of the phenomenon. In this case, a second, more-convenient possibility is to define r_{max} or τ_{max} as the values for which the correlation coefficient reaches its first minimum. Another possibility is to estimate the integral scale as the value for which the correlation coefficient attains $1/e$ of its maximum (equal to 1 for zero separation), i. e., to the value expected if an exponential decay of the correlation coefficient is assumed. These three possibilities are summarized in Fig. 10.10.

For the case of a periodic phenomenon, the integral scale is related to the period (in space or time), which can be evaluated by the position of maxima in the correlation coefficients; in this case, a reasonable estimation can only be performed when the first of these maxima exceeds a value of 0.3–0.4 in the correlation coefficient.

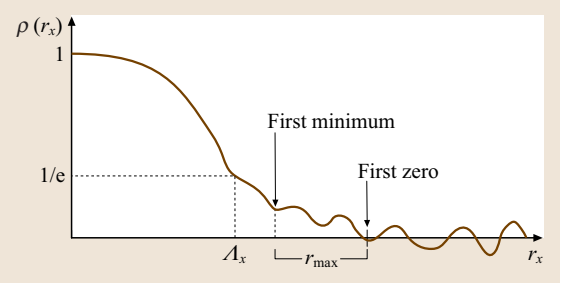

Fig. 10.10 Different evaluations for the integral length scale

For the Taylor microscale, it is necessary to distinguish between several possibilities. The first is connected to the determination of the microscale from the second-order derivative of the correlation coefficient at the origin. It is quite difficult to evaluate such a derivative and especially to determine how many correlation points near the origin must be used for such evaluation. An equivalent procedure is to fit a parabola to the data close to the origin and to determine the intersection with the horizontal axis (see the section on Taylor microscales and to Fig. 10.4). However, the presence of noise in the measurements adds a Dirac delta at the origin, thus preventing the determination of such a parabola; a plot of the correlation coefficient versus the square of the separation can support the evaluation of the effective number of points near the origin required for the fit to the parabola (*Romano* et al. [10.32]). For homogeneous (or stationary) flows the second-order derivative of the correlation coefficient can be replaced by the mean square derivative of the variable fluctuations (10.23). The evaluation of the mean square derivatives is itself not straightforward due to the increasing contribution of noise (see Chap. 23–Chap. 25 and sections devoted specifically to measurement systems); this procedure avoids the evaluation of the correlation coefficient and its second-order derivative.

For the velocity field, it is also possible to use the TKE dissipation rate, ε, in particular for the simplest case of isotropic flows if only a preliminary estimate of the Taylor microscale is required (see Sect. 10.1.3). The quantity ε can be evaluated from the mean square fluctuating velocity derivatives, from relatively simple estimates such as (10.42), or be evaluated from the spectra. In the following, several possible estimations of ε are given.

Another evaluation of the Taylor's microscale in time is derived from the analysis of the rate of zero-crossing of the fluctuating signal (the number of zero-crossing for unit time, N_0) [10.10]; the evaluation is given by

$$\tau_\lambda \approx \frac{\sqrt{2}}{\pi \dot{N}_0} \,. \tag{10.53}$$

The Taylor length microscale can be derived by using Taylor's hypothesis (Sect. 10.1.1). The previous relation can be derived exactly for a sinusoidal oscillating

signal [10.10]

$$q' = A \sin\left(\frac{2\pi t}{T_0}\right)$$

for which

$$\langle u'^2\rangle = \frac{A^2}{2}\,, \quad \left\langle \left(\frac{du'}{dt}\right)^2 \right\rangle = \frac{2A^2\pi^2}{T_0^2}\,, \quad \dot{N}_0 = \frac{2}{T_0}\,,$$

so that (10.53) holds exactly.

For practical evaluation of the smallest scales, it is necessary to consider that the evaluation of the TKE dissipation rate ε is required (Sect. 10.1.2). As already reported for the evaluation of the Taylor's microscale, ε can be derived in various ways. However, it is important to stress that, for general flow fields, the correct evaluation of ε requires the measurement of several mean square derivatives along different directions, which is also a challenging objective of experimental verification of advanced turbulence closure models (see Sect. 10.1.1, higher-order closures).

Here, some possible evaluations of dissipation rates are summarized (*Monin* and *Yaglom* [10.12], *George* and *Hussein* [10.18], *Pope* [10.4], *Antonia* et al. [10.33]).

For homogeneous turbulent flows, we find for velocity

$$\varepsilon = \nu \left\langle \frac{\partial u'_i}{\partial x_j} \frac{\partial u'_i}{\partial x_j} \right\rangle\,,$$

and for temperature

$$\varepsilon_\mathrm{T} = \alpha \left\langle \frac{\partial T'}{\partial x_j} \frac{\partial T'}{\partial x_j} \right\rangle\,,$$

with D replacing α for concentration. For inhomogeneous flows, additional cross-terms are involved (see Sect. 10.1.1, single-point equations). Another expression is for exactly homogeneous flows (i. e., flows in which fluctuations of a velocity component are independent of the considered point)

$$\varepsilon_\mathrm{hom} = 3\nu \left[\left\langle \left(\frac{\partial u'_1}{\partial x_1}\right)^2 \right\rangle + \left\langle \left(\frac{\partial u'_2}{\partial x_1}\right)^2 \right\rangle + \left\langle \left(\frac{\partial u'_3}{\partial x_1}\right)^2 \right\rangle \right]\,.$$

For local homogeneous axisymmetric turbulence, useful expressions are

$$\varepsilon_\mathrm{axi} = \nu \left[-\left\langle \left(\frac{\partial u'_1}{\partial x_1}\right)^2 \right\rangle + 2\left\langle \left(\frac{\partial u'_1}{\partial x_2}\right)^2 \right\rangle + 2\left\langle \left(\frac{\partial u'_2}{\partial x_1}\right)^2 \right\rangle + 8\left\langle \left(\frac{\partial u'_2}{\partial x_2}\right)^2 \right\rangle \right]\,,$$

$$\varepsilon_{\mathrm{T_{axi}}} = \alpha \left[\left\langle \left(\frac{\partial T'}{\partial x_1}\right)^2 \right\rangle + 2\left\langle \left(\frac{\partial T'}{\partial x_2}\right)^2 \right\rangle \right]\,.$$

For the isotropic case (see Sect. 10.1.1 on isotropy)

$$\varepsilon_\mathrm{iso} = 15\nu \left\langle \left(\frac{\partial u'_1}{\partial x_1}\right)^2 \right\rangle\,,$$

$$\varepsilon_{\mathrm{T_{iso}}} = 3\alpha \left\langle \left(\frac{\partial T'}{\partial x_1}\right)^2 \right\rangle\,.$$

For decaying isotropic turbulence, from (10.29), converting time derivatives into time, it is possible to derive the TKE dissipation from the fluctuating TKE decay (the same is obtained from the TKE equation)

$$\varepsilon_\mathrm{dec} = -\frac{\langle u\rangle}{2}\frac{d\langle K'\rangle}{dx}\,.$$

An overall estimation of TKE dissipation is derived from the approximate balance between the production and dissipation of kinetic energy (see Sect. 10.1.3, on Kolmogorov scales) and similarly for temperature

$$\varepsilon \approx \frac{\langle u\rangle^3}{\Lambda}\,, \quad \varepsilon_\mathrm{T} \approx \frac{\langle u\rangle\,\langle T\rangle^2}{\Lambda}\,.$$

The former result can also be reconsidered in terms of the fluctuating TKE, defining a scale Λ_ε slightly different from the integral scale:

$$\varepsilon \approx \frac{\left(K'/3\right)^{3/2}}{\Lambda_\varepsilon}\,.$$

From an estimate of the order of magnitude of the terms in the definition in terms of microscales (see Sect. 10.1.3 on Integral scales),

$$\varepsilon = \frac{30\nu\langle u'^2\rangle}{\lambda_f^2}\,, \quad \varepsilon_\mathrm{T} = \frac{6\alpha\langle T'^2\rangle}{\lambda_\mathrm{T}^2}\,.$$

From the integral of the energy spectrum (Sect. 10.1.1)

$$\varepsilon = 2\nu \int_0^\infty F^k_{u'_i u'_i} k^2 \mathrm{d}k\,.$$

10.2 Measuring Lagrangian Statistics in Intense Turbulence

Even though it has been intensively studied for well over a century, fluid turbulence remains a largely unsolved problem. A full characterization of turbulence is most likely contained within the Navier–Stokes equations, but these strongly nonlinear partial differential equations continue to resist analytical solution for turbulent flows. Researchers in turbulence therefore typically turn to phenomenological models based on the 1941 hypotheses of Kolmogorov (K41) [10.34], as well as more-recent extensions [10.11]. Kolmogorov's hypotheses were originally formulated in the Eulerian framework, where flow statistics are determined at fixed spatial locations. Like all quantities in fluid mechanics, however, both turbulence and the Kolmogorov hypotheses can be cast in the Lagrangian framework, where statistics are measured along the trajectories of individual fluid elements.

Much more is known about the Eulerian characteristics of turbulence than about its Lagrangian properties, primarily because robust and precise Lagrangian experiments have historically been extremely difficult, if not impossible at high Reynolds numbers. Since a general mapping between Eulerian and Lagrangian statistics remains elusive, we cannot fully understand turbulence without a full characterization of its Lagrangian nature as well as its Eulerian side. In addition, many problems, including mixing and transport, are inherently Lagrangian [10.35].

Lagrangian experiments have been carried out for many decades in field measurements in the atmosphere and ocean using balloons and floaters, but these devices are typically too large to measure the smallest scales of the turbulence, and the measurements they produce often have significant noise and uncertainty. Over the past 15 or so years, however, Lagrangian turbulence has become the subject of laboratory experiments with the development of powerful experimental techniques based on digital imaging and signal processing, and data comparable in quality to the best Eulerian results have been measured by many groups [10.36–53]. Here, we describe an optical Lagrangian particle tracking (LPT) technique capable of producing robust single- and multiparticle Lagrangian measurements [10.54–59]. We first discuss the image-processing algorithms used to determine particle trajectories, and then describe our implementation of the technique in the laboratory. Finally, we briefly show some results from our experiments, focusing on the separation of particle pairs in intense turbulence.

10.2.1 Image Processing

Optical particle tracking is at its heart an image-processing technique and an application of machine vision. The process of converting raw images of tracer particles to Lagrangian trajectories can broadly be split into three steps. First, the particles must be located in each image. The accuracy with which the particles are found is the primary factor that determines the accuracy of the LPT system. Next, if three-dimensional resolution is desired, the two-dimensional particle positions found from the images taken by each of the multiple cameras in the system must be matched to generate the three-dimensional particle coordinates. Finally, the particle motion must be tracked in time through many images, producing particle trajectories.

Particle Identification

A typical image taken by our LPT system is shown in Fig. 10.11. Several features of this image are notable in the context of particle tracking. The image consists of bright spots, corresponding to particle images, on a dark background. It is readily apparent, however, that the particles are not uniformly illuminated, and that the image contains background noise. Additionally, some particle images overlap with one another. Overlap is unfortunately unavoidable in three-dimensional LPT, since an

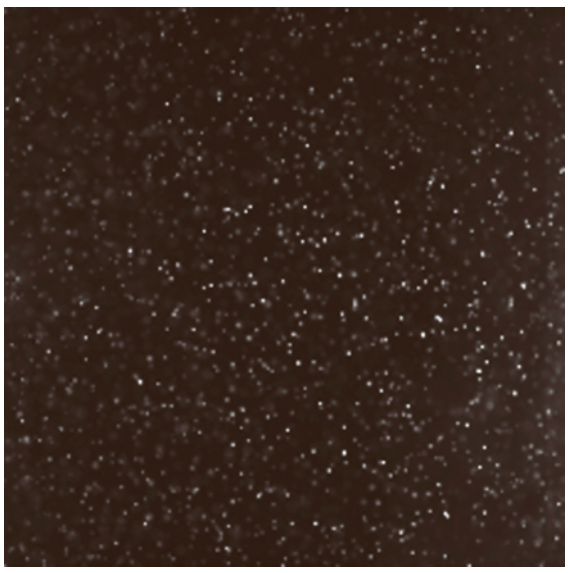

Fig. 10.11 A typical image of tracer particles taken in our LPT system

entire volume is illuminated rather than simply a plane, and this makes particle identification significantly more difficult than for isolated particle images.

Figure 10.11 makes it clear, then, that a good particle-finding algorithm must be able to handle nonuniform illumination, noise, and overlap without significant loss of accuracy. Additionally, the algorithm should be computationally efficient, since hundreds of thousands of images must be analyzed to produce well-converged turbulence statistics.

After extensive tests of many types of particle-finding algorithms [10.54], including algorithms based on weighted averaging, function fitting, and neural networks, we have chosen to use an algorithm based on one-dimensional Gaussians. This algorithm is fast, provides subpixel accuracy, is resistant to moderate noise levels, and can handle overlap. We now discuss the particle-finding procedure in detail.

To identify particles, we search the image for local maxima in image intensity above a small threshold, set empirically to a level above the average background noise. To find the intensity maxima, we simply step through the image row by row and compare each pixel's intensity with those of its eight neighbors. If the pixel's intensity is greater than or equal to those of its neighbors, we assume that the center of the particle image lies within that pixel. We neglect the outer ring of pixels in the image, since particles cannot be reliably located there.

To determine the coordinates of the particle with subpixel accuracy, we first assume that the intensity profile of the light received by the detector is Gaussian. In reality, the intensity profile will be some more complex function. Near the peak, however, where the center lies, the profile can be well approximated by a Gaussian. The horizontal and vertical coordinates of the particle center are then found by fitting two independent one-dimensional Gaussians. The fitting process is simple, and noniterative for speed. By taking the local maximum pixel as well as the pixels on either side of the maximum, an analytical form for the particle center can be obtained. Let us label the coordinates of the three horizontal pixels as x_i for $i = 1, 2, 3$, where x_2 is the local maximum pixel. We can then solve the system of equations

$$I_i = I_0 \exp\left[-\frac{1}{2}\left(\frac{x_i - x_c}{\sigma_x}\right)^2\right], \tag{10.54}$$

where I_i is the intensity of pixel x_i, I_0 is the undetermined overall Gaussian intensity, x_c is the horizontal coordinate of the particle center, and σ_x is the horizontal Gaussian width, for x_c, obtaining

$$x_c = \frac{1}{2}\frac{\left(x_1^2 - x_2^2\right)\ln(I_2/I_3) - \left(x_2^2 - x_3^2\right)\ln(I_1/I_2)}{(x_1 - x_2)\ln(I_2/I_3) - (x_2 - x_3)\ln(I_1/I_2)}\,. \tag{10.55}$$

The vertical coordinate of the center is found analogously. Since we use digital cameras, there is a finite number of possible pixel intensities. Every possible logarithm appearing in (10.55) can therefore be precomputed and stored in a lookup table, reducing the computational cost of finding a particle center to simply a few multiplications. In contrast, if we were to fit a full two-dimensional Gaussian intensity profile to the particle image, a nonlinear, iterative fitting algorithm would be required, significantly increasing the computational cost (by at least a factor of four in our tests).

By testing this algorithm on simulated images [10.54], we estimate that the average error in the determination of the particle center is less than 0.1 pixels. In addition to its accuracy, it is also fast and robust, and is an excellent choice for the processing of images without significant background noise. If the signal-to-noise ratio becomes very poor, however, other algorithms based on neural-network pattern recognition may perform better [10.54].

Stereomatching

Once the particle positions have been determined in the two-dimensional image spaces of each camera in the LPT system, the information from all of the cameras must be combined to reconstruct the three-dimensional coordinates of the particles. For applications where the particles have distinguishing features such as shape or color, this information can be used to assist the stereomatching algorithm. In a general LPT experiment, however, the tracer particles have no such features and the only information available for stereomatching is the photogrammetric condition stating that, for each camera, the camera projective center, the particle coordinates on the image plane, and the true particle coordinates in the laboratory frame must be collinear [10.36]. Furthermore, such lines of sight drawn from all the cameras will intersect at the true location of the particle. With appropriate system calibration, which we describe in Sect. 10.2.3, simple photogrammetry can then determine the locations of the particles in three-dimensional space.

If two particles lie on the same line of sight from a single camera, ambiguities can arise. This particle shadowing will occur more frequently as the seeding density of the particles is increased. By using more cam-

eras, however, shadowing becomes less of a problem since the amount of redundant information in the system is high. For example, *Dracos* [10.39] has shown that, for a reasonable particle seeding density, at least three cameras are needed in an LPT system.

The stereomatching algorithm we use is based on those of *Dracos* [10.39] and *Mann* et al. [10.42]. Consider a particle image p_i on one detector. As described above, we can project a line of sight from the perspective center of the camera through the particle image. We then in turn project this line of sight onto the image planes of the other cameras. Particle images on these images planes that fall within some tolerance ϵ of the projected line are considered possible matches for p_i. In this fashion, a list of possible matches for p_i is constructed for every other camera in the system. This process is then repeated for every particle image on every detector. The lists are checked for consistency, and the three-dimensional coordinates are found.

Particle Tracking

Temporal particle tracking is an example of a multidimensional assignment problem. The most general case consists of a sequence of N frames, each containing a potentially different number of particles. Solving the tracking problem requires the determination of the set of assignments between the particle positions in all temporally contiguous frame pairs so that the matched positions correspond to the same physical particle. More precisely, if we denote the i-th particle in the n-th frame by $\boldsymbol{x}_i^n$, we wish to find the set of links between $\boldsymbol{x}_i^n$ and $\boldsymbol{x}_j^{n+1}$, where the physical particle that was at position $\boldsymbol{x}_i$ in frame n is at position $\boldsymbol{x}_j$ in frame $n+1$, for all n, i, and j. To determine these links, we define ϕ_{ij}^n to be the "cost" of making a link between $\boldsymbol{x}_i^n$ and $\boldsymbol{x}_j^{n+1}$. If $\phi_{ij}^n = 0$, $\boldsymbol{x}_i^n$ and $\boldsymbol{x}_j^{n+1}$ refer to the same particle with perfect certainty; generally, however, $\phi_{ij}^n > 0$. The general solution to the tracking problem therefore requires minimizing

$$\Phi \equiv \sum_{n=0}^{N-1} \sum_{i=0}^{M_n} \sum_{j=0}^{M_{n+1}} \phi_{ij}^n \,, \tag{10.56}$$

where M_n is the number of particles in frame n. We must also allow for the possibility that some $\mathbf{x}_i^n$ or $\mathbf{x}_j^{n+1}$ will have no matches. This must be the case if $M_n \neq M_{n+1}$, and in an actual experiment corresponds to particles entering or leaving the measurement volume, or otherwise vanishing from view.

Minimizing Φ globally over all frames, as described above, is a problem of multidimensional assignment, and can be shown to be $\mathcal{NP}$-hard and therefore not tractable [10.60]. Instead, we restrict the number of frames over which we minimize Φ, in what is known as a *greedy-matching* approximation [10.61].

Greedy-matching algorithms differ in their specification of ϕ_{ij}^n. In general, however, the tracking cost is defined in terms of slowly changing variables. In the extreme case of variables that do not change, such as any distinguishing features of the particles such as color or shape, ϕ_{ij}^n could be specified as simply a binary function. In LPT, however, the particles are generally identical, and so characteristics of the motion must be used, including the particle position, velocity, and acceleration.

After testing several different algorithms using data from a direct numerical simulation (DNS) of turbulent flow [10.54], we have developed a four-frame predictive algorithm that performs well even in intense turbulence. Suppose that a particle track is partially generated up to frame n. We can then use the particle positions in frames n and $n-1$ to estimate a velocity, given by

$$\tilde{\mathbf{v}}_i^n = \frac{\mathbf{x}_i^n - \mathbf{x}_i^{n-1}}{\Delta t} \,, \tag{10.57}$$

where Δt is the time between frames. A possible position for the particle in frame $n+1$ is then estimated, given by

$$\tilde{\mathbf{x}}_i^{n+1} = \mathbf{x}_i^n + \tilde{\mathbf{v}}_i^n \Delta t \,. \tag{10.58}$$

A small search volume with an empirically determined size is constructed around the estimated position, and the particles in frame $n+1$ that fall within the volume are considered to be possible matches. For each of these $\mathbf{x}_j^{n+1}$, both a new velocity and an acceleration are estimated, given respectively by

$$\tilde{\mathbf{v}}_i^{n+1} = \frac{\mathbf{x}_j^{n+1} - \mathbf{x}_i^n}{\Delta t} \tag{10.59}$$

and

$$\tilde{\mathbf{a}}_i^{n+1} = \frac{\mathbf{x}_j^{n+1} - 2\mathbf{x}_i^n + \mathbf{x}_i^{n-1}}{\Delta t^2} \,. \tag{10.60}$$

Using these estimates, a possible position for the particle is estimated in frame $n+2$ for each $\mathbf{x}_j^{n+1}$ in the search volume, given by

$$\tilde{\mathbf{x}}_i^{n+2} = \mathbf{x}_i^n + \tilde{\mathbf{v}}_i^{n+1}(2\Delta t) + \frac{1}{2}\tilde{\mathbf{a}}_i^{n+1}(2\Delta t)^2 \,. \tag{10.61}$$

A second search volume is then constructed around $\tilde{\mathbf{a}}_i^{n+1}$. Let us denote the *closest* real particle in the search

volume to $\tilde{\mathbf{a}}_i^{n+1}$ by $\check{\mathbf{x}}_j^{n+2}$. The tracking cost ϕ_{ij}^n is then given by

$$\phi_{ij}^n = \left|\check{\mathbf{x}}_j^{n+2} - \tilde{\mathbf{x}}_i^{n+2}\right| . \tag{10.62}$$

In this way, the real particle in frame $n+1$ that leads to an estimated position closest to a real particle in frame $n+2$ is chosen to continue the track.

Occasionally, the same particle in frame $n+1$ will be the best match for two different particles in frame n. When such a conflict occurs, two choices are possible. The first is simply to give up and end both tracks, starting a new track with the particle in frame $n+1$. This choice guarantees that the tracking algorithm will not construct an incorrect track, but may artificially shorten the measured trajectories. The second possibility is to implement some kind of conflict resolution. One appealing possibility is to construct all of the ϕ_{ij}^n and then minimize the total cost for this frame pair, namely $\sum_{ij} \phi_{ij}^n$ [10.61]. As this is now a two-dimensional assignment problem, efficient algorithms exist to find the set of links with minimal cost [10.62]. In our tests, however, we found that this global cost minimization significantly reduced the accuracy of the tracking algorithm by frequently choosing incorrect links [10.54]. In our algorithm, we therefore use no conflict resolution and accept the tradeoff of shorter tracks for better accuracy.

The predictive algorithm we have described requires prior history of the particle trajectory to estimate future positions of the particle. For the first frame in the image sequence, however, this information is not available. In this case, we simply set $\tilde{\mathbf{v}}_i^n = 0$ and proceed as above. Prior information is also not available for particles that have newly entered the measurement volume in the middle of the image sequence. For this case, we set $\tilde{\mathbf{v}}_i^n$ to the average of the velocities of nearby particles, or to zero if there are no nearby neighbors.

Occasionally, particles will disappear from view for a short time while still remaining in the measurement volume. This occlusion can occur for many reasons. If the illumination of the particles fluctuates, the intensity of the particle image may fall below the threshold; images may also drop below threshold if some pixels on the detector have poor sensitivity or are nonfunctional. To account for the possibility of transient particle occlusion, and additionally to mitigate the effects of tracking conflicts, we have added a simple occlusion-handling system to our algorithm. If a partially constructed track finds no continuation in the next frame, the track is extrapolated using its estimated velocity and acceleration. This extrapolated position is then used in the next frame to try to find a continuation of the track. If no real continuation is found within a few frames, the track is considered to have ended, and the estimated positions are dropped.

10.2.2 Experimental Implementation

The LPT algorithm described above is general, and is applicable to any type of particle tracking experiment. Here, we describe the application of the technique in an actual experiment designed for the acquisition of Lagrangian data in high-Reynolds-number turbulence.

Flow

Central to any fluid-dynamics experiment is the flow itself. For a Lagrangian experiment where long particle tracks are desired, the flow should ideally meet several criteria. First, for an optical particle tracking experiment, the working fluid must be optically transparent. Second, the particles must remain in view for long periods of time. This is easier to achieve in practice with flows without a strong mean velocity field, though Lagrangian experiments have been conducted in wind and water tunnels [10.40, 63].

In our experiments, we have used a von Kármán swirling flow between counter-rotating disks [10.64]. 120 l of water is confined in a closed, cylindrical, plexiglass chamber 60.5 cm high and 48.3 cm in diameter. Eight round, glass windows 12.7 cm in diameter

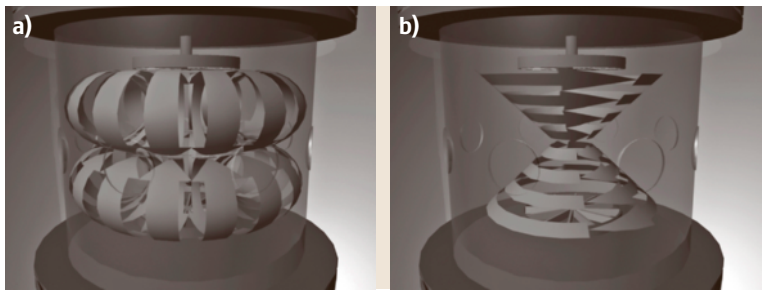

Fig. 10.12a,b Sketch of the large-scale flow **(a)**: decomposed into **(a)** pumping mode and **(b)** shearing mode

are attached around the centerline of the tank to provide optical access without lensing by the cylindrical tank walls. The top and bottom of the tank consist of hard-anodized aluminum plates. Each plate has an internal channel through which cooling water runs to remove the heat dissipated by the turbulence. Any dirt in the water is removed by pumping it through a recirculating filter loop, and bubbles are removed by pumping through a second recirculating loop open to the atmosphere.

The flow was driven by two counter-rotating disks 20.3 cm in diameter. Twelve straight vanes 4.3 cm high are attached to each disk so that the flow is forced inertially. Each disk was driven by a 1 kW direct-current (DC) motor. The large-scale flow was axisymmetric, and consisted of a pumping mode and a shearing mode, as sketched in Fig. 10.12. More details of the flow are given elsewhere [10.41,65,66]. Though the flow is anisotropic and inhomogeneous at large scales, it can generate very intense turbulence in a small amount of laboratory space. The strength of the turbulence is quantified by the Reynolds number; here, we use Re_λ, the Reynolds number based on the Taylor microscale. Re_λ, defined in isotropic turbulence as $Re_\lambda = \sqrt{15u'L/\nu}$, where u' is the root-mean-square velocity, L is the correlation length of the velocity field, and ν is the kinematic viscosity, is an intrinsic Reynolds number based on the turbulent velocity field itself rather than on an imposed external geometry. In our experiment, we can reach $Re_\lambda \approx 1000$.

Tracer Particles

The tracking algorithm described above can accurately follow the motion of many tracer particles simultaneously in three dimensions. The typical goal of a Lagrangian particle tracking experiment is, however, to gain information on the motion of the *fluid*. The accuracy to which this is accomplished therefore depends on the extent to which the tracer particles behave like true fluid elements. Any real particle will deviate to some degree from the motion of a true fluid element due both to its inertia and to its finite size. Since turbulent flows are highly chaotic, such deviations can lead to significantly different trajectories. The particle will be a good approximation to a fluid element if its density is the same as that of the working fluid, so that it is neutrally buoyant, and if it is very small, ideally smaller than the smallest length scale in the flow, the Kolmogorov length scale $\eta \equiv (\nu^3/\epsilon)^{1/4}$, where ϵ is the mean rate of energy dissipation per unit mass. The degree to which the tracer particle behaves as a fluid element is quantified by the Stokes number, defined as

$$St = \frac{1}{18}\frac{\rho_\mathrm{p} - \rho_\mathrm{f}}{\rho_\mathrm{f}}\left(\frac{d}{\eta}\right)^2 , \qquad (10.63)$$

where ρ_p and ρ_f are the densities of the particle and the fluid, respectively, and d is the particle diameter. In our experiments, the Stokes number ranges from 10^{-5} to 10^{-3}, and so our particles are good passive tracers [10.47,59].

Detectors

In intense turbulence, the smallest time scale in the flow, the Kolmogorov time scale $\tau_\eta \equiv \sqrt{\nu/\epsilon}$, is typically very short; at high Reynolds number in our flow, for example, τ_η is sub-millisecond. Resolving tracer particle motions on these time scales therefore requires extremely fast detectors, with speeds at least in the tens of kilohertz range if not faster. Such high imaging rates were not available in commercial cameras until very recently. In the past, therefore, we adapted the silicon strip detectors used in the vertex detectors of high-energy particle accelerators for use in Lagrangian particle tracking [10.44,47,67]. These one-dimensional detectors take images at a rate of 70 kHz, allowing full resolution of the Lagrangian acceleration. They have proved unsuitable, however, for simultaneous measurements of multiple tracers. Currently, we use the Phantom v7.1 complementary metal oxide semiconductor (CMOS) camera from Vision Research, Inc. for multiparticle experiments. At a resolution of 256×256 pixels, the Phantom v7.1 can record images at 27 kHz; as the number of sensor pixels is increased, the maximum frame rate drops. While we sacrifice some spatial resolution due to the small number of pixels in this camera, its temporal resolution allows us to resolve the Kolmogorov time scale well, and therefore to measure Lagrangian time derivatives accurately.

Illumination

With such fast cameras, the exposure time for each image is extremely short. A very intense light source is therefore required to illuminate the particles sufficiently. A pulsed source is also advantageous in a multicamera experiment since it can be used to synchronize the cameras: the detectors only record particle images while the light shines.

In our experiments, we have used two Q-switched, frequency-doubled solid-state Nd:YAG lasers for illumination, providing intense green light at 532 nm. One laser, pumped by flashlamps, achieved pulse rates of 30–70 kHz, with typical pulse widths of roughly

≈ 300 ns and a peak power of ≈ 60 W. The second laser, pumped by diode arrays, was capable of pulse rates of 10–120 kHz with pulse widths of ≈ 120 ns and a peak power of ≈ 90 W. Each laser had two Nd:YAG rods in series in the resonant cavity. The acousto-optical Q-switch both increased the power of the laser and controlled the pulse frequency. Three cameras were arranged in the forward-scattering direction from the lasers to maximize the intensity of the scattered light.

System Calibration

As discussed above, the tracking system must be calibrated before the three-dimensional positions of the particles can be determined, and the particles can be tracked. Calibration consists of determining the camera parameters and their locations in laboratory space. To determine these quantities, we use the calibration method described by *Tsai* [10.68].

Assuming a pinhole camera model, there are nine parameters that must be determined for each camera. Six of these specify the position of the camera in laboratory coordinates: three for the rotational positional and three for the translational. The additional three parameters describe the characteristics of the camera–lens system: one for the effective focal length, one for the radial distortion of the image, and one for a possible mismatch between the horizontal and vertical spacing of the pixels on the detector. We assume that the tangential distortion is negligible, which allows a significant simplification of the calibration model [10.68].

To set the model parameters we use a calibration mask consisting of a regular grid of dots mounted on a micrometer stage; images of the mask from three different cameras are shown in Fig. 10.13. The spacing of the dots is known, giving the true horizontal and vertical coordinates of the calibration dots, and the depth coordinate was measured from the micrometer on the calibration mount. By also measuring the dot positions from the camera images, the camera parameters can be determined, as described below.

Let us denote the laboratory coordinates of a particle by $\boldsymbol{x}_\mathrm{w}$ and the coordinates in the reference frame of the camera by $\boldsymbol{x}_\mathrm{c}$. The mapping between these frames is given by a rotation matrix $\hat{\boldsymbol{R}}$ and a translation vector $\boldsymbol{T}$, so that

$$\boldsymbol{x}_\mathrm{c} = \hat{\boldsymbol{R}}\boldsymbol{x}_w + \boldsymbol{T}. \tag{10.64}$$

The camera lens then projects $\boldsymbol{x}_\mathrm{c}$ onto the two-dimensional camera image plane. Assuming a pinhole camera with an effective focal length of f_eff, the ideal detector coordinates $\boldsymbol{x}_\mathrm{u}$ of the particle are given by

$$\begin{pmatrix} x_\mathrm{u} \\ y_\mathrm{u} \end{pmatrix} = \frac{f_\mathrm{eff}}{z_\mathrm{c}} \begin{pmatrix} x_\mathrm{c} \\ y_\mathrm{c} \end{pmatrix} . \tag{10.65}$$

The actual measured coordinates $\boldsymbol{x}_\mathrm{d}$ will, however, contain some radial distortion, and so

$$\boldsymbol{x}_\mathrm{d} = (1 + k_1 r^2)\boldsymbol{x}_\mathrm{u}, \tag{10.66}$$

where $r^2 = x_\mathrm{d}^2 + y_\mathrm{d}^2$. Since we neglect tangential distortion, the distorted and ideal positions of the particle must lie on a line passing through the center of the image [10.68]. Therefore,

$$\boldsymbol{x}_\mathrm{u} \times \boldsymbol{x}_\mathrm{d} = 0. \tag{10.67}$$

Finally, we allow a mismatch between the horizontal and vertical spacing, so that the final measured coordinates $\boldsymbol{x}_\mathrm{p}$ are given by

$$\begin{pmatrix} x_\mathrm{p} \\ y_\mathrm{p} \end{pmatrix} = \begin{pmatrix} s_\mathrm{x} x_\mathrm{d} \\ y_\mathrm{d} \end{pmatrix} , \tag{10.68}$$

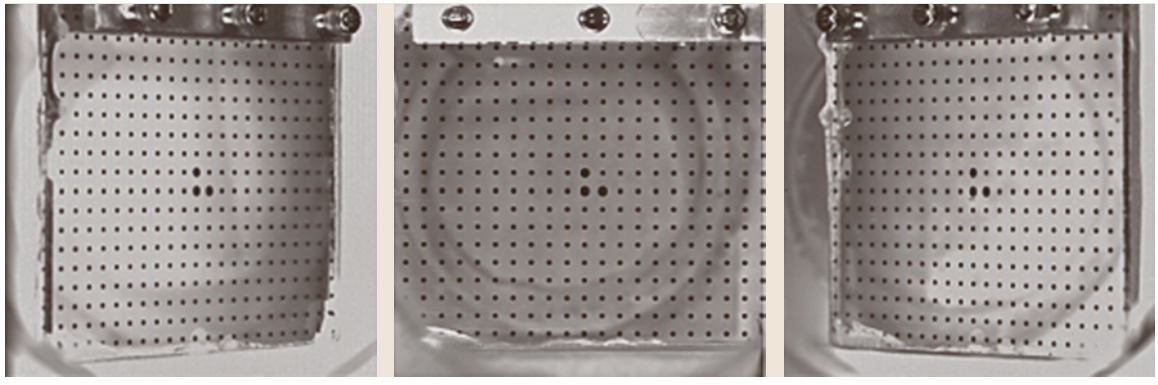

Fig. 10.13 Images of the calibration mask from each of the three cameras used in the particle tracking system

where s_x is a scale factor that is typically close to unity. Calibration therefore requires the determination of $\hat{\boldsymbol{R}}$, $\boldsymbol{T}$, f_{eff}, k_1, and s_x. By construction, we know the $\boldsymbol{x}_w$ of the dots on the calibration mask, and from the recorded camera images we can determine the $\boldsymbol{x}_p$ for each particle.

Following *Tsai* [10.68], we then write (10.67) as a set of seven linear equations, expressed as

$$\begin{pmatrix} -x_p x_w & -x_p y_w & -x_p z_w & y_p x_w & y_p y_w & y_p z_w & y_p \end{pmatrix} \times \begin{pmatrix} T_y^{-1} R_{21} \\ T_y^{-1} R_{22} \\ T_y^{-1} R_{23} \\ T_y^{-1} s_x R_{11} \\ T_y^{-1} s_x R_{12} \\ T_y^{-1} s_x R_{13} \\ T_y^{-1} s_x T_x \end{pmatrix} = x_p \,. \tag{10.69}$$

By using least-squares fits and the orthogonality of $\hat{\boldsymbol{R}}$, these equations allow the determination of the full rotation matrix, T_x, T_y, and s_x. Equation (10.66) may then be solved iteratively for the final three parameters after first estimating initial approximations of T_z and f_{eff} by setting k_1 to zero and using a least-squares fit.

After the parameters have been determined, the model can be used to map the measured particle positions into laboratory coordinates.

Temporal Differentiation

For most statistical measures in Lagrangian turbulence, velocities and accelerations must be calculated along particle trajectories. Simple finite differences, however, are not sufficient for calculating these time derivatives: the errors inherent in locating the particle centers will strongly contaminate such simple methods. Instead, we use a more-robust numerical differentiation scheme that also smooths the trajectory data. By convolving the particle tracks with a Gaussian smoothing and differentiating filter [10.49], we obtain time derivatives measured from a weighted average of many points.

The n-th-order derivative of the position in our scheme is given by

$$\frac{\mathrm{d}^n}{\mathrm{d}t^n} x(t) = \int_{-\infty}^{\infty} \tilde{x}(t-\tau) k_n(\tau)\,\mathrm{d}\tau \,, \tag{10.70}$$

where $\tilde{x}$ denotes the noisy measured data, and $k_n(\tau)$ is the Gaussian filtering and differentiating kernel defined by

$$k_n(\tau) = \frac{\mathrm{d}^n}{\mathrm{d}\tau^n}\left[\frac{1}{\sqrt{\pi}w}\exp\left(-\frac{\tau^2}{w^2}\right)\right] . \tag{10.71}$$

Integrating (10.70) by parts n times, the derivative in the kernel can be passed to the noisy position data; the surface term from each integration by parts vanishes since the Gaussian vanishes at infinity.

Measured tracks, however, are not infinitely long. Blindly applying (10.70), then, will produce a nonzero surface term due to the finite integration interval. We therefore truncate and renormalize the kernel before convolution with the particle trajectories.

Let us illustrate this process by considering the velocity kernel, given by (10.71) with $n = 1$. After truncation and renormalization, the kernel is given by

$$k_v(\tau) = A_v \tau \exp\left(-\frac{\tau^2}{w^2}\right) + B_v \,, \tag{10.72}$$

where the $1/(\sqrt{\pi}w)$ has been absorbed into A_v. Let us now restrict the integration domain to $[T, -T]$, where typically $(2T+1) \approx \tau_\eta$. In principle, we must also set w; for simplicity, however, we fix $w = T/1.5$ [10.49]. To fix the constant A_v and B_v, we use the conditions that the derivative of a constant must vanish and the derivative of t must be unity. Expressed using (10.70), these conditions are given by

$$\int_{-T}^{T} k_v(\tau)\,\mathrm{d}\tau = 0 \tag{10.73}$$

and

$$\int_{-T}^{T} (t-\tau) k_v(\tau)\,\mathrm{d}\tau = 1. \tag{10.74}$$

By solving these two equations simultaneously, we find that

$$A_v = \left[\frac{1}{2}w^2\left(w\sqrt{\pi}\,\mathrm{erf}\left(\frac{T}{w}\right) - 2Te^{\frac{-T^2}{w^2}}\right)\right]^{-1} \tag{10.75}$$

and

$$B_v = 0 \,. \tag{10.76}$$

The acceleration kernel is defined similarly. We note that, in the discrete case, $T = 1$ corresponds to a central difference scheme.

The differentiation scheme introduced here is more accurate than a simple finite-difference algorithm, but

still produces a signal that will contain errors. Here, we explicitly analyze these errors for the case of the velocity; errors in determining higher-order derivatives can be described similarly. We note that here we work in nondimensional time units.

As described above, the velocity in our scheme is given by

$$\tilde{u}(t) = \int_{-T}^{T} k_{\mathrm{v}}(\tau)\tilde{x}(t+\tau)\,\mathrm{d}\tau, \tag{10.77}$$

where

$$\tilde{x}(t) = x(t) + \epsilon_x(t). \tag{10.78}$$

Here, $x(t)$ is the true position of the particle and ϵ_x is the error in this measurement. We then rewrite the measured velocity as

$$\tilde{u}(t) = \int_{-T}^{T} k_{\mathrm{v}}(\tau)x(t+\tau)\,\mathrm{d}\tau + \int_{-T}^{T} k_{\mathrm{v}}(\tau)\epsilon_x(t+\tau)\,\mathrm{d}\tau. \tag{10.79}$$

The first term in this expression can be written as the sum of the true velocity $u(t)$ and an intrinsic error associated with the filtering process $\xi_{\mathrm{f}}(t; T, w)$. The second term is the propagation of the uncertainty in the determination of the particle center through the filter $\xi_{\mathrm{x}}(t; T, w)$. Since we fix $w = T/1.5$, both ξ_{f} and ξ_{x} are functions of time and the filter length T only.

By considering the case of $\xi_{\mathrm{x}}(t; T) = 0$, i. e., perfect determination of the particle centers, we can study the uncertainty introduced by the finite frequency response of our filter. In this case, the variance of the measured velocity will be given by

$$\langle\tilde{u}(t)^2\rangle = \left\langle \int_{-T}^{T} \mathrm{d}\tau k_{\mathrm{v}}(\tau)x(t+\tau) \times \int_{-T}^{T} \mathrm{d}\tau' k_{\mathrm{v}}(\tau')x(t+\tau') \right\rangle . \tag{10.80}$$

We can write

$$\begin{aligned}\tilde{u}(t) &= \int_{-T}^{T} \mathrm{d}\tau k_{\mathrm{v}}(\tau)x(t+\tau) \\ &= \int_{-T}^{T} \mathrm{d}\tau k_{\mathrm{v}}(\tau)\left[x(t) + \int_{t}^{t+\tau} \mathrm{d}t' u(t')\right] \\ &= \int_{-T}^{T} \mathrm{d}\tau k_{\mathrm{v}}(\tau) \int_{t}^{t+\tau} \mathrm{d}t' u(t')\,,\end{aligned} \tag{10.81}$$

since $x(t)$ is a constant and, by definition, the convolution of the velocity kernel with a constant vanishes. Therefore, we have

$$\langle\tilde{u}(t)^2\rangle = \int_{-T}^{T} \mathrm{d}\tau \int_{-T}^{T} \mathrm{d}\tau' k_{\mathrm{v}}(\tau)k_{\mathrm{v}}(\tau') \times \int_{t}^{t+\tau} \mathrm{d}t' \int_{t}^{t+\tau'} \mathrm{d}t'' \langle u(t')u(t'')\rangle\,. \tag{10.82}$$

Defining $\langle\xi_{\mathrm{f}}(t; T)^2\rangle \equiv \langle u^2(t)\rangle - \langle\tilde{u}(t)^2\rangle$, we therefore have

$$\langle\xi_{\mathrm{f}}(t; T)^2\rangle = \int_{-T}^{T} \mathrm{d}\tau \int_{-T}^{T} \mathrm{d}\tau' k_{\mathrm{v}}(\tau)k_{\mathrm{v}}(\tau') \times \int_{t}^{t+\tau} \mathrm{d}t' \int_{t}^{t+\tau'} \mathrm{d}t'' \left[\langle u^2\rangle - R(t'-t'')\right], \tag{10.83}$$

where $R(t'-t'') \equiv \langle u(t')u(t'')\rangle$ is the two-time velocity covariance and where we have assumed that the flow is stationary. The exact form of this function in turbulence, however, is not known. By turning to a DNS of low-Reynolds-number turbulence, however, we can estimate the magnitude of the error. We find that the error is less than 1% for $T < 70$, and so therefore that the error purely associated with the convolution process is negligible.

We now consider the propagated error in the determination of the particle centers. Assuming that $x(t)$ and ϵ_x are uncorrelated, the variance of $\xi_{\mathrm{x}}(t; T)$ is given by

$$\langle\xi_{\mathrm{x}}(t; T)^2\rangle = \int_{-T}^{T} \mathrm{d}\tau \int_{-T}^{T} \mathrm{d}\tau' k_{\mathrm{v}}(\tau)k_{\mathrm{v}}(\tau') \times \langle\epsilon_x(t+\tau)\epsilon_x(t+\tau')\rangle\,. \tag{10.84}$$

Let us now assume that the position error is δ-correlated in time and stationary, so that

$$\langle\epsilon_x(t+\tau)\epsilon_x(t+\tau')\rangle = \langle\epsilon_x^2\rangle\delta(\tau-\tau')\,, \tag{10.85}$$

where now ξ_{x} is a function of T only. We note that this assumption is not fully realistic, since the position er-

ror will be correlated while the particle center moves within a single camera pixel. In order to compensate for this underestimation of the error, we take $\langle \epsilon_x^2 \rangle^{1/2} = 0.1$ pixels, which is probably an overestimate of the position uncertainty. With the assumption of δ-correlation, equation (10.84) is tractable, and we have

$$\langle \xi_x(T)^2 \rangle = \langle \epsilon_x^2 \rangle \times \frac{-4(T/w) + \sqrt{2\pi}\exp(2T^2/w^2)\mathrm{erf}(\sqrt{2}T/w)}{2w^3[-2(T/w) + \sqrt{\pi}\exp(T^2/w^2)\mathrm{erf}(T/w)]^2} . \quad (10.86)$$

With $w = T/1.5$, this expression reduces to

$$\langle \xi_x(T)^2 \rangle = \frac{2.11\langle \epsilon_x^2 \rangle}{T^3} . \quad (10.87)$$

A similar analysis shows that the error in determining the acceleration scales as T^{-5}. These errors are, in general, not negligible, and must be taken into account in the calculation of turbulence statistics.

Finally, we note that it is instructive to consider how the relative error scales with turbulence parameters. Let us define α as the subpixel resolution (0.1 in our case), N_s to be the number of images taken per τ_η, N_T to be the filter length T in units of τ_η, and p to be the physical pixel size. Then the relative error in the velocity scales as

$$\frac{\langle \xi_x(T)^2 \rangle}{\langle u^2 \rangle} \sim \frac{\alpha^2}{N_s^3 N_T} \left(\frac{p}{L}\right)^2 Re_\lambda^2 , \quad (10.88)$$

where L is the integral length scale. It is clear then that at high Reynolds number a simple finite-difference scheme (recall that $T = 1$ corresponds to taking central differences) is insufficient for determining the velocity accurately. For the acceleration, the problem is even more acute, and the relative error scales as

$$\frac{\langle \xi_x(T)^2 \rangle_{\mathrm{accel}}}{\langle a^2 \rangle} \sim \frac{\alpha^2}{N_s^5 N_T} Re_\lambda^3 . \quad (10.89)$$

10.2.3 Turbulent Relative Dispersion

Turbulent flows abound with long-range correlations. As such, the statistics of a single Lagrangian tracer will never be sufficient to characterize turbulence fully; instead, we must turn to the joint statistics of many tracers. The simplest such multiparticle problem is that of the separation rates of pairs of fluid elements, known as turbulent relative dispersion. We have measured turbulent dispersion in our LPT experiment [10.56, 59]; here, we briefly present some of our results as an example of the type of analysis possible with LPT.

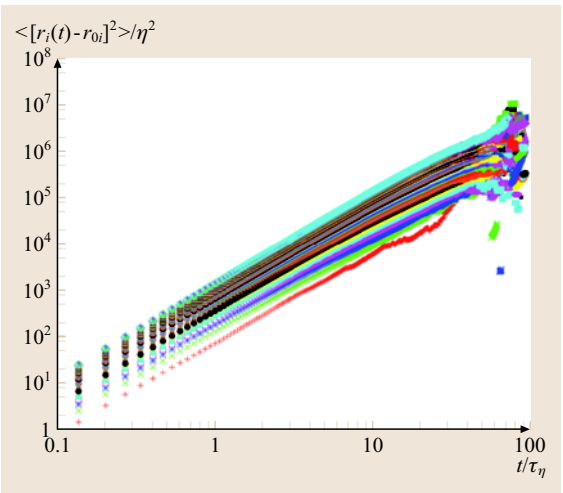

Fig. 10.14 Evolution of the mean-square particle separation at $Re_\lambda = 815$. Each set of symbols represents a bin of initial separations 1 mm ($\approx 43\eta$) wide, ranging from 0–1 mm to 49–50 mm. With both axes normalized by the Kolmogorov scales, each data curve follows a power law for over two decades in time

Under the action of Brownian motion, the mean-square separation between two fluid elements in a quiescent fluid will grow linearly in time. In a tur-

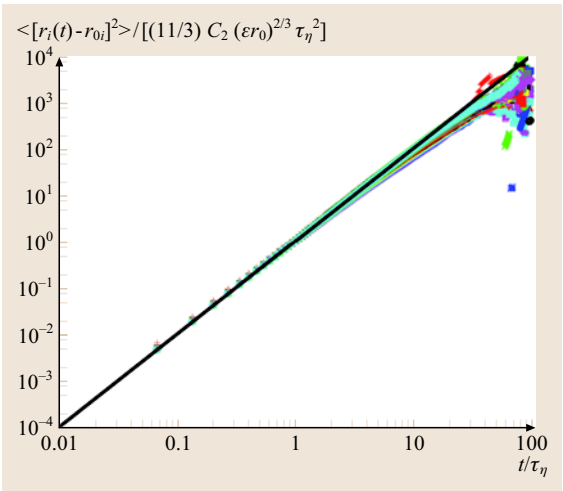

Fig. 10.15 Scale collapse of the mean-square particle separation. The same data as in Fig. 10.14 is scaled by Batchelor's constant $(11/3)C_2(\epsilon r_0)^{2/3}$ and an almost perfect collapse of the data is seen for all 50 initial separations

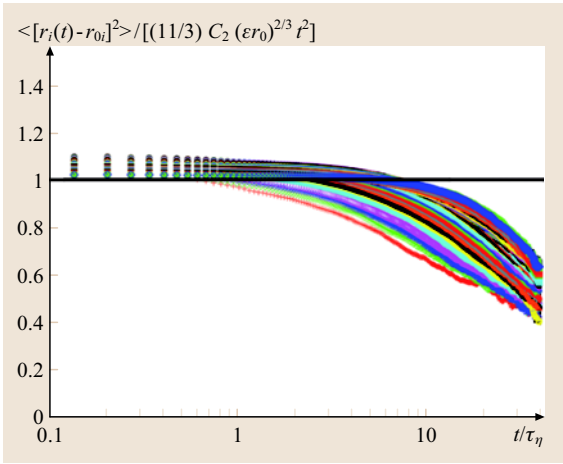

Fig. 10.16 Compensated mean-square particle separation. The time axis is scaled by τ_η. The data for different initial separations deviate from the Batchelor prediction at different times

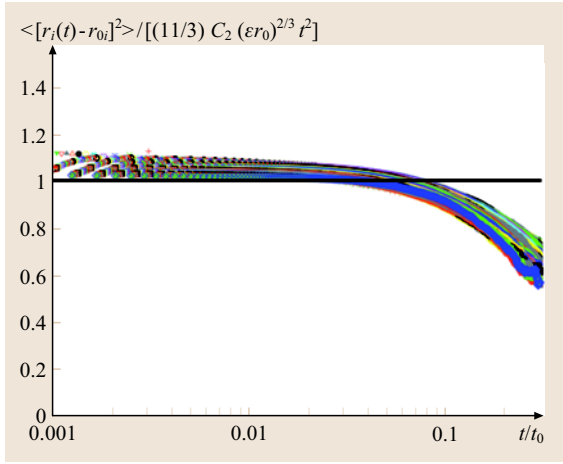

Fig. 10.17 Compensated mean-square particle separation with time scaled by t_0. Plotted in this way, there is a scale collapse in both space and time

bulent flow at sufficiently large scales, i. e., above the integral scales of the flow, pairs of fluid elements will also experience this linear Taylor diffusion [10.69]. In the inertial range, however, fluid element pairs in turbulence will separate superdiffusively, explaining why turbulent flows mix so efficiently.

Based on simple physical arguments and measurements of diffusion over a wide range of scales, *Richardson* [10.70] suggested that the mean-square pair separation should grow as t^3; subsequently, *Obukhov* [10.71] refined his work and wrote that

$$\langle r^2 \rangle = g\epsilon t^3, \tag{10.90}$$

in the inertial range where energy neither enters nor leaves the system, and where r is the distance between the particles and g is known as the Richardson constant. Such Richardson–Obukhov scaling has proved very challenging to observe, however, and estimates of the Richardson constant span more than an order of magnitude [10.72].

In 1950, *Batchelor* [10.73] realized that while the pair retains a memory of its initial separation r_0, the mean-square separation should grow only as t^2 rather than t^3. He reasoned that this memory should persist for times on the order of the lifetime of an eddy of size r_0, given by $t_0 = (r_0^2/\epsilon)^{1/3}$. After this time, if the Reynolds number is high enough, the pair should move into the Richardson–Obukhov regime. Taking Batchelor's arguments into account, we can write [10.56, 59, 74]

$$\langle [\mathbf{r}(t) - \mathbf{r}_0]^2 \rangle = \begin{cases} \frac{11}{3} C_2 (\epsilon r_0)^{2/3} t^2 \,, & t \ll t_0 \\ g\epsilon t^3 \,, & t_0 \ll t \ll T_\mathrm{L} \end{cases} \tag{10.91}$$

where C_2 is the scaling constant of the second-order Eulerian velocity structure function with a well-known

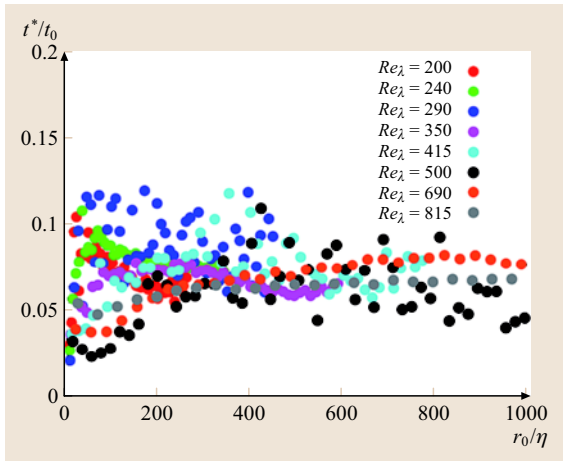

Fig. 10.18 Deviation from Batchelor's prediction; t^* measures the time when the relative dispersion data deviate by more than 5% from Batchelor's prediction. t^* is plotted against the initial separation for eight different Reynolds numbers. Irrespective of Reynolds number, $t^* = (0.071 \pm 0.009) t_0$

value of 2.13 ± 0.22 [10.75] and T_L is the integral time scale.

We have measured relative dispersion from the tracer particle trajectories in a $5 \times 5 \times 5$ cm^3 volume in the center of our experiment over a range of Reynolds numbers [10.56, 59]. In Fig. 10.14, we show our measurements of $\langle [\boldsymbol{r}(t) - \boldsymbol{r}_0]^2 \rangle$ at $Re_\lambda = 815$ with both axes normalized by the Kolmogorov scales. Figure 10.14 shows the dispersion for 50 different bins of initial separations, 1 mm wide ($\approx 43\eta$) and ranging from 0–1 mm to 49–50 mm. It is clear that, for each of these initial separations, even though the largest is approximately 70% of the integral scale L, the data follows a power law for more than two decades in time. The data, however, do not collapse for the different initial separations, suggesting that the initial separation remains a relevant parameter and that therefore the data cannot be following the Richardson–Obukhov law. Recalling Batchelor's prediction for the short-time behavior of the relative dispersion, in Fig. 10.15 we scale the same data by $(11/3)C_2(\epsilon r_0)^{2/3}$ and observe a nearly perfect collapse of the data for the various initial separations. We emphasize that the dark line drawn in Fig. 10.15 is not a fit but is rather Batchelor's predicted power law.

If we now look closer at the agreement of our data with Batchelor's prediction by compensating our experimental results by $(11/3)C_2(\epsilon r_0)^{2/3}t^2$, as shown in Fig. 10.16, we observe that the data deviate from the Batchelor prediction at times that vary with the initial separation. In order to correct for this effect, we scale time by Batchelor's $t_0 = (r_0^2/\epsilon)^{1/3}$, as shown in Fig. 10.17. This new scaling clearly collapses the data for the various initial separations much better, with each curve deviating from Batchelor's prediction at essentially the same value of (t/t_0). Our data therefore confirm both Batchelor's scaling argument and the time for which he predicted it would hold. Moreover, the value t^* for which the data deviate from Batchelor's prediction appears to be independent of Reynolds number. In Fig. 10.18, we define t^* as the time when the data deviate by 5% from Batchelor's prediction. For the entire range of Reynolds numbers tested, $t^* = (0.071 \pm 0.009)t_0$.

10.2.4 Concluding Remarks

Experimentally, Lagrangian turbulence is still very much a nascent field. It will be many years before the available Lagrangian data can rival the wealth of information we have about the Eulerian description of turbulence. Nevertheless, great progress has already been made in the development of Lagrangian experimental techniques, and these measurements are now nearly as accurate and robust as their Eulerian counterparts.

Here, we have presented a general Lagrangian particle tracking algorithm as well as our experimental implementation of the technique in an actual high-Reynolds-number flow. In addition, to demonstrate the utility of such a technique, we have shown measurements of turbulent relative dispersion, the simplest multiparticle Lagrangian problem. As Lagrangian experiments develop, we expect progress both in theory and experiment in describing more-complex multiparticle statistics and thereby probing the structure of turbulence and the nature of intermittency in great detail.

10.3 Elastic Turbulence in Viscoelastic Flows

10.3.1 Basics

This section deals with a new class of a chaotic (random) flow coined elastic turbulence that was observed in viscoelastic flows of polymer solutions [10.76]. The section is organized as follow. In the first part hydrodynamic description of dilute polymer solution flows and nondimensional parameters that follows from these equations to characterize the flows are presented. Variation of one of this control parameters that is responsible for the elastic properties of a fluid can lead to a new elastic instability in various flows, distinguished by the presence of curvilinear trajectories. Theoretical criteria for the elastic instability in three different flows together with their experimental verification are discussed. To complete the basics, the rheometric properties of polymer solutions used and their relation to Boger fluids are given. The first observation of elastic turbulence, in the flow between two plates, is described. Then experimental measuring techniques used to characterize the flow are given, and a complete description of the results of measurements together with discussion of the results are presented. Finally, the role of elastic stress, a recent theory of elastic turbulence, and comparative studies of elastic versus hydrodynamic turbulence are discussed. The third subsection deals with the description of the elastic turbulence in a curvilinear channel, or Dean flow, where a particularly detailed experiment on mixing due

to elastic turbulence was conducted [10.77]. A summary of the results is given at the end of the Section.

Hydrodynamic Description of Dilute Polymer Solution Flows

Solutions of flexible high-molecular-weight polymers are viscoelastic liquids, and they differ from Newtonian fluids in many aspects [10.78]. The most striking elastic property of these polymer solutions is probably the dependence of mechanical stresses in the flow on the history of the flow. So, the stresses do not immediately become zero when fluid motion stops, but rather decay with some characteristic relaxation time λ, which can be well above a second. When a polymer solution is sufficiently dilute, its stress tensor τ can be divided into two parts, $\tau = \tau_s + \tau_p$. Here the elastic stress tensor, τ_p, is due to the polymer molecules, which are stretched in the flow, and depends on history of the flow. The first term, τ_s, is defined by the viscosity of the Newtonian solvent, η_s, and the rate of strain in the flow, $\tau_s = \eta_s [\nabla \boldsymbol{V} + (\nabla \boldsymbol{V})^T]$. So, the equation of motion for a dilute polymer solution looks like

$$\frac{\partial \boldsymbol{V}}{\partial t} + (\boldsymbol{V}\cdot\nabla)\boldsymbol{V} = -\nabla p/\rho + (\eta_s/\rho)\nabla^2 \boldsymbol{V} + \nabla\tau_p/\rho\,, \tag{10.92}$$

where p is pressure, and ρ is the density of the fluid. One can see that τ_p enters the equation of motion linearly. The equation has a nonlinear term, $(\boldsymbol{V}\nabla)\boldsymbol{V}$, which is inertial in nature. The Reynolds number defines the ratio of this nonlinear term to the viscous dissipative term, $\nu\nabla^2\boldsymbol{V}$. So the degree of nonlinearity of the equation of motion can still be defined by the Reynolds number $Re = VL\rho/\eta_s$ for a polymer solution. Therefore, turbulence in fluids at high Re is a paradigm for a strongly nonlinear phenomenon in spatially extended systems [10.79, 80].

The simplest model incorporating the elastic nature of the polymer stress tensor, τ_p, is a Maxwell-type constitutive equation [10.78] with a single relaxation time λ

$$\tau_p + \lambda\frac{D\tau_p}{Dt} = \eta_p[\nabla\boldsymbol{V} + (\nabla\boldsymbol{V})^T]\,. \tag{10.93}$$

Here $\frac{D\tau_p}{Dt}$ is a material time derivative of the polymer stress, and $\eta_p = \eta - \eta_s$ is the polymer contribution to the total viscosity η. An appropriate expression for the time derivative $\frac{D\tau_p}{Dt}$ has to take into account that the stress is carried by fluid elements, which move, rotate, and deform in the flow. The translational motion implies an advection term $(\boldsymbol{V}\nabla)\tau_p$ in an appropriate expression for $\frac{D\tau_p}{Dt}$, while the rotation and deformation of the fluid particles should lead to contributions like $(\nabla\boldsymbol{V})\tau_p$ or $\tau_p(\nabla\boldsymbol{V})$ [10.78]. Therefore, along with terms linear in τ_p and $\boldsymbol{V}$, some nonlinear terms, in which τ_p is coupled to $\boldsymbol{V}$, should appear in the constitutive relation. A simple model equation for $\frac{D\tau_p}{Dt}$, which is commonly used for description of dilute polymer solutions, is the upper convected time derivative,

$$\frac{D\tau_p}{Dt} = \frac{\partial\tau_p}{\partial t} + (\boldsymbol{V}\nabla)\tau_p - (\nabla\boldsymbol{V})^T\tau_p - \tau_p(\nabla\boldsymbol{V})\,. \tag{10.94}$$

The equations (10.93, 94) together with the expression for τ_s constitute the Oldroyd-B model of polymer solution rheology [10.78]. One can see that nonlinear terms in the constitutive equation (10.93, 94) are all of the order $\lambda(V/L)\tau_p$. The ratio of those nonlinear terms to the linear relaxation term τ_p is given by a dimensionless expression $\lambda(V/L)$, which is usually called the Weissenberg number Wi that represents the ratio of the relaxation time to the characteristic flow time. The relaxation term τ_p is somewhat analogous to the dissipation term in the Navier–Stokes equation.

One can expect the mechanical properties of the polymer solutions to become notably nonlinear at sufficiently large Weissenberg numbers. Indeed, quite a few effects originating from nonlinear polymer stresses have been known for a long time [10.78]. So, in a simple shear flow of a polymer solution there is a difference between normal stresses along the direction of the flow and along the direction of velocity gradient. At low shear rates this normal stress difference N_1 is proportional to the shear rate squared (see Sect. 9.1.1). When flow lines are curvilinear, this gives rise to a volume force acting on the liquid in the direction of the curvature, the *hoop stress*. Therefore, if a rotating rod is inserted into an open vessel with a highly elastic polymer solution, the liquid starts to climb up the rod instead of being pushed outwards [10.81]. This phenomenon is known as *rod climbing*, or the *Weissenberg effect*. Further, in a purely extensional flow, the resistance of a polymer solution depends on the rate of extension in a strongly nonlinear fashion. There is a sharp growth in the elastic stresses when the rate of extension exceeds $1/(2\lambda)$, that is at $Wi > 1/2$. As a result, the apparent viscosity of a dilute polymer solution can increase by up to three orders of magnitude [10.82]. Both the Weissenberg effect and the growth of extensional flow resistance have been most clearly observed in viscous polymer solutions and in flows with quite low Re, where nonlinear inertial effects are insignificant.

A natural question arising here is, whether there may exist some kind of turbulent flow produced by the nonlinear polymer stresses alone, in the absence of any significant inertial effects, at low *Re*. An important step in this direction was made about a decade and a half ago when purely elastic instabilities were experimentally identified in a rotational flow between two plates [10.83] and in a Couette–Taylor (CT) flow between two cylinders [10.84].

Elastic Instability and its Experimental Observations in Various Curvilinear Flows

Purely elastic instabilities occur at *Wi* numbers of order unity and vanishingly small *Re*. As a result of these instabilities, secondary vortex flows are developed [10.84], and the flow resistance increases [10.83]. The analysis showed that the nonlinear mechanical properties of the polymer solution can indeed lead to a flow instability, and a simple mechanism for this purely elastic instability was proposed.

During the past decade the purely elastic instabilities in viscoelastic fluids have been a subject of many theoretical and experimental studies, which are partially reviewed in [10.85, 86]. After the pioneering work by *Larson*, *Muller* and *Shaqfeh* [10.84, 87], purely elastic instabilities were also found in other shear flows with curvilinear streamlines. Those included the flow between a rotating cone and a plate (Sect. 9.1.1) and the Taylor–Dean flow [10.85, 86]. The original theoretical analysis of [10.87] was refined, and more-elaborate experiments were carried out. A few new mechanisms of flow instability driven by nonlinear elastic stresses were suggested for cone-and-plate and Taylor–Dean flows. The original mechanism proposed in [10.87] was verified experimentally in [10.88].

The most thorough and detail studies were conducted on the elastic instability in Couette–Taylor (CT) flow between two coaxial cylinders. In spite of the fact that instabilities in viscoelastic fluids were studied for decades, the purely elastic instability in CT flow was first investigated both experimentally and theoretically rather recently [10.84, 87]. The mechanism for the elastic instability in the CT system suggested in [10.87], is based on the Oldroyd-B model. The primary flow in the CT system with the inner cylinder rotating (Couette flow) is a pure shear flow in the r–θ plane that generates a normal stress difference $N_1 \equiv \tau_{\theta\theta} - \tau_{rr} = 2\eta_p\lambda(\dot{\gamma}_{r\theta})^2$, and a radial force N_1/r per unit volume. Here r, θ are cylindrical coordinates in the plane perpendicular to the cylinder axis, $\tau_{\theta\theta}$ and τ_{rr} are the components of the polymer stress tensor τ_p, and $\dot{\gamma}_{r\theta}$ is the only nonzero component of the rate-of-strain tensor $\dot{\gamma}$. A secondary flow in the CT flow includes regions of elongational flow in the r-direction with $\dot{\epsilon} \equiv \partial v_r/\partial r \neq 0$. The radial extensional flow stretches the polymer macromolecular coils in the r-direction, though it is a small perturbation on the top of the azimuthal stretching produced by the primary shear flow. However, being stretched in the radial direction, the macromolecular coils become more susceptible to the basic shear flow. The coupling between the radial and shear flow leads to a further increase in shear stresses. Thus, the result is further stretching of the polymer in the θ-direction that generates additional normal stress difference. So, the elastic instability mechanism is based on the coupling between the perturbative radial elongational flow and the strong azimuthal shear flow that results in a radial force. The latter reinforces the radial flow. As pointed out in [10.88], this transition can be only a finite-amplitude (first-order) transition. The corresponding criterion for the instability is

$$K \equiv \frac{\eta_p}{\eta_s}\frac{d}{R_1}Wi^2. \tag{10.95}$$

Here d and R_1 are the gap and the inner cylinder radius, respectively. The elastic instability occurs when the parameter K exceeds a certain threshold value [10.87]. This criterion is valid at sufficiently small values of η_p/η_s and in the small-gap-ratio limit, d/R_1. A more-general expression is given in [10.87]. When the gap ratio, d/R_1, and the polymer viscosity ratio, η_p/η_s, are fixed the elastic instability is just defined by the critical Weissenberg number Wi_c.

As was suggested in [10.89], where the CT flow was discussed, there is some analogy between flow transitions driven by elasticity and inertia. So, the inertially driven Taylor instability occurs at constant Taylor number [10.79, 80], $Ta = \frac{d}{R_1}Re^2$, while the elastic instability is controlled by the parameter K from (10.95) [10.87, 88]. The Weissenberg number is defined here as $Wi = \lambda\Omega R/d$, where Ω is the angular velocity of the rotating inner cylinder. (It was termed the Deborah number in some of the original texts [10.87–89].) The Weissenberg number appears to be analogous to the Reynolds number. The geometric parameter determining curvature, d/R_1, enters the expressions for both *Ta* and K. Scales of time and velocity for the purely elastic flow transition are given by λ and d/λ, respectively. As was shown in [10.89] these are analogous to t_{vd} and d/t_{vd}, which define scales of time and velocity for the inertially driven flow transitions. Here t_{vd} is the viscous diffusion time, defined as $t_{vd} = d^2/\nu$.

Nevertheless, along with all those analogies, there are still some important differences between flow transitions driven by inertia and elasticity. For example, it is an experimental fact that *any* laminar flow of a Newtonian fluid becomes unstable at sufficiently high *Re*, and all high-Reynolds-number flows are turbulent. This includes rectilinear shear flows such as Poiseuille flow in a circular pipe and plane Couette flow, which are supposed to be linearly stable at any *Re*. In contrast, purely elastic flow instabilities in shear flows have only been observed so far in systems with curvilinear streamlines. All these instabilities are supposed to be driven by the hoop stress, which originates from the normal stress differences.

This difference between the inertial and elastic instabilities originates, of course, from the distinct governing equations. There are, however, some purely practical factors that can explain rather well the lack of observations of purely elastic flow transitions in rectilinear shear flows. Inertial instabilities in rectilinear shear flows of Newtonian fluids occur at quite high Reynolds numbers. Those are typically about two orders of magnitude higher than *Re*, at which curvilinear shear flows with large gap ratios become unstable. A priori, one may suggest that rectilinear and curvilinear shear flows would have a similar relation between *Wi* at thresholds of the purely elastic flow instabilities as well. The problem is, however, that while it is rather easy to generate high-*Re* flows with low-viscosity Newtonian fluids, it is usually impossible to reach the corresponding high values of *Wi* in shear flows of elastic polymer solutions. That is, there always exist rather severe practical limitations restricting nonlinearity in elastic polymer stresses in shear flows. Their molecular mechanisms have recently been elucidated in a seminal paper by Chu's group [10.90].

Polymer molecules have finite extensibility, and their relaxation time decreases when they are stretched in a shear flow. This *thinning* of the relaxation time at high *Wi* is usually quite a strong and well-recognized effect. In fact, different variations of the basic Oldroyd-B model have been specially developed to take into account this shear thinning [10.78]. A significant decrease of λ with shear rate $\dot{\gamma}$ renders growth of the Weissenberg number $Wi = \lambda(\dot{\gamma})\dot{\gamma}$ much slower than linear in $\dot{\gamma}$. Substantial stretching of the polymer molecules in the primary shear flow also reduces their ability for further extension and the susceptibility of the elastic stresses to flow perturbations, which is necessary for the generation of flow instabilities and secondary vortex flows [10.87]. Finally, high shear rates cause mechanical degradation of the polymer molecules, which leads to a permanent reduction of elasticity during experimental runs and a decay of λ that can be very fast at high *Wi*. Because of all these reasons it was found to be very difficult or even impossible to observe elastic instabilities, when expected values of *Wi* at the instability threshold were high. This was the case in curvilinear flows with small gap ratios [10.91], and small viscosity ratios [10.88].

The first experimental observations of the elastic instability in CT flow found Wi_c indeed rather close to the theoretical prediction [10.86,87]. However, the observed critical modes were different from the predicted axisymmetric one. This discrepancy was resolved later both theoretically [10.92] and then experimentally [10.88]. In fact it was shown that the non-axisymmetric mode becomes unstable first, and the bifurcation is backward, as was verified experimentally. In spite of this, the instability mechanism remains as first suggested and verified in [10.87, 88].

A purely elastic instability apparently also occurs by a similar mechanism in other rotational shear flows, namely concentric cone-and-plate and plate-and-plate geometries (Sect. 9.1.1). There the secondary flow is also driven by a *hoop stress*, and by the coupling between the primary shear flow and secondary elongation flow in the axial direction. Historically a transition in fluid rheology was first observed experimentally in these geometries [10.83], and Magda and Larson suggested that its origin lies in an elastic flow instability. A complete set of numerical and experimental studies of the elastic instability in these flows was carried on in [10.91, 93, 94]. Due to the more-complicated flow structure than in CT flow, no analytic expression for the stability criterion is available in either of these cases. However, some common features for all rotational shear flows can be pointed out. For all systems the threshold of the elastic instability strongly depends on the aspect ratio, which is defined differently in each case. The instability criterion also depends on the viscosity ratio, though the functional form of this dependence was found only in CT flow. In all systems the most unstable mode is non-axisymmetric and oscillatory, and the transition is discontinuous, or first order (inverse bifurcation).

Another curvilinear flow that is relevant to further results is a flow through a curved channel driven by a streamwise pressure gradient, which was first studied for a Newtonian fluid by *Dean* [10.95]. He found that the instability is defined similarly to CT flow by $Re^2 d/R_1$ when it exceeds some critical value. The linear stability analysis for the Oldroyd-B fluid and experimental observation of the instability in the elastic Dean flow were performed by *Joo* and *Shaqfeh* [10.96–98]. It was

predicted by numerical calculations and verified experimentally that the stability of the pressure-driven flow through a curved channel is defined by a criterion (in a small-aspect-ratio limit) that is rather similar to that found in CT flow (10.95) with a rather close critical value [10.97, 98]. However, in contrast to the rotational shear flows the most unstable mode is stationary and axisymmetric that shows up in a secondary toroidal vortex flow centered near the outer curved surface. The dependence of the stability threshold on the aspect ratio indicates that, like in rotational shear flows, the curvature is of crucial importance for the instability to occur. The elastic instability in the Dean flow is also driven by the *hoop stress* but the mechanism is rather different [10.97] and is related to the existence a normal stress gradient across the streamlines. The necessary condition for the instability is $\partial\tau_{\theta\theta}/\partial r > 0$, i. e., a larger hoop stress is located outward from the center of curvature. Then a small radial inward flow is reinforced by the increased hoop stress gradient. Thus, all three flow configurations with curvilinear trajectories considered in this chapter exhibit the elastic instability. Their instability criterion as well as the most unstable mode are rather well investigated and known.

Experimental Considerations to Observe Elastic Turbulence

In order to maximize the nonlinear elastic effects and to have a better opportunity to observe the elastic turbulence one has to choose experimental conditions quite carefully [10.76]. First, it is important to obtain an elastic instability at a possibly low critical Weissenberg number Wi_c. For that purpose the gap ratio and the viscosity ratio had to be possibly large. Therefore, one should use a polymer solution with a rather large η_p/η of about 1/4. [Further increase of the polymer concentration (or of η_p/η) was not very efficient, and would also complicate the solution rheology, including large shear thinning of the solution viscosity.] One should use a large aspect ratio, either in the CT flow or the swirling flow between two plates. In the swirling flow the experiments were carried out with a large gap ratio, between about 0.2 and 0.53 with the possibility to vary it.

An appropriate polymer sample for the solution that would not suffer major mechanical degradation under experimental flow conditions had to be chosen. So, the fluids most often used in experiments on elastic instabilities were so-called Boger fluids [10.99]. These fluids are highly elastic. They are obtained by solving high-molecular-weight polymers at low concentration (dilute solution) in a viscous Newtonian solvent. The Boger fluids are almost universally used as model viscoelastic fluids. Their relaxation times can be quite large, reaching seconds or even minutes, while their rheological properties are semiquantitatively described by the simple Oldroyd-B model.

The limit for extensibility of the polymer molecules had to be high compared with their typical conformations at the instability threshold. We used polyacrylamide (PAA) with a large average molecular weight of $M_w = 18\times10^6$ g/mol and a broad molecular-weight distribution (and low concentration of polyacrylic acid monomers). This commercial polymer sample proved to be remarkably stable with respect to mechanical degradation, which allowed us to reach high values of Wi and explore strongly nonlinear flow regimes. The high molecular weight of the polymers resulted in a large characteristic relaxation time λ even with solvents of moderate viscosity, and at a small characteristic stress, $\tau_0 = \eta_s/\lambda$. One can learn from (10.94, 95) that τ_0 sets a scale for the polymer stress at which its nonlinearity becomes significant. Therefore, the value of τ_0 together with η_p/η and d/R determine the polymer stress τ_p in the primary shear flow at the instability threshold. It is rather natural to suggest that, when polymer molecules transduce less stress, they are also less subjected to mechanical degradation. Further, molecular interpretation of the Weissenberg number in a shear flow relates it to the degree of deformation of polymer molecules from their relaxed random coil conformations. So $Wi = 1$ can be regarded as the characteristic value at which extension of polymer molecules becomes considerably larger than the size of relaxed coils. High molecular weight and flexibility of a polymer suggests a large number of Kuhn segments [10.78, 100] in the polymer chain, and a high ratio between its contour length (size, when fully extended) and the size (radius of gyration R_g) of a relaxed coil. (For a polymer molecule in a good solvent, with $R_g \sim M_w^{3/5}$, this ratio should increase as $M_w^{2/5}$ [10.100]. We would like to point out here that addition of NaCl to the solution reduces R_g.) Therefore, by using a higher-M_w polymer, we increased the domain of extensibility starting from the typical conformation at Wi_c, which opened the way for richer flow dynamics above the elastic instability threshold.

Rheometric Properties of Polymer Solutions

Several series of experiments on elastic turbulence in different experimental setups conducted during the last several years were based on the same stock (master) polymer solution of PAA ($M_w = 18\times10^6$ g/mol supplied by Polysciences). First we dissolved 0.9 g of PAA

powder and 3 g of NaCl in 275 ml of deionized water by gentle shaking. (Addition of NaCl was necessary to improve the solubility of PAA.) Next the solution was mixed for 3 h in a commercial mixer with a propeller at a moderate speed. The idea behind this procedure was to cause mechanical degradation of PAA molecules with the highest weights, and to *cut* the high-M_w tail of the broad molecular-weight distribution of the PAA sample. In a solution with a broad distribution of polymer molecular weights the heaviest molecules, which are most vulnerable to mechanical degradation, may also make a major contribution to the solution elasticity. A possible negative effect of this is significant degradation of elasticity during experimental runs, and inconsistency in the experimental results. We found empirically that the procedure of predegradation in the mixer leads to a substantial reduction of degradation during the experiments and to substantial improvement of the consistency. Finally, 9 g of isopropanol was added to the solution (to preserve it from aging) and water was added up to 300 g. The final concentrations of PAA, NaCl and isopropanol in the stock solution were 3000 ppm, 1%, and 3%, respectively.

As a viscous Newtonian solvent for PAA, we used a solution of $\approx 65\%$ sugar (saccharose) in all experiments, if it is not mentioned specifically otherwise. Viscosity and relaxation time were measured with the same AR-1000 rheometer in a temperature-controlled narrow-gap Mooney–Ewart (Couette) geometry. The solvent viscosity was $\eta_s = 0.324\,\mathrm{Pa\,s}$ at 12 °C and $\eta_s = 0.114\,\mathrm{Pa\,s}$ at 22 °C. The PAA concentration was 80 ppm.

Solution 1, used in the early experiments at low temperature (12 °C), contained 1% NaCl to fix the ionic contents. Viscosity η was slowly decreasing with $\dot\gamma$, so that its shear thinning was about 7% per decade of $\dot\gamma$. At a shear rate of $\dot\gamma = 1\,\mathrm{s}^{-1}$, corresponding to the onset of a purely elastic instability in the standard configuration (see below), η was 0.424 Pa s, and the viscosity ratio was $\eta_p/\eta = 0.235$. The polymer relaxation time, λ, was measured in oscillatory tests (Sect. 9.1) with a shear rate amplitude of $1\,\mathrm{s}^{-1}$ in a range of angular frequencies, ω. Then $\lambda(\omega)$ at $\omega \to 0$, estimated as 3.4 s, was chosen as a representative relaxation time, λ. The diffusion coefficient for the saccharose molecules was about $D = 8.5e-7\,\mathrm{cm}^2/\mathrm{s}$ [10.101].

Solution 2, used in the later experiments at higher temperature (22 °C), had a viscosity of $\eta = 0.138\,\mathrm{Pas}$ at a shear rate of $2\,\mathrm{s}^{-1}$, and a viscosity ratio of $\eta_p/\eta = 0.174$. The polymer relaxation time obtained by the rheometric measurements via small oscillations using both a AR-1000 rheometer from TA Instruments and a Vilastic viscoelasticity analyzer (Vilastic-3, Vilastic Scientific, Austin, TX) as a function of shear rate showed the relaxation time scaling with *shear thinning* as $\lambda \sim \dot\gamma^{-\alpha}$, with $\alpha \simeq 0.3$ similar to that found earlier for solutions with lower-molecular-weight PAA samples [10.88], and the relaxation time in the limit of $\dot\gamma \to 0$ as $\lambda(0) = 4.7$ s.

10.3.2 Elastic Turbulence in Swirling Flow Between Two Plates

Some flow patterns observed above the purely elastic instability threshold in the curvilinear flows had a rather disordered appearance and exhibited chaotic velocity spectra. This was first mentioned in [10.88, 102] and then specifically in [10.89] for CT flow. So, it was reasonable to suggest that under some conditions a truly *turbulent* flow might be excited by elastic stresses at vanishingly small *Re*. This idea was explicitly stated in [10.89], where an analogy between elastic and inertial flow transitions was discussed. In fact, irregular flow patterns and growth of flow resistance in elastic polymer solutions at low *Re* were observed even before the purely elastic instabilities were identified [10.103]. These flow phenomena were even sometimes coined *elastic turbulence*. In all these cases, however, the term *turbulence* was used in a rather loose fashion, without a proper definition. More importantly, no quantitative data on either the flow velocity field or the spatial and temporal velocity spectra in these irregular flows were ever presented.

Although the notion of turbulence is widely used in scientific and technical literature, there is no unique, commonly accepted definition. Therefore, turbulent flow is usually identified by its main features. Turbulence implies fluid motion on a broad range of temporal and spatial scales, so that many degrees of freedom are excited in the system. There are no characteristic scales of time and space in the flow, except for those restricting the excited temporal and spatial domains from above and below. Turbulent flow is also usually accompanied by a significant increase in momentum and mass transfer. That is, the flow resistance and rate of mixing in a turbulent flow become much higher than they would be in an imaginary laminar flow with the same *Re*.

In recent publications [10.76, 77, 104] it was shown how these features of turbulence appeared in a highly elastic polymer solution at low Reynolds numbers in two curvilinear flows. The first quantitative experiments were done in a swirling flow between two plates with

a wide gap, and the phenomenon was coined elastic turbulence. In this section we discuss the results of the experiments on the elastically driven turbulent flow in two experimental setups where the most complete studies were carried out, namely a swirling flow between two plates and an open flow in a curved channel [10.76, 77, 104–109]

Experimental Setup and Procedure

The experimental apparatus is schematically shown in Fig. 10.19.

Polymer solution was held in a stationary cylindrical cup with a flat bottom (lower plate). A coaxial rotating upper plate was just touching the surface of the fluid. The cup was mounted on top of a commercial rheometer, AR-1000 from TA instruments. The upper plate was attached to the shaft of the rheometer, which allowed precise control (within 0.5%) of its angular velocity Ω and measurements of the torque T (Ω-mode), or opposite control (within 0.5%) of T and measurements of Ω (T-mode). The average shear stress at the upper plate, τ_w, was calculated using the equation $T = \tau_w \int r \mathrm{d}S$, which gave $\tau_w \equiv 3T/(2\pi R^3)$, where the integration is over the upper plate surface.

The moment of inertia of the shaft of the rheometer was $I_s \approx 14\,\mu\mathrm{Nms}^2$ and that of the upper plate I_d was about $61\,\mu\mathrm{Nms}^2$ for setup 1, and about $84\,\mu\mathrm{Nms}^2$ for setup 2. The accuracy of the angular speed measurements in constant-torque mode is about 2% and the accuracy of the torque measurements in the constant-speed mode is about 1%. One has to point out here that smallness of the fluctuation rate of the angular velocity is not a sufficient criterion to have constant-speed forcing. Corresponding to the Ω-mode, $(I_s + I_d)\partial\Omega/\partial t$ should also be much smaller than typical values of the torque T.

The sidewalls of the cup were machined from a single piece of perspex, which was optically clear. The cup was circular on the inside and square on the outside in a horizontal cross section. This allowed measurements of the flow velocity in the horizontal plane by a laser Doppler velocimeter (LDV) (Sect. 5.3.1) with two crossing frequency-shifted beams. By appropriate positioning and orientation of the beam-crossing region, azimuthal (longitudinal) and radial (spanwise) velocity components, V_θ and V_r, respectively, could be measured at different r and z. Here (r, θ, z) are cylindrical coordinates. The bottom of the cup was machined of stainless steel and the temperature was stabilized at 12 °C by circulation of water below the bottom plate.

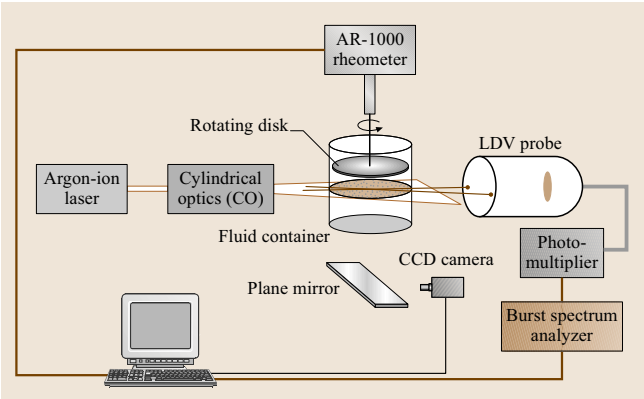

Fig. 10.19 Overview of the swirling flow apparatus

A slightly modified version of the setup was designed to photograph the flow from below, to use particle image velocimetry (PIV)(Sect. 5.3.1) and particle tracking velocimetry (PTV) techniques, and to observe mixing in the flow. A special cup of the same shape but with a transparent bottom (lower plate, made of perspex) was attached to the rheometer concentrically with the shaft but above the rheometer base, and a mirror tilted by 45° was placed under the cup, as schematically shown in Fig. 10.19. The mirror was used both to illuminate the fluid by diffuse light and to relay images of the flow to a charge-coupled device (CCD) camera. The camera was equipped with a regular video lens and mounted horizontally near the rheometer (Fig. 10.19). The source of the diffuse light was an illuminated white screen around the camera. The images were digitized by an 8-bit 512×512 frame grabber in the case of flow visualization and mixing, and at 12 bits with 640×512 pixels at 25 frame/s and 1280×1024 at 12.5 frame/s using a PixelFly digital camera (PCO, Germany) in the case of PIV and PTV. In order to provide thermal stabilization, the whole rheometer was placed in the thermally isolated box with through flow of temperature-controlled air.

In the basic setup used in the early experiments, the radii of the upper plate and the cup were $R_1 = 38$ mm and $R_2 = 43.6$ mm, respectively, and the distance between the plates was $d = 10$ mm. The configuration was similar to devices with rotating flow between two plates used in experiments on purely elastic instability [10.83, 86, 91, 94]. Its gap ratio, d/R, was significantly higher, though. In order to study the dependence of the flow conditions on the size of the system, two smaller setups, a half-size and a quarter-size system, with all the dimensions reduced by factors of two and four, respectively, were

used. Each time, when dimensions of an experimental setup are nonstandard, this is stated explicitly in the text.

In the later experiments two setups were used. In setup 1 a cylindrical container of radius $R_c = 2.2\,\text{cm}$ and a disk with radius $R_d = 2\,\text{cm}$ were used, while setup 2 had $R_c = 4.9\,\text{cm}$ and a disk with $R_d = 4.8\,\text{cm}$. The distance between the disk and the bottom plate was $d = 1\,\text{cm}$ in both setups. The system was illuminated laterally by a thin (30 μm in the center of the setup and about 130 μm at the edges of the setup) laser sheet through the transparent walls of the fluid container at the mid distance between the plates. The laser sheet was generated by passing a laser beam delivered by a 300 mW argon-ion laser through a block of two crossed cylindrical lenses (CO) mounted in a telescopic arrangement. The main flow investigation tool was the digital PIV technique. As flow tracers 10 μm fluorescent beads were used. We acquired 2000 pairs of flow images every 120 ms using a digital camera. The time delay between consecutive images was 40 ms. Time series of velocity fields were obtained by using a multipass PIV algorithm [10.108]. The accuracy of the method was carefully checked by running test experiments with the solvent, in the same range of mean particle displacements and under similar illumination conditions. Although the instrumental error increases more or less linearly with the mean particle displacement, it never exceeded 5% of the mean displacement. The spatial resolution was about 120 velocity vectors over 10 cm. By postprocessing the velocity fields, we obtained the profiles of the velocity components, fields of fluctuations of each velocity component, spatial spectra of the velocity fluctuations, velocity gradients and their fluctuations, structure functions of gradients, and Eulerian velocity correlation functions. The space–time measurements together with simultaneous global measurements of the flow resistance provided a rather complete description of the different flow regimes as a function of Wi [10.109]. A Lagrangian frame flow investigation was also conducted [10.107].

In a swirling flow between two plates the shear rate is quite inhomogeneous over the fluid bulk, even when the flow is laminar. So, the choice of a representative shear rate becomes somewhat arbitrary. We decided to consider the simple expression $\Omega R/d$ as a characteristic shear rate, and to define the Weissenberg number as $Wi = \lambda\Omega R/d$. The Reynolds number was defined as $Re = \Omega R d\rho/\eta$.

In order to evaluate the growth of flow resistance due to elastic instability and irregular secondary flow in the system, the average shear stress near the upper plate τ_w^{lam} in an imaginary laminar shear flow at the same Ω had to be estimated. The stress τ_w^{lam} depends on an average shear rate $\dot{\gamma}_{av}$ at the upper plate, and on the viscosity of the polymer solution η at this shear rate; an appropriate expression for it is $\tau_w^{lam} = \eta(\dot{\gamma}_{av})\dot{\gamma}_{av}$. The average shear rate $\dot{\gamma}_{av}$ was estimated from measurements of the ratio τ_w/η_0 in a laminar flow of a Newtonian fluid with a large viscosity η_0 at low Re. The shear rate in the laminar flow, calculated as $\dot{\gamma}_{av} = \tau_w/\eta_0$, was proportional to Ω, being $\dot{\gamma}_{av} = 1.12\Omega R/d$ in the standard configuration, and gave a properly weighted average over the surface of the upper plate.

Observation of Elastic Turbulence

Flow Resistance. The first indication of a strongly nonlinear state in the swirling flow was significant growth of the flow resistance above the elastic instability threshold, which can be characterized by the ratio τ_w/τ_w^{lam}, a measure of strength of turbulence and of the turbulent resistance. The dependence of τ_w/τ_w^{lam} on the shear rate, $\dot{\gamma} = \Omega R/d$, is shown in Fig. 10.20.

A sharp transition in the flow of the polymer solution (curve 1, black line) occurs at $\dot{\gamma} \simeq 1\,\text{s}^{-1}$ (corresponding to $Wi = 3.5$) and is manifested by a significant increase in τ_w compared to the laminar flow. The Reynolds number at the transition point is about 0.3, so that inertial effects are quite negligible there. The transition has pro-

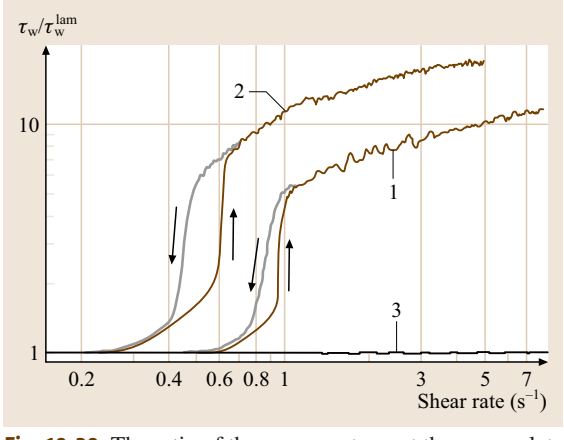

Fig. 10.20 The ratio of the average stress at the upper plate τ_w measured in the flow, to the stress τ_w^{lam} in an imaginary laminar shear flow with the same boundary conditions, as a function of the shear rate $\dot{\gamma}$. Curves 1 and 2 are for the polymer solution flow with gaps of $d = 10\,\text{mm}$ and 20 mm, respectively. The shear rate was gradually varied in time. *Thin black lines* represent increasing $\dot{\gamma}$; *thick gray lines* represent decreasing $\dot{\gamma}$. Curve 3 is for the pure solvent

nounced hysteresis (thick gray line, corresponding to a slow reduction of $\dot{\gamma}$), which is rather typical of a purely elastic flow instability [10.88]. The higher the shear rate, the higher τ_w/τ_w^{lam}. The latter reaches a value about 12 times larger than it would be in a laminar flow at the highest $\dot{\gamma}$. In the same range of shear rates flow of the pure solvent (curve 3) is completely laminar and the ratio τ_w/τ_w^{lam} is unity within the resolution of the rheometer (about 1%). For a gap ratio of 0.526 the the ratio τ_w/τ_w^{lam} reaches a value of 19 (curve 2 in Fig. 10.20). For Newtonian fluids in the same flow geometry such a growth of the flow resistance is found at Re values of about 2×10^4. For flow in a circular pipe this value of τ_w/τ_w^{lam} is reached at $Re \simeq 10^5$, which is usually considered as a region of rather developed turbulence [10.79, 80].

In the setup with a radius of $R_1 = 4.8$ cm and an aspect ratio of 0.21 accurate power (P) measurements in the Ω-mode reveal, besides a drastic increase in the flow resistance, scalings of the average injected power $P \sim Wi^{\beta_1}$ and the rms of power fluctuations $P_{rms} \sim Wi^{\beta_2}$ with $\beta_1 \simeq 3.34 \pm 0.05$ and $\beta_2 \simeq 3.2 \pm 0.3$ (Fig. 10.21).

Here the injected power was calculated as $P = T\Omega$, and the shear thinning of the polymer relaxation time, $\lambda(\dot{\gamma})$, was taken into account. For low values of Wi in the laminar regime the injected power grows as $P_{lam} \sim Wi^{2.85}$, or quadratically with Ω, which is expected for the laminar flow. Due to the smallness of $Re < 16$, a nonlinear inertial contribution is negligible. So additional growth of the average injected power in the elastic turbulence compared to its laminar values occurs solely due to elastic stresses τ_p^{turb}. Therefore, according to the fit in Fig. 10.21 $P/P_{lam} \propto \tau_p^{turb} \propto Wi^{0.49}$.

Temporal and Spatial Velocity Fluctuations Spectra. Temporal spectra of the azimuthal and radial components of the velocity in the horizontal plane were measured with LDV at various locations at the cell and

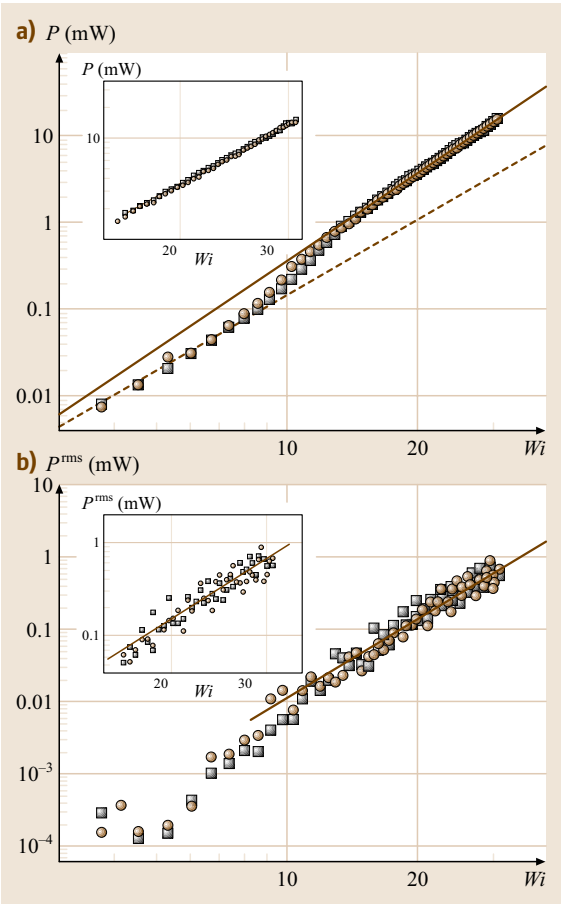

Fig. 10.21 **(a)** Dependence of the mean power P on the control parameter, Wi. *Squares*: increasing Wi, *circles*: decreasing Wi. The *full line* is a guide to the eye $Wi^{3.34}$. The *dotted line* is $Wi^{2.85}$. The *inset* shows a power-law fit, $Wi^{3.34\pm0.05}$. **(b)** Dependence of the rms power fluctuations P^{rms} on Wi. *Squares*: increasing Wi, *circles*: decreasing Wi. The *full lines* are power laws $Wi^{3.21}$. The *inset* shows the power-law fits $Wi^{3.21\pm0.3}$. Data were collected in setup 2 in the Ω-forcing mode

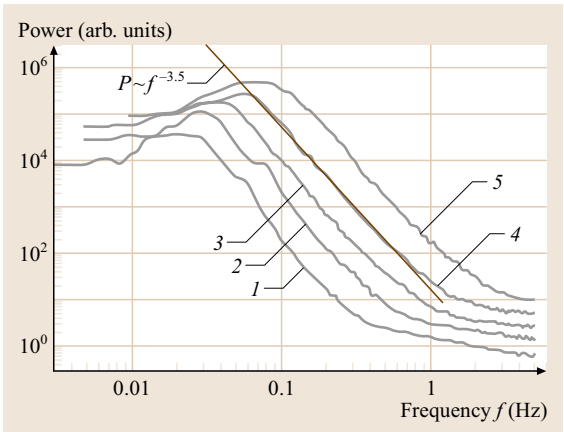

Fig. 10.22 Power spectra of the azimuthal velocity fluctuations in the standard setup at different shear rates $\dot{\gamma}$. The fluid velocity was measured by LDV in the center of the flow. The *curves* 1–5 correspond to $\dot{\gamma} = 1.25$, 1.85, 2.7, 4, and 5.9 s^{-1}, respectively (all above the transition point $\dot{\gamma} \simeq 1$). The power P of fluctuations is fitted by a power law $P \sim f^{-3.5}$ for $\dot{\gamma} = 4\,s^{-1}$ over about a decade in frequencies, f

had similar appearance [10.76, 104]. The azimuthal component of the velocity spectra measured in the center of the setup, where its average value was zero, at different constant shear rates $\dot{\gamma}$ (all above the elastic instability threshold) are shown in Fig. 10.22.

The power of the fluctuations and their characteristic frequencies increase with $\dot{\gamma}$, but the spectra remain very similar in appearance. In particular, the spectra do not have distinct peaks, and do span a broad range of about an order of magnitude in frequencies, where the power of the fluctuations decays according to a power law $P \sim f^{-\alpha}$. (Flattening of the curves at high f is due to instrumental noise.) The exponent α is about 3.5, which is much larger than the Kolmogorov exponent of 5/3 found for velocity spectra of high-Re inertial turbulence [10.79, 80].

To obtain quantitative information about the spatial structure of the fluctuating velocity field from the LDV measurements, we explored velocity spectra in various off-center points with nonzero average azimuthal velocity $\bar{V}_\theta$. The spectra of fluctuations of the radial component of velocity V_r at $\dot{\gamma} = 4\,\mathrm{s}^{-1}$ ($Wi = 13.5$) at four different radii are shown in Fig. 10.23; they look similar to the spectra in Fig. 10.22 with a similar power-law decay. They were all measured at $z = d/2$, where z is the distance from the upper plate. The root-mean-square values of the fluctuations at all four points were rather close, varying between 0.88 and 0.99 mm/s.

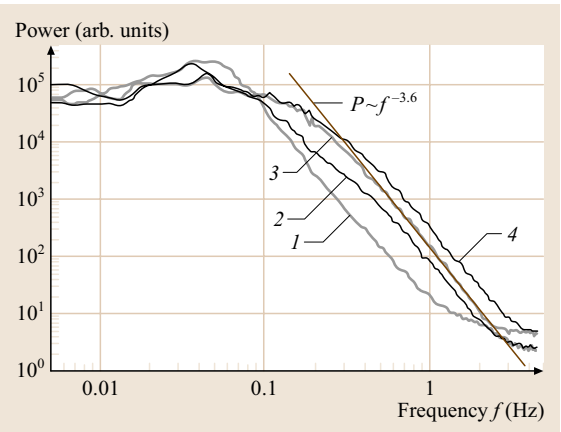

Fig. 10.23 Power spectra of the fluctuations of the radial velocity V_r at $\dot{\gamma} = 4\,\mathrm{s}^{-1}$ measured at $z/d = 0.5$ at different radii. Curves 1–4 correspond to $r = 0$, $r = d/2$, $r = 2d$ and $r = 3d$, respectively. The average flow velocities (V_θ, V_r) in mm/s are (0,0), (0.13, 0.19), (3.81, 1.17), (6.99, 0.89) for *curves* 1–4, respectively

One can learn from Fig. 10.23 that, as the measurement point moves away from the center, the characteristic frequencies of the fluctuations become higher. The most reasonable explanation for this is growth of the average azimuthal velocity $\bar{V}_\theta$, which was 3.81 mm/s and 6.99 mm/s, at $r = 2d$ and $r = 3d$, respectively. So, the fluctuations of the velocity in time at these two points are mainly due to fluctuations in space, which are advected by the large mean flow velocity $\bar{V}_\theta$. Applying the Taylor hypothesis, we can view the spectra in time as spectra in space, with the relation between the frequency and the wavenumber given by $k = 2\pi f/\bar{V}_\theta$. Then the power-law decay regions in curves 3 and 4 imply that the fluid motion is excited in the whole corresponding ranges of k. The ranges of the spatial scales where the motion is excited span about an order of magnitude for both curves. The exponents α in the power laws $P \sim f^{-\alpha}$ (and, so, $P \sim k^{-\alpha}$) are again quite large: about 3.6 for $r = 2d$ and about 3.3 for $r = 3d$ [10.104].

In a separate experiment the spatial velocity power spectra were measured by using PIV measurements. These were obtained by averaging 2000 instantaneous spatial spectra. Although the finite spatial resolution of PIV, which limits the accessible range of wavenumbers, leads to an artificial cutoff at $k \approx 3000\,\mathrm{m}^{-1}$, a power-law decay with $k^{-3.5}$ is clearly observed

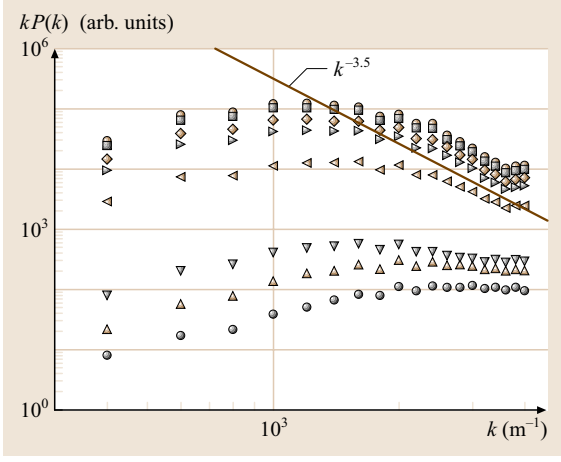

Fig. 10.24 Power spectra of fluctuations of azimuthal velocity component at different Wi. *Circles*: $Wi = 4.41$, *up triangles*: $Wi = 5.72$, *down triangles*: $Wi = 8.32$, *left triangles*: $Wi = 11.1$, *right triangles*: $Wi = 12.7$, *diamonds*: $Wi = 16$, *half filled squares*: $Wi = 18$, *empty circles*: $Wi = 19$. *Solid line* presents the power law decay $k^{-3.5}$. Data were collected in setup 1

(Fig. 10.24 [10.109]). This is rather consistent with the scaling obtained above for the velocity power spectra in the frequency domain. These large values of α imply that the power of the fluctuations decays very quickly as the size of the eddies decreases. The main contribution to fluctuations of both velocity and velocity gradients [the power of the latter should scale as $k^{-(\alpha-2)}$] should therefore be due to the largest eddies.

This also indicates that the Taylor hypothesis is applicable to this chaotic flow [10.108]. The agreement between the velocity spectra measured at a single point in the frequency domain [10.76, 104] and the directly measured spectra in the k-domain [10.109] deserves brief discussion. Following *Lumley* [10.110], the relation between the spatial spectrum, $P(k)$ and the frequency spectrum, $P(f)$ can be written as $P(k) = VP(f) - \frac{I_t^2}{2}\frac{\mathrm{d}^2(k^2P(k))}{\mathrm{d}k^2} + O(I_t^4)$, where $I_t = V_\theta^{\mathrm{rms}}/V_\theta$, $V_\theta^{\mathrm{rms}} \equiv \overline{V_\theta^2}_t^{1/2}$ and V_θ are the rms values of the fluctuations of the azimuthal velocity and the average azimuthal velocity, respectively. If $P(k) \propto k^{\alpha_2}$ and $P(f) \propto f^{\alpha_1}$, the equation above leads to: $\alpha_2 - \alpha_1 \propto \log[1 + \frac{I_t^2}{2}\alpha_2(\alpha_2+2)]/\log(k)$. If one inserts into the last equation $\alpha_2 \approx -3.6$, the difference between the exponents is (for $k \approx 1000\,\mathrm{m}^{-1}$) as small as $\alpha_2 - \alpha_1 \approx 0.2$. Thus, the experimental resolution does not allow us to observe the difference in the scaling exponents for the spatial and temporal spectra [10.109].

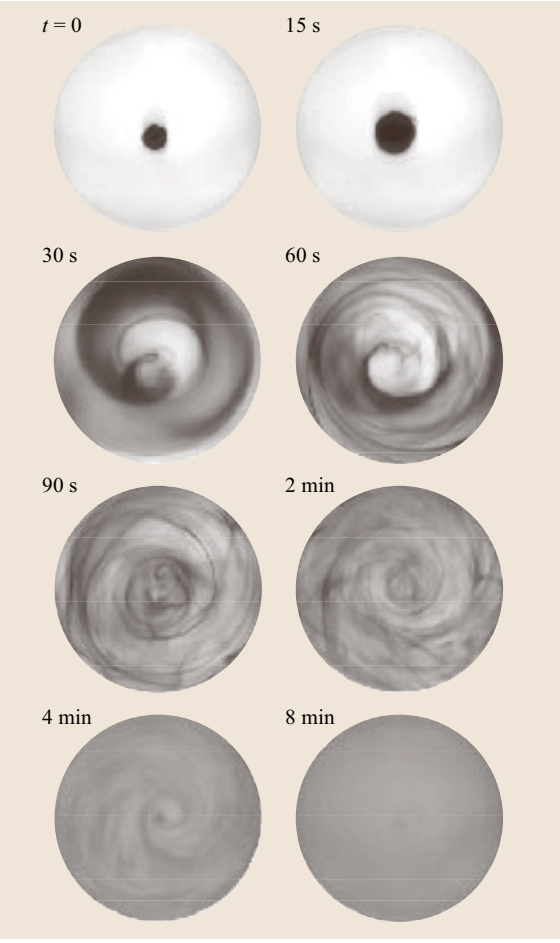

Fig. 10.25 Snapshots of consecutive stages of mixing of a droplet of ink in the polymer solution in the half-size setup, viewed from below. The area of the photographs corresponds to the area of the white upper plate. Rotation of the upper plate at $\Omega = 1.47\,\mathrm{s}^{-1}$ ($\dot{\gamma} = 5.6\,\mathrm{s}^{-1}$) was started suddenly at $t = 0$

Mixing in the Flow. Mixing in the flow was observed using a droplet of black ink added to the working fluid before rotation of the upper plate was started (Fig. 10.25). Using a micropipette the droplet was carefully placed near the center (at $r = 0$) at about half of the fluid depth. The ink was dissolved in a concentrated sugar syrup, to match the density of the droplet with the density of the working fluid.

Consecutive stages of mixing in the polymer solution are shown in Fig. 10.25.

Rotation of the upper plate was started abruptly at $t = 0$ at a shear rate of $\dot{\gamma} = 5.6\,\mathrm{s}^{-1}$. It took about one minute for the irregular flow to develop after the rotation of the upper plate was started. (Development of the irregular flow was judged by growth of the flow resistance, which was saturated after about one minute [10.111].) So, no significant changes in the ink distribution occurred during the first 15 s (Fig. 10.25). After 30 s the ink spread over the surface of the lower plate by the large toroidal vortex discussed above. In the snapshots taken at later times (60, 90, and 120 s in Fig. 10.25) one can see many fine-scale structures. Those may be due either to excitation of the fluid motion on small spatial scales or significant stretching of fluid elements along their Lagrangian trajectories by randomly fluctuating large-scale eddies. The contrast of the patterns gradually decreases with time, which indicates progressing mixing. The pattern in the last snapshot, taken 8 min after the flow had been started, appears completely homogeneous. From the appearance of the mixing patterns in Fig. 10.25, the characteristic time of mixing can be estimated as 120 s, corresponding to about 30 full turns of the upper plate. The time required for mixing by molecular diffusion

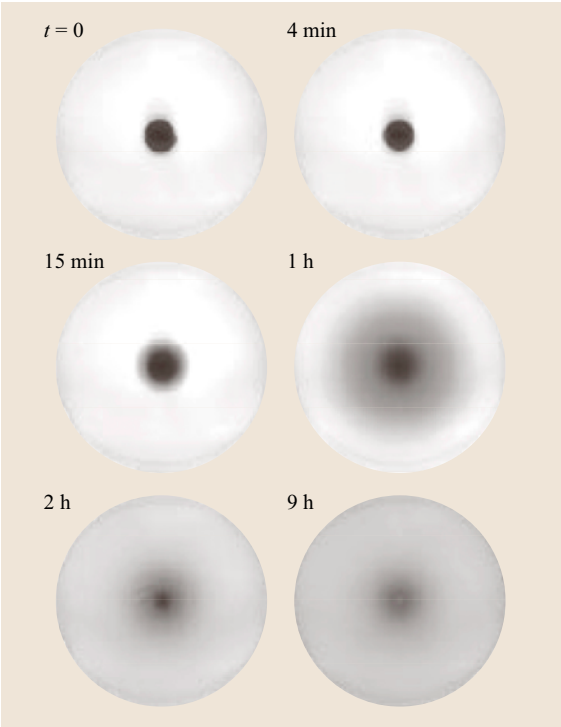

Fig. 10.26 Snapshots of consecutive stages of mixing of a droplet of ink in the pure solvent in the half-size setup, viewed from below. Rotation of the upper plate at $\Omega = 1.47\,\mathrm{s}^{-1}$ was started suddenly at $t = 0$

without macroscopic flow can be estimated as dR/D, which gives a value of about 10^6 s, i. e., at least four orders of magnitude larger than the mixing time observed in the flow [10.104].

Mixing in the flow of the pure solvent at the same shear rate is shown for comparison in Fig. 10.26.

One can see that the distribution of the ink remained inhomogeneous even after 9 h, although the ink became somewhat spread out the time. The Reynolds number was about 0.5, and there were some nonvanishing inertial effects in the flow [10.104].

Summarizing the experimental results, we conclude that the flow of the elastic polymer solution at sufficiently high Wi indeed has all the main features of developed turbulence stated above. The fluid motion is excited in broad ranges of frequencies and wavenumbers, both spanning about an order of magnitude. The flow is accompanied by a dramatic increase in the rate of transfer of momentum and mass. In terms of the strength of the turbulent resistance, the mixing rate, and the span of scales in space and time at which the fluid motion is excited, the observed flow can be compared to turbulence of a Newtonian fluid in a pipe at Re of about 10^5. This apparently turbulent fluid motion in the swirling flow between two plates arises at very low Re, where inertial effects are negligible, solely because of the nonlinear mechanical properties of the elastic polymer solution. We therefore call the phenomenon *elastic turbulence*. Distinctions between the elastic turbulence and the usual inertial turbulence observed in Newtonian fluids at high Re are discussed below.

Further Properties of Elastic Turbulence

Power Fluctuations and the Statistics of Injected Power. The injected power fluctuations were measured for different Wi in the elastic turbulence regime in two modes: Ω-forcing (Fig. 10.27) and T-forcing (Fig. 10.28). For each value of Wi the statistics of the power fluctuations were collected with 180 000 data points evenly sampled in time ($t_s \approx 0.038$ s). The time series of the injected power at different Wi for both modes are presented in both figures. In the elastic turbulence regime the probability distribution functions (PDFs) of the power fluctuations deviate strongly from the Gaussian distribution for both forcing modes. The PDFs in the Ω-forcing mode have a left-side skewness, while in the T-forcing mode they show a right-side skewness. Since the injected power fluctuations reflect fluctuations of the turbulent elastic stress averaged over the upper plate, one can conclude that the statistics of the elastic stress deviate strongly from Gaussian statistics and are therefore intermittent. The Wi dependencies of both P/P_{rms} (Fig. 10.21) the skewness of the PDF in elastic turbulence suggest an analogy with similar behavior in hydrodynamic turbulence, though the reasons for the effects are entirely different [10.112, 113].

Flow Structure and Velocity Profiles. To characterize the structure of the velocity field and velocity profiles flow visualization (PIV and LDV) techniques were used in various experiments and setups [10.104, 108, 109]. An impression of the flow structure in elastic turbulence can be obtained from just a few snapshots of the flow, visualized by seeding with light-reflecting flakes (1% of Kalliroscope liquid). The upper plate was black, so the bright regions indicate where the flakes are oriented parallel to the upper plate. The patterns of the polymer solution flow above the transition at $Wi = 6.5$ (Fig. 10.29a, b), and at $Wi = 13$ (Fig. 10.29c, e), appear quite irregular and exhibit structures of different sizes. One can see, however, that the structures tend to have a spiral-like form, which is probably imposed

by the average azimuthal flow and circular symmetry of the setup. Further, there is a dark spot in the middle, which appears in most of the snapshots. This corresponds to the center of a large, persistent toroidal vortex, which has dimensions of the whole setup (see also below). The direction of vortical motion was inwards near the upper plate, downwards near the center and outwards near the lower plate [10.104]. The average flow velocity along the radial direction was measured by LDV at a few points, and the results agreed quite well with the presence of the large, persistent toroidal vortex. The flow of the pure solvent at the same shear rate was completely laminar, as can be seen from the snapshot in Fig. 10.29f, which appears quite uniform [10.104].

Quantitative characterization of the global flow structure and its dynamics was obtained via PIV. Instantaneous images of fields of the horizontal components of the velocity as well as averaged images over 2000 fields taken equidistant between the plates in setup 1 for several values of Wi are presented in Fig. 10.30, 31. The left column in Fig. 10.30 shows the instantaneous vector fields at three increasing values of Wi, while the right column shows the averaged vector field at the same Wi values. One can easily identify the core of the toroidal vortex, which appears in all the images above the thresh-

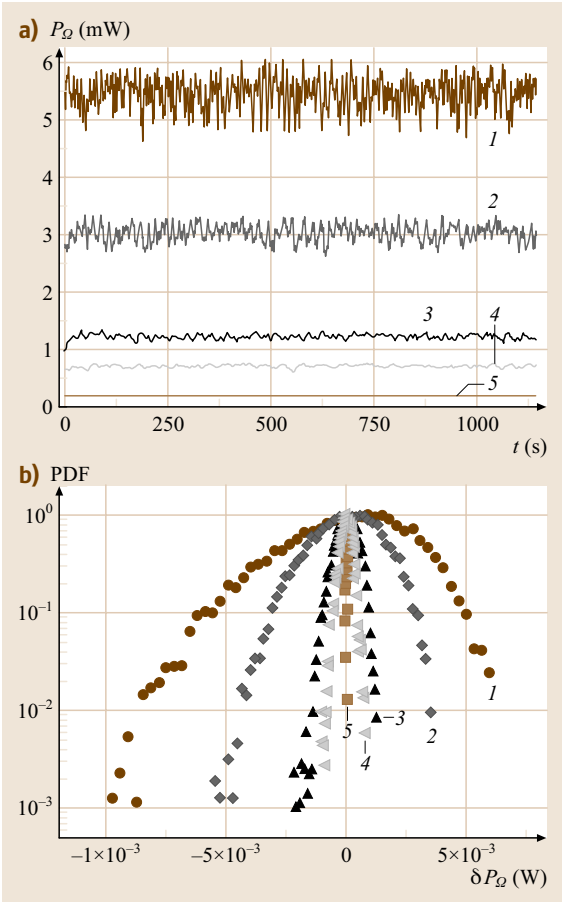

Fig. 10.27 **(a)** Time series (partially shown) of the injected power in the constant Ω-forcing regime for different Wi. **(b)** PDF of the power fluctuations in constant Ω forcing regime for different Wi. The curves are: (5) $Wi = 5$, (4) $Wi = 19$, (3) $Wi = 24$, (2) $Wi = 31.5$, (1) $Wi = 40$. Data were collected in setup 2

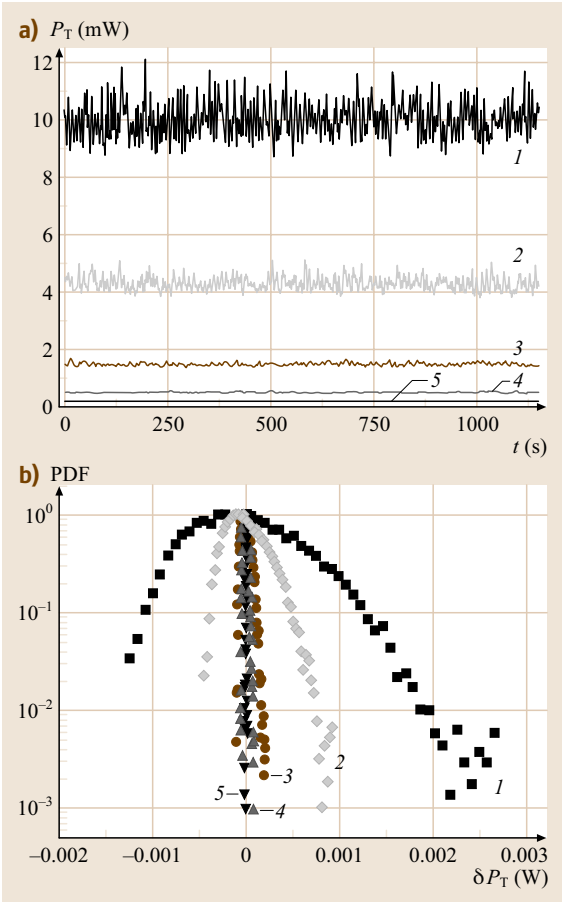

Fig. 10.28 **(a)** Time series (partially shown) of the injected power in constant T forcing regime for different Wi. **(b)** The PDF of the power fluctuations in the constant T-forcing regime for different Wi. The curves are: (5) $Wi = 5$, (4) $Wi = 17$, (3) $Wi = 25$, (2) $Wi = 34$, (1) $Wi = 46$. Data were collected in setup 2

old for the instability, and a spiral vortex that in addition occurs in the elastic turbulence regime. These flow structures and their reorganization can also be observed in separate presentations of the averaged azimuthal, radial components, and rms of fluctuations of the azimuthal velocity component of the velocity field at the same Wi (Fig. 10.31, 32). The profile of the average azimuthal velocity V_θ below the elastic instability exhibits a linear increase along a radius with a slope, Ω^{-1}, that corresponds to rigid-body rotation (inset in Fig. 10.33a), while there is no motion in the radial direction, $V_r \approx 0$ (Fig. 10.33b). Above the instability one can clearly see the creation of the core of the toroidal vortex at the cell center, and restructuring in the radial motion [10.109].

The large, toroidal vortex driven by the hoop stress is actually quite well known in swirling flows of elastic fluids [10.78, 114], and inhomogeneity of the shear-rate profile in the primary laminar flow has long been recognized as the origin of this phenomenon. In our system this vortex first arises as a stationary structure at low shear rates. As can be learned from Fig. 10.20 (curve 1 at $\dot{\gamma} < 0.75\ s^{-1}$ and curve 2 at $\dot{\gamma} < 0.4\ s^{-1}$), the toroidal vortex leads to some increase in the flow resistance even before the elastic instability, so we can conclude that the transition to elastic turbulence in the swirling flow between two plates is mediated by this vortex. The toroidal vortex provides a smooth, large-scale velocity field (see the right-hand panels in Fig. 10.30), which is randomly fluctuating in time (left-hand panels in Fig. 10.30), and in which the fluid and the embedded stress tensor are chaotically advected. This type of advection can create variations of the stress over a range of smaller scales, which may cause small-scale fluid motion [10.115, 116]. This would be analogous to generation of small-scale concentration variations in chaotic mixing by large fluctuating vortices.

The large-scale toroidal vortex is also responsible for the ring-shaped topology of fluctuations of the azimuthal velocity $V_\theta^{\mathrm{rms}} \equiv \overline{V_\theta^2}^{1/2}$ (Fig. 10.32). The velocity fluctuations in the laminar regime are only due to

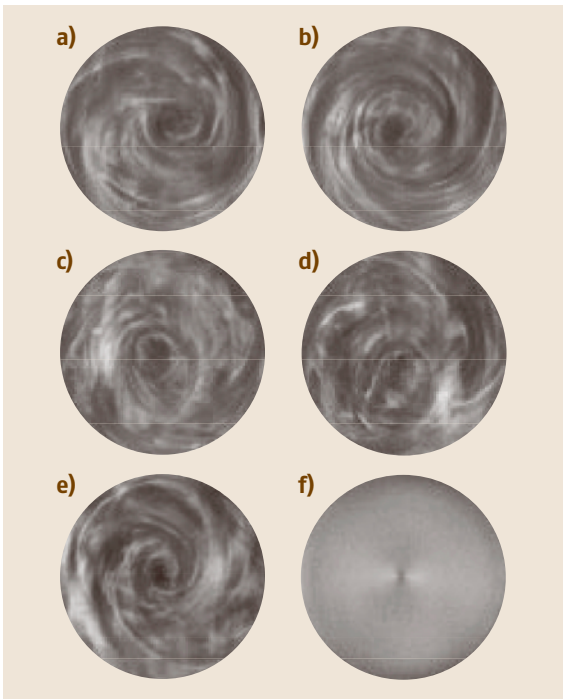

Fig. 10.29a–f Representative snapshots of the flow taken from below. The field of view corresponds to the upper plate area. The flow was visualized by seeding the fluid with light-reflecting flakes. **(a)**, **(b)** the polymer solution at $Wi = 6.5$, $Re = 0.35$; **(c)**, **(d)**, **(e)** the polymer solution at $Wi = 13$, $Re = 0.7$; **(f)** the pure solvent at $Re = 1$

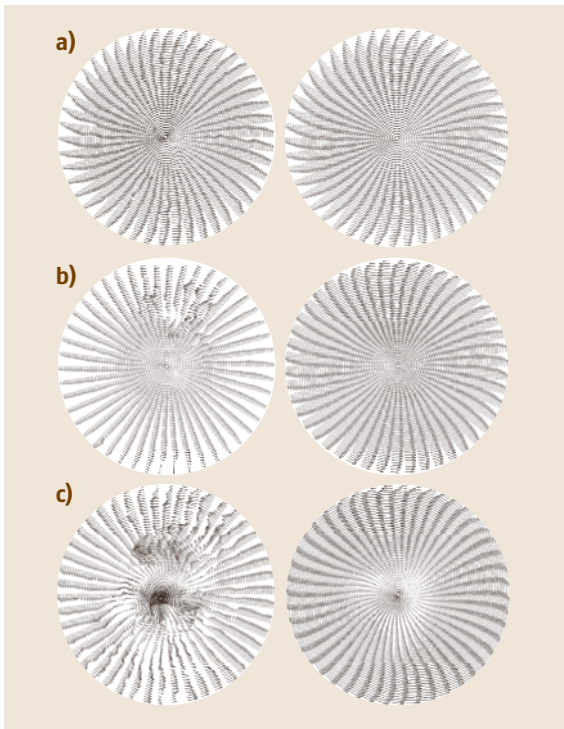

Fig. 10.30a–c Instantaneous (*left column*) and time-averaged (*right column*) velocity fields for different values Wi: **(a)** $Wi = 2.48$ **(b)** $Wi = 9.88$ **(c)** $Wi = 18.96$. Data were collected in setup 1 at the mid distance between the plates

instrumental noise, which does not exceed 5% of the average value (panel a in Fig. 10.32). The average radial velocity changes sign at about half of the radius (see Fig. 10.33b). At higher value of Wi the toroidal vortex forces a transition to elastic turbulence, which is characterized by the second flow structure reorganization to the spiral vortex (Fig. 10.30, 31) and the scaling region in P, $P_{\rm rms}$ (Fig. 10.21). At the same time the circular symmetry of $V_\theta^{\rm rms}$ is broken and becomes dipolar (Fig. 10.32). The radial profiles of V_θ and V_r also change drastically. These structural transitions in the flow are also reflected in the average radial gradients of the azimuthal velocity field and its average vorticity field, which are presented in Fig. 10.34 for several values of Wi.

To learn more about the velocity field generated by elastic turbulence, we measured the average velocity and rms of the velocity fluctuations at different points. Profiles in the z-direction of the average azimuthal velocity $\overline{V}_\theta$ and of the rms fluctuations $V_\theta^{\rm rms}$ at different flow conditions are shown in Fig. 10.35 [10.104].

The measurements were done at $r = 2d$, which is rather far from the edge of the upper plate ($R - r = 1.8d$). The profile of $\bar{V}_\theta$ in a low-Re flow of the pure solvent is an almost straight line (Fig. 10.35, curve 3). The elasticity-driven turbulent flow significantly changes the distribution of $\bar{V}_\theta$. It produces a high-shear-rate layer near the upper plate (Fig. 10.35 curve 1), and a low-shear-rate region near the middle of the gap (at $z/d = 0.5$). Such a distribution of $\bar{V}_\theta$ is reminiscent of the average velocity profiles in usual high-Re turbulence. The perturbation of the $\bar{V}_\theta$ profile becomes stronger when $\dot{\gamma}$ is increased (Fig. 10.35, curve 2). In particular, the slope of the $\overline{V}_\theta$ curve at small z/d becomes larger, which obviously corresponds to growth of $\tau_{\rm w}/\tau_{\rm w}^{\rm lam}$ with $\dot{\gamma}$ (Fig. 10.20).

Fluctuations of the azimuthal velocity (curve 4 in Fig. 10.35) are small near the upper plate, reach a maximum at $z/d \simeq 0.25$, and start to decrease at larger z. Again, such a distribution of $V_\theta^{\rm rms}$ along the z-direction is reminiscent of the velocity fluctuations in turbulent flows of Newtonian fluids [10.79, 80]. The rms fluctuations reach a value of about $0.5d/\lambda$, so that the rate of deformation produced by the fluctuating velocity field is on the order of $1/\lambda$. That implies an essentially nonlinear relation between the rate of deformation and the fluctuating elastic stress. The maximal rms value of the velocity fluctuations at $\dot{\gamma} = 4\,{\rm s}^{-1}$ was about 1.55 mm/s, which was about 7.5% of the upper-plate velocity ($V_{\rm max}$) at $r = 2d$ and about 25% of the local value of $\overline{V}_\theta$ [10.104].

Another way to characterize a turbulent flow is to display the radial profiles (azimuthally averaged) of the turbulent intensity, defined as $I_t = V_\theta^{\rm rms}/V_\theta$ at several values of Wi (Fig. 10.36) [10.109]. The velocity fluctuations in the laminar regime occur only due to instrumental errors and do not exceed 5% of the mean values. Above the elastic transition, $I_{\rm t}$ increases sharply but remains rather uniform at 20–30% in a peripheral region for radius ratios $r/R_{\rm C}$ of 0.2–1 (see Fig. 10.36). In the case of elastic turbulence, $I_{\rm t}$ further increases, and its dependence on Wi, presented in the inset in Fig. 10.36, exhibits a power-law scaling, $I_t \sim Wi^{0.49}$ [10.109].

The PIV measurements of the time-dependent velocity fields allowed us to calculate the average velocity gradients and vertical vorticity, and their rms fluctuations without involving the Taylor hypothesis, which is questionable in a smooth, random flow. Typical radial distribution of the velocity gradients and vorticity averaged in an azimuthal direction spatially and over 2000 images temporally is rather uniform in the bulk for all Wi but increases sharply near the wall (Fig. 10.37), while the rms of the velocity gradients and vorticity gradually increase along a radius (Fig. 10.38). The dependence of the average vertical vorticity on Wi is displayed in

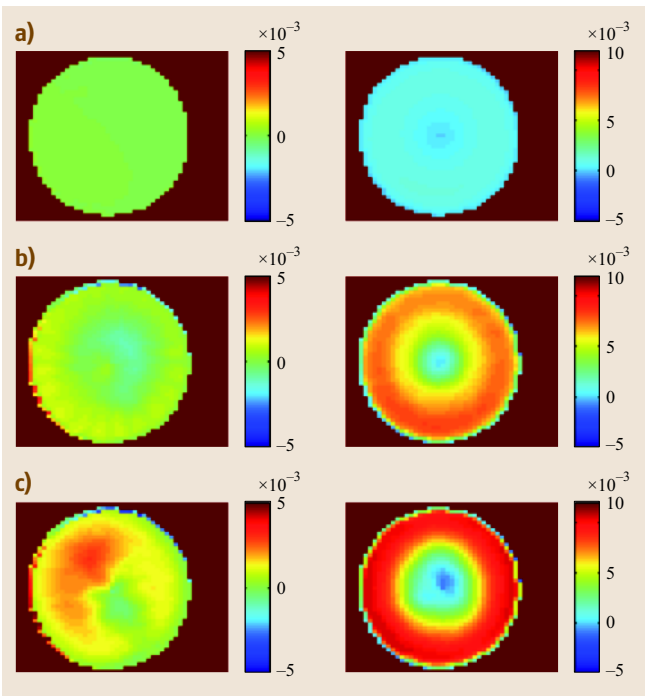

Fig. 10.31a–c Distribution of the radial (*left column*) and the azimuthal velocity components (*right column*) for different values of Wi: **(a)** $Wi = 2.48$, **(b)** $Wi = 9.88$, **(c)** $Wi = 18.96$. Data were collected in setup 1 at the mid distance between the plates

Fig. 10.37a, exhibiting a tendency to saturation at higher Wi for vorticity in the bulk and gradual growth near the wall. On the other hand, the rms of the vorticity fluctuations definitely level off at $Wi > 15$. A similar behavior is displayed by all components of the velocity gradient, which is consistent with theoretical predictions, though the saturated value $\omega_z^{\mathrm{rms}}\lambda \approx 2.5$ is rather high [10.115, 116] (see further discussion of this issue below). The relation between the rms fluctuations of the velocity gradients and the Eulerian correlation time will be discussed in the next section.

Velocity and Velocity Gradient Fields Statistics and Wi Dependence. Characteristic probability distribution functions (PDFs) of the azimuthal component of the flow velocity in the regime of elastic turbulence are shown in Fig. 10.39. A similar PDF was found for the radial velocity component [10.104]. These distributions were obtained from LDV measurements taken at $r = 2d$, $z = 0.25d$ at a shear rate of $4\,\mathrm{s}^{-1}$. One can see that the distribution has only minor skewness and is very nearly Gaussian.

The PDF for the gradients of velocity (rates of deformation) in the azimuthal direction (and similarly for transverse), obtained from the same LDV time series, is shown in Fig. 10.40. The rates of deformation are multiplied by the relaxation time λ to make them dimensionless. The velocity gradients were estimated using the Taylor hypothesis, with smoothing over a distance of about 1.45 mm. The difference ΔV between consecutive velocity readings with even time intervals of $\Delta t = 0.22\,\mathrm{s}$ was divided by Δt and by the average velocity $\overline{V} = (\overline{V}_\theta^2 + \overline{V}_r^2)^{1/2} = 6.6\,\mathrm{mm/s}$. One can see that the distribution of $\partial V_\theta / r\partial\theta$ (as well as $\partial V_r / r\partial\theta$) cannot be fitted by a Gaussian curve [10.104]. In contrast to the velocity distribution in Fig. 10.39, the PDF in Fig. 10.40 has a well-pronounced exponential tail, which implies significant intermittency of the velocity gradients. The situation of nearly Gaussian statistics of velocities and essentially non-Gaussian, strongly intermittent distributions of velocity gradients is actually quite typical for high-Re inertial turbulence [10.117]. Hence, the elastic turbulence also resembles high-Re inertial turbulent flows in this respect.

The statistical properties of elastic turbulence can be characterized in many ways. Besides the PDF of the local velocity and velocity gradients and the power spectrum of velocity fluctuations in the frequency and wavenumber domains, one can calculate various correlation and structure functions of the velocity and velocity gradients. Their scalings can give information on the degree of deviation from a Gaussian random field, a standard approach in hydrodynamics to quantify intermittency and to compare it with the corresponding scaling in known cases. First, let us find typical spatial and temporal correlation scales in the elastic turbulence.

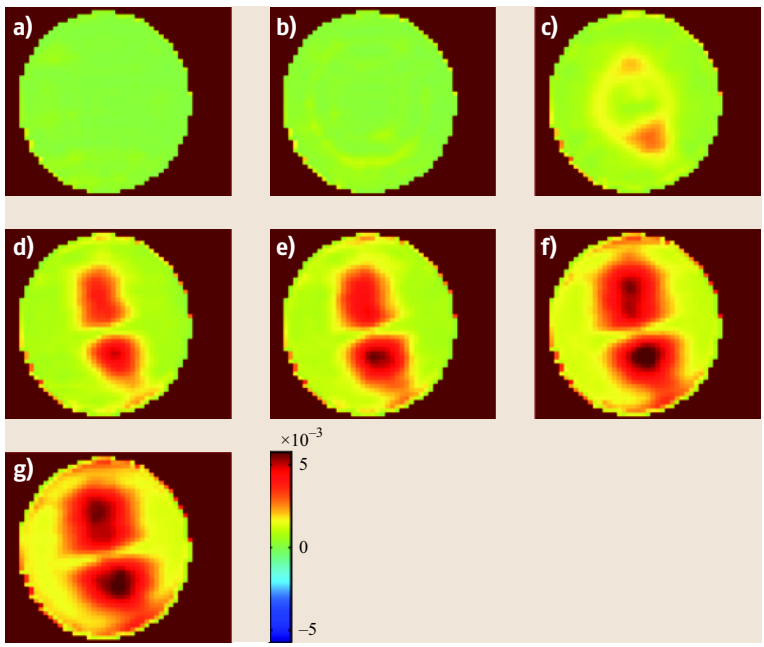

Fig. 10.32a–g Fields of fluctuations of the azimuthal velocity at different Wi: **(a)** $Wi = 8.32$, **(b)** $Wi = 9.88$, **(c)** $Wi = 11.1$, **(d)** $Wi = 12.72$, **(e)** $Wi = 13.83$, **(f)** $Wi = 17$, **(g)** $Wi = 19$. Data were collected in setup 1 at the mid distance between the plates

A typical scale on which the elastic stress is correlated can be estimated as $L = 2\pi \int P(k)\mathrm{d}k / \int kP(k)\mathrm{d}k$ and in the elastic turbulence regime one gets $L \simeq 5.9\,\mathrm{cm}$, i. e., on the order of the cell size. The Eulerian correlation time is defined as $\tau_c = \int tC(t)\mathrm{d}t / \int C(t)\mathrm{d}t$, where $C(t) = \overline{V(T)V(T+t)}/v^{\mathrm{rms}}v^{\mathrm{rms}}$ is the Eulerian correlation function. Figure 10.41 presents τ_c as a function of Wi at some radial positions in the cell. The correlation time drops significantly in the transition region and then saturates in the elastic turbulence region similar to the rms of the vorticity (velocity gradients) fluctuations. It is worth pointing out that the inverse of the saturated value of the correlation time is of the order of the saturated value of ω_z^{rms} and λ^{-1}, as expected by theory [10.115, 116].

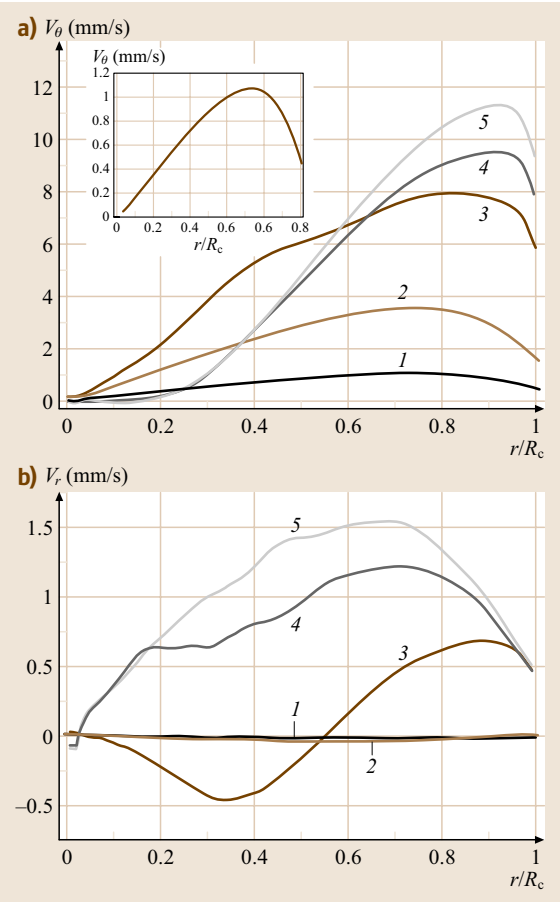

Fig. 10.33 **(a)** Profiles of the average azimuthal velocity V_θ for several values of Wi. The *inset* shows a typical laminar profile of the azimuthal velocity component. **(b)** Profiles of the average radial velocity V_r for several values of Wi. The curves are: (1) $Wi = 2.48$, (2) $Wi = 4.41$, (3) $Wi = 11.1$, (4) $Wi = 15$, (5) $Wi = 18$. Data were collected in setup 1 at the mid distance between the plates

Using PIV data one can also calculate the structure functions of the velocity gradients defined as $S_p(r) = \langle |\frac{\partial V_\theta(r_0+r)}{\partial r} - \frac{\partial V_\theta(r_0)}{\partial r}|^p \rangle_{r_0}$. Similar to inertial turbulence, let us look for a scaling in the range of scales corresponding to the power-law decay of the velocity spectra (Fig. 10.24) in the form $S_p(r) = r^{\zeta_p}$. The dependence of the scaling exponent ζ_p on the order of the structure functions p is presented in Fig. 10.42. The deviation from a linear dependence that is characteristic to the Gaussian field is clearly observed and is rather close to the analogous dependence for a passive scalar [10.118]. The relation between the passive-scalar problem and the statistics of the velocity gradient are discussed in the next subsection.

As noted in Sect. 10.3.1 on flow resistance, the comparison of the velocity power spectra in the frequency and wavenumber domains leads to the conclusion that the Taylor hypothesis is applicable in spatially smooth random-in-time flows, a representative of which is elastic turbulence. On the other hand, from Fig. 10.35 one learns that, in the cell interior at $r/R_c < 0.2$, the rms velocity fluctuation becomes much larger that the mean velocity, which casts doubt on the applicability of the Taylor hypothesis. The validity of the Taylor hypothesis in this flow was investigated experimentally in detail [10.108]. By using cross-correlation technique as well as the structure function approach, it was shown that the breakdown of the Taylor hypothesis occurs near the cell center due to strong velocity fluctuations, while the flow smoothness and the lack of scale separations in the elastic turbulence limit the quantitative applicability of the Taylor hypothesis close to the boundaries. However, the latter deficiency can be corrected by a proper choice of the advection velocity [10.108].

Role of the Elastic Stress and Theory of the Elastic Turbulence

Along with the apparent similarity in phenomenology between the elastic and inertial turbulence, there are also a few important distinctions, which are reflected in the dependence of the onset of elastic instability and the scaling of the main characteristics of elastic turbulence with system size and fluid viscosity. These results were found to be in sharp contradiction with the corresponding dependence in Newtonian fluid mechanics but quite in line with the concept of viscoelastic similarity suggested for purely elastic instability [10.88]. As was shown in [10.89], an increase in the viscosity

of the solvent should lead to a transition to elastic turbulence at lower velocity, a prediction that was verified experimentally [10.104]. When the size of the setup is proportionally reduced, the velocity required for excitation of elastic turbulence should increase. This property was examined in setups twice and four times smaller than the main one [10.104]. Transition to the elastic turbulence is expected to occur at the same characteristic stress, and its dependence on Wi is supposed to be the same for all system sizes, as was also verified experimentally [10.104]. The equivalence of the statistical properties of the velocity field and the mixing patterns in elastic turbulence has also been demonstrated [10.104].

An obvious reason for the differences in the scalings in inertial and elastic turbulence is the different physical mechanisms that underlie these two kinds of turbulent motion. As is well known, the high flow resistance in high-Re inertial turbulence is due to large Reynolds stresses. The Reynolds stress tensor is defined as the average value $\rho\langle V_i V_j\rangle$, where V_i and V_j are different components of the flow velocity. In the case of elastic turbulence the Reynolds stresses are quite small, since Re is low. So, the high flow resistance in elastic turbulence is due to a large elastic stress, τ_p [10.111]. Therefore, one can suggest that in the case of elastic turbulence it would be more relevant to study the field of stresses and of rates of deformations rather than the velocity field. It would certainly be quite instructive to explore the spatial structure and temporal distribution of the elastic stress, but there is currently no technique for local measurements of τ_p in a turbulent flow. On the other hand, large-scale properties of the τ_p field can be inferred from measurements of the torque or injected power.

It is now widely accepted that the statistical properties of a random flow in the elastic turbulent regime and significant increase in the contribution of the polymer stresses to the flow resistance are associated with significant polymer stretching in a random flow. To support this theoretical vision, experimental studies of polymer stretching in a 3-D random flow between two plates were conducted in macro- and microscale setups [10.111, 119]. The first experiment was performed in a swirling flow setup with a high aspect ratio of $R/d = 1$, where $R = 30\,\text{mm}$, and with a very viscous solvent, $\eta_s = 1.36\,\text{Pa s}$ to suppress inertia [10.111]. By experimental analysis and estimates of the contributions of the Reynolds, viscous, and elastic stresses to the shear stress on the upper plate, we found that the Reynolds stress constitutes less than 0.1% of the total stresses, and that the viscous stress is rather constant. So, as a result of a secondary random 3-D flow superimposed on a primary applied shear flow between two plates, the polymer contribution to the shear stress increases by

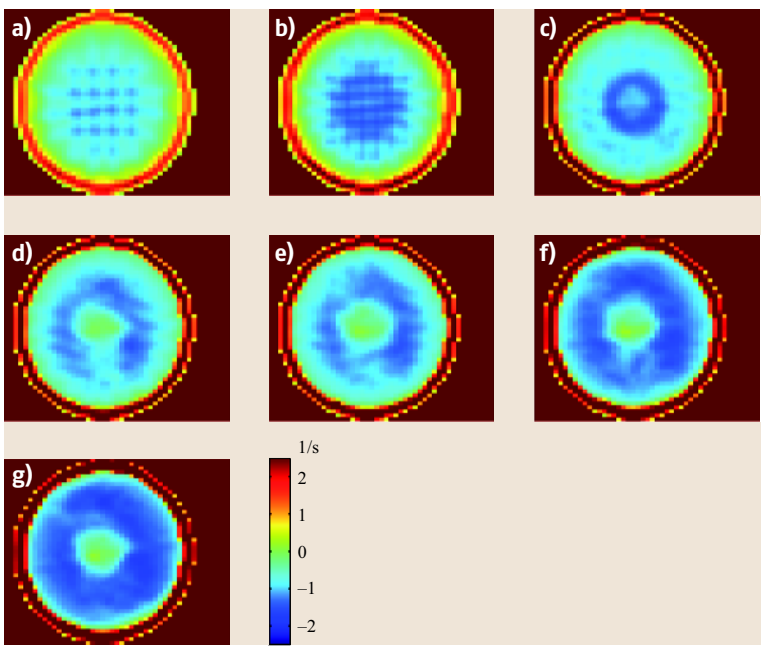

Fig. 10.34a–g The average vertical component of the vorticity ω_z at different Wi: **(a)** $Wi = 8.32$, **(b)** $Wi = 9.88$, **(c)** $Wi = 11.1$, **(d)** $Wi = 12.72$, **(e)** $Wi = 13.83$, **(f)** $Wi = 17$, **(g)** $Wi = 19$. Data were collected in setup 1 at the mid distance between the plates. The *squared pattern* visible in panels **(a,b)** is a result of the combination of the peak-locking effect and numerical differentiation and should be disregarded

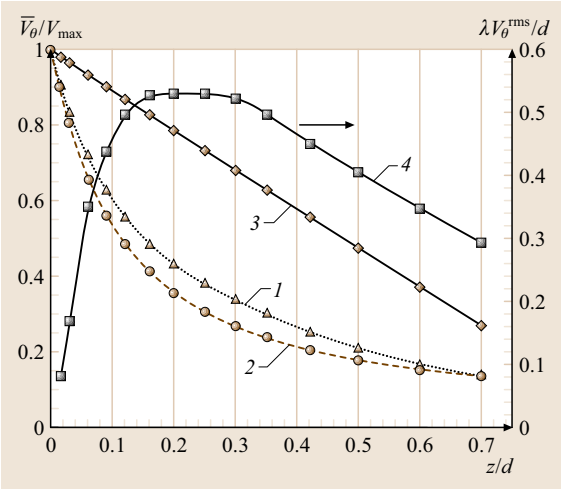

Fig. 10.35 Average azimuthal velocity $\overline{V}_\theta$ (y-axis on the *left, curves* 1–3), and rms fluctuations of the azimuthal velocity V_θ^{rms} (y-axis on the *right, curve* 4), as functions of the distance z from the upper plate. The measurements were done at $r = 2d$. The average velocities are divided by the upper plate velocity at $r = 2d$. *Curve* 1: polymer solution at $\dot{\gamma} = 2.7\,s^{-1}$; *curves* 2,4 polymer solution at $\dot{\gamma} = 4\,s^{-1}$ (Fig. 10.21, 22, 23, 26); *curve* 3 pure solvent at $\dot{\gamma} = 4\,s^{-1}$, $Re \simeq 1.2$. The rms velocity fluctuations in the polymer solution (*curve* 4) is multiplied by λ/d to make it dimensionless

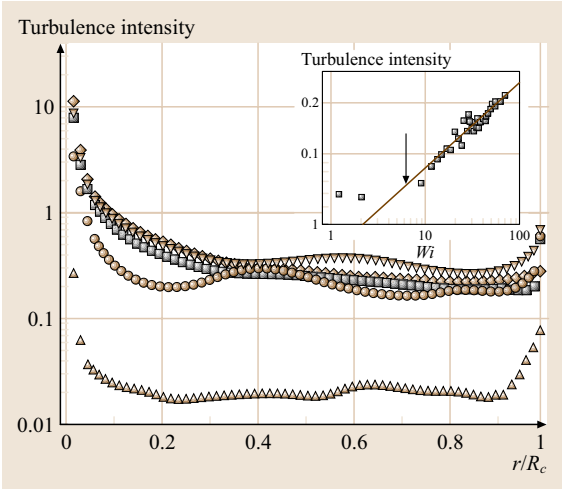

Fig. 10.36 Turbulence intensity versus the reduced radial coordinate at different Wi. *Rhombus*: $Wi = 31.56$, *squares*: $Wi = 27.73$, *down triangles*: $Wi = 23.67$, *circles* $Wi = 7.54$, *up triangles*: $Wi = 2.82$. The *inset* shows the dependence of the turbulence intensity on Wi at $r/R_c = 0.85$ obtained from LDV measurements. The *full line* is a power-law fit $I_t \propto Wi^{0.49\pm0.06}$. The *arrow* indicates the onset of the elastic instability. The data were collected in setup 2

as much as 170 times. If one assumes linear elasticity of the flow-stretched polymer molecules (PAA), then the elastic stress causes a 13-fold polymer extension [10.111].

Thus, the first logical step in theoretical exploration of the whole problem of turbulent hydrodynamics of a dilute polymer solution was to describe a single polymer stretching in a random flow. More than 30 years ago *Lumley* [10.110] first suggested a semiquantitative theory for polymer stretching in a random flow. Since then, numerous publications on theoretical as well as numerical calculations of mean polymer extension in a stochastic flow as a function of Wi with the aim of qualitatively verifying the predicted coil-stretch transition have been published [10.120–122]. However, the statistics of a random flow was not related to the statistics of the polymer extension in these works. Recently Lumley's theory was revised, and a quantitative theory of the coil-stretch transition of a polymer molecule in a 3-D random flow was developed [10.123, 124]. The dynamics of a polymer molecule are sensitive to fluid motion at the dissipation scale, where the velocity field is spatially smooth and random in time [10.110]. On this scale polymer stretching is determined only by the velocity gradient tensor, $\nabla_i V_j$, which varies randomly in time and space: $\partial_t R_i = R_j \nabla_j V_i - R_i/\lambda(R) + \zeta_i$. Here R_i is the end-to-end vector and R is the end-to-end distance for the stretched polymer molecule, respectively, $\lambda(R)$ is the polymer relaxation time, which is R-dependent, and ζ_i is the thermal noise. At $R \ll R_{max}$ the linear regime of polymer relaxation is characterized by the polymer relaxation time $\lambda_{rel} = \lambda(0)$, where R_{max} is the maximum end-to-end stretched polymer length. At $R \gg R_g$ one can use, e.g., the FENE (finitely extensible, nonlinear elastic) model with $\lambda(R) = \lambda(0)(1 - R^2/R_{max}^2)$. In a 3-D random flow $\nabla_i V_j$ always has an eigenvalue with a positive real part, so that there exists a direction with a pure elongation flow [10.125]. The direction and rate of the elongation flow change randomly as a fluid element rotates and moves along the Lagrangian trajectory. If $\nabla_i V_j$ remains correlated within finite time intervals, the overall statistically averaged stretching of the fluid element will increase exponentially fast in time. The rate of stretching is defined by the maximal Lyapunov exponent α of the turbulent flow, which is the average

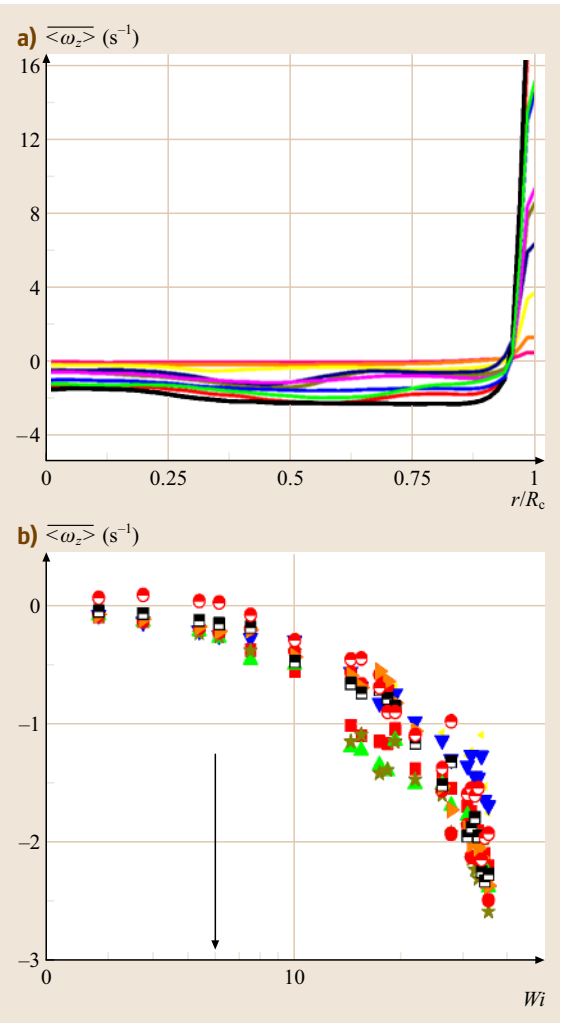

Fig. 10.37 **(a)** Profiles of the vorticity $\langle\omega_z\rangle$ averaged in an azimuthal direction spatially and over 2000 images temporally at different Wi: black-$Wi = 34.5$, red-$Wi = 32.3$, green-$Wi = 27.73$, blue-$Wi = 26.13$, magenta-$Wi = 19.29$, dark yellow-$Wi = 17.43$, dark blue-$Wi = 14.48$, yellow-$Wi = 10$, orange-$Wi = 5.4$, pink-$Wi = 2.82$ **(b)** The dependence of the average vorticity on Wi at different radial positions. *Squares*-$r/R_c = 0.33$, *circles*-$r/R_c = 0.66$, *up triangles*-$r/R_c = 0.4$, *down triangles*-$r/R_c = 0.2$, *left triangles*-$r/R_c = 0.1$, *right triangles*-$r/R_c = 0.7$, *stars*-$r/R_c = 0.5$, *half-filled squares*-$r/R_c = 0.8$, *half-filled circles*-$r/R_c = 0.9$. The *arrow* indicates the onset of the elastic instability. Data were collected in setup 2

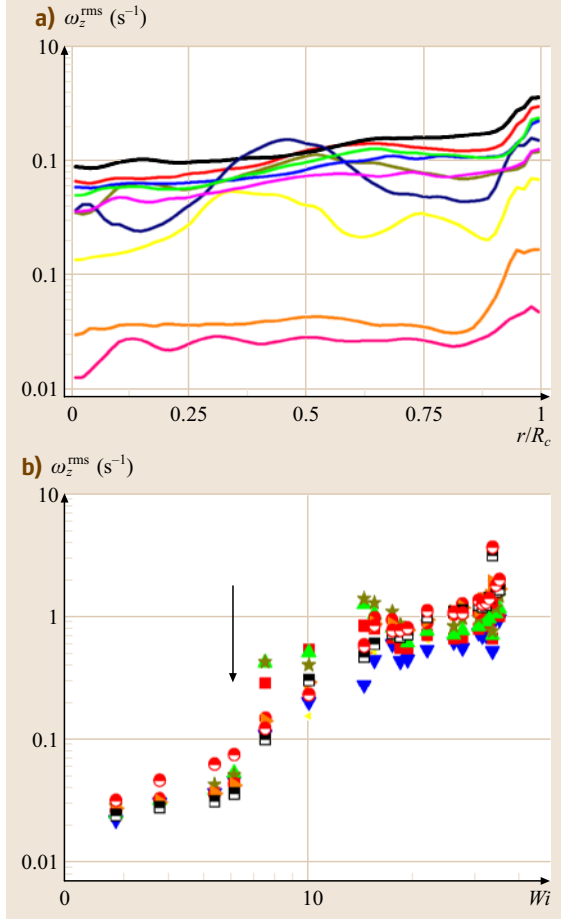

Fig. 10.38 **(a)** Profiles of the rms fluctuations of the vorticity ω_z^{rms} at different Wi: black-$Wi = 34.5$, red-$Wi = 32.3$, green-$Wi = 27.73$, blue-$Wi = 26.13$, magenta-$Wi = 19.29$, dark yellow-$Wi = 17.43$, dark blue-$Wi = 14.48$, yellow-$Wi = 10$, orange-$Wi = 5.4$, pink-$Wi = 2.82$. **(b)** Dependence of the rms of fluctuations of the vorticity on Wi at different radial positions. *Squares*-r/R_c=0.33, *circles*-$r/R_c = 0.66$, *up triangles*-$r/R_c = 0.4$, *down triangles*-$r/R_c = 0.2$, *left triangles*-$r/R_c = 0.1$, *right triangles*-$r/R_c = 0.7$, *stars*-$r/R_c = 0.5$, *half-filled squares*-$r/R_c = 0.8$, *half-filled circles*-$r/R_c = 0.9$. The *arrow* indicates the onset of the elastic instability. Data were collected in setup 2

logarithmic rate of separation of two initially close trajectories, where the value of α is usually on the order of the rms of the fluctuations of the velocity gradient, $\left(\frac{\partial V_i}{\partial r_j}\right)^{rms} \equiv \overline{\left(\frac{\partial V_i}{\partial r_j}\right)^2}^{1/2}$. Stretching of a polymer molecule follows deformation of the surrounding fluid element. So the statistics

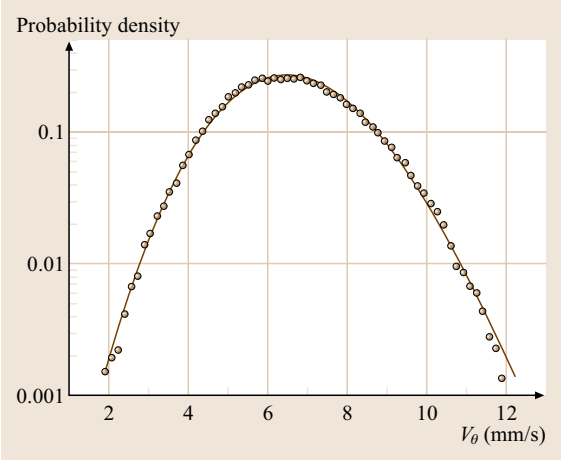

Fig. 10.39 Probability distribution functions (PDF) of the azimuthal flow velocity V_θ measured at $r = 2d, z = d/4$, and $\dot{\gamma} = 4\ \mathrm{s}^{-1}$ (*circles*). The *solid line* represents the Gaussian fit with some skew

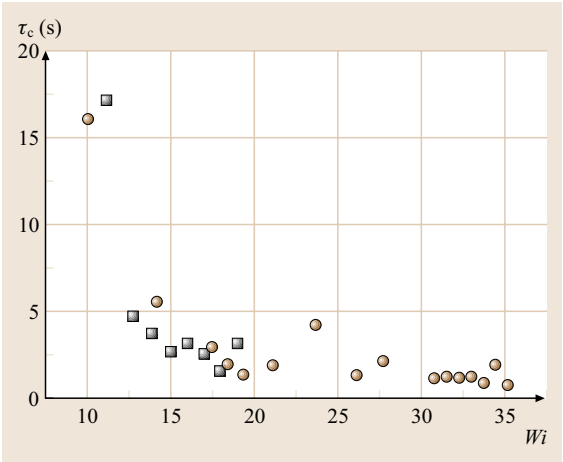

Fig. 10.41 Eulerian correlation times of the azimuthal velocity component as function of Wi. *Squares*: setup 1, *circles*: setup 2

of polymer stretching in a random, smooth flow depends critically on the value of $\lambda\alpha$ [or equivalently $\lambda \left(\partial V_i/\partial r_j\right)^{\mathrm{rms}}$], which plays the role of a local Weissenberg number for a random flow, Wi'. According to the theory [10.110, 123], the polymer molecules should become vastly stretched if the condition $\lambda\alpha > 1$ is fulfilled, and the coil-stretch transition is defined by the relation $\lambda_{\mathrm{cr}}\alpha = 1$, similar to that in an elongation flow with the strain rate α [10.126]. A somewhat surprising conclusion of the theory is that a generic random flow is on average an extensional flow at every point, with the rate of extension $\dot{\varepsilon} = \alpha$ and unlimited Henky strain. Dramatic extension of the flexible polymer molecules in the turbulent flow environment, inferred here from the bulk measurements of the flow resistance, has recently been confirmed by direct visualization of individual polymer molecules in a random flow [10.119]. According to the recent theory [10.123], the tail of the

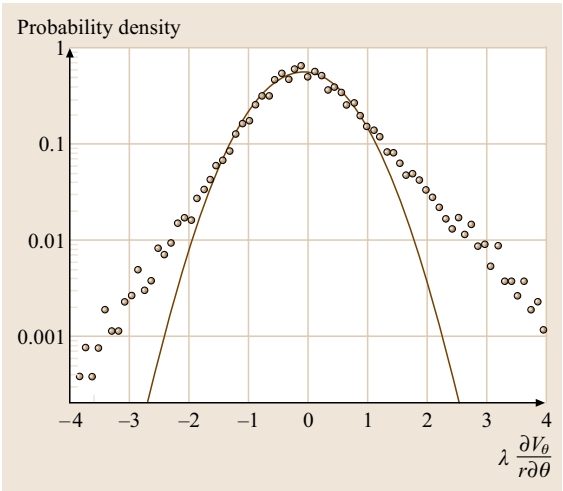

Fig. 10.40 Probability distribution functions (PDF) of the longitudinal velocity gradient, $\frac{\partial V_\theta}{r\partial\theta}$ measured at $r = 2d, z = d/4$ and $\dot{\gamma} = 4\,\mathrm{s}^{-1}$ (*circles*). The velocity gradients are made dimensionless by multiplication by the relaxation time λ. The *solid line* represents a Gaussian fit

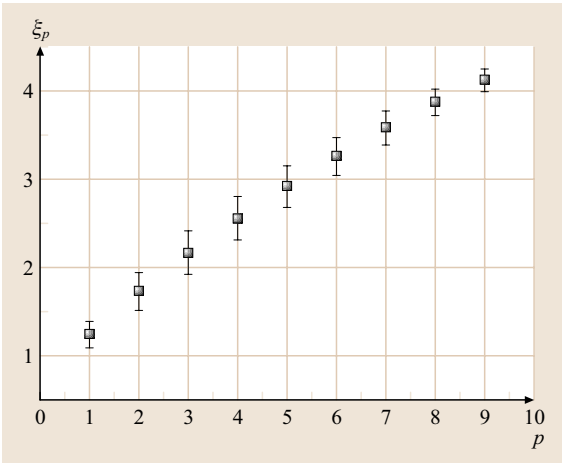

Fig. 10.42 Dependence of the scaling exponent ξ_{p} of the order of the structure function of the velocity gradients p

PDF of the molecular extensions is described by the power law $P(R_i) \sim R_i^{-\beta-1}$, where $\beta \sim (\lambda^{-1} - \alpha)$ in the vicinity of the transition. Positive β corresponds to the majority of the polymer molecules being unstretched. On the contrary, at $\beta < 0$ a significant fraction of the molecules is strongly stretched, and their finite size is defined by the feedback reaction of the polymers on the flow [10.123] and by the nonlinearity of molecular elasticity [10.124]. Thus, the condition $\beta = 0$ can be interpreted as the criterion for the coil-stretch transition in turbulent flows [10.123]. This criterion was quantitatively verified in the experiment by statistical analysis of both a velocity field in the Lagrangian frame (by statistical analysis of the Lyapunov exponents to define the average one) in the elastic turbulence and of a single polymer stretching in the same flow [10.119].

In the framework of the molecular theory of polymer dynamics the tensor τ_p is found to be proportional to the polymer concentration n and to the average polymer conformation tensor, $\tau_{p,ij} \sim n\lambda^{-1}\langle R_i R_j\rangle$ (if one neglects the thermal noise and uses the Hookean approximation). The growth of the elastic stresses is also evidence of significant extension of the polymer molecules in the flow. So, we can suggest that the elastic stress tensor τ_p should be the object of primary importance and interest in the elasticity-driven turbulent flow, and that it may be appropriate to view elastic turbulence as turbulence of the τ_p field.

The next crucial step towards a theoretical description of elastic turbulence was to relate the elastic stress field to the linearly decaying passive field problem [10.115, 116, 124, 127]. As was shown in [10.115], the elastic stress tensor can be rewritten as uniaxial, i. e., $\tau_{ik} = B_i B_k$, if the contribution to the elastic stress due to thermal fluctuations and polymer internal nonlinearity can be neglected. Then (10.93, 94) can be rewritten for the vector B_i in a form that is similar to the equation for the magnetic field in magnetohydrodynamics [10.116]. Then in the case of the elastic turbulence one obtains:

$$\partial_t \boldsymbol{B} + (\boldsymbol{V}\nabla)\boldsymbol{B} = (\boldsymbol{B}\nabla)V - \boldsymbol{B}/\lambda\,. \tag{10.96}$$

This equation, complemented by the equation of motion rewritten as

$$\nabla P = \rho(\boldsymbol{B}\nabla)\boldsymbol{B} + \eta\nabla^2\boldsymbol{V}\,, \tag{10.97}$$

and by the boundary conditions, leads to instability at $Wi > 1$, as already explained in detail. The instability eventually results in a chaotic, statistically steady dynamics. As was explained above for a single polymer stretching, a steady state occurs due to a back reaction of the stretched polymers (or the elastic stress in (10.97)) on the velocity field. Thus, stationarity of the statistics implies that the velocity gradients on a small scale should be limited by some mechanism. The saturation mechanism suggested in [10.115] assumes that both dissipative terms in (10.96, 97), namely viscous $\nu\nabla^2 V$ and relaxation B/λ, are of the same order. Then the velocity gradients become smaller when the scale decreases, and become of the same order as λ^{-1} on a small scale fixed by the stationarity condition. This means that in the chaotic flow the velocity fluctuations dominate on the scale of the system size. So, the elastic stress can be estimated as

$$\tau_p = B^2 \sim \nu\nabla_i V_j \sim \frac{\eta}{\lambda}\,. \tag{10.98}$$

The large-scale velocity fluctuations produce smaller-scale fluctuations in $\boldsymbol{B}$ via (10.96) that in turn induce small-scale fluctuations of the velocity via (10.97). Velocity gradients become smaller as the scale decreases, since the large-scale velocity gradient is of the order of λ^{-1}. The small-scale fields $\boldsymbol{v}$ and $\boldsymbol{B}'$ evolve passively in the large-scale fields $\boldsymbol{V}$ and $\boldsymbol{B}$, where $\boldsymbol{v}, \boldsymbol{B}' \ll \boldsymbol{V}, \boldsymbol{B}$. Thus, this problem is reduced to a linearly decaying passive field problem considered in [10.128]. In the case of elastic turbulence the equation of motion for v is dissipative, and one can neglect the gradient terms, since $\nabla\boldsymbol{B}' \sim \nabla\boldsymbol{B}$ and $\nabla\boldsymbol{v} \ll \nabla\boldsymbol{V}$.

The saturation of the rms fluctuations of the vorticity at high values of Wi observed in the data in Fig. 10.38 gives us the possibility to test which of the two theoretical mechanisms discussed above, either the feedback reaction of a molecule on the flow or the nonlinearity of molecular elasticity, primary leads to the saturation. As one finds from Fig. 10.38, $(\partial V_i/\partial r_j)^{\mathrm{rms}} \simeq 1\,\mathrm{s}^{-1}$. This gives for the local Weissenberg number, $Wi' = \lambda(\partial V_i/\partial r_j)^{\mathrm{rms}} \simeq 2.5$, which exceeds the unity value predicted for the linear molecule elasticity and the feedback mechanism discussed [10.123]. So, this value indicates that the nonlinearity of molecular elasticity is mostly responsible for the saturation [10.124].

The analysis of the equations for the small-scale fluctuations of both fields leads to the power-like decaying spectrum for the elastic stress that in a spherical presentation looks like $\langle B'_i B'_j\rangle \sim F(k) \sim (k)^{-\alpha}$, where $\alpha > 3$. It is clear that the field B'_i (and therefore the field $B'_i B'_j = \nabla_i v_j$) is the passive field in the problem. The mechanism leading to the power-law spectrum for small-scale fluctuations of $\boldsymbol{B}'$ in a chaotic flow is rather general and directly related to the Batchelor scaling of a passive scalar revealed long ago [10.125]. A linear relation between small-scale fluctuations of the fields $\boldsymbol{B}'$ and

$\boldsymbol{v}$ allows the establishment of the power-law spectrum of the velocity, which in a spherical representation looks like $E(k) \sim k^{-\alpha}$, where $\alpha > 3$, in good agreement with the experimental values of $\alpha = 3.3-3.6$ (Fig. 10.22, 24). Since the velocity spectrum decays faster than k^{-3}, the elastic turbulent flow is smooth and strongly correlated on the global scale. This is the main feature of the Batchelor regime, where spatially smooth and random-in-time flow is observed [10.125]. The smoothness of the velocity field in elastic turbulence was experimentally tested by investigating the shape of the cross-correlation functions of the velocity field [10.108]. It was found that the second-order spatial derivative of the velocity field was about an order of magnitude smaller than the first-order derivative, which is a direct confirmation of the flow smoothness [10.108]. It should be emphasized that, in contrast to hydrodynamic inertial turbulence, in elastic turbulence the algebraic power spectrum decay is not related to the energy cascade and any conservation law, since the main energy dissipation occurs at the largest scales. The rapid decay of the fluctuation power with k implies a velocity field in which the main contribution to deformation and stirring (stretching and folding) on all scales comes from the randomly fluctuating velocity field at the largest scale of the system. So, it is suggested that the leading mechanism for the generation of small-scale (high-k) fluctuations in the elastic stress is advection of the fluid (which carries the stress) in this fluctuating large-scale velocity field. Hence, the fluctuating velocity field and stress tensor can both be decomposed into large- and small-scale components, and the leading mechanism for the generation of the small-scale (high-k) portions is advection by the fluctuating large-scale flow. The theory considers the elastic stress tensor as passively advected in a random velocity field, which is analogous to the concept of a passively advected vector in the magnetic dynamo theory [10.116]. Thus, the mechanism leading to the algebraic power spectra for the elastic stress and the velocity in this case is related to advection and linear decay accompanied by stretching of the fluid element carrying the elastic stress.

It follows from the stationarity of statistics of both fields that the velocity gradients $\nabla_i V_j$ are of the same order as λ^{-1} in the bulk. This leads to the formation of a boundary layer, where $\nabla_i V_j$ exceeds λ^{-1} and drops to the value in the bulk. The boundary layers at the upper plate and the walls are clearly observed in the experiment (Figs. 10.33, 35), where the flow is mainly shear dominated, and therefore, the polymers are weakly stretched [10.90, 119].

The saturation of the rms fluctuations of the vorticity (and velocity gradients) and thus of the elastic stress in the bulk that results from (10.98) and from the experimental observations naturally explains the power-law behavior of the injected power, $\frac{P}{P_{\text{lam}}} \sim Wi^{0.49}$, obtained from the plot in Fig. 10.21a. Indeed, the injected power is proportional to the torque, $P = T\Omega$. The latter is just the shear stress τ_{w} averaged over the upper plate. As was shown above, the flow resistance (or torque) growth above the instability threshold occurs solely due to growth of the elastic stress τ_{p}. In the elastic turbulence regime, however, the theory predicts $\tau_{\text{p}} \sim \eta/\lambda$. On the other hand, it was found that, due to shear thinning of the solution used, $\lambda \sim \Omega^{-0.3}$. Thus, the theoretically expected growth of the mean injected power with respect to its laminar value, P_{lam}, should be solely due to the elastic stress and has the following power-law scaling: $P/P_{\text{lam}} \sim \tau_{\text{p}} \sim Wi^{0.43}$. The latter is rather close to the experimentally observed scaling $P/P_{\text{lam}} \sim \tau_p \sim Wi^{0.49}$. Thus, this scaling is consistent with the saturation of the rms of the fluctuations of the vorticity (and the velocity gradients) in the elastic turbulence observed experimentally [10.109]

Based on this discussion, one can suggest the following scenario for the development of elastic turbulence. The polymer molecules are stretched in the primary shear flow, which leads to a large elastic stress. The elastic stress renders the primary shear flow unstable and causes an irregular secondary flow. The flow acts back on the polymer molecules, stretching them further and raising the elastic stress even more [10.111]. This makes the flow increasingly turbulent, until a kind of a saturated dynamic state is finally reached. This state implies some mutually consistent fields of average stresses and velocities, and their fluctuations, related to each other by the equation of motion and the constitutive equation.

10.3.3 Elastic Turbulence in a Curved Channel: Dean Flow

Experimental Setup and Procedure

Experimental Setup and its Fabrication. Another experimental system where elastic turbulence was studied in detail is flow in a curvilinear channel, or Dean flow. The main motivation for the experiments on Dean flow was to carry out a detailed quantitative study of mixing in elastic turbulence [10.77]. It is an open flow that allows extended continuous experimental runs with reproducible and well-controlled initial conditions, and easy collection of extensive data at different stages of mixing. Meanwhile the elastic turbulence and mixing ex-

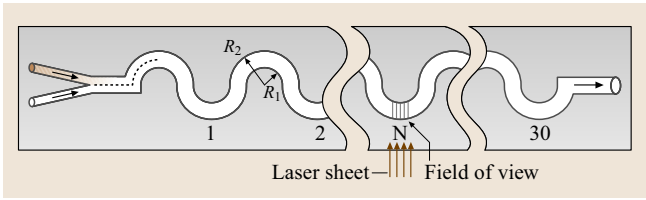

Fig. 10.43 Schematic of the curvilinear channel showing the inlet, a region of observation, and the outlet

periments were conducted in macro- and microchannels of similar geometry. The macrochannel, schematically shown in Fig. 10.43, had a uniform depth of $d = 3$ mm, machined in a transparent bar of perspex, and was sealed from above by a transparent window.

The channel consisted of a sequence of smoothly connected half-rings with inner and outer radii of $R_1 = 3$ mm and $R_2 = 6$ mm, respectively; it was square in cross section, and had quite a high gap ratio of $d/R_1 = 1$, which was intended to facilitate the development of an elastic instability at low Wi and of intensive irregular flow above the instability threshold. The macrochannels had, depending on the specific experiment, 40 to 64 repeating units, each one being 18 mm

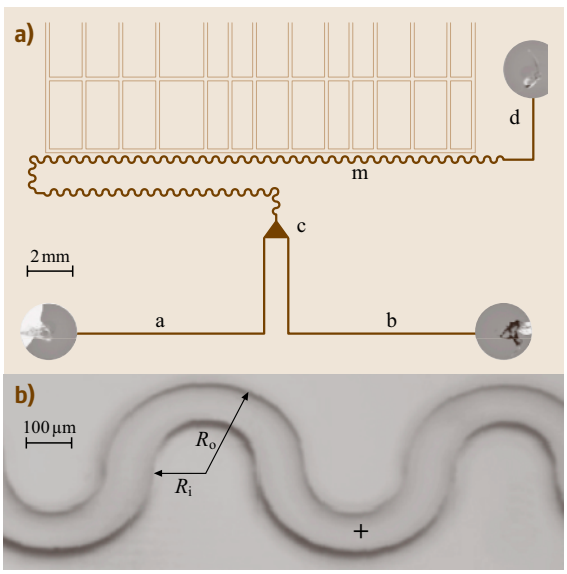

Fig. 10.44 **(a)** Photograph of the microfluidic device. The microchannel was filled with ink for better contrast. **(b)** Photograph of a section of the functional curvilinear element. The point where instantaneous flow velocity measurements (averaged over a $20 \times 20\ \mu m^2$ region) were made is marked by a *cross*

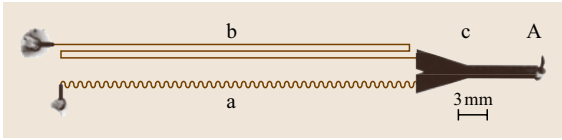

Fig. 10.45 Photograph of the microfluidic device. The microchannels were filled with ink for better contrast

in length. Because of the periodic structure of the channel, it is convenient to use the number of a segment N starting from the inlet as a discrete linear coordinate along the channel [10.77, 104].

The experiments were conducted in a microchannel consisting of 64 smoothly connected half-rings with inner and outer radii of $R_1 = 100\ \mu m$ and $R_2 = 200\ \mu m$, respectively, and a uniform thickness of $d = 100\ \mu m$. This channel has the same proportions as the macroscopic channel but its dimensions are reduced by a factor of 30 (Fig. 10.44 [10.105]). Another microchannel with 46 identical segments of the same geometry and sizes was used to measure the flow resistance (Fig. 10.45 [10.106]). The auxiliary rectilinear channel (b) has a width of 90 µm and a total length of about 72.5 mm. Channel (b) and the comparator region (c) serve to make differential in situ measurements of flux versus pressure by the method described in [10.129].

The microchannel devices consist of a silicon elastomer (Sylgard 184, Dow Corning) chip sealed to a #1 microscope cover glass. The channel structure of the chip was fabricated using soft lithography [10.130]. First, a negative master mold was fabricated in UV-curable epoxy (SOTEC microsystems SU8-1070) using conventional photolithography. The epoxy was spun onto a silicon wafer at 1800 rpm for 60 s to create a 100 µm layer and patterned by using a high-resolution negative transparency mask. Liquid elastomer was poured onto the mold to a thickness of ≈ 5 mm and cured in an 80 °C oven for 1.5 h. The elastomer was then peeled off the mold, trimmed to its final size, and liquid-feeding ports were punched using a 20 gauge luer stub. The patterned side of the chip was bonded to the cover glass by overnight baking in an oven at 80 °C.

Flow Control. The flow in the microchannels was generated and controlled by pressure differences between the inlets and the outlet (Fig. 10.45). The pressures were generated hydrostatically using long vertical rails with precise rulers and sliding stages. Working liquids were kept in 30 ml plastic syringes, which were held upright, open to the atmosphere and connected to the two inlets and the outlet by plastic tubing with an internal diameter

of 0.76 mm. The pressure drop in the tubing was estimated to be less than 1% of the total. The two syringes feeding the inlets were attached to the sliding stages. The difference in liquid elevation between these two syringes and the outlet syringe was measured and adjusted with a precision of about 0.1 mm corresponding to 1 Pa in pressure. The dependence of the volumetric low rate Q in the curvilinear channel on the pressure difference between inlet 1 and the outlet (Fig. 10.45) was determined with a relative precision of about 0.5% using an in situ measurement technique described in [10.129]. A syringe pump (PHD 2000, Harvard Apparatus, Boston) with a 50 ml gastight Hamilton syringe was used for an absolute flow-rate calibration [10.129].

Measuring Flow Velocity. The flow velocity in a macrochannel was measured directly by LDV. Because of the small width of the channel, special effort was made to obtain high spatial resolution by reducing the region of space where the two laser beams crossed, and reduction of the distance between the interference fringes. Focusing lenses with a small focal length (about 25 mm) were used, and the angle between the beams was raised to about 90° in air (and about 60° in the liquid). As a result, the region of beam crossing was decreased to 15 μm × 15 μm × 40 μm, and the distance between the fringes was 0.44 μm [10.77, 104].

Measurements of the flow velocity in a microchannel were carried out using custom developed microscopic particle image velocimetry (micro-PIV). The polymer solution was seeded with 0.2 μm yellow–green fluorescent beads (Polysciences, Warrington), and epi-fluorescent imaging of the flow in the microchannel (Fig. 10.46) was made with an inverted microscope (Olympus IMT2, Warrington) and narrow-band excitation and emission filters in the dichroic filter cube. The objective was a long-working-distance lens with 20×, N.A. = 0.40, and the images were projected onto a CCD array with a 640 × 480 pixel resolution (PixelFly camera from PCO, Germany) digitized to 12 bits. Snapshots of the flow were taken with even time intervals of 40 ms, and digitally postprocessed. Images of out-of-focus particles were disregarded. The velocity field was found by cross-correlating positions of the particles in two consecutive snapshots, and the particle velocity vectors were neighbor-validated. (The calculated velocity field corresponded to the time interval between the two snapshots.) The collected time series represent velocity averaged over a 20 μm × 20 μm square region at the middle plane of the channel. Its position in the channel is equidistant from the channel walls (at $R = 150$ μm) and equidistant from the interconnections of the two half-rings at $N = 35$ [10.105, 106, 109].

Measuring Tracer Concentration Profile. The liquids to be mixed were fed into the macrochannel by two identical syringe pumps through two separate tubing lines, always at equal discharge rates. The chemical composition of the two liquids was always identical as well, with the only difference being a low concentration ($c_0 = 2$ ppm) of a fluorescent dye (fluorescein) added to one of them with the diffusion constant of the dye taken as that for the saccharose molecules, $D = 8.5 \times 10^{-7}$ cm^2/s. They were prepared from the

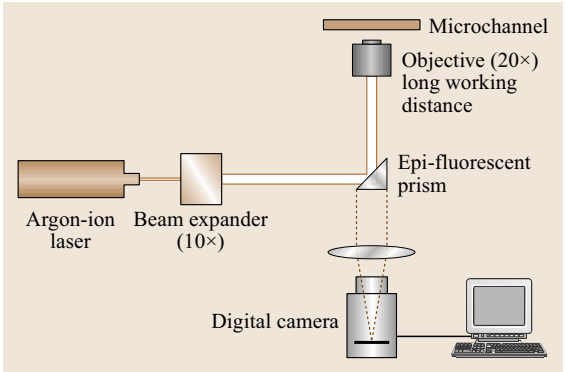

Fig. 10.46 Overview of the micro-PIV setup

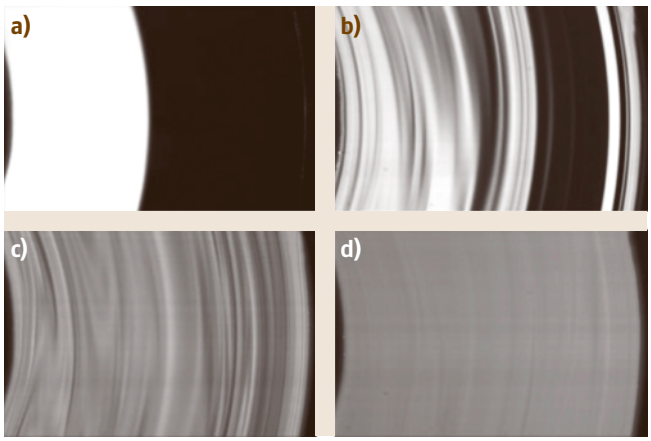

Fig. 10.47a–d Photographs of the flow taken with the laser sheet visualization at different N. The field of view is 3.07 × 2.06 mm, and corresponds to the region shown in Fig. 10.43 (rotated 90° counterclockwise). *Bright regions* correspond to high concentration of the fluorescent dye. **(a)** Flow of the pure solvent at $N = 29$; **(b)**–**(d)**, flow of the polymer solution at $Wi = 6.7$ and at $N = 8$, 29, 54, respectively

same stock of a carefully filtered liquid, which was divided into two equal parts. A small amount of a concentrated solution of the dye was added to one part, while the other part was diluted by an equal amount of pure water. This method of preparation provided very good matching of the densities and refraction indices of the liquids. The channel was illuminated from one side by an argon-ion laser beam converted by two cylindrical lenses into a broad sheet of light with a thickness of about 40 μm in the region of observation. This produced a thin cut of the three-dimensional mixing pattern, parallel to the top and bottom of the channel at half of the channel depth [10.77, 104].

Fluorescent light emitted by the liquid in the direction perpendicular to the beam and to the macrochannel plane was projected onto a CCD array by a camera lens and digitized by an 8-bit, 512×512 frame grabber. Using homogeneous solutions with different amounts of dye, we found the intensity of the fluorescent light captured by the camera to be linearly proportional to the dye concentration. Therefore, the concentration of the dye was evaluated from the fluorescent light intensity (Fig. 10.47) [10.77, 104].

The experiments on mixing in microchannels were carried out by adding fluorescent dyes with low diffusivity to the solution and using them as tracers. We used a few different samples of fluorescein-conjugated dextran (FITCD, Sigma) with average molecular weights M varying from 10^4 g/mol to 2×10^6 g/mol. In spite of the relatively high molecular weight of FITCD, it did not have a measurable influence on the solution relaxation time due to the high rigidity of the polysaccharide molecules. The diffusion coefficients of the FITCD samples in water were estimated using the data in [10.131], giving values of 9.1×10^{-7}–7.4×10^{-8} cm^2/s that corresponded to a broad range of biological macromolecules. The diffusion coefficients in the solvent used were estimated under the assumption that $D\sim1/\eta_s$, resulting in $D_1=6.6\times10^{-9}$ and $D_2=5.4\times10^{-10}$ cm^2/s for 10^4 g/mol and 2×10^6 g/mol FITCD, respectively [10.105, 106].

The concentrations of the fluorescent dyes, which were used as passive tracers in the experiments on mixing in the microchannel, were evaluated using a commercial confocal microscope (Fluoview FV500, Olympus), which was equipped with 40×, N.A.= 0.85 infinity corrected objective and a 12 bit photomultiplier. The scanning was done at a rate of 56 lines per second and 512 pixels per line, corresponding to a step of 0.18 μm per pixel [10.105].

Observation of Elastic Turbulence

Flow Resistance. The flow resistance in the microchannel was measured by measuring the volumetric flux rate, Q, in a broad range of applied pressure drops and by calculating the resistance factor $Z=\Delta p_s/Q$, where Δp_s is the pressure drop per segment. The resistance factor is a constant proportional to the viscosity for Newtonian fluids in linear, low-Re regime, and can be used as a measure of turbulent flow resistance in large channels at high Re. Figure 10.48 shows the dependence of Z on Q, after Z is divided by the resistance factor Z_0 found for a Newtonian liquid with the same viscosity. The ratio Z/Z_0 is

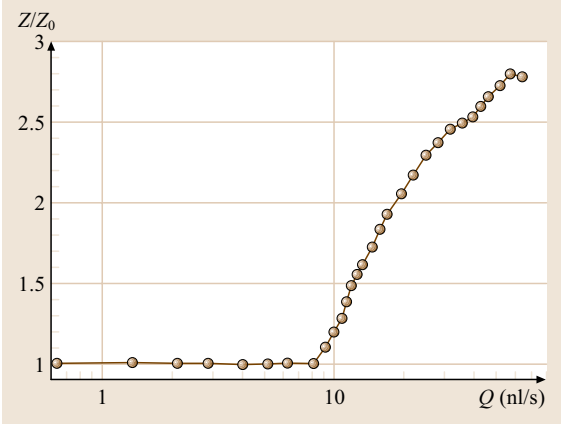

Fig. 10.48 Dependence of the normalized resistance Z/Z_0 in the flow of solution 1 through the curvilinear channel on the volumetric flow rate Q on a semilogarithmic scale

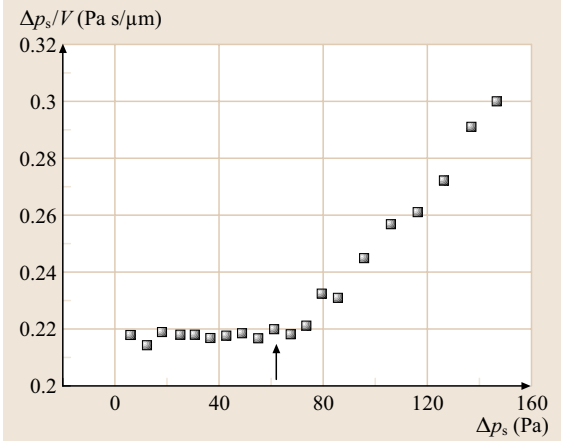

Fig. 10.49 Flow resistance, $\Delta p_s/V$ versus Δp_s. The *arrow* indicates the onset of the elastic instability

constant and equal to unity in the linear regime at low Q. At Q of about 8.5 nl/s, however, a nonlinear transition occurs; Z/Z_0 starts to grow and reaches a factor of about 2.8 at high Q. The Reynolds number was always much lower than unity, so inertial effects were always negligible [10.106].

Another way to measure the flow resistance is to measure an average flow velocity through a microchannel at various pressure drops by the micro-PIV technique. Using this method, an analog of the flow resistance, $\Delta p_s/V$, versus the pressure drop per segment, Δp_s, is shown in Fig. 10.49 [10.105]. The elastic instability occurs at $\Delta p_s \approx 50$ Pa, and the flow resistance grows up to 1.4-fold in the elastic turbulence regime.

Flow Structure, Velocity and Velocity Gradient Fields, Velocity Fluctuations Spectra, and Velocity Statistics. The flow structure and velocity flow field in the microchannel were investigated by combined micro-PIV and micro-PTV techniques for a broad range of flow rates. Above the instability threshold an initially stationary longitudinal vortex becomes time dependent. As one can see in Fig. 10.50, the vortical structure fills the whole channel cross-section and is quite spatially smooth with irregular velocity fluctuations in time [10.109]. One gets a similar impression from measurements of the transversal velocity component at several off-center locations in a macrochannel. Indeed, we found nonzero averages, which typically persisted for a few minutes and changed their sign rather randomly in time. This situation can be explained by the presence of persistent longitudinal vortical structures in the flow. These vortices probably fill the channel cross section, with their vorticity direction jumping between parallel and antiparallel to the mean flow [10.104].

The spatial smoothness of the channel flow in elastic turbulence was investigated by measuring profiles of the longitudinal and transversal velocity components by micro-PTV for different values of Wi (Fig. 10.51). One notices that, even below the transition (squares, circles, and triangles in Fig. 10.51), the profiles of the longitudinal velocity component are clearly nonparabolic and nonsymmetric. This apparent difference with respect to the case of a laminar Poiseuille flow in a straight channel has been also observed in experiments with a pure solvent (data not shown) and is confirmed by recent numerical simulations by A. Kumar (private communication) in a low-Re flow in a similar geometry [10.109].

The longitudinal velocity profile allows us to estimate the critical Weissenberg number of the elastic transition $Wi_c = \lambda(\dot\gamma)\dot\gamma_c$, where the critical shear rate

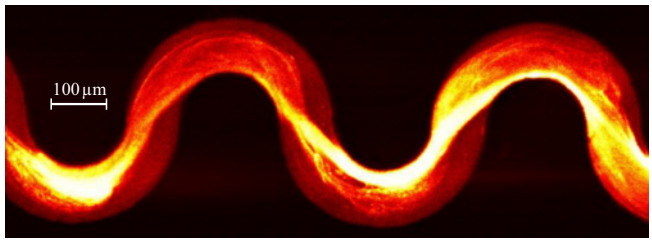

Fig. 10.50 Mid-plane horizontal confocal snapshot. The flow is seeded with 0.2 µm fluorescent spheres. The driving pressure is 120 Pa per channel segment

$\dot\gamma_c$ is calculated as $\dot\gamma_c = 2V_\theta^{max}/d$, where V_θ^{max} is the maximum longitudinal velocity of the profile. Indeed, at the critical pressure difference corresponding to the onset of instability, $\Delta p_s \approx 50$ Pa, one gets $\dot\gamma_c \simeq 4.2\,s^{-1}$, which leads to $Wi_c \simeq 13$ with $\lambda(\dot\gamma_c) \simeq 3.1$ s. On the other hand, one can use the time-averaged longitudinal velocity gradient across the channel, $\overline{\partial V_\theta/\partial r}$, at the transition to estimate Wi_c. Using the data in Fig. 10.54, one then obtains $Wi_c \simeq 9.3$. This critical value Wi_c is in fair agreement with the value obtained theoretically from the linear stability criterion for the aspect ratio, $d/R_1 = 1$ and $S = 0.82$, in the experiment. Then, using the instability criterion for the Dean flow one obtains $K_c \simeq 9$, which leads to $Wi_c \simeq 9$ [10.96–98], while $Re \simeq 8\times10^{-5}$.

PTV measurements also provide us with the possibility of measuring time series of the flow velocity at specific points in the flow. The rms fluctuations of both horizontal velocity components in the center of the microchannel as a function of Wi are shown in Fig. 10.52, 53. The fluctuations are practically absent in the laminar regime, while at $Wi_c \simeq 13$ the rms of both velocity components start to grow sharply. These measurements can be used as another indication of the transition and appearance of the elastic turbulence regime [10.109].

Figure 10.52 shows the time-averaged longitudinal velocity $\bar V_\theta$ as a function of the driving pressure difference. One observes that in a laminar regime the velocity growth is linear but slows above the transition. Other important information is provided in Fig. 10.45, where the average longitudinal velocity gradient across the channel at three locations as a function of Wi is presented.

The statistical properties of the velocity field are characterized by the correlation function, which is presented in Fig. 10.55 together with a typical time series of the instantaneous longitudinal velocity far above the transition. The temporal dependence has well-expressed chaotic appearance that is confirmed by the shape of the

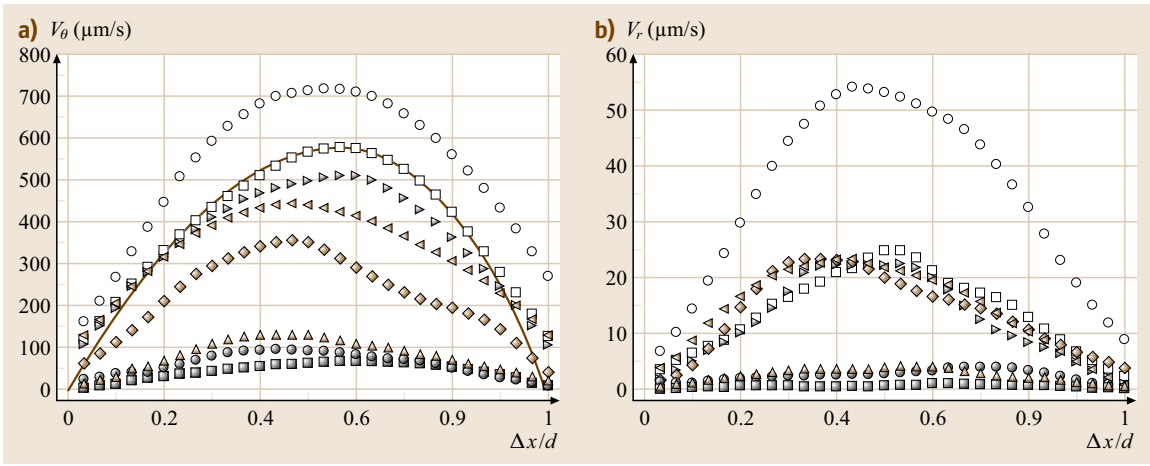

Fig. 10.51a,b Profiles of the (a) longitudinal velocity component, V_θ and (b) radial velocity component V_r across the microchannel. The symbols correspond to: *Full squares*: $Wi = 3.84$, *circles*: $Wi = 6.75$, *up triangles*: $Wi = 8.49$, *rhombus*: $Wi = 13.56$, *left triangles*: $Wi = 14.83$, *right triangles*: $Wi = 19.4$, *open squares*: $Wi = 20.15$, *open circles*: $Wi = 22$; the *full line* is the result of numerical simulations

autocorrelation function, which decays monotonically without distinct peaks [10.106].

Figure 10.56 shows the power spectra of the fluctuations of the longitudinal and transversal components of the velocity in the polymer solution flow in the macrochannel at $Wi = 6.7$. The measurements were done at $N = 12$, near the middle of the half-ring in the middle of the channel. A spectrum of the velocity fluctuations in the flow of the pure solvent at the same Q, giving just instrumental noise, is shown for comparison. The mean velocity was $\bar{V} = 6.6\,\mathrm{mm/s}$; the rms fluctuations V_{rms} were $0.09\bar{V}$ and $0.04\bar{V}$ in the longitudinal and transversal directions, respectively [10.77, 104]. The power spectra exhibit the power-law decay $P \sim f^{-\alpha}$ with an exponent $\alpha \simeq 3.3$ that is consistent with similar

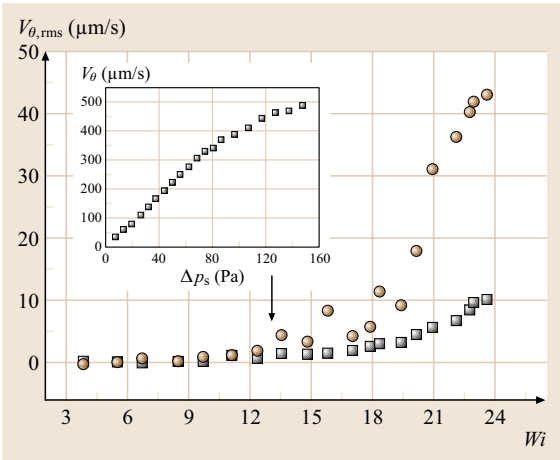

Fig. 10.52 Dependence of the rms fluctuations of the longitudinal component of the flow velocity $V_{\theta,\mathrm{rms}}$ on Wi at the center of the microchannel. The *squares* are the instrumental error. The *arrow* indicates the onset of the elastic instability. *Inset*: dependence of the time average of the longitudinal velocity component $\overline{V_\theta}$ at the center of the microchannel on the pressure drop per channel segment Δp_s

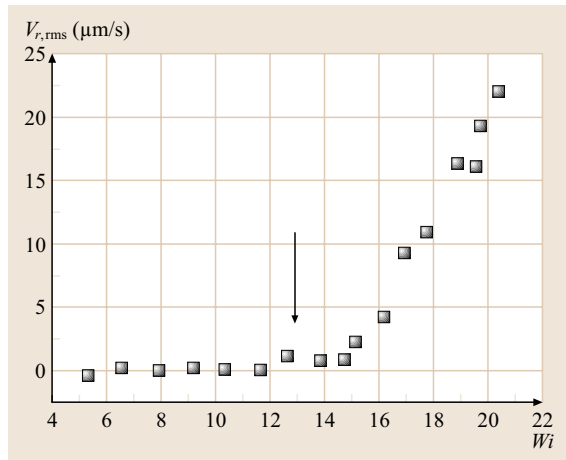

Fig. 10.53 Dependence of the rms fluctuations of the radial component of the flow velocity $V_{r,\mathrm{rms}}$ on Wi at the center of the microchannel. The *arrow* indicates the onset of the elastic instability

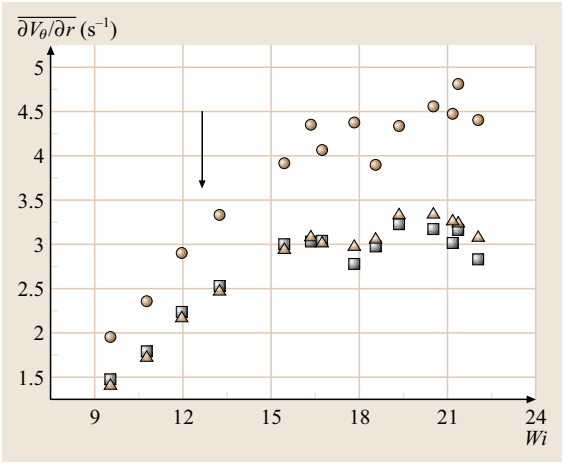

Fig. 10.54 Dependence of the average gradients of the longitudinal component of the flow velocity, $\overline{\partial V_\theta/\partial r}$ on Wi, at three different points having the same radial coordinate, $r = d/2$ but different polar angles, $\theta = -\pi/2, 0, \pi/2$. The *arrow* indicates the onset of the elastic instability. *Circles*: 0, *squares*: $\pi/2$, *triangles*: $-\pi/2$

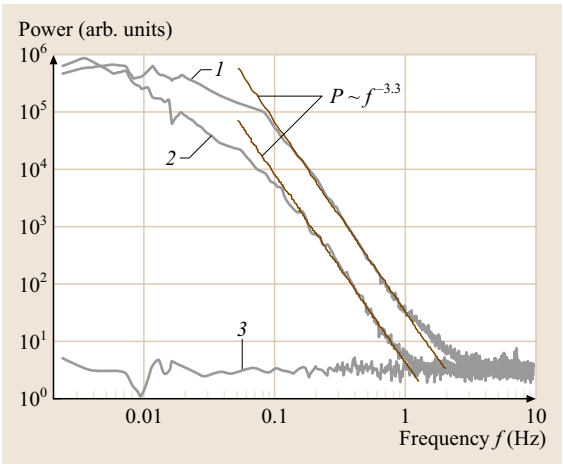

Fig. 10.56 Power (P) of the fluctuations of velocity in the middle of the channel at $N = 12$ as a function of frequency f. The spectra in the polymer solution flow at $Wi = 6.7$ for the velocity components along and across the mean flow are shown by *curves* 1 and 2, respectively. *Curve* 3 shows the velocity spectrum across the mean flow for the pure solvent at the same Q

measurements in other setups and with the theoretical estimates [10.76, 77, 104, 115, 116].

Mixing in the Flow. Mixing in macrochannels was studied at quite small Reynolds numbers, reaching only 0.6 for the highest Q that was explored. Therefore, the flow of the pure solvent always remained laminar and no mixing occurred (Fig. 10.47a). The boundary separating the liquid with and without the dye was smooth and parallel to the direction of flow and only became somewhat smeared due to molecular diffusion as the liquid advanced downstream. The flow of the polymer solution was laminar and stationary up to a value of Q corresponding to Wi_c (and $Re = 0.06$), at which an elastic instability occurred. This instability led to irregular flow and fast mixing of the liquids [10.77, 104].

A few typical mixing patterns at different N in the polymer solution above the instability threshold are shown in the photographs in Fig. 10.47b–d. More insight into the structure and evolution of the mixing patterns can be obtained from space–time diagrams. Representative diagrams taken at $Wi = 6.7$ at four different N are shown in Fig. 10.57. The brightness profiles along a single line perpendicular to the channel near the middle of a half-ring (a horizontal line going through the middle of a snapshot in Fig. 10.47) were captured at even time intervals of 80 ms and plotted from top to bottom.

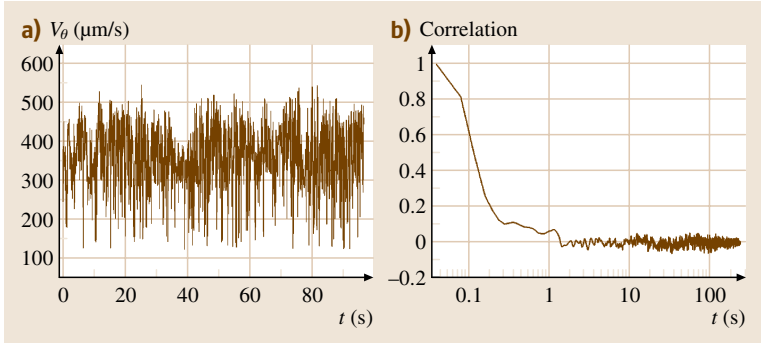

Fig. 10.55 **(a)** Time series of the longitudinal flow velocity V_θ at the center of the microchannel at $Wi = 20.93$. **(b)** Autocorrelation function of V_θ based on about 6000 individual velocity measurements

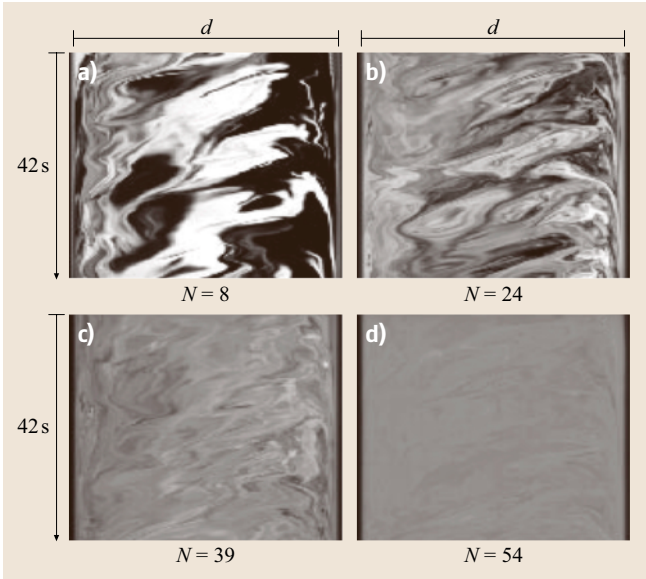

Fig. 10.57 Representative space–time diagrams of the polymer solution flow at $Wi = 6.7$ taken at different positions N along the channel

The diagrams in Fig. 10.57 share the same chaotic appearance and show features at comparable scales, but they lose contrast as liquid advances downstream and becomes progressively mixed [10.77, 104].

As illustrated by the space–time diagrams in Fig. 10.57, mixing in the polymer solution flow above the instability threshold was a random process calling for statistical analysis [10.77, 104]. A simple parameter characterizing the homogeneity of the mixture is the rms deviation of the dye concentration from its average value $\bar{c} = c_0/2$ divided by the average value itself $c_{\mathrm{rms}} = \langle (c - \bar{c})^2 \rangle^{1/2} / \bar{c}$. A small value of c_{rms} indicates strong homogeneity and good mixing of the liquids. At the channel entrance, where the two injected liquids are perfectly separated, c_{rms} is unity, and it should become zero for a perfectly mixed liquid.

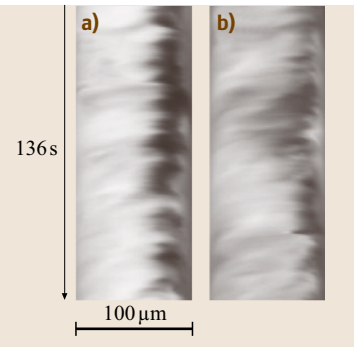

Fig. 10.59a,b Space–time plots of the FITCD distribution across the channel taken at **(a)** $N = 12$ and **(b)** $N = 18$. Confocal scanning was done along the same line across the channel in the mid-plane at equal distances from the half-ring interconnections, with even time intervals of 0.0177 s. Profiles of the FITCD concentration at consecutive moments of time are plotted from the top to bottom

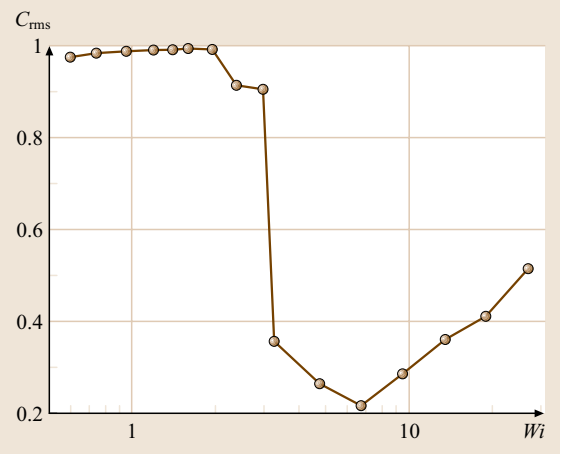

Fig. 10.58 Dependence of c_{rms} (the normalized root mean square of concentration deviations from the average) on the Weissenberg number Wi measured near the channel exit at $N = 29$ (semilogarithmic coordinates)

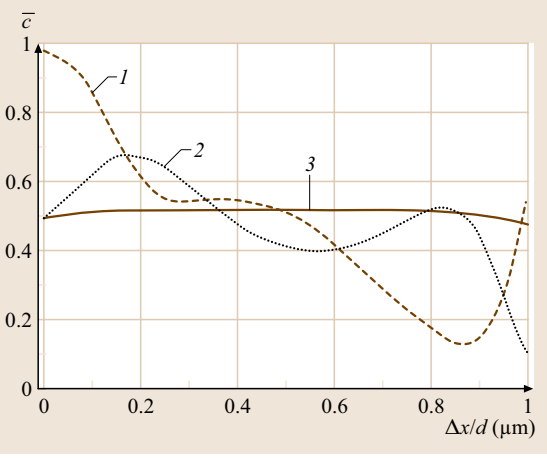

Fig. 10.60 Time average of FITCD concentration $\bar{c}$ as a function of the normalized coordinate across the microchannel at different locations downstream: (1) $N = 7$, (2) $N = 11$, and (3) $N = 41$

The dependence of c_{rms} on Wi near the exit of the channel, at $N = 29$, is presented in Fig. 10.58. The statistics of the dye concentration was evaluated from space–time diagrams similar to those in Fig. 10.57. The regions near the walls of the channel with a width of $0.1d$ were excluded from the statistics, because of possible image aberrations. In a stationary flow regime ($Wi < Wi_c$), when the concentration profile did not change in time, the brightness profiles were measured over short time intervals (about 100 s). In the regime of an irregular flow, however, the profile of concentration was strongly fluctuating. So, in order to obtain representative statistics of c, the measurements of the brightness profile were taken over quite long intervals of time (20–30 min), which typically corresponded to the total liquid discharge of about 10^3 d^3 [10.77, 104].

The plot in Fig. 10.58 is somewhat analogous to that in Fig. 10.20, 48, 49, which show the dependence of the flow resistance on Wi. Indeed, the decrease in c_{rms} is an integral result of mass transfer produced by the irregular flow in the channel, just as growth of the flow resistance is an integral characteristic of increase of momentum transfer in elastic turbulence. The most striking feature of the plot in Fig. 10.58 is certainly an abrupt drop in c_{rms} at Wi_c, where the irregular motion of the liquid sets in.

We studied the dependence of c_{rms} on N at $Wi = 6.7$, corresponding to the greatest homogeneity of the mixture near the channel exit (Fig. 10.58), and found c_{rms} to decay exponentially with distance from the inlet with a characteristic decay length ΔN of about 15 segments [10.77, 104]. One can learn from Fig. 10.58 that, if Wi is raised above 6.7, c_{rms} starts to increase again. The most plausible explanation for this is saturation of the growth of the velocity fluctuations together with reduction of the residence time in the flow at growing Wi (and average flow velocity $\bar{V} = Q/d^2$). If the ratio between the fluctuating and average flow velocities remains constant, while they both increase, the stirring in the flow remains the same, but there is less time available for molecular diffusion, and homogeneity is reduced as a result. This situation can be quantitatively described by the growth of the Peclet number $Pe = \bar{V}d/D$. It was recently found, for a flow of a polymer solution in a channel of the same shape and at similar Wi, that the characteristic length ΔN increases as $Pe^{0.25}$ [10.105]. This suggests that c_{rms} should start increasing with Wi once growth of the velocity fluctuations has slowed down.

The typical mixing time in the channel at $Wi = 6.7$ was found to be 3–4 orders of magnitude shorter than the diffusion time, d^2/D, for the small molecules of fluorescein [10.77]. The dependence of the efficiency of mixing at the optimal flow conditions (for the 80 ppm solution it was $Wi = 6.7$) on the concentration of the polymers was surprisingly weak (although Wi_c grew quickly as the polymer concentration decreased). So, for a solution with a polymer concentration of 10 ppm ($\eta/\eta_s = 1.03$), c_{rms} values as low as 0.29 could be reached at $N = 29$. (measured at $Re = 0.065$, where inertial effects were still negligible). Excitation of irregular flow and active mixing was observed down to polymer concentrations of 7 ppm [10.77, 104].

Quantitatively similar results for mixing were observed in a microchannel [10.105, 106]. We studied in detail mixing of fluorescent-conjugated dextran (FITCD) with 2×10^6 g/mol molecular weight in the channel at $\Delta P = 124$ Pa, corresponding to a flow rate of about twice above the nonlinear transition threshold and a cross-channel space–time-averaged longitudinal velocity of about 173 μm/s. Variation of the tracer concentration profiles with time at different distances from the inlet is illustrated by the space–time plots in Fig. 10.59a,b. One can observe that the tracer concentration appears to fluctuate quite randomly without any apparent scale in time or space. Next, one can see in Fig. 10.59a, taken at $N = 12$, that the left side of the channel, where the tracer was initially injected, looks much brighter and has a much higher average concentration of the tracer. Although also noticeable in Fig. 10.59b taken further downstream, at $N = 18$, this feature is clearly weaker there.

Thus, stirring by the fluctuating velocity field seems to create a more-symmetric distribution of the tracer between the two sides of the channel. In order to validate this observation, we measured the time average of the tracer concentration $\bar{c}$ at different positions across the channel and at different N (Fig. 10.60).

One can see that the cross-channel distribution of $\bar{c}/c_0$ close to the inlet, at $N = 7$, is strongly influenced by the asymmetric conditions at the channel entrance. As one can observe from the curve at $N = 11$, however, the imprint of the initial conditions is clearly fading as the liquid advances downstream and being stirred. Further downstream, at $N = 41$, asymmetry in the tracer distribution introduced by the initial conditions has disappeared completely. Fading of the influence of the initial condition with time and restoration of symmetry in flow in a statistical sense are both distinct features of chaotic and turbulent flows. Therefore, the curves in Fig. 10.60 provide further evidence for the truly chaotic nature of the flow in the microchannel [10.105, 106].

10.3.4 Conclusions

Summarizing these experimental results, we conclude that the flow at sufficiently high Wi in curved macro- and microchannels exhibits main features that are rather similar to those observed in the swirling flow between two disks. Above the elastic instability threshold the flow of the polymer solution in the channel, firstly, exhibits two major features of turbulent flows: a major increase in the flow resistance and in the rate of mixing, and secondly, the fluid motion generates the velocity power spectra across a wide range of frequencies as well as wavenumber domains, which provides solid evidence for the turbulent character of the flow, particularly due to the absence of peaks in the spectra in Fig. 10.56 similar to those observed in the swirling flow (Fig. 10.22, 23). The spectra of both longitudinal and transversal velocity components do not exhibit any distinct peaks and have broad regions of power-law decay with an exponent of about -3.3. Since the power spectra in Fig. 10.56 were measured at a point with a high mean flow velocity (10 times higher than a characteristic fluctuating velocity), we can use the Taylor hypothesis and argue that the spectra in Fig. 10.56 actually reflect the spatial structure of the flow. Then the power-law decay region can be transferred to the spatial domain, with the power of the velocity fluctuations scaling as $P \sim k^{-3.3}$ with the wavenumber k (see the remark on this subject in the previous section). We also notice here that the exponent of -3.3 in Fig. 10.56 is very close to those measured in the flow between two plates, which varied from -3.3 to -3.6 depending on the position. So, one can suggest that the decay of the power of the velocity fluctuations with an exponent of around -3.5 is a rather general feature of elasticity-induced turbulent flows.

The functional form of the velocity power spectra, $P \sim k^{-3.3}$, suggests that the power of fluctuations of velocity gradients scales like $k^{-1.3}$. An integral of $k^{-1.3}$ diverges for $k \to 0$ and converges at $k \to \infty$. This means that the main contribution to the fluctuations of the velocity gradients and the velocity differences at all scales comes from the largest eddies, having dimensions of the whole system (the diameter of the channel or the gap between the plates). This conclusion has an immediate implication for mixing in the flow: it should result in the same type of patterns and in functionally the same statistics as in the case of a completely homogeneous flow, $\boldsymbol{V}(\boldsymbol{r}, t) = \boldsymbol{V}_0(t) + \frac{\partial \boldsymbol{V}}{\partial \boldsymbol{r}}(t)(\boldsymbol{r} - \boldsymbol{r}(0))$, randomly varying in time ($\boldsymbol{r}$ is the position vector).

Such a flow is a realization of the so-called Batchelor regime of mixing [10.125], and the problem of the statistics of a tracer (dye) distribution in it has been solved analytically recently [10.118, 132, 133]. The Batchelor regime occurs at small scales (below the Kolmogorov dissipation scale [10.79, 117]) in usual (high-Re) turbulence, and is rather difficult to realize in the laboratory otherwise. Therefore, the elastic turbulent flow in the channel provided a very convenient experimental system for quantitative study of mixing in this regime [10.77, 104–106]. The experimental results on the correlation functions and PDF of dye concentration, and on their dependence on mixing time, agreed very well with the theoretical predictions [10.77, 105, 106]. A practical message of the experiments is that very viscous liquids can be efficiently mixed in curvilinear channels at very low flow rates by adding high-molecular-weight polymers at very low concentrations. This method of mixing, we believe, can find some industrial and laboratory applications [10.134].

10.4 Measurements for Large-Eddy Simulations

The choice of measurement technique for experimental turbulence research depends upon how turbulence is defined, in particular what type of decomposition is envisioned. In the classical Reynolds-averaged Navier–Stokes (RANS) decomposition, turbulence is defined as the deviation from the ensemble-averaged mean velocity field (Sect. 10.1.2) [10.4, 6]. For statistically stationary flows, ergodicity is often assumed and ensemble averaging is replaced with the more-practical method of time averaging. Hence for RANS, point measurement techniques such as hot wires or LDV that record long time records of turbulence signals are appropriate and have a long history of applications to turbulence research (Sect. 10.1.1). Combined with time averaging, these signals allow one to measure the mean velocity and moments of the velocity, for instance classical Reynolds stresses $\sigma_{ij}^{\mathrm{Re}} = -\overline{u'_i u'_j}$, where an overbar denotes statistical (ensemble or time) averaging. Such data have supported model developments by providing detailed databases to which RANS simulation results can be compared, and have also provided fundamental insights into turbulent flow

that have inspired and tested concepts for model developments.

In large-eddy simulation (LES) of turbulence [10.4, 135, 136], the most-often used decomposition involves spatial, three-dimensional filtering, rather than time averaging. In LES, the effects of the unresolved motions are included in the equations through new stresses (momentum fluxes) that must be parameterized by means of closure relations, and experimental data can be employed to support model development and the validation of numerical simulations. Since the type of data needed differs in significant aspects from that which is classically employed in the context of RANS, these measurement techniques are covered separately in the present section. The section briefly reviews LES and the specific data requirements for LES (Sect. 10.4.1), and then describes the experimental methods that have been employed to obtain such data starting with arrays of point measurement techniques (Sect. 10.4.2) and optical planar velocimetry measurement methods (Sect. 10.4.3). Sample results from the latter applied to studies of LES models are presented in (Sect. 10.4.4). The application of optical volumetric techniques for 3-D velocity measurements are described in (Sect. 10.4.5). Scalar fluctuation measurements using optical techniques and their applications to the study of LES variables of interest to scalar mixing and combustion are reviewed in Sect. 10.4.6.

10.4.1 Large-Eddy Simulation and Data Requirements

In LES, the objective is to solve equations for the velocity field convolved with a spatial filter at a scale Δ. The filtered velocity field is defined according to

$$\tilde{u}_i(\boldsymbol{x}) = \iiint u_i(\boldsymbol{x}')G_\Delta(\boldsymbol{x}-\boldsymbol{x}')\mathrm{d}^3\boldsymbol{x}' \,, \tag{10.99}$$

where $G_\Delta(\boldsymbol{x})$ is a filter function (here assumed to be spatially homogeneous, i. e., only a function of $\boldsymbol{x}-\boldsymbol{x}'$, for simplicity), of characteristic scale Δ. An example is the Gaussian filter $G_\Delta(\boldsymbol{x}) = [6/(\pi\Delta^2)]\exp(-6x^2/\Delta^2)$. The decomposition of the velocity field into large (resolved or filtered) and small [unresolved or subgrid-scale stress (SGS)] scales may be performed using other types of filters [10.4, 136, 137] such as the spectral cutoff filter and the box, or top-hat, filter. The spectral cutoff filter has the desirable property that it is also a projection in the sense that twice-filtered fields are equal to single-filtered fields and it thus cleanly separates between scales. A drawback is that, when filtering spatially localized phenomena, it causes nonlocal oscillatory behavior and, since the filter has negative lobes, the resulting stress tensor does not follow some important realizability conditions [10.138]. The box filter, on the other hand, has good spatial localization but does not allow unambiguous separation between scales because of spectral overlap. The Gaussian filter has intermediate localization properties in both physical and spectral space, although it is closer to the box filter and also has spectral overlap. Convolving the Navier–Stokes equations with such filters yields the LES equations for incompressible flow

$$\frac{\partial\tilde{u}_i}{\partial t} + \tilde{u}_j\frac{\partial\tilde{u}_i}{\partial x_j} = -\frac{1}{\rho}\frac{\partial\tilde{p}}{\partial x_i} + \nu\nabla^2\tilde{u}_i - \frac{\partial}{\partial x_j}\tau_{ij} + \tilde{f}_i \,,$$
$$\frac{\partial\tilde{u}_i}{\partial x_i} = 0 \,; \tag{10.100}$$

f_i is the external forcing and τ_{ij} is the subgrid-scale stress (SGS) tensor defined as

$$\tau_{ij} = \widetilde{u_i u_j} - \tilde{u}_i\tilde{u}_j \,. \tag{10.101}$$

This tensor arises due to the spatial filtering of the nonlinear term in the Navier–Stokes equations, and is the LES analog of the classical Reynolds stress in RANS. To highlight the analogy, we note that the classical (kinematic) Reynolds stress $\sigma_{ij}^{\mathrm{Re}}$ can also be written as $-\sigma_{ij}^{\mathrm{Re}} \equiv \overline{u'_i u'_j} = \overline{u_i u_j} - \bar{u}_i\bar{u}_j$, where an overbar still denotes statistical (ensemble or time) averaging. With an SGS model (closure), i. e., replacing τ_{ij} with an expression in terms of the filtered resolved velocity $\tilde{\boldsymbol{u}}$, the LES equations may be discretized at a spatial resolution on the order of the filter scale Δ.

The most popular models for the subgrid-scale stress belong to two classes: eddy viscosity and similarity (or nonlinear) models. The first was introduced by *Smagorinsky* [10.139] and bears his name. It reads, for the deviatoric part of the stress ($= \tau_{ij} - \frac{1}{3}\tau_{kk}\delta_{ij}$)

$$\tau_{ij}^S = -2(C_\mathrm{s}^\Delta\Delta)^2|\tilde{S}|\tilde{S}_{ij} \,, \tag{10.102}$$

where $\tilde{S}_{ij}$ is the filtered stain rate and $|\tilde{S}| = \sqrt{2\tilde{S}_{ij}\tilde{S}_{ij}}$ is its magnitude. The Smagorinsky coefficient C_s^Δ must be specified [10.140], or it may be determined dynamically from the simulated large-scale fields as proposed by *Germano* et al. [10.141]. This procedure was based on the Germano identity [10.142],

$$L_{ij} = \tau_{ij}(\alpha\Delta) - \overline{\tau_{ij}(\Delta)} \,, \tag{10.103}$$

relating the SGS stresses at scales $\alpha\Delta$ and Δ, where $\alpha > 1$ and typically $\alpha = 2$ (an overbar denotes filtering at the scale $\alpha\Delta$). The tensor L_{ij} is the so-called resolved stress tensor defined as

$$L_{ij} = \overline{\tilde{u}_i\tilde{u}_j} - \bar{\tilde{u}}_i\bar{\tilde{u}}_j \,. \tag{10.104}$$

Substituting the Samgorinsky model for the two stress terms on the right-hand side results in

$$L_{ij} - \frac{1}{3} L_{kk}\delta_{ij} = \left(C_s^{\Delta}\right)^2 M_{ij} \,,$$
$$\text{where } M_{ij} = -2\Delta^2 \left[\alpha^2 \left(\frac{C_s^{\alpha\Delta}}{C_s^{\Delta}} \right)^2 \overline{|\tilde{S}|\tilde{S}_{ij}} - \overline{|\tilde{S}|\tilde{S}_{ij}} \right] . \quad (10.105)$$

Assuming scale invariance, i. e., $C_s^{\alpha\Delta} = C_s^{\Delta}$, one can determine C_s^{Δ} based on variables available during LES. Minimizing the ensemble-averaged error between the right- and left-hand sides of this equation leads to [10.141, 143, 144]

$$\left(C_s^{\Delta,\mathrm{dyn}}\right)^2 = \frac{\langle L_{ij} M_{ij} \rangle}{\langle M_{ij} M_{ij} \rangle} \,. \quad (10.106)$$

The dynamic model has been used extensively in numerous applications of LES (see reviews in *Piomelli* [10.145] and *Meneveau and Katz* [10.146]). For an overview of several other eddy-viscosity SGS models, see *Lesieur and Metais* [10.135] and *Meneveau and Katz* [10.146].

The second type of model is related to the similarity model of *Bardina* et al. [10.147] and was originally introduced based on analysis of direct numerical simulation data. Further evidence was obtained from detailed analysis of experimental data, as reviewed in Sect. 10.4.4 below. A computationally convenient version of this model is the nonlinear model [10.148–150] that is expressed in terms of the resolved velocity gradient tensor as

$$\tau_{ij}^{\mathrm{NL}} = c_A \Delta^2 \tilde{A}_{ik} \tilde{A}_{jk} \,, \quad \tilde{A}_{ij} = \frac{\partial \tilde{u}_i}{\partial x_j} \,. \quad (10.107)$$

Both models may be linearly combined to form so-called mixed models [10.147]. These models also bear a resemblance to so-called deconvolution models [10.151].

For the transport of a scalar c (e.g., concentration, temperature), the filtered scalar transport equation yields SGS fluxes of the form $q_i = \widetilde{u_i c} - \tilde{u}_i \tilde{c}$ [10.152]. To quantify mixing of a conserved scalar, its variance $\widetilde{c^2} - \tilde{c}^2$ and the scalar-variance dissipation rate $\chi = \gamma[\widetilde{(\nabla c)\cdot(\nabla c)} - \nabla\tilde{c}\cdot\nabla\tilde{c}]$ are often used but must be modeled since they are not resolved in LES [10.153, 154]). In chemically reacting flows, unresolved scalar consumption rates are often written in terms of the difference $\widetilde{|\nabla c|} - |\nabla\tilde{c}|$ [10.155], which is also not resolved due to the nonlinearity inherent in the absolute value.

Studies of LES and SGS modeling based on empirical data can be divided into two broad categories *Piomelli* et al. [10.156]: a posteriori tests and a priori analysis. In a posteriori tests, the results from a simulation that utilizes a particular SGS model to be studied are compared with available data. These data can originate from direct numerical simulation (DNS) or from experiments, these being complementary approaches. DNS provides full databases with all fields resolved in three dimensions, but at limited Reynolds numbers. Experimental data may provide access to high-Reynolds-number flows in possibly complex flow conditions, but acquisition of multicomponent and multipoint velocity experimental data is challenging.

For a posteriori tests the data are processed statistically before comparing with LES output in order to provide mean velocity profiles, rms distributions, spectra, etc.. Since the LES only provides the filtered variables, for meaningful comparisons two options are available:

1. The subgrid model provides missing statistics and one may compare the statistics of the unfiltered fields.
2. The data must be filtered at a scale comparable to the LES filter scale and the statistics of the filtered fields are compared.

A posteriori tests are considered to be unambiguous tests of the combined performance of a SGS model coupled with its numerical implementation. Because of their integrated nature, they do not normally provide much insight into the detailed physics of a model and the reasons why they do, or do not, work.

In a priori analysis, one focuses upon the quantities to be modeled, such as the SGS stress or force as computed directly from data according to their definition (10.101), and compares them to model expressions that may depend upon local filtered large-scale variables. Conversely, a priori analysis allows one to focus on particular features of a model under more controlled conditions. However, a priori tests do not account for the feedback that may occur between the SGS model and the resolved scales in an actual simulation. Consequently, it has been found that good a priori behavior does not necessarily imply good performance in simulations (e.g., the similarity model). Nevertheless, by isolating specific features of the SGS physics and models, a priori studies have motivated significant fundamental advances in LES and SGS modeling.

In both a posteriori and a priori studies, one requires well-resolved data that must be filtered in space.

Since LES simulates a range of scales, and one wishes to resolve significant parts of the small-scale motions, the measurement technique must be able to resolve a significant range of length and time scales. These requirements typically imply that multipoint measurement techniques are required in experiments to support LES and SGS model developments. Experimental techniques that can record multipoint data are needed also because LES is often required to predict more than just single-point statistics, for instance spectra or spatial correlation functions.

One of the most interesting aspects of the interactions among small and large scales in LES is the rate at which energy is transferred between these scales. From the transport equations for resolved and SGS kinetic energy (e.g., *Piomelli* et al. [10.157]), this exchange can be identified as the term

$$\Pi_\Delta = -\left\langle \tau_{ij}\tilde{S}_{ij}\right\rangle , \tag{10.108}$$

often called the SGS kinetic-energy dissipation rate. A cascade of kinetic energy from large to small scales is characterized by positive values of Π_Δ. Many SGS stress models are calibrated by matching the modeled and real SGS dissipation, making it a central parameter that needs to be measured during a priori studies. Measurement of Π_Δ consists of evaluating as many components of the SGS stress tensor and filtered strain-rate tensor as are available from the measurement instrument, evaluating the tensor contraction, and time or ensemble averaging to obtain a statistically meaningful result. For isotropic turbulence filtered in the inertial range, the SGS dissipation is almost equal to the viscous dissipation rate [10.4, 137, 140]. As described below, often only a subset of the tensor components needed to evaluate the contractions in (10.108) are available. For instance, if two components of velocity are available in the (x_1, x_2) planes, a two-dimensional (2-D) surrogate of SGS dissipation may be evaluated according to

$$\Pi_{\Delta-2\mathrm{D}} = -(\langle\tau_{11}\tilde{S}_{11}\rangle + \langle\tau_{22}\tilde{S}_{22}\rangle + 2\langle\tau_{12}\tilde{S}_{12}\rangle) . \tag{10.109}$$

For isotropic turbulence these in-plane contributors constitute 7/15 of the total value. To measure the model coefficients in a priori tests, the ensemble-averaged SGS dissipation can be matched to the measured values. For instance, for the Smagorinsky model this leads to the following expression

$$(C_S^\Delta)^2 = \frac{\Pi_\Delta}{\Delta^2\left\langle(2\tilde{S}_{ij}\tilde{S}_{ij})^{\frac{3}{2}}\right\rangle} , \tag{10.110}$$

in which the numerator and denominators can be measured.

10.4.2 Arrays of Single-Point Instruments for Studies of SGS Dynamics

Classical single-point measurement techniques include hot-wire anemometers (Sect. 5.2), laser Doppler anemometers (Sect. 5.3.1), sonic anemometers (Sect. 5.7), Pitot probes, etc. Using a single-point sensor only temporal filtering can be performed. Using Taylor's hypothesis this can be interpreted as one-dimensional spatial filtering in the streamwise direction. Resolving sufficient spatial resolution usually means that good high-frequency response is required (eliminating, for instance, Pitot probes from consideration).

Following this approach and using only single-point sensors (hot-wire probes), *Meneveau* [10.158] and *Meneveau and O'Neil* [10.159] analyzed data in grid turbulence to study stress–velocity correlations and the scaling of dissipation as a function of length scale, respectively, and *O'Neil and Meneveau* [10.160] considered turbulence in a cylinder wake. *Porté-Agel* et al. [10.161] studied turbulence and scalar transport in the atmospheric boundary layer using data from a single sonic anemometer. The accuracy of such one-dimensional (1-D) filtering and Taylor's hypothesis have been addressed for wall-bounded flows using DNS [10.162], LES [10.163], and field-measurement data using 2-D filtering (*Porté-Agel* et al. [10.164], see below). The results show that one-dimensional filtering does not sufficiently filter out the cross-stream variability of the turbulence. For quantitatively accurate results, these analyses show that at least two-dimensional filtering should be used.

The two-dimensional data thus required can be obtained using optical techniques based on light sheets (Sect. 10.4.3 and Sect. 10.4.4). If one is limited to point sensors, an array of point sensors arranged along a line perpendicular to the mean velocity must be used. This approach has been proposed by *Tong* et al. [10.165] and applied in *Porté-Agel* et al. [10.164, 166] and *Horst* et al. [10.167] for sonic anemometer measurements in the atmospheric boundary layer. It has also been applied to hot-wire measurements in laboratory turbulence. Compared to fully 3-D filtering, the accuracy of 2-D filtering and Taylor's hypothesis was found to be quite good based on the DNS [10.162], LES [10.163], and atmospheric field [10.168] studies.

For laboratory turbulence studies using hot-wire arrays, the spatial and temporal resolutions of each sensor

is typically on the order of about 0.5 mm and 10–20 kHz, respectively. Turbulence in wind-tunnel flows typically has Kolmogorov scales on the order of 0.1–0.2 mm and advection velocities on the order of 10 m/s, and thus frequencies on the order of 50 kHz. Therefore, typical hot-wire probes under-resolve the Kolmogorov scale and Kolmogorov advection frequency in the flows considered by factors of about three to five. Also, the spacing between sensors in an array significantly exceeds the Kolmogorov scale η_K, typically by factors of five or more. Thus, these measurements do not fully resolve the viscous dissipation range of turbulence. However, just as Reynolds stresses are dominated by the large-scale turbulence fluctuations and their measurement does not require resolution of the viscous range [10.4], in LES the SGS stresses or scalar fluxes are dominated by scales near the filter scale Δ. Thus to measure the SGS momentum or scalar fluxes with reasonable accuracy, measurement resolutions of $\Delta/10$ to $\Delta/5$ are often considered to be sufficient. Thus, for instance, an experiment with spatial resolution of $5\eta_K$ allows accurate measurement of SGS fluxes at scales of 25 to $50\eta_K$, i. e., scales of interest in the inertial range of turbulence.

A complete analysis of the errors incurred when not fully resolving the entire range of scales is difficult to perform and depends upon the variables of interest. For instance, the error analysis presented in *Cerutti* and *Meneveau* [10.170] shows that, when evaluating the average value of the trace of the SGS tensor ($\langle\tau_{ii}\rangle$) from four probes separated by a distance $\Delta/2$ using a discrete box filter in the cross-stream direction, errors are on the order of 6%. This analysis is based on analytical integration of a theoretical spectrum where one assumes an ideal inertial range of turbulence. Evaluating the actual uncertainty in more complex flows with anisotropic and inhomogeneous statistics is a challenging task.

Results from a priori studies using arrays of point sensors include the works of *Cerutti* and *Meneveau* [10.170] and *Cerutti* et al. [10.171], who used four-probe hot-wire arrays in a wind tunnel to measure filtered turbulence signals and SGS stresses. The results were used to quantify so-called spectral hyperviscosity models. Later, *Kang* and *Meneveau* [10.172] used hot-wire arrays for a study of SGS anisotropy in a turbulent wake, showing that the covariance tensors of SGS quantities and filtered velocity gradients became more isotropic at small scales. However, for third-order moments associated with energy flux and SGS dissipation, the approach to isotropy was exceedingly slow. *Kang* and *Meneveau* [10.173] quantified the direct ef-

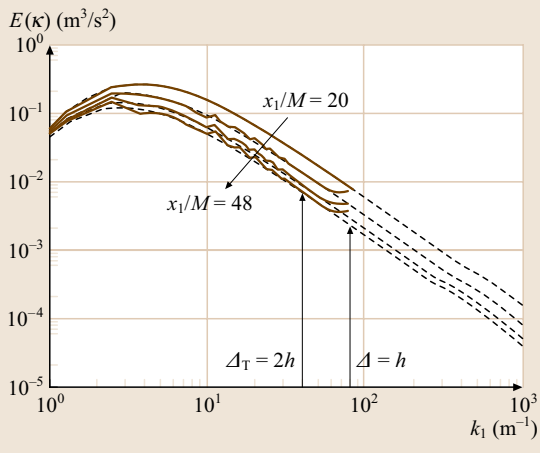

Fig. 10.61 Three-dimensional radial energy spectra in decaying isotropic turbulence. The *solid* and *dashed lines* represent the results from LES (using the dynamic Smagorinsky model) and experiments, respectively. The experimental spectra are shown in their entirety without filtering. The filter cutoff is at wavenumber $k_1 = \pi/\Delta = 78.5\,\mathrm{m}^{-1}$. The test-filter scale is at $k_1 = \pi/2\Delta$. (after *Kang* et al. [10.169], with permission)

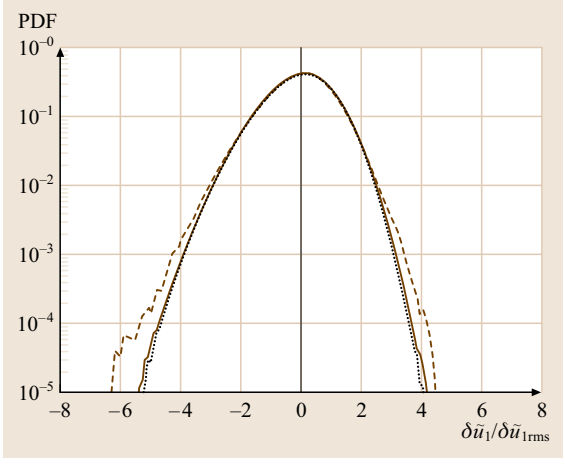

Fig. 10.62 Probability density function of the filtered velocity increment $\delta\tilde{u}_1 = \tilde{u}_1(x_1 + r) - \tilde{u}_1(x_1)$ at a displacement $r = \Delta$ and at 48 mesh sizes downstream of the active grid. The filter size was $\Delta = 0.08$ (m). The velocity increments are normalized with their root-mean-square values. *Dashed line*: experimental data; *dotted line*: Smagorinsky model; *dashed-dot line* (indistiguisheable from dotted line): dynamic Smagorinsky model; *solid line*: dynamic mixed nonlinear model (after *Kang* et al. [10.169], with permission)

fect of coherent structures in a cylinder wake on SGS dynamics and found that they had a surprisingly strong impact across scales, even at filter scales significantly smaller than the size of the coherent structures. Thus the approach to isotropy appears much slower than is assumed in most models for many practical applications of LES. *Chen* et al. [10.174] used hot- and cold-wire arrays consisting of three hot- and cold-wire probes to study a heated turbulent jet flow. Their study focused on joint statistics in the context of filtered density function methods in LES.

Array-filtered data have also been used for a posteriori tests of LES turbulence models. *Kang* et al. [10.169] generated a database from measurements in a wind tunnel (a remake of the *Comte-Bellot* and *Corrsin* [10.175] turbulence decay experiment) behind an active grid. Active grids can generate turbulence at significantly higher Reynolds number [10.176] than passive grids and hence are a useful tool for turbulence generation in LES studies, which typically focus on high-Re flows ($Re_\lambda \approx 720$ was achieved at the first measurement station of *Kang* et al. [10.169]). The energy spectra at four downstream distances from the grid, ranging from 20 to 48 grid-mesh sizes, were measured and documented for subsequent initialization of, and comparison with, LES. The data were recorded using an array of four X-wire probes with which different filter sizes could be achieved by varying the probe separation. Besides the spectra, higher-order statistics of the filtered velocity were quantified by measuring probability density functions, hyperflatness and skewness coefficients of two-point velocity increments. The data were used to study the ability of LES to reproduce both the spectral and higher-order statistics of the resolved velocity field. Specifically, the Smagorinsky, dynamic Smagorinsky, and dynamic mixed nonlinear models were considered. Overall, it is found that these various LES models predicted accurate low-order statistics and spectra of resolved scales in isotropic turbulence during the decay. For instance, Fig. 10.61 shows the time evolution of radial energy spectra deduced from the experimental data; the solid lines are the results from LES using the dynamic model. As can be seen, there is very good agreement in the range of wavenumbers resolved by the LES, except for a small pile-up of energy next to the cutoff wavenumber.

To quantify the ability of LES to reproduce higher-order statistics, probability density functions of filtered velocity increments were measured and compared to LES; the results are shown in Fig. 10.62. It can be seen that the three models underpredicted the intermittency of longitudinal velocity increments at small distances.

Turbulence in the atmospheric surface layer also poses important modeling challenges for LES. Various experimental field campaigns to deploy arrays of sonic anemometers have been undertaken. *Tong* et al. [10.163] and *Porté-Agel* et al. [10.164] performed experiments in which a horizontal array of sonic anemometers, at a single height, was used to sample the wind turbulence fluctuations. A next generation of experiments [10.166, 167, 177, 178] incorporated another horizontal array of sonic anemometers at a second height, allowing vertical gradients to be evaluated in conjunction with 2-D horizontal filtering. Such a configuration allowed for the computation of the full filtered strain-rate tensor, and comparisons of all tensor components and associated geometric alignments. A priori studies of the Smagorinsky model coefficient measured again using (10.110) were performed [10.178]. Results were used to quantify the effects of atmospheric thermal stratification and distance to the ground on the characteristic trends of the coefficient. *Kleissl* et al. [10.179] used test filtering at various scales to examine the performance of the dynamic (see [10.141]) and scale-dependent dynamic (see [10.180]) models based on the data. They found that the scale-dependent version of the model gave much better predictions of the coefficients and the trends that had been observed in *Kleissl* et al. [10.178].

10.4.3 Planar Particle Image Velocimetry (PIV) for SGS Dynamics and LES

The ideal experimental data for a priori evaluation of SGS stress models for LES must simultaneously resolve a wide range of length scales at a large number of measurement locations. Consequently, the instantaneous spatial distribution of two or three velocity components in sample planes provided by particle image velocimetry (PIV) (Sect. 5.3.2) is an ideal tool for obtaining such data. Spatial filtering of the instantaneous velocity distribution, typically using a box filter, provides the resolved flow, which can then be derived to obtain the in-plane components of the filtered velocity gradient tensor, frequently used in SGS stress models. The SGS stresses can also be calculated directly, based on the definition given in (10.101). Planar PIV provides entire planes of filtered and SGS variables, while arrays of single-point measurements described in Sect. 10.4.2 provided such data only along a single coordinate (time). 2-D maps of the local, instantaneous SGS dissipation, $(\Pi(\boldsymbol{x}, t))$, de-

fined as in (10.108) but without the averaging operator, can also be obtained from planar PIV data. Its instantaneous value can be positive, i. e., energy flowing from resolved to SGS scales or negative, i. e., backscatter of energy from subgrid to resolved scales. However, its ensemble-averaged value (10.108) is typically, but not always, positive, as described in detail in this section.

Planar PIV data only provides the in-plane components of (contributors to) the SGS dissipation. The first application of PIV data to evaluate SGS stress models was reported in *Liu* et al. [10.149] using 2-D data obtained in the far field of a round jet. Bearing in mind that these measurements were performed during the early 1990s, double-exposure film photography was the only means of obtaining PIV data that could be spatially filtered at different scales to measured trends. Their 56×56 mm negatives were scanned and converted to 5000×5000 pixels arrays, and autocorrelation analysis [10.181] was used to calculate the velocity, taking advantage of the unidirectional flow in the jet. The dissipation rate and related scales of the turbulence were estimated by calculating the ensemble-averaged, radial two-dimensional spectra of both velocity components. Fitting a Kolmogorov spectrum with a -5/3 slope line to the *inertial* part of these spectra provided the dissipation rate.

To account for the missing out-of-plane components, *Liu* et al. [10.149] used various estimates based on assumed local turbulence isotropy. Several spatial filters were used to calculate the SGS stresses and filtered velocity gradients, including:

1. A *box* or *top-hat* filter, i. e., a spatially averaged velocity over a domain with size Δ surrounding a point. The filtered area size ranged from 8×8 to 32×32 velocity vectors. Because of its simplicity, it has been the most popular method.
2. A truncated Gaussian filter.
3. A spectral cutoff filter, which inherently involved significant truncation errors in a velocity field with finite size. Consequently, spectral cutoff filters have had very limited use.

To be consistent with the data that would be available during LES, spatial velocity gradient were calculated using coarse grids, i. e., at scales of the filtered field. The results enabled direct observations of the spatial distributions of stresses in comparison to modeled values. Lack of agreement between the measured stresses and the predictions of the Smagorinsky model with a fixed coefficient was clearly evident, as also confirmed by calculation of the correlation coefficients between measured and predicted stresses. These trends confirmed prior findings based on direct numerical simulations at lower Reynolds numbers [10.147, 148].

10.4.4 Case Studies and Sample Results Using Planar PIV Measurements

To examine the relationships between flow structures at different scales, *Liu* et al. [10.149] decomposed the velocity field into logarithmic bands. Observed similarity and coherence between structures in consecutive bands led to a reformulation of the stress scale-similarity model,

$$\tau_{ij}^{\mathrm{L}} = c_{\mathrm{L}} L_{ij} \,, \tag{10.111}$$

where an overbar indicates filtering at scale $\alpha\Delta(\alpha \geq 1)$, and L_{ij} is the *resolved stress* (10.104), i. e., the stress that would be obtained by filtering products of the resolved velocity components available from the LES data. For $\alpha = 1$, the scale-similarity model coincides with the *Bardina* et al. [10.147] model. The measured correlation coefficients of the similarity model with the measured stress were substantially higher than those of the eddy-viscosity closures, in agreement with visual comparisons between distributions of measured and modeled values. The model coefficient was also calculated by matching the modeled and measured SGS dissipation, i. e.,

$$C_{\mathrm{L}} = \frac{\langle \tau_{ij} \tilde{S}_{ij} \rangle}{\langle L_{ij} \tilde{S}_{ij} \rangle} \,. \tag{10.112}$$

The experimental values were $C_{\mathrm{L}} \approx 1$. The first-order approximation of the similarity model, the nonlinear (or Clark model, *Clark* et al. [10.148]) model (10.107), maintained a high correlation with measured stresses. To avoid stability problems during simulations, already observed by *Bardina* et al. [10.147], these similarity models need to be combined with eddy-viscosity model, leading to a mixed model (for a review of the relevant literature, see *Meneveau and Katz* [10.146] and *Vreman* et al. [10.181]). These models also maintained the high correlation with the measured stress, but the eddy-viscosity term contributed to a positive SGS dissipation, reducing problems associated with numerical instability.

Using the PIV data of *Liu* et al. [10.149], *Meneveau and Katz* [10.182] explicitly evaluated the errors and established the accuracy with which models reproduced flow features at scales falling between the grid and test filters. The analysis demonstrated that the mixed nonlinear model yielded less error than the dynamic Smagorinsky and dynamic mixed model involving the similarity model.

Bastiaans et al. [10.183] used 2-D particle tracking velocimetry (PTV) to examine the SGS stresses, dissipation, and model predictions in a confined free convection flow generated by a transitional thermal plume. Their measured distributions of in-plane stress components and SGS dissipation rate showed regions of mean-energy backscatter within the plume, and on both sides of the impingement region on the upper wall of their facility. A priori testing of the Smagorinsky model showed reasonable qualitative agreement for the shear and wall-normal stress, except for regions located close to the wall, but their values differed within the plume. Predictions of normal SGS stress components by the dynamic model with a wide range of coefficients showed some improvements, but their values were still underestimated. For the shear stress, the dynamic model predictions had the wrong sign. However, inherently, the dynamic model provided reasonable values for the mean SGS dissipation rate. Near the no-slip wall, the predictions of Π_Δ depended on how the dynamic procedure was implemented.

Liu et al. [10.184] studied experimentally the response, evolution, and modeling of SGS stresses during rapid straining of turbulence. A unique experimental setup generated nearly isotropic turbulence with very low mean velocity in a water tank by means of four symmetrically located spinning grids. Spatially uniform rapid axisymmetric expansion, i. e., an axisymmetric stagnation-point flow, was generated by pushing two disks towards each other in the central portion of the tank. The rod connected to each disk was pushed by a cam, which was driven by precision stepping motors. In order to produce time-independent straining, the distance between the plate and the stagnation point $x_\mathrm{p}(t)$ had to be of the form $x_\mathrm{p}(t) = x_\mathrm{p}(t_0)\exp[-S^*(t-t_0)]$, where S^* was the mean strain rate. Consequently the speed of the plates was $U(t) = S^* x_\mathrm{p}(t)$. The shape of the cams was designed to produce the desired displacement.

The velocity was measured using 2-D PIV on a horizontal plane containing the axis of the plate and the stagnation point. The light sheet was generated by a copper vapor laser, and images were recorded on 35 mm film using a movie camera operating at 33 frame/s. An electro-optical image shifting technique involving a ferroelectric liquid crystal [10.185] was used to eliminate the problem of directional ambiguity in the double-exposure images. Each dataset consisted of 10 images. Results of 10 such experiments were used during the data analysis. The initial dissipation rate ε_0 and Kolmogorov scale, $\eta_0 = (\nu^3/\varepsilon_0)^{1/4}$, were again estimated from radial two-dimensional spectra of both velocity components, which had clear inertial ranges with a $-5/3$ slope. One-dimensional spectra obtained for perpendicular planes were used for confirming that local isotropy indeed existed. Subsequently, the rms values of velocity fluctuations provided the integral scale $L_0 = {u'}^3/\varepsilon_0$ the Taylor microscale, $\lambda = u'(15\nu/\varepsilon_0)^{1/2}$, and the Taylor microscale Reynolds number, $Re_\lambda = u'\lambda/\nu$ (=290). The dimensionless straining parameter was $S^* k_0/\varepsilon_0 = 17$, where k_0 was the turbulent kinetic energy prior to straining.

Ensemble and spatial averaging of the PIV data for each phase of the straining process provided S^*, and spatial box filtering provided in-plane SGS stresses and the velocity gradient tensor $\tilde{A}_{ij}$. When straining started, the initially isotropic turbulence became anisotropic, with the compressed τ_{11} increasing and becoming scale dependent immediately, while the extended τ_{22} responded slowly, eventually also increasing, but remaining scale independent. To elucidate the phenomena, the velocity was decomposed into a turbulent part, $u_i^\mathrm{T}(x_i, t)$, and an applied straining part, $U_i(x_i, t)$. Accordingly, the SGS stress was decomposed into three elements: a turbulence part τ_{ij}^T, a cross-term τ_{ij}^C, and an applied straining part τ_{ij}^M, where

$$\begin{aligned}
\tau_{ij}^\mathrm{T} &= \widetilde{u_i^\mathrm{T} u_j^\mathrm{T}} - \tilde{u}_i^\mathrm{T}\tilde{u}_j^\mathrm{T}\,,\\
\tau_{ij}^\mathrm{C} &= \widetilde{u_i^\mathrm{T} U_j} - \tilde{u}_i^\mathrm{T}\tilde{U}_j + \widetilde{U_i u_j^\mathrm{T}} - \tilde{U}_i\tilde{u}_j^\mathrm{T}\,,\\
\tau_{ij}^\mathrm{M} &= \widetilde{U_i U_j} - \tilde{U}_i\tilde{U}_j = \frac{\Delta^2}{12}\frac{\partial U_i}{\partial x_m}\frac{\partial U_j}{\partial x_m}\,.
\end{aligned} \tag{10.113}$$

For spatially uniform mean straining: $\tau_{11}^\mathrm{M} = (\Delta^2/12)\langle\tilde{S}_{11}\rangle^2$, $\tau_{22}^\mathrm{M} = (\Delta^2/12)\langle\tilde{S}_{22}\rangle^2$, $\tau_{12}^\mathrm{M} = 0$. Analysis of the data showed that $\langle\tau_{ij}^\mathrm{T}\rangle \sim \Delta^{\frac{2}{3}}$, in agreement with Kolmogorov scaling, and that $\tau_{ij}^\mathrm{C} \sim \Delta$. The data also confirmed $\tau_{ij}^\mathrm{M} \sim \Delta^2$. At large filter scales, all the stress elements became comparable. The measured data were compared to predictions of rapid distortion theory (RDT [10.186]). Comparing the evolution of the predicted and measured normal stress components, the experimental results were more isotropic than RDT predictions. The evolution of the anisotropy tensor

$$\begin{aligned}
b_{ij}^\tau &= \frac{r_{ij}}{r_{kk}} - \frac{1}{3}\delta_{ij}\,,\\
r_{ij}(t) &= \frac{[\tau_{ij}(t_i)]_{\text{spatially and ensemble-averaged}}}{[\tau_{ij}(t_0)]_{\text{spatially and ensemble-averaged}}}\,,
\end{aligned} \tag{10.114}$$

where t_i represents a certain phase in the straining process, is shown in Fig. 10.63 below (Fig. 12 in *Liu*

et al. [10.184]). As is evident, b_{ij} became increasingly isotropic with decreasing scale. However, even at the largest scale considered (280η), b_{ij} is still less anisotropic than the RDT prediction. This trend is not surprising since the measured characteristic time scale for eddies of size Δ, $T_\Delta = \varepsilon^{1/3}\Delta^{2/3}$, is comparable to the time scale of the applied straining. Thus, the basic assumption of RDT, namely that $S^{*-1} \ll T_\Delta$, does not apply to that study.

Analysis of correlation coefficients between the modeled and measured SGS stresses showed that rapid straining did not affect the high correlation values for the similarity model, and only slightly increased the low correlation coefficients for the Smagorinsky model. Another method for evaluating models was based on the squared error between the real and modeled SGS force, i. e., the divergence of the SGS stresses. The error of the Smagorinsky model was significantly larger than that of the similarity model but both were substantial. Trends of the ensemble-averaged SGS dissipation for each phase of the straining process were also compared to those calculated based on eddy-viscosity and similarity models. During straining the SGS dissipation increased (as expected) and became scale dependent, increasing with filter size. The measured SGS stress model coefficients, calculated using pairs of equations combining (10.110) and (10.112), showed that straining decreased C_L by more than 50%, and more than doubled C_s^2. The latter indicated that a model with fixed coefficients would underpredict dissipation, in contradiction to the expectation that the Smagorinsky model should overdissipate energy in highly strained flows. To explain these trends, the contributions of the turbulent, cross- and applied straining parts of the SGS stress were examined separately, and showed opposing trends. The turbulent part decreased during straining, in agreement with *McMillan and Ferziger* [10.187]. Conversely, the dissipation associated with the cross-term increased substantially, and remained high during straining. The applied straining part increased during the acceleration phase, and slightly decreased during the constant-straining stage. The opposing trends of the similarity and eddy-viscosity models during rapid straining motivated the introduction of a mixed model of the form

$$\tau_{ij}^{\text{mix}} = \sigma c_L L_{ij} - 2(1-\sigma)\left(C_s^\Delta \Delta\right)^2 |\tilde{S}|\tilde{S}_{ij} \,. \quad (10.115)$$

Using previously determined empirical coefficients for each model, i. e., $c_L = 1$ and $C_s^\Delta = 0.09$, the fitted value of $\sigma = 0.30$ was remarkably accurate in predicting the correct total SGS dissipation throughout the entire experiment, including the acceleration stage. The similarity term reproduced the effects of the mixed and mean terms whereas the Smagorinsky term was similar to the dissipation by the turbulent stresses. However, model coefficients that reproduced the correct amount of SGS dissipation severely underpredicted the magnitude of $\langle \tau_{ij} \rangle$ both before and during the distortion. For $\langle \tau_{11} \rangle$ there was a discrepancy of nearly a factor of 3.

Conditional averaging of the data of *Liu* et al. [10.184] was also used by *Meneveau and Katz* [10.188] to study how regions of large-scale straining, rotation, and energy cascade rate were affected the SGS force and dissipation rate. The locally isotropic jet data showed that the SGS force surrounding points of large strain-rate magnitude was nearly radial. In a divergence-free velocity field, the SGS force could only affect the resolved pressure field. Being directed outwards, the SGS force decreased the resolved pressure in regions of high strain-rate magnitude. Similar trends were obtained in regions of large dissipation, but there was no effect of the resolved vorticity. In the rapidly distorted flow, the SGS force in regions of large positive dissipation decreased the resolved pressure, and opposed the mean deformation. In regions of large energy backscatter, the SGS force acted to favor the mean deformation. In terms of model performance, the mixed model fared better than the Smagorinsky or the similarity models alone. However, there were substantial discrepancies between the modeled and predicted forces.

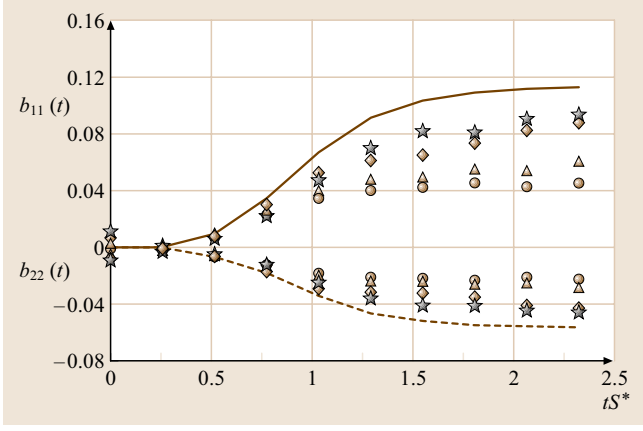

Fig. 10.63 Evolution of the mean subgrid-scale stress during straining of turbulence, as measured using planar PIV. Shown is the anisotropy tensor b_{ij} of normalized stress r_{ij}. The *solid line* and *upper set of symbols*: 11 component; *dashed line* and *lower set of symbols*: 22 component. *Stars*: $\Delta/\eta = 280$, *rhombs*: $\Delta/\eta = 80$, *triangles*: $\Delta/\eta = 40$, *circles*: $\Delta/\eta = 20$; *lines*: 2-D filtered RDT prediction (*Liu* et al. [10.184], with permission from CUP)

The study of the effect of rapid distortion on the dynamics of SGS stresses was expanded in *Chen* et al. [10.189, 190]. A larger experimental setup (Fig. 10.64) was used to generate a controlled planar straining–relaxation–destraining cycle of initially isotropic turbulence.

Locally isotropic turbulence at moderately high Reynolds numbers, with very low mean velocity, was again generated using four symmetrically located active grids. The uniform planar straining was applied by translating a piston vertically at prescribed velocities. The piston occupied almost the entire width of the 20 cm-wide tank. The bottom surface of the piston had rounded corners to prevent possible flow separation, which was critical when the flow was destrained. The piston was driven by a precision, programmable, linear electric actuator.

The piston maximum velocity was 1 m/s, and its maximum displacement was 76.2 cm. The sample area for PIV measurements, 9×9.5 cm, was located near the center-bottom of the tank. The images were recorded using a $2K\times2K$ digital camera at 5 Hz, this time in a cross-correlation mode, synchronized with the piston phase. To increase the number of phases being examined to 48, data were acquired with varying initial delays. The size of the interrogation windows was 32×32 pixels, which with 50% overlap provided 121×121 vectors with a spacing of 0.7 mm. At every phase, 1000 instantaneous realizations gave a sufficient ensemble set for statistical convergence. The evolution of ensemble- and spatially averaged strain rate during the experiments is shown in Fig. 10.65. Spatial spectra at different locations confirmed the existence of local isotropy and homogeneity, and provided estimates for the dissipation rate, for the Kolmogorov scale $\eta_0 \sim 130\,\mu$m, $L_0 = 0.13$ m, $Re_\lambda \sim 400$, and $S_{\max}k_0/\varepsilon_0 \sim 9.5$, where the subscript zero refers to conditions prior to straining.

The Reynolds stress components responded as expected to the applied straining (see Fig. 11 of *Chen* et al. [10.190]). During the first half of the straining phase, with increasing strain magnitude $\langle u'_1u'_1\rangle$, the stress in the extended direction decreased while $\langle u'_2u'_2\rangle$, the stress in the contracted direction, increased. Subsequently, until the end of the relaxation period, $\langle u'_2u'_2\rangle$ decreased gradually and $\langle u'_1u'_1\rangle$ remained approximately constant. At the end of the relaxation regime, the turbulence had not yet returned to an isotropic state. During destraining, the compressed $\langle u'_1u'_1\rangle$ increased rapidly, while $\langle u'_2u'_2\rangle$ continued with its decreasing trend, reaching a minimum value later than the destraining peak. A comparison of the measured stresses and anisotropy tensor to the predictions of RDT showed that RDT gave the correct trends but overestimated $\langle u'_2u'_2\rangle$ and underestimated $\langle u'_1u'_1\rangle$, thus overpredicting the de-

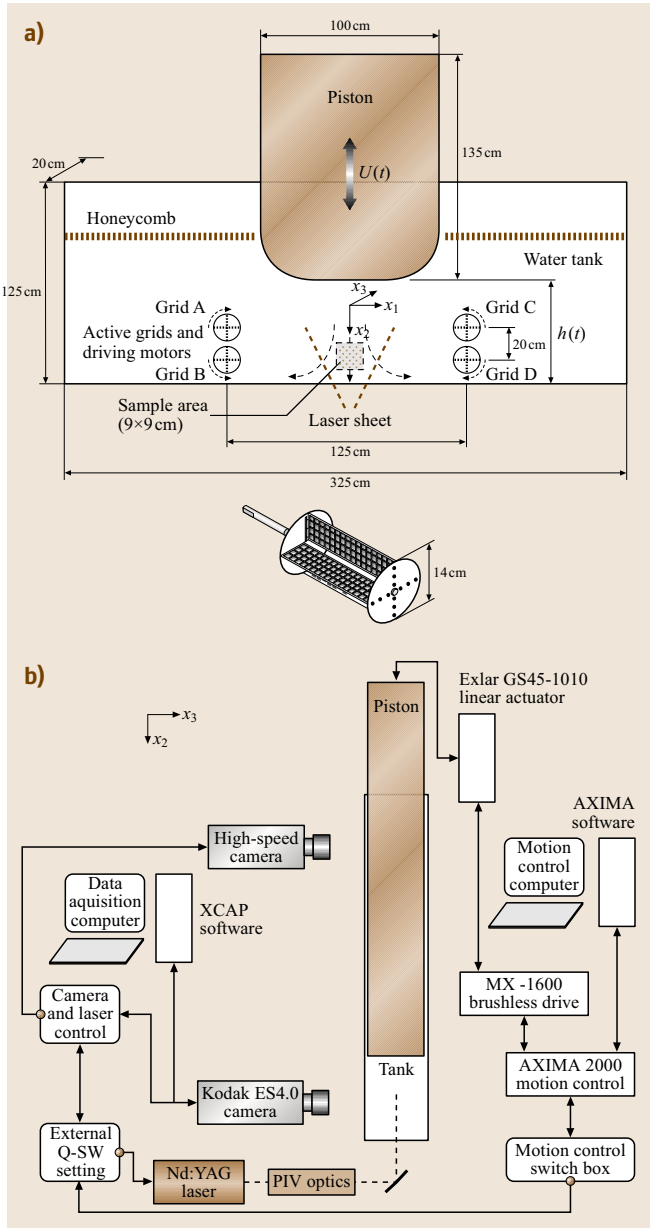

Fig. 10.64a,b Schematic diagram of facility for rapid straining and destraining turbulence experiment. **(a)** Tank and piston and a sketch of the spinning grids. **(b)** Instrumentation used to record PIV data, phase-locked with the piston motion cylce (after *Chen* et al. [10.190] with permission from CUP)

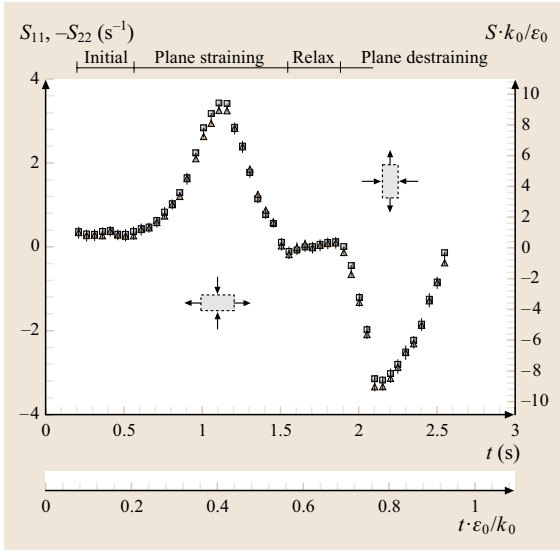

gree of anisotropy. The predicted magnitudes were only comparable to the measured data at initial times. The turbulence production rate

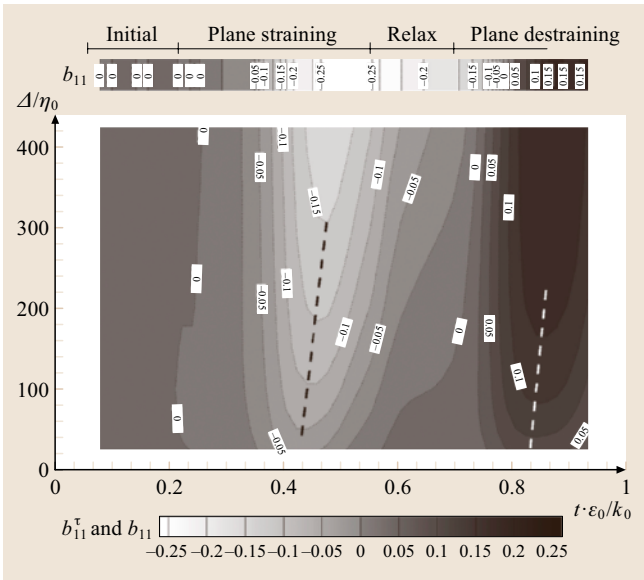

Fig. 10.66 Contour plot of the mean SGS stress anisotropy tensor component (11) as a function of dimensionless time during the straining–destraining cycle, and as function of the filter scale Δ/η. The *top bar* shows the corresponding Reynolds stress anisotropy as a function of time. Measurements were performed using planar PIV (after *Chen* et al. [10.190], with permission from CUP)

Fig. 10.65 Evolution of mean strain, spatially averaged rate S_{11} (*squares*) and S_{22} (*triangles*) during straining and destraining experiment (after *Chen* et al. [10.189], with permission from ASME). The *error bars* represent the standard deviation of spatial distribution. Measurements were performed using PIV

$$\Psi = -\langle u'_i u'_j \rangle \frac{\partial \langle u_i \rangle}{\partial x_j} \approx -\langle u'_1 u'_1 \rangle \times \frac{\partial \langle u_1 \rangle}{\partial x_1} - \langle u'_2 u'_2 \rangle \frac{\partial \langle u_2 \rangle}{\partial x_2} , \quad (10.116)$$

well approximated from the in-plane components, followed the amplitude of the applied strain during the straining period. Once the straining stopped, Ψ vanished. During the destraining period, the production rate became negative initially, and turned to positive values, which were much smaller than those during the straining phase. The occurrence of negative production was a result of $S(t) = \partial\langle u_1 \rangle/\partial x_1 = -\partial\langle u_2 \rangle/\partial x_2$ becoming negative while $\langle u'_1 u'_1 \rangle < \langle u'_2 u'_2 \rangle$.

For homogeneous turbulence, common wisdom is that SGS variables in the LES context will tend to their RANS counterparts as the filter scale approaches the integral scale of turbulence. The PIV data obtained in the strain–destraining experiment were particularly well suited to verify such expectations for a spatially homogeneous, but temporally highly complex, flow. To perform this analysis, the SGS stress was calculated over scales ranging from 25 to $430\eta_0$. Figure 10.66 (*Chen* et al. [10.190]) shows the evolution of $b_{11}^{\tau,2D}$, the mean 2-D surrogate of the anisotropy tensor of the subgrid scales, where

$$b_{ij}^{\tau,2D} = \langle \tau_{ij} \rangle - \frac{1}{2} \langle \tau_{kk} \rangle \delta_{ij} , \quad (10.117)$$

along with the 2D surrogate of the corresponding Reynolds stress anisotropy tensor component, $b_{11}^{Re,2D}$, where

$$b_{ij}^{Re,2D} = \langle u'_i u'_j(t) \rangle / \langle u'_i u'_j(t_0) \rangle - \frac{1}{2} \langle u'_k u'_k(t) \rangle / \langle u'_k u'_k(t_0) \rangle \delta_{ij} \quad (10.118)$$

(definitions used here differ from (10.114) since the present flow is planar while in the experiments of *Liu* et al. [10.184] it was axisymmetric). As is evident, the lag in the response of $b_{11}^{\tau,2D}$ to the applied straining increases with filter scale, i. e., the small scales respond earlier than the large scales. This trend is consistent with RDT, in contrast to the *energy cascade* process, in which the energy is first fed into the large scales, before cascading to small scales. Figure 10.66 also confirms that,

when the spatial filter scale approaches the integral scale, the response lag and magnitude of the SGS stress tend to those of the Reynolds stress. Note that for these data $L_0/\eta_0 \approx 930$, i. e., the largest filter scale, is still less than 50% of the integral scale.

A comparison between the trends of the turbulence production rate and those of $\langle \Pi_{\Delta-2D} \rangle$, presented in Fig. 10.67 (*Chen* et al. [10.190]). Prior to straining and during the relaxation period, the SGS dissipation was nearly scale independent. However, it became scale dependent during the straining and destraining periods. The SGS dissipation peak during destraining was only about 50% of the peak during straining, in spite of the fact that the amplitudes of straining and destraining were about the same. For large filter size, at the beginning of the destraining phase $\langle \Pi_{\text{D-2D}} \rangle$, became negative, i. e., there was energy backscatter, also consistent with the occurrence of negative production during the same period. This was caused by differences in the initial conditions, which for the straining phase was isotropic turbulence but for the destraining phase involved anisotropic turbulence that arose from a relaxation period that was too short to allow the turbulence to return to isotropy. When the contributions to the SGS dissipation were decomposed into turbulent, mixed, and mean straining parts, the turbulent contribution was by far the most dominant. These results further confirm that, as Δ approaches L_0, the mean SGS dissipation tends toward Ψ. The difference in their magnitudes occurs in part due to the scale gap, but mostly due to the missing out-of-plane components in $\langle \Pi_{\text{D-2D}} \rangle$. *Chen* et al. [10.190] also examined the evolution of energy spectra during the straining–destraining cycle. This analysis confirmed that small scales responded earlier than large scales to the straining. Furthermore, they also showed that RDT gave relatively good predictions during early phases of the cycle, especially at large scales, for which the underlying assumptions of RDT were better satisfied. As relaxation started, the data and predictions deviated from each other, as expected.

The evolution of the Smagorinsky coefficient C_s^2 was measured [10.189] from the PIV data (using (10.110)); C_s^2 decreased as straining or destraining started since $2\Delta^2 \langle |\widetilde{S}| \widetilde{S}_{ij} \widetilde{S}_{ij} \rangle$ responded more quickly to the applied strain than the SGS dissipation, but then increased above the equilibrium value. This deviation increased with Δ. The standard dynamic Smagorinsky coefficient, $(C_s^{\Delta,\text{dyn}})^2$, also calculated from the data but using (10.106) with $\alpha = 2$, was compared to $(C_s^{\Delta})^2$. Results showed that the dynamic model overpredicted the response to straining and destraining. Furthermore, the

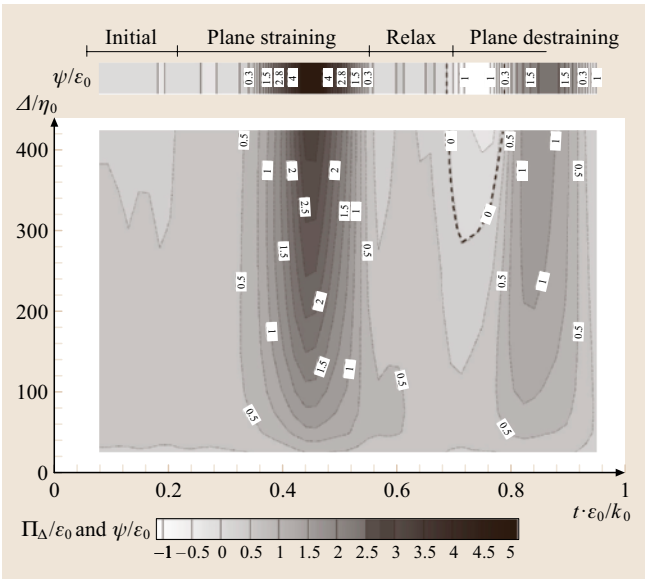

Fig. 10.67 Contour plot of mean SGS dissipation rate as a function of dimensionless time during the straining–destraining cycle, and as a function of filter scale Δ/η. The *top bar* shows the corresponding Reynolds production as function of time. The *dashed line* denotes the zero contour, meaning that in the enclosed top U-shaped region, the mean SGS dissipation is negative. (After *Chen* et al. [10.190], with permission from CUP)

scale-dependent dynamic model [10.161, 179] was also tested, now involving a second test-filter scale of 4Δ. Results did not improve and, in parts of the cycle, were even worse. Examination of the coefficients of the nonlinear dynamic mixed models showed only limited improvements over the standard dynamic Smagorinsky model results. The data were used to trace the origin of these behaviors to scale-dependent variations of the response time of turbulence to the applied straining. They showed that, even in a spatially simple (but temporally complex) flow, serious modeling challenges for LES remain.

Use of PIV data for the analysis of SGS dynamics in spatially complex flow environments with nonuniform mean flow poses further special challenges. For example, the flow structure within turbomachines involves interactions between multiple wakes generated by upstream blades with wakes and blades located downstream. Consequently, the spatial scales of the mean flow and turbulence are comparable in magnitude to the resolution of PIV measurements. Spatial filtering of such a flow field separates both the mean (phase-averaged) flow as well as the turbulence to the mean and subgrid parts, each with its own kinetic energy and fluxes.

As described in *Chow* et al. [10.191], the existence of multiple energy and flux terms may lead to confusion about the relationships between the RANS production rate (Ψ) and the SGS dissipation of kinetic energy. Their experiments were performed in a two-stage axial turbomachine flow-visualization facility containing fluid (a solution of NaI in water) with an optical index of refraction that matched that of the acrylic blades. The unobstructed view of the entire stage enabled 2-D and stereo PIV measurements in numerous sample planes. Data provided insight into the flow within turbomachines at unprecedented levels of detail, enabling the investigation of various wake–blade, wake–wake, and wake–boundary layer interactions. Such data provided a unique database for both a posteriori and a priori testing of turbulence models. The data have already been used for a posteriori testing of RANS models [10.192].

For a priori LES studies, the data were used to examine the SGS dissipation in a near-rotor wake. There the PIV data showed that the phase-averaged SGS dissipation could be negative, even when the Reynolds production rate was positive. Negative mean SGS dissipation was also measured within the stator of a centrifugal pump [10.193]. An attempt to elucidate this paradoxical result led to the identification of all the relevant kinetic-energy and energy-flux terms that resulted from spatial filtering, followed by ensemble averaging of data as one would do while analyzing the SGS dynamics. The total spatially filtered and ensemble-averaged kinetic energy, $\langle\widetilde{K}\rangle$, was decomposed into four parts,

$$\langle\widetilde{K}\rangle \equiv 0.5\langle\widetilde{u_i}\widetilde{u_i}\rangle = K^{\mathrm{mr}} + K^{\mathrm{ms}} + K^{\mathrm{fr}} + K^{\mathrm{fs}} , \tag{10.119}$$

where $K^{\mathrm{mr}} = 0.5\langle\tilde{u}_i\rangle\langle\tilde{u}_i\rangle$ and $K^{\mathrm{ms}} = 0.5(\widetilde{\langle u_i\rangle\langle u_i\rangle} - \langle\tilde{u}_i\rangle\langle\tilde{u}_i\rangle)$ are the mean resolved (mr) and the mean subgrid (ms) kinetic energies, respectively; $K^{\mathrm{fr}} = 0.5\langle\widetilde{u'_i u'_i}\rangle$ is the fluctuating resolved (fr) kinetic energy, and $K^{fs} = 0.5(\langle\widetilde{u'_i u'_i}\rangle - \langle\tilde{u'}_i\tilde{u'}_i\rangle)$ is the fluctuating subgrid (fs) kinetic energy. Distributions of these components for the rotor near wake, using a box spatial filter of 5×5 vectors ($\approx 25\%$ of the near wake width), are presented in Fig. 10.68

The values of $K^{\mathrm{mr}}_{\mathrm{rel}}$, the only non-Galilean invariant term, are presented in the rotor frame of reference; K^{ms} has a two-layer structure as the boundary layers on both sides of the blade extend to the wake region. This represents the kinetic energy lost when a nonuniform mean flow field is spatially filtered, and has nothing to do with the turbulence. It decays at a faster rate than the other terms, in part due to wake spreading and the use of a fixed filter size, which increases the mean resolved part at the expense of the mean subgrid part. The distribution of K^{fr}, the resolved part of the turbulent kinetic energy, is biased toward the suction side, indicating higher injections of resolved turbulence

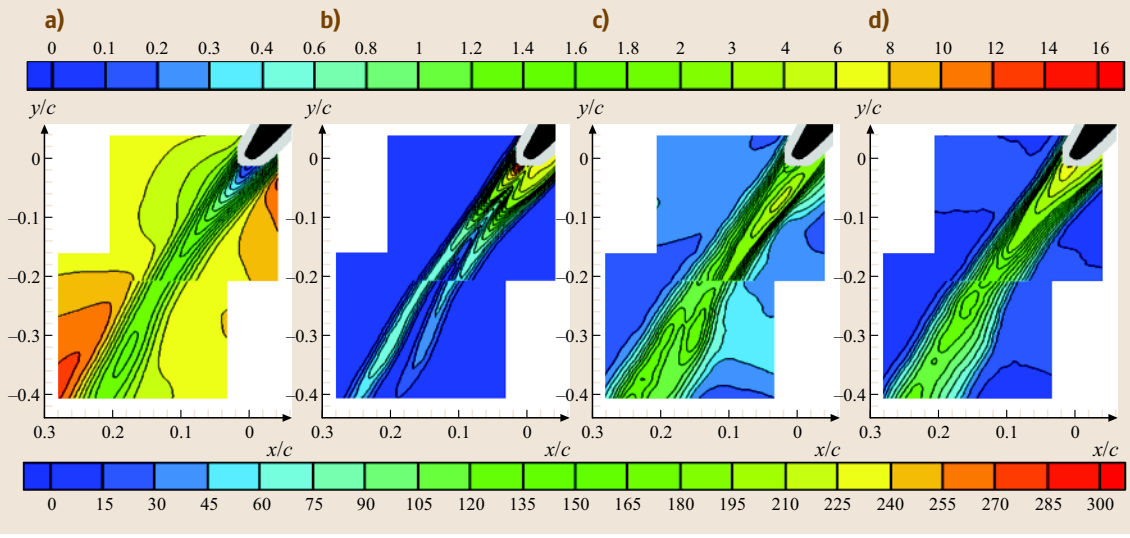

Fig. 10.68a–d Distributions of **(a)** $K^{\mathrm{mr}}_{\mathrm{rel}}$ **(b)** K^{ms} **(c)** K^{fr}, and **(d)** K^{fs} normalized by $U^2_{\mathrm{tip}} 3\times10^{-3}$ measured using PIV in an index-matched turbomachine facility. The *gray mask* around the blade covers points where spatial filtering overlaps with the blade (after *Chow* et al. [10.191], with permission from AIP)

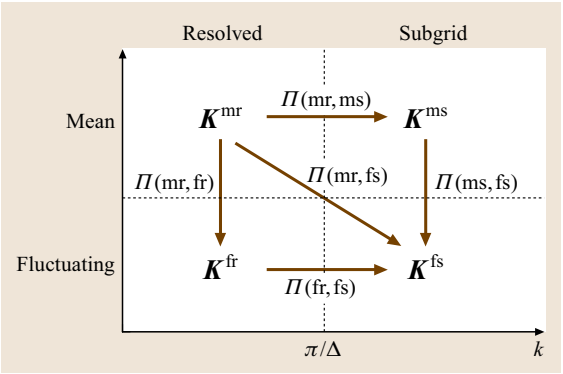

Fig. 10.69 A diagram showing the components of the kinetic energy and energy fluxes between them (after *Chow* et al. [10.191], with permission from AIP)

from the suction-side boundary layer. Regions of elevated turbulence on both sides of the rotor wake are caused by chopped wake segments of the upstream blades.

The evolution equations for each of the four kinetic-energy parts can be used to define various energy fluxes across the various regions. Specifically, it was shown in *Chow* et al. [10.191] that defining the following stresses and strain rates as $\tau_{ij}^{m} = \widetilde{\langle u_i\rangle\langle u_j\rangle} - \langle\tilde{u}_i\rangle\langle\tilde{u}_j\rangle$, $\tau_{ij}^{f} \equiv \langle\widetilde{u_i'u_j'}\rangle - \langle\tilde{u}_i'\tilde{u}_j'\rangle$, $\tau'_{ij} = \tau_{ij} - \langle\tau_{ij}\rangle$, $S'_{ij} = S_{ij} - \langle S_{ij}\rangle$ and $R_{ij}^{r} = -\langle\tilde{u}'_i\tilde{u}'_j\rangle$, the energy fluxes between the different kinetic energy parts are

$$\begin{aligned}
\Pi(\mathrm{mr,ms}) &= -\tau_{ij}^{m}\langle\tilde{S}_{ij}\rangle\,,\\
\Pi(\mathrm{mr,fs}) &= -\tau_{ij}^{f}\langle\tilde{S}_{ij}\rangle\,,\\
\Pi(\mathrm{mr,fr}) &= R_{ij}^{r}\langle\tilde{S}_{ij}\rangle\,,\\
\Pi(\mathrm{ms,fs}) &= \widetilde{R_{ij}\langle S_{ij}\rangle} - \tilde{R}_{ij}\langle\tilde{S}_{ij}\rangle\,,\\
\Pi(\mathrm{fr,fs}) &= -\left\langle\tau'\tilde{S}'_{ij}\right\rangle\,. \qquad (10.120)
\end{aligned}$$

In these expressions the energy fluxes are denoted as Π (donor, receiver). For clarity, the relationships between the various terms and fluxes are illustrated in Fig. 10.69, and the distributions of in-plane contributions to these flux terms are presented in Fig. 10.70. The sum of energy fluxes from the resolved to subgrid scales, i. e., in the horizontal direction in Fig. 10.69, is the ensemble-averaged SGS energy flux of (10.108)

$$\begin{aligned}
\Pi_{\Delta} &= -\langle\tau_{ij}\tilde{S}_{ij}\rangle = \Pi(\mathrm{mr,ms})\\
&\quad + \Pi(\mathrm{mr,fs}) + \Pi(\mathrm{fr,fs})\,. \qquad (10.121)
\end{aligned}$$

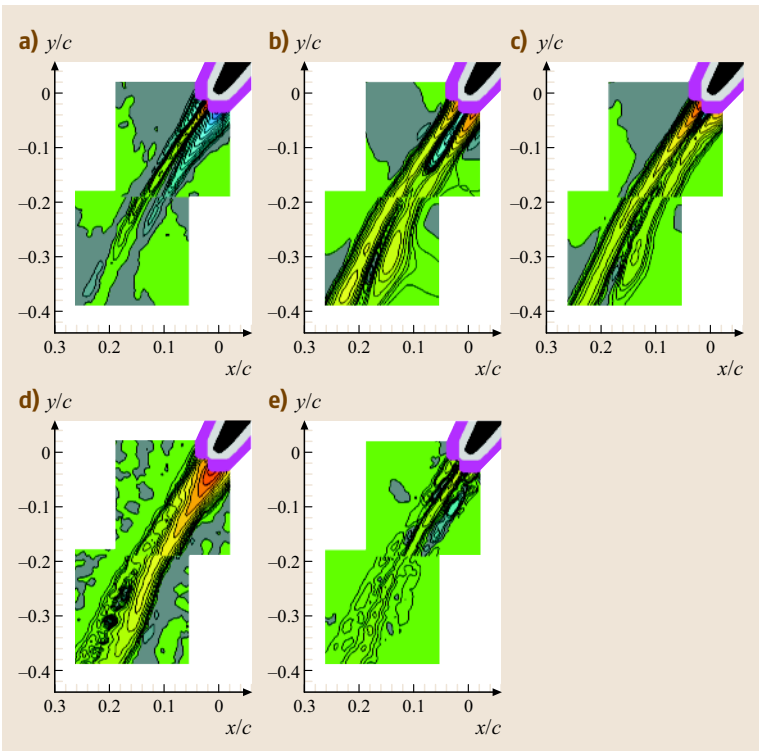

Fig. 10.70a–e Distributions of **(a)** $\Pi(\mathrm{mr,ms})$, **(b)** $\Pi(\mathrm{mr,fr})$, **(c)** $\Pi(\mathrm{mr,fs})$, **(d)** $\Pi(\mathrm{ms,fs})$, and **(e)** $\Pi(\mathrm{fr,fs})$. All quantities are normalized by $U_{\mathrm{tip}}^3/c^3 10^{-3}$ (after *Chow* et al. [10.191], with permission from AIP)

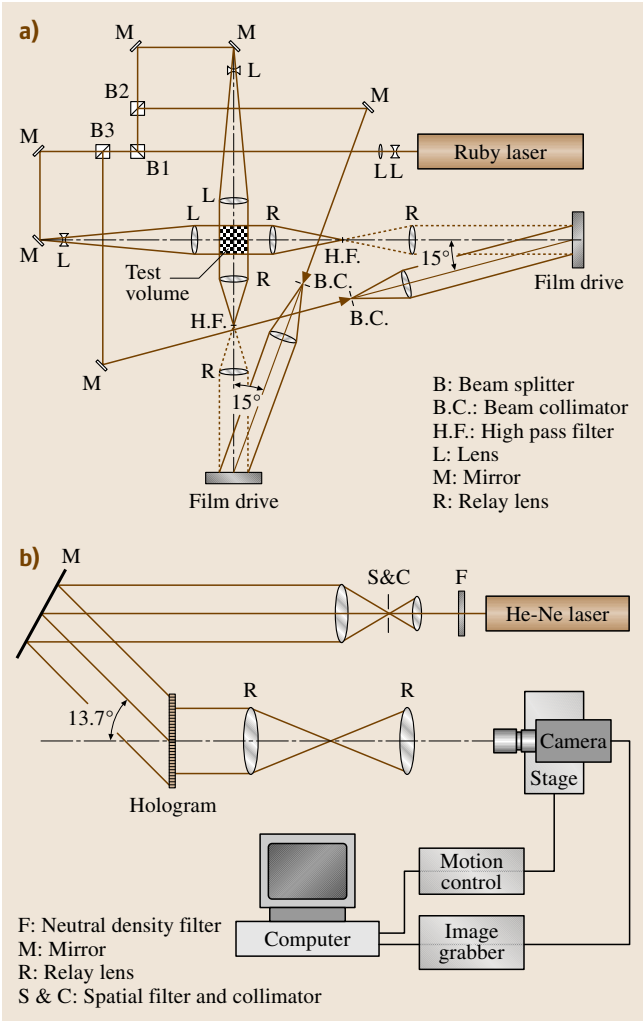

Fig. 10.71a,b Optical setup of: **(a)** the dual-view, hybrid off-axis HPIV system; and **(b)** reconstruction and scanning systems. (After *Tao et al.* [10.194], with permission from CUP)

The sum of fluxes from the mean components to the fluctuating parts, i. e., downward in Fig. 10.69, is the filtered kinetic-energy production rate,

$$\tilde{\Psi} = \widetilde{R_{ij}\langle S_{ij}\rangle} = \Pi(\mathrm{mr,fr}) + \Pi(\mathrm{mr,fs}) + \Pi(\mathrm{ms,fs})\,. \tag{10.122}$$

As is evident, $\tilde{\Psi}$ and $\tilde{P}$ have only one common term Π(mr,fs). Note that Π(mr,ms) involves only the mean flow, i. e., it has nothing to do with the turbulence, but it has a substantial impact on the SGS dissipation. The negative areas seen in Fig. 10.70 emanating from the boundary layers on both sides of the blade indicate flux from the subgrid to the resolved scales due to the growth of the wake. The highest positive flux occurs from the mean subgrid to the fluctuating subgrid kinetic energy [Π(ms,fs)]. This term dominates the total production rate, i. e., most of the turbulence is produced by the subgrid mean flow. Negative production of resolved turbulence [Π(ms,fr)] occurs downstream of the blade trailing edge as the boundary-layer turbulence is fed into a region with adverse velocity gradients. This analysis highlights that the production and SGS dissipation rate may have substantially different trends and magnitudes in spatially nonuniform flows. The results also highlight the usefulness of planar PIV data with good spatial resolution in elucidating important concepts at the interface between LES and RANS.

10.4.5 Holographic PIV Measurements of SGS Dynamics

Holographic particle image velocimetry (HPIV) is an experimental technique that provides three-dimensional velocity distributions and their gradients within a sample volume with extended depth. This technique consists of recording double-exposure holograms of a flow seeded with particles, and determining the 3-D velocity distributions by measuring the displacements of these particles. Until recently, holograms have been recorded only on high-resolution film, and then reconstructed optically to create a 3-D image of the original sample volume. The 3-D images are scanned to obtain 2-D slices through the 3-D volume, and then analyzed using various PIV- or PTV-based techniques. Various methods for recording holograms have been developed with optical setups ranging from simple but resolution-limited, inline holography to complex, high-resolution off-axis holography setups [10.194–201]. Achieving the 3-D vector distributions that can be filtered spatially at different scales, an ideal requirement for studying SGS dynamics, has been a challenge. Consequently, there have been very few applications of HPIV to address issues relevant to LES.

Tao et al. [10.194, 200] adapted an off-axis optical technique that had been introduced by *Zhang* et al. [10.197]. As illustrated in Fig. 10.71, this hybrid system combined the advantages of both inline and off-axis holography without having their drawbacks. In this setup, the subject beam illuminated the sample volume along the optical axis and the film recorded forward-scattered light from particles, similar to inline holography. However, a separate beam was used

as the reference. A spatial high-pass filter was introduced between the sample volume and the film drive. It consisted of two identical lenses separated by twice their focal lengths and a pin installed at the focus of the first relay lens. The unscattered part of the subject beam was focused by the first relay lens and blocked by the pin. However, the light scattered from particles could still reach the film with minimum obstruction. This system reduced the speckle noise associated with inline holography, and allowed an increase in the intensity of the subject beam without overexposing the film.

This hybrid method provided the two velocity components that were perpendicular to the optical axis at high accuracy ($\approx 1\%$). The third component was significantly less accurate due to the *depth-of-focus problem*, namely that the traces of a particle persisted in out-of-plane sections over a substantial depth of about 1 mm. Several potential methods to overcome or at least alleviate this problem have been introduced, but none has succeeded in providing data in all three directions at the same level of precision in applications involving large volumes. The only available option to maintains a comparable level of accuracy was to record two perpendicular (or inclined) holograms simultaneously, as shown in Fig. 10.71a. Each hologram provided two velocity components and the 3-D data was obtained by combining the results. Using correlations, the redundant velocity component (out of the plane in the sketch) helped in precision matching of the two sets. Subsequently, *Sheng* et al. [10.201] introduced a technique that maintained the advantages of recording two orthogonal views, but required only one window and one recording system. This method was based on placing a mirror in the test section that reflected the object beam at an angle of 45°. Particles located in the volume in which the incident and reflected beams from the mirror overlapped were illuminated twice in perpendicular directions. Both views were recorded on the same hologram. Recently, (*Sheng* et al. [10.202]) showed that inline digital holographic microscopy substantially alleviated the depth-of-focus problem (but did not eliminate it) to a level that enabled measurements of 3-D particle motions at high resolution using a single view. Additional background on digital holography can be found in *Meng* et al. [10.203].

The HPIV measurements reported in *Tao* et al. [10.194, 200] were performed within a fully developed turbulent water flow in a square duct with a width H of 57 mm, and center-line mean velocity U of 2.1 m/s. The sample volume was $57 \times 57 \times 45\,\text{mm}^3$. The water was seeded with neutrally buoyant 20 μm particles at a concentration of $8-12\,/\text{mm}^3$. Double-exposure holograms, delayed by 60 μs, were recorded, and reconstructed using the setup of Fig. 10.71b. The illumination angle accounts for reference-beam angle and wavelength differences. A video camera equipped with a microscope objective automatically scanned the sample volume at a resolution of 4.9 μm/pixel, patched the images, enhanced them, and determined the velocity using in-house-developed PIV procedures [10.204]. The interrogation window size was 192×192 pixel ($0.93 \times 0.93\,\text{mm}^2$). Unlike typical PIV, but similar to *Hart* [10.205], the images were compressed during acquisition and the correlation was computed directly from the compressed data. This approach maintained the high magnification without paying the penalty of a large database.

For the evaluation of SGS stress models for LES, the measurements focused on the 3-D velocity fields away from the immediate vicinity (5.25 mm) of the walls ($y^+ > 10^3$). With 65% overlap between the windows, each data set contained $136 \times 130 \times 128$ vectors with a spacing of 0.33 mm. A sample 3-D velocity map is presented in Fig. 10.72. Based on the measured spectra, the turbulent length scales were: $\eta \approx 100\,\mu\text{m}$, $\lambda \approx 3.4\,\text{mm}$ and $Re_\lambda \approx 310$. The data were filtered by a 3-D, spa-

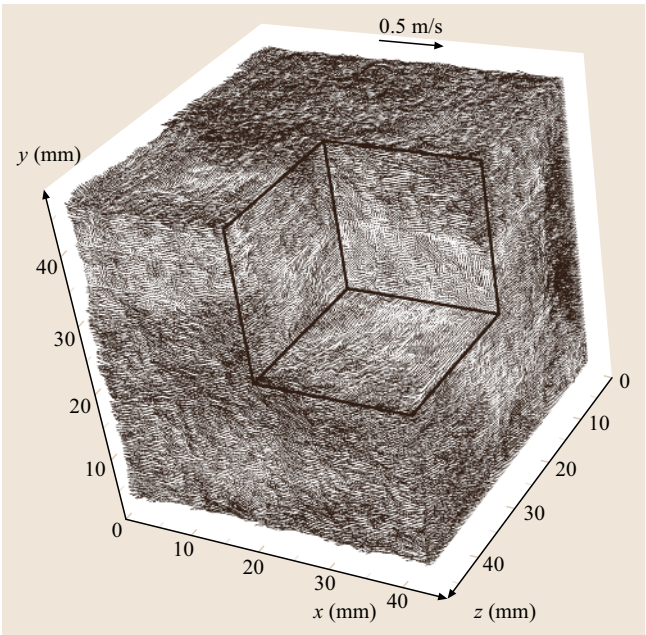

Fig. 10.72 Sample three-dimensional instantaneous vector map of turbulent flow in a square pipe measured using the setup shown in Fig. 10.71 (After *Tao et al.* [10.194], with permission from CUP)

tial box filter at $\Delta = 3.3$ mm ($= 33\eta$), i. e., in the inertial range of turbulence, which provided the SGS stresses, SGS dissipation, along with the filtered vorticity and strain-rate tensor. The uncertainty was about 2% for instantaneous velocity, and 15% for filtered velocity gradients. Data quality was evaluated by determining how well it satisfied the divergence-free condition.

Tao et al. [10.194, 200] examined the alignment trends of filtered vorticity and SGS stress components with respect to the local orientations of the eigenvectors of the filtered strain-rate tensor. Probability density functions (PDF) of scalar parameters characterizing the tensorial eigenvalue structure (following *Lund* and *Rogers* [10.206]) showed that the most probable strain state was axisymmetric extension, and the most probable SGS stress state was axisymmetric contraction. Regions of high SGS dissipation were strongly correlated with these preferred strain-rate and stress topologies. The nonlinear model showed the same trends but overpredicted the occurrence of the preferred stress state.

The relative alignment between SGS stress and strain-rate tensors is a fundamental issue in turbulence modeling since eddy-viscosity model assumes that they are aligned. During analysis, the eigenvalues of $\tilde{S}_{ij}$ were denoted as α_s, β_s and γ_s, where $\alpha_s \geq \beta_s \geq \gamma_s$, and the corresponding eigenvectors were $\boldsymbol{\alpha}_s$, $\boldsymbol{\beta}_s$ and $\boldsymbol{\gamma}_s$. Similarly, $\boldsymbol{\alpha}_{-\tau}$, $\boldsymbol{\beta}_{-\tau}$ and $\boldsymbol{\gamma}_{-\tau}$ denoted unit vectors aligned with the most compressive, intermediate, and most extensive eigenvectors of the deviatoric part of $-\tau_{ij}$, respectively. The data showed that the filtered vorticity vector was preferentially aligned with $\boldsymbol{\beta}_s$, the intermediate strain-rate eigenvector, in agreement with previous numerical and experimental data [10.207–209]. The vorticity was also preferentially aligned perpendicularly to $\boldsymbol{\gamma}_t$ but had no preferred direction in the $\boldsymbol{\alpha}_{-\tau}$–$\boldsymbol{\beta}_{-\tau}$ plane [10.200].

Three angles were needed to define the alignment of a symmetric tensor in a coordinate system defined by the eigenvectors of another symmetric tensor.

Two angles, e.g., $\boldsymbol{\phi}(\boldsymbol{\alpha}_{-\tau} - \boldsymbol{\beta}_s)$ and $\cos[\boldsymbol{\theta}(\boldsymbol{\alpha}_{-\tau} - \boldsymbol{\alpha}_s)]$, define the orientation of one of the eigenvectors of the SGS stress tensor ($\boldsymbol{\alpha}_{-\tau}$ in this example) in a coordinate system defined by the filtered strain-rate eigendirections. The third angle described the orientation of another SGS stress eigenvector with respect to the projection of an axis of the SGS strain rate onto a plane perpendicular to the first SGS eigenvector. This choice preserved statistical consistency, i. e., when tested against a random velocity field these variables generated a uniform 3-D joint PDF.

Figure 10.73a and b show the 3-D joint PDF of alignment between the filtered strain-rate and the SGS stress tensors obtained by analyzing nine instantaneous velocity distributions. The 3-D alignment is presented twice using different basic axial directions in order to demonstrate the dominant features; Fig. 10.73a shows the alignment of the most contracting SGS stress direction $\boldsymbol{\alpha}_{-\tau}$ better, whereas Fig. 10.73b illustrates the alignment of $\boldsymbol{\gamma}_{-\tau}$, the more extensive stress, more clearly. It is observed that $\boldsymbol{\gamma}_{-\tau}$ is preferentially aligned at 32° to $\boldsymbol{\gamma}_S$, i. e., $\cos[\boldsymbol{\theta}(\boldsymbol{\gamma}_{-\tau} - \boldsymbol{\gamma}_s)] \approx 0.85$, irrespective of the other angles. From Fig. 10.73a it is evident that there are actually two distinct regions with high probability peaks. The two preferred 3-D alignments of this bimodal behavior are illustrated by inserts for clarity. The same trends were subsequently also identified in DNS and atmospheric data [10.210], indicating that these trends were not limited to the present flow geometry. Clearly, the SGS stress eigenvectors were not aligned with the filtered stain rate, in contradiction to the basic assumptions of eddy-viscosity models. Conditional averaging demonstrated that the bimodal behavior was related to the vorticity magnitude. The configuration denoted by $\alpha\beta\gamma$–$\beta\alpha\gamma$ was much more pronounced in regions of high vorticity and the configuration $\alpha\beta\gamma$–$\alpha\beta\gamma$ became equally or more dominant in regions with intermediate levels of vorticity. Some of these trends could be explained based on analysis of the nonlinear model assuming the resolved vorticity was aligned with $\boldsymbol{\beta}_s$ and that the strain-rate structure was axisymmetric expansion. This alignment trend persisted, with varying angles and peak probabilities, throughout the conditional samplings based on the magnitudes of SGS dissipation, vorticity, and strain rate [10.194].

Joint PDFs involving the measured and the nonlinear model for SGS dissipation showed significant differences in the trends, even though the nonlinear model stress eigenvectors were preferentially aligned to the same direction as those of the measured stresses. Using a mixed model, the SGS dissipation PDFs agreed better with the experimental data. However, in regions with high strain rate, high vorticity, and especially where the strain rate had a plane shearing or axisymmetric contraction topology, the mixed model still produced excessive negative SGS dissipation.

Using the same data, *van der Bos* et al. [10.211] examined the effects of SGS motions on the dynamics of $\tilde{A}_{ij}$ (10.107) based on the restricted Euler equations [10.212, 213], which was amenable to analytical solution. They showed that the tensor $\partial^2\tau_{kj}/\partial x_i \partial x_k$, i. e., the gradient of the SGS force, appeared in the transport equation of $\tilde{A}_{ij}$. Following *Cantwell* [10.213] they examined the two invariants of $\tilde{A}_{ij}$, namely

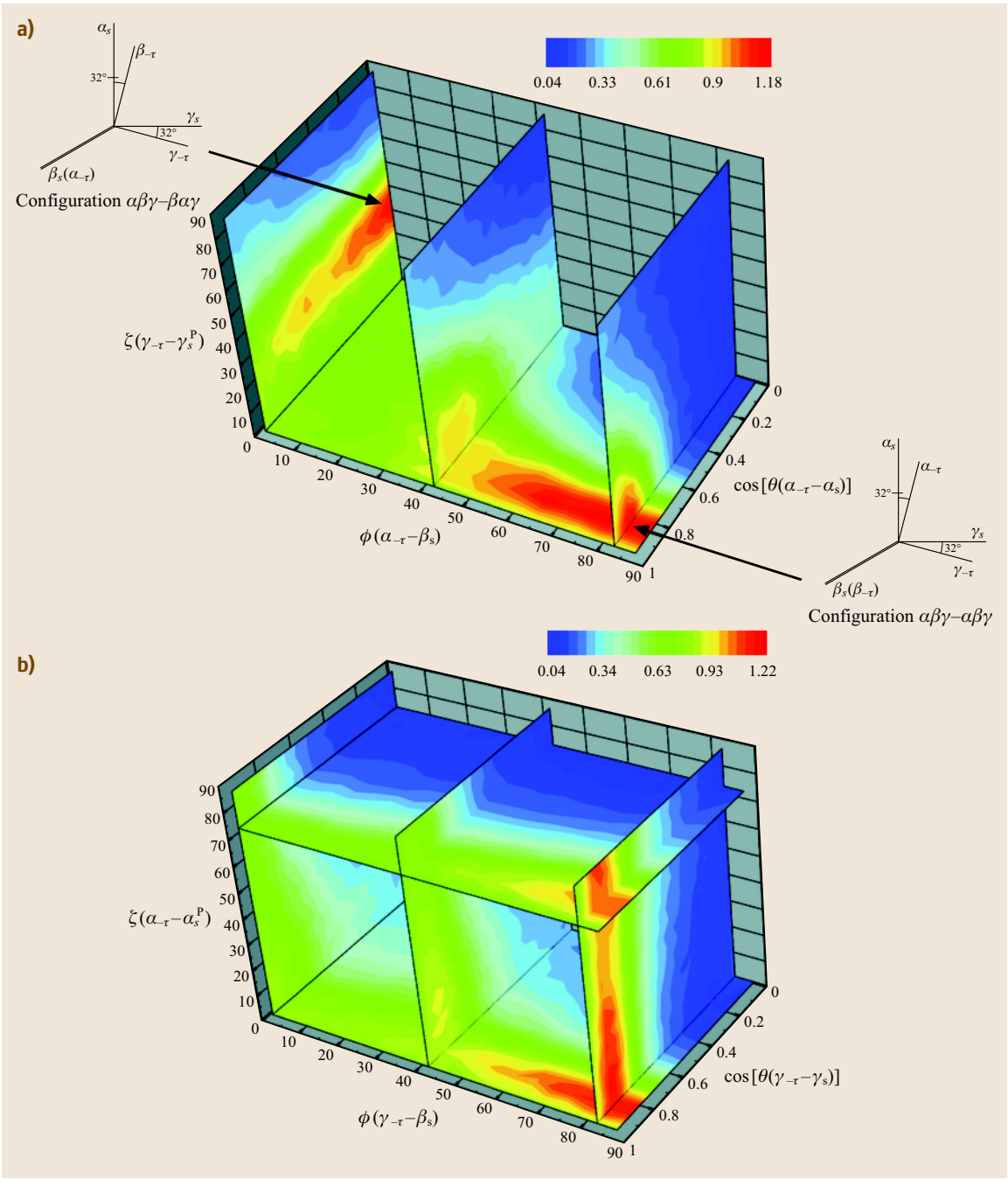

Fig. 10.73a,b The joint PDF of the relative alignment between the eigenvectors of $\tilde{S}_{ij}$ and $-\tau_{ij}^{d}$: **(a)** results based on eigenvector $\boldsymbol{\alpha}_{-\tau}$ and including sketches illustrating the alignment of the SGS stress eigenvectors at the points of peak probability, and **(b)** based on $\boldsymbol{\gamma}_{-\tau}$. In the coordinate system shown, a random alignment would correspond to a uniform probability density of $(\pi/2)^{-2} \approx 0.396$. (After *Tao et al.* [10.194], with permission from CUP)

$Q_\Delta = -\tilde{A}_{im}\tilde{A}_{mi}/3$ and $R_\Delta = -\tilde{A}_{im}\tilde{A}_{mk}\tilde{A}_{ki}/3$. The effects of the SGS stress tensor on Q_Δ and R_Δ was quantified unambiguously by evaluating conditional averages that appear in the evolution equation for the joint probability distribution function of these invariants. The results showed that the SGS stresses opposed the formation of the inherent finite-time singularity along the Vieillefosse tail, which led towards $R_\Delta > 0$ and $Q_\Delta < 0$, and that the effect was significant. Trends in the SGS dissipation and other variables were quantified in different parts of the (Q_Δ, R_Δ) plane. A priori tests of the Smagorinsky, nonlinear, and mixed models showed that all reproduced the real SGS stress effect along the Vieillefosse tail, preventing the finite-time singularity, but they all failed in other regions of the (Q_Δ, R_Δ) plane. The data were also used to suggest improvements to the mixed model.

10.4.6 Scalar Concentration Measurements for SGS Mixing and Combustion Studies

Predicting the transport of scalars caused by turbulence is important for various applications such as combustion, mixing, aero-optics. As mentioned before, the prediction of subgrid variance and the scalar-variance dissipation rate are crucial ingredients in a number of LES closures for scalar transport and combustion. To measure these variables experimentally one requires well-resolved measurements of the scalar field (e.g., scalar concentration, or temperature). Several techniques for measurements of scalar fields exist. Probably the most commonly employed technique is based on laser-induced fluorescence (LIF). Planar laser-induced fluorescence (PLIF) is described in Sect. 7.4. By assuming a relationship between the recorded intensity of the emitted light and the concentration of the fluorescent dye in the flow, maps of concentration can be recorded.

Scanning a light sheet at very high speed across a volume, *Dahm* et al. [10.214] reconstructed quasi-3-D distributions of scalar concentration and followed its time evolution. Based on these data, *Cook and Riley* [10.153] analyzed various models for the subgrid scalar variance

$$\widetilde{c^2} - \tilde{c}^2 \tag{10.123}$$

and explored predictions from so-called presumed PDF models of mixing. In canonical turbulent flows the spectral characteristics of scalar distributions quite similar to those of the velocity field (including spectral slopes of -1.4 to -1.7 in the inertial–convective subrange), the scalar subgrid variance is also expected to be dominated by the largest of the unresolved scales. Thus spatial resolution is not typically required to reach the smallest scales of the scalar field (typically the Batchelor scale), but rather some fraction of the filtering scale, such as $\Delta/5$ to $\Delta/10$.

Studies of the SGS scalar fluxes

$$q_i = \widetilde{u_i c} - \tilde{u}_i \tilde{c} \tag{10.124}$$

require simultaneous measurement of the scalar concentration and velocity. Such measurements can be performed with coupled PIV and LIF (*Su and Mungal* [10.215]). Analysis of such data has recently been used to study SGS scalar fluxes in a cross-flow turbulent jet (*Sun* and *Su* [10.216]). For the study of SGS turbulent heat fluxes in the atmosphere, arrays of sonic anemometers allow simultaneous measurement of velocity and temperature, and the evaluation of SGS heat fluxes and their properties [10.166, 217]. Since scalar fluxes are expected to be dominated by the largest unresolved scales, spatial resolution down to about $\Delta/5$ to $\Delta/10$ is expected to be sufficient to resolve the most important aspects of the SGS scalar flux.

The same is not true when one wishes to evaluate the scalar dissipation rate

$$\chi = \gamma(\widetilde{(\nabla c)(\nabla c)} - \nabla\tilde{c}\nabla\tilde{c}) \tag{10.125}$$

for which scalar gradients must be resolved at the small scales (i. e., the Batchelor scale). Only very well-resolved data can be used to evaluate the scalar dissipation rate.

PLIF has also been used to measure the scalar surface density for modeling of turbulent combustion [10.218]. The surface density at the subgrid scales can be quantified by the difference

$$|\widetilde{\nabla c}| - |\nabla\tilde{c}| \tag{10.126}$$

and requires the evaluation of scalar gradients at the smallest scales before taking the absolute value and filtering. Due to the limitations of planar LIF, only two of the three gradient terms can be captured and assumptions about the third direction must be made when interpreting the results.

References

10.1 G.K. Batchelor: *An Introduction to Fluid Dynamics* (Cambridge Univ. Press, Cambridge 1967)

10.2 O.A. Ladyzenskaya: *Mathematical Theory of Viscous Incompressible Flow* (Gordon Breach, New York 1970)

10.3 S. Goldstein: Fluid Mechanics in the first half of this century, Annu. Rev. Fluid Mech. **1**, 1–29 (1969)

10.4 S.B. Pope: *Turbulent Flows* (Cambridge Univ. Press, Cambridge 2000)

10.5 L.F. Richardson: *Weather Prediction by Numerical Process* (Cambridge Univ. Press, Cambridge 1922)

10.6 H. Tennekes, J.L. Lumley: *A First Course in Turbulence* (MIT, Boston 1972)

10.7 A. Celani: *Hydrodynamic Turbulence, PhD Course* (Scuola Nazionale Fisica della Materia ISI, Torino 2004)

10.8 H. Tennekes: Eulerian and Lagrangian time microscales in isotropic turbulence, J. Fluid Mech. **67**, 561–567 (1975)

10.9 J.S. Bendat, A.G. Piersol: *Random Data: Analysis and Measurement Procedures* (Wiley Interscience, New York 1971)

10.10 J.O. Hinze: *Turbulence* (McGraw-Hill, New York 1975)

10.11 U. Frisch: *Turbulence: The Legacy of A.N. Kolmogorov* (Cambridge Univ. Press, Cambridge 1995)

10.12 A.S. Monin, A.M. Yaglom: *Statistical Fluid Mechanics: Mechanics of Turbulence* (MIT Press, Boston 1975)

10.13 G.P. Romano, R.A. Antonia: Longitudinal and transverse structure functions in a turbulent round jet: effect of initial conditions and Reynolds number, J. Fluid Mech. **436**, 231–248 (2001)

10.14 H.R.E. Van Maanen: *Retrieval of Turbulence and Turbulence Properties from Randomly Sampled Laser-Doppler Anemometry Data with Noise, PhD Thesis* (TU Delft, Delft 1999)

10.15 J.T. Taylor: The spectrum of turbulence, Proc R. Soc. Lond. A **164**, 476–490 (1938)

10.16 G.P. Romano: Analysis of two-point velocity measurements in near-wall flows, Exp. Fluids **20**, 68–83 (1995)

10.17 P.S. Bernard, J.M. Wallace: *Turbulent Flow: Analysis, Measurement and Prediction* (Wiley, New York 2002)

10.18 W.K. George, H.J. Hussein: Locally axisymmetric turbulence, J. Fluid Mech. **233**, 1–23 (1991)

10.19 T. Zhou, R.A. Antonia, L. Danaila, F. Anselmet: Approach to the 'four-fifths law' for grid turbulence, J. Turbul. **1**, 5.1–5.12 (2000)

10.20 F. Anselmet, R.A. Antonia, M. Ould Rouis: Relations between third-order and second-order structure functions for axisymmetric turbulence, J. Turbul. **1**, 3.1–3.10 (2000)

10.21 L. Danaila, R.A. Antonia, P. Burattini: Progress in studying small-scale turbulence using "exact" two-point equations, New J. Phys. **6**, 128 (2004)

10.22 C. Tropea: Post-processing of Experimental and Numerical Data. In: *von Karman Lec. Ser. 2003-03*, ed. by P. Millan, M.L. Riethmuller (von Karman Institute, Bruxelles 2003)

10.23 W.D. Mc Comb: *The Physics of Fluid Turbulence* (Clarendon, New York 1990)

10.24 L.W.B. Browne, R.A. Antonia, D.A. Sha: Turbulent energy dissipation in a wake, J. Fluid Mech. **179**, 307–326 (1987)

10.25 R.A. Antonia, J. Mi: Temperature dissipation in a turbulent round jet, J. Fluid Mech. **250**, 531–551 (1993)

10.26 L.H. Benedict: *Direct Measurements of Turbulent Dissipation Rate in Flow over a Backwards-Facing Step using LDA. Ph.D. Thesis* (North Carolina State Univ., Raleigh 1995)

10.27 G.P. Romano, F. Bagnoli: The measurement of velocity and velocity gradients in a turbulent channel by using different particle tracers. In: *Advances in Turbulence VI*, ed. by S. Gavrilakis, L. Machiels, P.A. Monkewitz (Kluwer Academic, Dordrecht 1996) pp. 525–526

10.28 L.H. Benedict, R.D. Gould: Towards better uncertainty estimates for turbulence statistics, Exp. Fluids **22**, 129–136 (1996)

10.29 M. Lesieur: *Turbulence in Fluids* (Kluwer Academic, Dordrecht 1990)

10.30 J. Mathieu, J. Scott: *An Introduction to Turbulent Flow* (Cambridge Univ. Press, Cambridge 2000)

10.31 G.K. Batchelor: *The Theory of Homogeneous Turbulence* (Cambridge University Press, Cambridge 1953)

10.32 G.P. Romano, R.A. Antonia, T. Zhou: Evaluation of LDA temporal and spatial velocity structure functions in a low Reynolds number turbulent channel flow, Exp. Fluids **27**, 368–377 (1999)

10.33 R.A. Antonia, R.J. Smalley, T. Zhou, F. Anselmet, L. Danaila: Similarity of energy structure functions in decaying homogeneous isotropic turbulence, J. Fluid Mech. **487**, 245–269 (2003)

10.34 A.N. Kolmogorov: The local structure of turbulence in incompressible viscous fluid for very large Reynolds numbers, Dokl. Akad. Nauk SSSR **30**, 301–305 (1941)

10.35 P.K. Yeung: Lagrangian investigations of turbulence, Annu. Rev. Fluid Mech. **34**, 115–142 (2002)

10.36 H.-G. Maas, A. Gruen, D. Papantoniou: Particle tracking velocimetry in three-dimensional flows – Part 1. Photogrammetric determination of particle coordinates, Exp. Fluids **15**, 133–146 (1993)

10.37 N.A. Malik, T. Dracos, D.A. Papantoniou: Particle tracking velocimetry in three-dimensional flows –

Part 2. Particle tracking, Exp. Fluids **15**, 279–294 (1993)
10.38 H.-G. Maas: Contributions of digital photogrammetry to 3-D PTV. In: *in: Three-Dimensional Velocity and Vorticity Measuring and Image Analysis Techniques*, ed. by Th. Dracos (Kluwer Academic, Dordrecht 1996) pp. 191–207
10.39 T. Dracos: Particle tracking in three-dimensional space. In: *Three-Dimensional Velocity and Vorticity Measuring and Image Analysis Techniques*, ed. by T. by: Dracos. (Kluwer Academic, Dordrecht 1996) pp. 129–152
10.40 M. Virant, T. Dracos: 3D PTV and its application on Lagrangian motion, Meas. Sci. Technol. **8**, 1539–1552 (1997)
10.41 G.A. Voth, K. Satyanarayan, E. Bodenschatz: Lagrangian acceleration measurements at large Reynolds numbers, Phys. Fluids **10**, 2268–2280 (1998)
10.42 J. Mann, S. Ott, J.S. Andersen: *Experimental Study of Relative, Turbulent Diffusion, Risø-R-1036(EN)* (Risø National Laboratory, Roskilde 1999)
10.43 S. Ott, J. Mann: An experimental investigation of the relative diffusion of particle pairs in three-dimensional turbulent flow, J. Fluid Mech. **422**, 207–223 (2000)
10.44 A. La Porta, G.A. Voth, A.M. Crawford, J. Alexander, E. Bodenschatz: Fluid particle accelerations in fully developed turbulence, Nature **409**, 1017–1019 (2001)
10.45 N. Mordant, P. Metz, O. Michel, J.-F. Pinton: Measurement of Lagrangian velocity in fully developed turbulence, Phys. Rev. Lett. **87**, 214501 (2001)
10.46 N. Mordant, J.-F. Pinton, O. Michel: Time-resolved tracking of a sound scatterer in a complex flow: Nonstationary signal analysis and applications, J. Acoust. Soc. Am. **112**, 108–118 (2002)
10.47 G.A. Voth, A. La Porta, A.M. Crawford, J. Alexander, E. Bodenschatz: Measurement of particle accelerations in fully developed turbulence, J. Fluid Mech. **469**, 121–160 (2002)
10.48 N. Mordant, E. Lévêque, J.-F. Pinton: Experimental and numerical study of the Lagrangian dynamics of high Reynolds turbulence, New J. Phys. **6**, 116 (2004)
10.49 N. Mordant, A.M. Crawford, E. Bodenschatz: Experimental Lagrangian acceleration probability density function measurement, Physica D **193**, 245–251 (2004)
10.50 N. Mordant, A. Crawford, E. Bodenschatz: Three-dimensional structure of the Lagrangian acceleration in turbulent flows, Phys. Rev. Lett. **93**, 214501 (2004)
10.51 N. Mordant, P. Metz, J.-F. Pinton, O. Michel: Acoustical technique for Lagrangian velocity measurement, Rev. Sci. Instr. **76**, 025105 (2005)
10.52 A.M. Crawford, N. Mordant, E. Bodenschatz: Joint statistics of the Lagrangian acceleration and velocity in fully developed turbulence, Phys. Rev. Lett. **94**, 024501 (2005)
10.53 B. Lüthi, A. Tsinober, W. Kinzelbach: Lagrangian measurements of vorticity dynamics in turbulent flow, J. Fluid Mech. **528**, 87–118 (2005)
10.54 N.T. Ouellette, H. Xu, E. Bodenschatz: A quantitative study of three-dimensional Lagrangian particle tracking algorithms, Exp. Fluids **40**, 301–313 (2006)
10.55 H. Xu, M. Bourgoin, N.T. Ouellette, E. Bodenschatz: High order Lagrangian velocity statistics in turbulence, Phys. Rev. Lett. **96**, 024503 (2006)
10.56 M. Bourgoin, N.T. Ouellette, H. Xu, J. Berg, E. Bodenschatz: The role of pair dispersion in turbulent flow, Science **311**, 835–838 (2006)
10.57 H. Xu, N.T. Ouellette, E. Bodenschatz: The multifractal dimension of Lagrangian turbulence, Phys. Rev. Lett. **96**, 114503 (2006)
10.58 N.T. Ouellette, H. Xu, M. Bourgoin, E. Bodenschatz: Small-scale anisotropy in Lagrangian turbulence, New J. Phys. **8**, 102 (2006)
10.59 N.T. Ouellette, H. Xu, M. Bourgoin, E. Bodenschatz: An experimental study of turbulent relative dispersion models, New J. Phys. **8**, 109 (2006)
10.60 C.J. Veenman, M.J.T. Reinders, E. Backer: Establishing motion correspondence using extended temporal scope, Artif. Intell. **145**, 227–243 (2003)
10.61 C.J. Veenman, M.J.T. Reinders, E. Backer: Resolving motion correspondence for densely moving points, IEEE T. Pattern Anal. **23**, 54–72 (2001)
10.62 F. Bourgeois, J.-C. Lasalle: An extension of the Munkres algorithm for the assignment problem to rectangular matrices, Commun. ACM **14**, 802–804 (1971)
10.63 A. Gylfason, S. Ayyalasomayajula, Z. Warhaft: Lagrangian measurements of inertial particles in wind tunnel turbulence, Bull. Am. Phys. Soc. **50**, 65 (2005)
10.64 P.J. Zandbergen, D. Dijkstra: Von Kármán swirling flows, Annu. Rev. Fluid. Mech. **19**, 465–491 (1987)
10.65 G.A. Voth: *Lagrangian acceleration measurements in turbulence at large reynolds numbers, PhD thesis* (Cornell Univ., Ithaca 2000)
10.66 A.M. Crawford: *Particle tracking measurements in fully developed turbulence: water and dilute polymer solutions, PhD thesis* (Cornell Univ., Ithaca 2004)
10.67 G.A. Voth, A. La Porta, A.M. Crawford, C. Ward, E. Bodenschatz, J. Alexander: A silicon strip detector system for high resolution particle tracking in turbulence, Rev. Sci. Instr. **12**, 4348–4353 (2001)
10.68 R.Y. Tsai: A versatile camera calibration technique for high-accuracy 3D machine vision metrology using off-the-shelf TV cameras and lenses, IEEE T. Robotic. Autom. **RA-3**, 323–344 (1987)
10.69 G.I. Taylor: Diffusion by continuous movements, Proc. Lond. Math. Soc. **20**, 196–212 (1922)

10.70 L.F. Richardson: Atmospheric diffusion shown on a distance-neighbour graph, Proc. R. Soc. Lond. A **110**, 709–737 (1926)
10.71 A.M. Obukhov: Spectral energy distribution in turbulent flow, Izv. Akad. Nauk SSSR **5**, 453–566 (1941)
10.72 B.L. Sawford: Turbulent relative dispersion, Annu. Rev. Fluid Mech. **33**, 289–317 (2001)
10.73 G.K. Batchelor: The application of the similarity theory of turbulence to atmospheric diffusion, Q. J. R. Meteorol. Soc. **76**, 133–146 (1950)
10.74 N.T. Ouellette: *Probing the Statistical Structure of Turbulence with Measurements of Tracer Particle Tracks* (Cornell Univ., Ithaca 2006)
10.75 K.R. Sreenivasan: On the universality of the Kolmogorov constant, Phys. Fluids **7**, 2778–2784 (1995)
10.76 A. Groisman, V. Steinberg: Elastic turbulence in a polymer solution flow, Nature **405**, 53–55 (2000)
10.77 A. Groisman, V. Steinberg: Efficient mixing at low Reynolds numbers using polymer additives, Nature **410**, 905–908 (2001)
10.78 R.B. Bird, C.F. Curtiss, R.C. Armstrong, O. Hassager: *Dynamics of Polymeric Liquids* (Wiley, New York 1987)
10.79 L.D. Landau, E.M. Lifschitz: *Fluid Mechanics* (Pergamon, Oxford 1987)
10.80 D.J. Tritton: *Physical Fluid Dynamics* (Clarendon, Oxford 1988)
10.81 K. Weissenberg: A continuum theory of rheological phenomena, Nature **159**, 310–311 (1947)
10.82 V. Tirtaatmadja, T. Sridhar: A filament stretching device for measurement of extensional viscosity, J. Rheology **37**, 1081–1102 (1993)
10.83 J.J. Magda, R.G. Larson: A transition occurring in ideal elastic liquids during shear flow, J. Non-Newtonian Fluid Mech. **30**, 1–19 (1988)
10.84 S.J. Muller, R.G. Larson, E.S.G. Shaqfeh: A purely elastic transition in Taylor-Coueete flow, Rheol. Acta **28**, 499–503 (1989)
10.85 R.G. Larson: Instabilities in viscoelastic flows, Rheol. Acta **31**, 213–263 (1992)
10.86 E.S.G. Shaqfeh: Purely elastic instabilities in viscometric flows, Annu. Rev. Fluid Mech. **28**, 129–185 (1996)
10.87 R.G. Larson, E.S.G. Shaqfeh, S.J. Muller: A purely elastic instability in Taylor-Couette flow, J. Fluid Mech. **218**, 573–600 (1990)
10.88 A. Groisman, V. Steinberg: Mechanism of elastic instability in Couette flow of polymer solutions: Experiment, Phys. Fluids **10**, 2451–2463 (1998)
10.89 A. Groisman, V. Steinberg: Elastic versus inertial instability in a polymer solution flow, Europhys. Lett. **43**, 165–170 (1998)
10.90 D.E. Smith, H.P. Babcock, S. Chu: Single-polymer dynamics in steady shear flow, Science **283**, 1724–1727 (1999)
10.91 J.A. Byars, A. Öztekin, R.A. Brown, G.H. McKinley: Spiral instabilities in the flow of highly elastic fluids between rotating parallel disks J, Fluid Mech. **271**, 173–197 (1994)
10.92 M. Avgousti, A.N. Beris: Non-axisymmetric modes in viscoelastic Taylor-Couette flow, J. Non-Newtonian Fluid Mech. **50**, 225–251 (1993)
10.93 A. Öztekin, R.A. Brown: Instability of a viscoelastic fluid between rotating parallel disks: analysis for the Oldroyd-B fluid, J. Fluid Mech. **255**, 473–502 (1993)
10.94 G.H. McKinley, J.A. Byars, R.A. Brown, R.C. Armstrong: Observations on the elastic instability in cone-and-plate and parallel-plate flows of a polyisobutylene Boger fluid, J. Non-Newtonian Fluid Mech. **40**, 201–229 (1991)
10.95 W.R. Dean: Fluid motion in a curved channel, Proc. R. Soc. London Ser. A **121**, 402–420 (1928)
10.96 Y.L. Joo, E.S.G. Shaqfeh: Viscoelastic Poiseuille flow through a curved channel: Anew elastic instability, Phys. Fluids A **3**, 1691–1694 (1991)
10.97 Y.L. Joo, E.S.G. Shaqfeh: A purely elastic instability in Dean and Taylor-Dean flow, Phys. Fluids A **4**, 524–543 (1992)
10.98 Y.L. Joo, E.S.G. Shaqfeh: Observations of purely elastic instabilities in the Taylor-Dean flow of a Boger fluid, J. Fluid Mech. **262**, 27–73 (1994)
10.99 D.V. Boger: A highly elastic constant-viscosity fluid, J. Non-Netonian Fluid Mech. **3**, 87–91 (1978)
10.100 M. Doi, S.F. Edwards: *The Theory of Polymer Dynamics* (Clarendon, Oxford 1988)
10.101 E. Washburn (Ed.): International Critical Tables, Vol. 5 (McGraw-Hill, New York 1929)
10.102 A. Groisman, V. Steinberg: Couette-Taylor flow in a dilute polymer solution, Phys. Rev. Lett. **77**, 1480–1483 (1996)
10.103 H.W. Giesekus: About flow stability of viscoelastic fluids, Rheol. Acta **5**, 239–252 (1968)
10.104 A. Groisman, V. Steinberg: Elastic turbulence in curvilinear flows of polymer solutions, New J. Phys. **6**, 29.1–29.48 (2004)
10.105 T. Burghelea, E. Segre, V. Steinberg: Mixing by polymers: Experimental test of decay regime of mixing, Phys. Rev. Lett. **92**, 164501–1–164501–4 (2004)
10.106 T. Burghelea, E. Segre, I. Bar-Joseph, A. Groisman, V. Steinberg: Chaotic flow and efficient mixing in a microchannel with a polymer solution, Phys. Rev. E **69**, 066305–1–066305–8 (2004)
10.107 T. Burghelea, E. Segre, V. Steinberg: Statistics of particle pair separations in the elastic turbulent flow of a dilute polymer solution, Europhys. Lett. **68**, 529–535 (2004)
10.108 T. Burghelea, E. Segre, V. Steinberg: Validity of the taylor hypothesis in a random spatially smooth flow, Phys. Fluids **17**, 103101(1–8) (2005)
10.109 T. Burghelea, E. Segre, V. Steinberg: Elastic turbulence in a swirling flow, Phys. Fluids **19**, 053104 (2007)

10.110 J. Lumley: On the solution of equations describing small scale deformations, Symp. Math. **9**, 315 (1972)
10.111 A. Groisman, V. Steinberg: Stretching of polymers in a random three-dimensional flow, Phys. Rev. Lett. **86**, 934–937 (2001)
10.112 N. Mordant, J.-P. Pinton, F. Chilla: Characterization of turbulence in a closed flow, J. Phys. II Paris **7**, 1729–1742 (1997)
10.113 J.H. Titon, O. Cadot: The statistics of power injected in a closed turbulent flow: Constant torque forcing versus constant velocity forcing, Phys. Fluids **15**, 625–640 (2003)
10.114 J.R. Stokes, L.J.W. Graham, N.J. Lawson, D.V. Boger: Swirling flow of viscoelatic fluids,Part 1, Part 2, J. Fluid Mech. **429**, 67–153 (2001)
10.115 E. Balkovsky, A. Fouxon, V. Lebedev: Turbulence of polymer solutions, Phys. Rev. E **64**, 056301–1–0563011–4 (2001)
10.116 A. Fouxon, V. Lebedev: Spectra of turbulence in dilute polymer solutions, Phys. Fluids **15**, 2060–2072 (2003)
10.117 U. Frish: *Turbulence: The Legacy of A. N. Kolmogorov* (Cambridge Univ. Press, New York 1995)
10.118 B.I. Shraiman, E.D. Siggia: Scalar turbulence, Nature **405**, 639–646 (2000)
10.119 S. Gerashchenko, C. Chevallard, V. Steinberg: Single polymer dynamics: Coil-stretch transition in a random flow, Europhys. Lett. **71**, 221–227 (2005)
10.120 N. Phan-Thien: Cone-and-plate flow of an Oldroyd-B fluid is unstable, J. Non-Newtonian Fluid Mech. **17**, 37–44 (1985)
10.121 E.S.G. Shaqfeh, D.L. Koch: Polymer stretch in dilute fixed beds of fibres or spheres, J. Fluid Mech. **244**, 17–25 (1992)
10.122 A.B. Mosler, E.S.G. Shaqfeh: The conformation change of model polymers in stochastic flow fields: Flow through fixed beds, Phys. Fluids **9**, 1222–1234 (1997)
10.123 E. Balkovsky, A. Fouxon, V. Lebedev: Turbulent dynamics of polymer solutions, Phys. Rev. Lett. **84**, 4765–4768 (2000)
10.124 M. Chertkov: Polymer stretching by turbulence, Phys. Rev. Lett. **84**, 4761–4764 (2000)
10.125 G.K. Batchelor: Small scale variation of convected quantities like temperature in turbulent fluid, J. Fluid Mech. **5**, 113–167 (1959)
10.126 P.G. de Gennes: Coil-stretch transition of dilute flexible polymers under ultrahigh velocity gradients, J. Chem. Phys. **60**, 5030–5042 (1974)
10.127 M. Chertkov: Passive advection in nonlinear medium, Phys. Fluids **11**, 2257–2262 (1999)
10.128 M. Chertkov: On how a joint interaction of two innocent partmers (smooth advection and linear damping) produces a strong intermittency, Phys. Fluids **10**, 3017–3019 (1998)
10.129 A. Groisman, M. Enzelberger, S.R. Quake: Microfluidic Memory and Control Devices, Science **300**, 955–958 (2003)
10.130 Y.N. Xia, G.M. Whitesides: Soft lithography, Annu. Rev. Mater. Sci. **28**, 153–184 (1998)
10.131 Chi Wu: Laser light-scattering characterization of the molecular weight distribution of dextran, Macromolecules **26**, 3821–3825 (1993)
10.132 M. Chertkov, G. Falkovich, I. Kolokolov, V. Lebedev: Statistics of a passive scalar advected by a large-scale two-dimensional velocity field: Analytic solution, Phys. Rev. E **51**, 5609–5627 (1995)
10.133 E. Balkovsky, A. Fouxon: Universal long-time properties of lagrangian statistics in the Batchelor regime and their application to the passive scalar problem, Phys. Rev. E **6**, 4164–4174 (1999)
10.134 V. Steinberg, A. Groisman: Device and Method for Mixing Substances, US Patent No. **6,632,014 B2**, Oct. 14, 2003
10.135 M. Lesieur, O. Metais: New trends in large-eddy simulations of turbulence, Annu. Rev. Fluid Mech. **28**, 45–82 (1996)
10.136 P. Sagaut: *Large Eddy Simulation for Incompressible Flow*, 3rd edn. (Springer, Heidelberg 2005)
10.137 A. Leonard: Energy cascade in large-eddy simulations of turbulent fluid flows, Adv. Geophys. **18**, 237 (1974)
10.138 B. Vreman, B. Geurts, H. Kuerten: Realizability conditions for the turbulent stress tensor in large-eddy simulation, J. Fluid Mech. **278**, 351–362 (1994)
10.139 J. Smagorinsky: General circulation experiments with the primitive equations, Part 1: The basic experiment, Mon. Weath. Rev. **91**, 99–164 (1963)
10.140 D.K. Lilly: The representation of small-scale turbulence in numerical simulation experiments, Proc. IBM Sci. Comput. Symp. Environ. Sci. **195** (1967)
10.141 M. Germano, U. Piomelli, P. Moin, W. Cabot: A dynamic subgrid-scale eddy viscosity model, Phys. Fluids A **3**, 1760–1765 (1991)
10.142 M. Germano: Turbulence: The filtering approach, J. Fluid Mech. **238**, 325–336 (1992)
10.143 D.K. Lilly: A proposed modification of the Germano subgrid-scale closure method, Phys. Fluids A **4**, 633–635 (1992)
10.144 S. Ghosal, T.S. Lund, P. Moin, W.H. Cabot: A dynamic localization model for large eddy simulations of turbulent flow, J. Fluid Mech. **286**, 299 (1995)
10.145 U. Piomelli: Large eddy simulation: achievements and challenges, Prog. Aerosp. Sci. **35**, 335–362 (1999)
10.146 C. Meneveau, J. Katz: Scale-invariance and turbulence models for large-eddy simulation, Annu. Rev. Fluid Mech. **32**, 1–32 (2000)
10.147 J. Bardina, J. Ferziger, Reynolds: Improved subgrid scale models for large eddy simulation, AIAA Paper **80-1357** (1980)
10.148 R.A. Clark, J.H. Ferziger, W.C. Reynolds: Evaluation of subgrid models using an accurately simulated turbulent flow, J. Fluid Mech. **91**, 1 (1979)

10.149 S. Liu, C. Meneveau, J. Katz: On the properties of similarity subgrid-scale models as deduced from measurements in a turbulent jet, J. Fluid Mech. **275**, 83 (1994)

10.150 V. Borue, S.A. Orszag: Local energy flux and subgrid-scale statistics in three-dimensional turbulence, J. Fluid Mech. **366**, 1–31 (1998)

10.151 S. Stolz, N.A. Adams, L. Kleiser: An approximate deconvolution model for large-eddy simulation with application to incompressible wall-bounded flows, Phys. Fluids **13**, 997–1015 (2001)

10.152 P. Moin, K.D. Squires, W.H. Cabot, S. Lee: A dynamic subgrid-scale model for compressible turbulence and scalar transport, Phys. Fluids A **3**, 2746–2757 (1991)

10.153 A. Cook, J.J. Riley: A subgrid model for equilibrium chemistry in turbulent flows, Phys. Fluids **6**, 2868–2870 (1994)

10.154 C. Jimenez, L. Valiño, C. Dopazo: Subgrid scale variance and dissipation of a scalar field in large eddy simulations, Phys. Fluids **13**, 2433 (2001)

10.155 D. Veynante, L. Vervich: Turbulent combustion modeling, Progr. Energy Combust. Sci. **28**, 193 (2002)

10.156 U. Piomelli, P. Moin, J.H. Ferziger: Model consistency in large eddy simulation of turbulent channel flows, Phys. Fluids **31**, 1884–1891 (1988)

10.157 U. Piomelli, W.H. Cabot, P. Moin, S. Lee: Subgrid scale backscatter in turbulent and transitional flows, Phys. Fluids A **3**, 1766–1771 (1991)

10.158 C. Meneveau: Statistics of subgrid-scale stresses: Necessary conditions and experimental tests, Phys. Fluids **6**, 815 (1994)

10.159 C. Meneveau, J. O'Neil: Scaling laws of the dissipation rate of turbulent subgrid-scale kinetic energy, Phys. Rev. E **49**, 2866 (1994)

10.160 J. O'Neil, C. Meneveau: Subgrid-scale stresses and their modelling in a turbulent plane wake, J. Fluid Mech. **347**, 253–293 (1997)

10.161 F. Porté-Agel, C. Meneveau, M.B. Parlange: Some basic properties of the surrogate subgrid-scale heat flux in the atmospheric boundary layer, Bound. Layer Met. **88**, 425 (1998)

10.162 J.A. Murray, U. Piomelli, J.M. Wallace: Spatial and temporal filtering of experimental data for a-priori studies of subgrid-scale stresses, Phys. Fluids **8**, 1978–1980 (1996)

10.163 C.N. Tong, J.C. Wyngaard, S. Khanna, J.G. Brasseur: Resolvable- and subgrid-scale measurement in the atmospheric surface layer: Technique and issues, J. Atmos. Sci. **55**, 3114–3126 (1998)

10.164 F. Porté-Agel, M.B. Parlange, C. Meneveau, W.E. Eichinger, M. Pahlow: Subgrid-scale dissipation in the atmospheric surface layer: Effects of stability and filter dimension, J. Hydrometero. **1**, 75–87 (2000)

10.165 C.N. Tong, J.C. Wyngaard, J.G. Brasseur: Experimental study of the subgrid-scale stress in the atmospheric surface layer, J. Atmos. Sci. **56**(14), 2277–2292 (1998)

10.166 F. Porté-Agel, M.B. Parlange, C. Meneveau, W.E. Eichinger: A priori field study of the subgrid-scale heat fluxes and dissipation in the atmospheric surface layer, J. Atmos. Sci **58**, 2673–2698 (2001)

10.167 T. Horst, J. Kleissl, D. Lenschow, C. Meneveau, C.-H. Moeng, M.B. Parlange, P.P. Sullivan, J.C. Weil: HATS: Field observations to obtain spatially-filtered turbulence fields from crosswind arrays of sonic anemometers in the atmospheric surface layer, J. Atmos. Sci. **61**, 1655–1681 (2004)

10.168 C. Higgins, C. Meneveau, M.B. Parlange: The effect of filter dimension on the components of the subgrid-scale stress and tensor alignments in the atmospheric surface layer, J. Atmos. Ocean. Tech., **24**, 360 (2007)

10.169 H.S. Kang, S. Chester, C. Meneveau: Decaying turbulence in an active-grid-generated flow and comparisons with large-eddy simulation, J. Fluid Mech. **480**, 129–160 (2003)

10.170 S. Cerutti, C. Meneveau: Statistics of filtered velocity in grid and wake turbulence, Phys. Fluids **12**, 1143–1165 (2000)

10.171 S. Cerutti, C. Meneveau, O.M. Knio: Spectral and hyper eddy-viscosity in high Reynolds number turbulence, J. Fluid Mech. **421**, 307–338 (2000)

10.172 H.S. Kang, C. Meneveau: Universality of LES model parameters across a turbulent wake behind a heated cylinder, J. Turbul. **3**, N32 (2002)

10.173 H.S. Kang, C. Meneveau: Effect of large-scale coherent structures on subgrid-scale stress and strain-rate eigenvector alignments in turbulent shear flow, Phys. Fluids **17**, 055103 (2005)

10.174 Q. Chen, D. Wang, H. Zhang, C. Tong.: Effects of subgrid-scale turbulence on resolvable-scale velocity–scalar statistics, J. Turbul. **6**, N36 (2005)

10.175 G. Comte-Bellot, S. Corrsin: Simple Eulerian time correlation of full- and narrow-band velocity signals in grid-generated, 'isotropic' turbulence, J. Fluid Mech. **48**, 273–337 (1971)

10.176 L. Mydlarski, Z. Warhaft: On the onset of high Reynolds number grid generated wind tunnel turbulence, J. Fluid Mech. **320**, 331–368 (1996)

10.177 F. Porté-Agel, M. Pahlow, C. Meneveau, M.B. Parlange: Atmospheric stability effect on subgrid scale physics for large-eddy simulation, Adv. Water Resour. **24**, 1085–1102 (2001)

10.178 J. Kleissl, C. Meneveau, M.B. Parlange: On the magnitude and variability of subgrid-scale eddy-diffusion coefficients in the atmospheric surface layer, J. Atmos. Sci. **60**, 2372–2388 (2003)

10.179 J. Kleissl, M.B. Parlange, C. Meneveau: Field experimental study of dynamic Smagorinsky models in the atmospheric surface layer, J. Atmos. Sci. **61**(18), 2296–2307 (2004)

10.180 F. Porté-Agel, C. Meneveau, M.B. Parlange: A scale-dependent dynamic model for large-eddy simulation: Applications to a neutral atmospheric boundary layer, J. Fluid Mech. **415**, 261 (2000)

10.181 B. Vreman, B. Geurts, H. Kuerten: Large-eddy simulation of the turbulent mixing layer, J. Fluid Mech. **339**, 357–390 (1997)

10.182 C. Meneveau, J. Katz: Dynamic testing of subgrid models in LES based on the Germano identity, Phys. Fluids **11**, 1 (1999)

10.183 R.J.M. Bastiaans, C.C.M. Rindt, A.A. Van Steenhoven: Experimental analysis of a confined transitional plume with respect to subgrid-scale modelling, Int. J. Heat Mass Transfer **41**, 3989–4007 (1998)

10.184 S. Liu, J. Katz, C. Meneveau: Evolution and modeling of subgrid scale during rapid straining of turbulence, J. Fluid Mech. **387**, 281–320 (1999)

10.185 L. Bertuccioli, S. Gopalan, J. Katz: Image shifting for PIV using birefringent and ferroelectric liquid crystals, Exp. Fluids **21**, 341–346 (1996)

10.186 M.J. Lee: Distortion of homogeneous turbulence by axisymmetric strain and dilation, Phys. Fluids A **1**, 1541–1557 (1989)

10.187 O.J. McMillan, J.H. Ferziger: Direct testing of subgrid-scale models, AIAA. J. **17**, 1340 (1979)

10.188 C. Meneveau, J. Katz: Conditional subgrid force and dissipation in locally isotropic and rapidly strained turbulence, Phys. Fluids **11**, 2317 (1999)

10.189 J. Chen, J. Katz, C. Meneveau: The implication of mismatch between stress and strain-rate in turbulence subjected to rapid straining and destraining on dynamic LES models, J. Fluids Eng. **127**, 840–850 (2005)

10.190 J. Chen, C. Meneveau, J. Katz: Scale Interactions of Turbulence Subjected to a Straining-Relaxation-Destraining Cycle, J. Fluid Mech. **562**, 123 (2006)

10.191 Y.-C. Chow, O. Uzol, J. Katz, C. Meneveau: Decomposition of the spatially filtered and ensemble averaged kinetic energy, the associated fluxes and scaling trends in a rotor wake, Phys. Fluids **17**, 085102 (2005)

10.192 O. Uzol, D. Brzozowski, Y.-C. Chow, J. Katz, C. Meneveau: A Database of PIV Measurements within a Turbomachinery Stage and Sample Comparisons with Unsteady RANS, J. Turbul. **8**, N10 (2007)

10.193 M. Sinha, J. Katz, C. Meneveau: Quantitative visualization of the flow in a centrifugal pump with diffuser vanes, Part B: Addressing passage-averaged and LES modeling issues in in turbomachinery flows, J. Fluids Eng. **122**, 108–116 (2000)

10.194 B. Tao, J. Katz, C. Meneveau: Statistical geometry of subgrid-scale stresses determined from holographic particle image velocimetry measurements, J. Fluid Mech. **467**, 35–78 (2002)

10.195 H. Meng, F. Hussain: In-line recording and off-axis viewing technique for holographic particle velocimetry, Appl. Opt. **34**, 1827–1840 (1995)

10.196 D.H. Barnhart, R.J. Adrian, G.C. Papen: Phase-conjugate holographic system for high-resolution particle-image velocimetry, Appl. Opt. **33**, 7159–7170 (1994)

10.197 J. Zhang, B. Tao, J. Katz: Turbulent flow measurement in a square duct with hybrid holographic PIV, Exp. Fluids **23**, 373–381 (1997)

10.198 Y. Pu, H. Meng: An advanced off-axis holographic particle image velocimetry (HPIV) system, Exp. Fluids **29**, 184–197 (2000)

10.199 S.F. Herrmann, K.D. Hinsch: Light-in-flight holographic particle image velocimetry for wind-tunnel applications, Meas. Sci. Technol. **15**, 613–621 (2004)

10.200 B. Tao, J. Katz, C. Meneveau: Geometry and scale relationships in high Reynolds number turbulence determined from 3-D holographic velocimetry, Phys. Fluids **12**, 941–944 (2000)

10.201 J. Sheng, E. Malkiel, J. Katz: Single beam two-views holographic particle image velocimetry, Appl. Opt. **42**, 235–250 (2003)

10.202 J. Sheng, E. Malkiel, J. Katz: Digital holographic microscope for measuring three-dimensional particle distributions and motions, Appl. Opt. **45**, 3893–3901 (2006)

10.203 H. Meng, G. Pan, Y. Pu, S.H. Woodward: Holographic particle image velocimetry: From film to digital recording, Meas. Sci. Technol. **15**, 673 (2004)

10.204 G.I. Roth, J. Katz: Five techniques for increasing the speed and accuracy of PIV interrogation, Meas. Sci. Technol. **12**, 238–245 (2001)

10.205 D.P. Hart: High-speed PIV analysis using compressed image correlation, J. Fluids Eng. **120**, 463 (1998)

10.206 T. Lund, M. Rogers: An improved measure of strain state probability in turbulent flows, Phys. Fluids **6**, 1838–1847 (1994)

10.207 W.T. Ashurst, A.R. Kerstein, R.M. Kerr, C.H. Gibson: Alignment of vorticity and scalar gradient with strain rate in simulated Navier-Stokes turbulence, Phys. Fluids **30**, 2343–2353 (1987)

10.208 A. Tsinober, E. Kit, T. Dracos: Experimental investigation of the field of velocity gradients in turbulent flows, J. Fluid Mech. **242**, 169–192 (1992)

10.209 A. Vincent, M. Meneguzzi: The dynamics of vorticity tubes in homogeneous turbulence, J. Fluid Mech. **258**, 245–254 (1994)

10.210 C.W. Higgins, M.B. Parlange, C. Meneveau: Alignment trends of velocity gradients and subgrid-scale fluxes in the turbulent atmospheric boundary layer, Bound. Lay. Meteorol. **109**(1), 58–59 (2003)

10.211 F. Van der Bos, B. Tao, C. Meneveau, J. Katz: Effects of small-scale turbulent motions on the filtered velocity gradient tensor as deduced from holographic PIV measurements, Phys. Fluids **14**, 2456–2474 (2002)

10.212 P. Vieillefosse: Local interaction between vorticity and shear in a perfect incompressible fluid, J. Phys. **43**, 837–842 (1982)
10.213 B.J. Cantwell: Exact solution of a restricted Euler equation for the velocity gradient tensor, Phys. Fluids A **4**, 782–793 (1992)
10.214 W.J.A. Dahm, K.B. Southerland, K.A. Buch: Direct, high-resolution, four-dimensional measuremenets of the fine scale structure of $Sc \gg 1$ molecular mixing in turbulent flows, Phys. Fluids A **3**, 1115–1127 (1991)
10.215 L.K. Su, M.G. Mungal: Simultaneous measurements of scalar and velocity field evolution in turbulent crossflowing jets, J. Fluid Mech. **513**, 1–45 (2004)
10.216 Sun O.S., Su L.K.: Experimental assessment of scalar mixing models for large-eddy simulation, AIAA paper 2004-2550 (2004)
10.217 C. Higgins, M.B. Parlange, C. Meneveau: Turbulent heat flux and temperature gradent alignments in the lower atmosphere, Geophys. Res. Lett. **31**, L22105 (2004)
10.218 R. Knikker, D. Veynante, C. Meneveau: A dynamic flame surface density model for large eddy simulation of turbulent premixed combustion, Phys. Fluids **16**, L91–L94 (2004)